11/09/04

AFRL-MN-EG-TR-2004-7112

Comprehensive Property Characterization of Nanotube Buckypaper-Reinforced Composite Materials

Ben Wang

Florida A&M University
Florida State University College of Engineering
Tallahassee, FL 32310-6046

APRIL 2004

CONTRACT NO. F08630-01-1-0010

FINAL REPORT FOR PERIOD - SEPTEMBER 2001 – APRIL 2004

AIR FORCE RESEARCH LABORATORY, MUNITIONS DIRECTORATE

Air Force Materiel Command ■ United States Air Force ■ Eglin Air Force Base

NOTICE

When Government drawings, specifications, or other data are used for any purpose other than in connection with a definitely Government-related procurement, the United States Government incurs no responsibility or any obligation whatsoever. The fact that the Government may have formulated or in any way supplied the said drawings, specifications, or other data, is not to be regarded by implication, or otherwise in any manner construed, as licensing the holder, or any other person or corporation; or as conveying any rights or permission to manufacture, use, or sell any patented invention that may in any way be related thereto.

This technical report is releasable to the National Technical Information Services (NTIS). At NTIS it will be available to the general public, including foreign nations.

Contract Number: F08630-01-1-0010

Contractor: Florida A&M University

This technical report has been reviewed and is approved for publication.

FOR THE COMMANDER

FREDRICK A. DAVIS
Technical Director
Assessment and Demonstrations Division

CHARLES J. COTTRELL
Program Manager

Anyone having need for a copy of this report should first contact the Defense Technical Information Center (DTIC) at the address shown below. If you are a registered DTIC User, DTIC can provide you with a copy. Please do not request copies from the Air Force Research Laboratory, Munitions Directorate. Requests for additional copies should be directed to:

Defense Technical Information Center (DTIC)
8725 John J. Kingman Road, Ste 0944
Ft Belvoir, VA 22060-6218

This report is published in the interest of the scientific and technical information exchange. Publication of this report does not constitute approval or disapproval of the ideas or findings

If your address has changed, if you wish to be removed from our mailing list, or if your organization no longer employs the addressee, please notify AFRL/MNAV, Eglin AFB FL 32542-6810, to help us maintain a current mailing list. Do not return copies of this report unless contractual obligations or notice on a specific document requires that it be returned.

REPORT DOCUMENTATION PAGE

Form Approved
OMB No. 0704-0188

1. REPORT DATE *(DD-MM-YYYY)*	2. REPORT TYPE	3. DATES COVERED *(From - To)*
14-07-2004	Final	September 2003 - April 2004

4. TITLE AND SUBTITLE
Comprehensive Property Characterization of Nanotube

Buckeypaper Reinforced Composite Materials

5a. CONTRACT NUMBER

5b. GRANT NUMBER
F08630-01-1-0010

5c. PROGRAM ELEMENT NUMBER
62602F

6. AUTHOR
Ben Wang

5d. PROJECT NUMBER
2502

5e. TASK NUMBER
99

5f. WORK UNIT NUMBER
06

7. PERFORMING ORGANIZATION NAME AND ADDRESS

Florida A&M University
Florida State University College of Engineering
Tallahassee, FL 32310-6046

8. PERFORMING ORGANIZATION REPORT NUMBER

9. SPONSORING / MONITORING AGENCY NAME(S) AND ADDRESS(ES)
Air Force Research Laboratory, Munitions Directorate
AFRL/MNAV
101 W. Eglin Blvd.
Eglin AFB, FL 32542-6810

10. SPONSOR/MONITOR'S ACRONYM(S)
AFRL-MN-EG

11. SPONSOR/MONITOR'S REPORT NUMBER(S)
AFRL-MN-EG-TR-2004-7112

12. DISTRIBUTION / AVAILABILITY STATEMENT
DISTRIBUTION approved for public release; distribution unlimited

13. SUPPLEMENTARY NOTES none

14. ABSTRACT

Recent investigations have shown that single wall nanotubes possess remarkable mechanical properties exceeding those of any other composite reinforcement materials. In this research, a novel technical approach was developed to fabricate bulk polymeric matrix nano-composites with controlled nano-structures, desired alignment, and high tube loading. Instead of directly mixing nanotubes and resin, a special resin infiltration method was used to impregnate buckypapers, which are thin preformed sheets of well-controlled and dispersed porous single wall nanotube networks. A special technique was developed to facilitate the resin infiltration through the bucky papers to achieve good impregnation between the nanotubes and the epoxy resin. The molecular interactions between the nanotubes and the resin molecules were explored using molecular dynamics simulation. A demonstration sandwich wing structure was successfully developed to demonstrate the feasibility of using buckpaper-resin nano-composites for structural applications. The results of this research demonstrate the effectiveness of using the buckypaper – resin infiltration method to manufacture nano-composites with controlled tube dispersion, orientation, and high tubular loading.

15. SUBJECT TERMS
nanotubes, buckypaper, composite materials

16. SECURITY CLASSIFICATION OF:			17. LIMITATION OF ABSTRACT	18. NUMBER OF PAGES	19a. NAME OF RESPONSIBLE PERSON
a. REPORT	b. ABSTRACT	c. THIS PAGE			Prog Mgr:Charles J. Cottrell
UNCLASSIFED	UNCLASSIFIED	UNCLASSIFIED	UL	204	19b. TELEPHONE NUMBER 850-882-2220, ext 3472

Comprehensive Property Characterization of Nanotube Buckypaper-Reinforced Composite Materials

F08630-01-1-0010

Ben Wang[1], Richard Liang[1], Chuck Zhang[1] and Leslie Kramer[2]
[1]Florida Advance Center for Composite Technologies (FAC^{2}T)
Department of Industrial & Manufacturing Engineering
Florida A&M University – Florida State University College of Engineering
Tallahassee, FL 32310-6046
[2]Lockheed Martin Missiles and Fire Control - Orlando
Orlando, FL 32819-8907

Abstract

Recent investigations have shown that SWNTs possess remarkable mechanical properties exceeding those of any existing composite reinforcement materials, such as IM7 carbon fibers. The exceptional thermal and electrical properties of SWNTs also demonstrate great potential for developing multifunctional materials. However, using nanotubes as reinforcements to produce quality composites is still a challenging issue due to their nanoscale dimension, unique chemical characteristics and intensive molecular interactions with resin molecules during composite processing.

In this research, a novel technical approach was developed to fabricate bulk polymeric matrix nanocomposites with controlled nanostructures, desired alignment and high tube loading. Instead of directly mixing nanotubes and resin, a special resin infiltration method was used to impregnate buckypapers, which are thin preformed sheets of well-controlled and dispersed porous SWNT networks. Buckypaper preparation involves a multiple-step process for dispersion and filtration of nanotube suspensions. Magnetically aligned buckypapers were produced to achieve desired tube alignment by filtrating well-dispersed nanotube suspensions through a filter placed in a high strength magnetic field at National High Magnetic Field Laboratory in Tallahassee, FL. A special technique was developed to facilitate the resin infiltration through the buckypapers to achieve good impregnation between the nanotubes and epoxy resin. The resin matrix used in this research was an Epon 862/EPI CURE W system. Multiple-layers of resin impregnated random or aligned buckypapers were stacked together and cured to fabricate bulk solid composite samples. The influences of the processing parameters on the buckypaper quality and tube alignment in magnetically aligned buckypapers were investigated. The results show that the new processing approach can effectively fabricate nanotube composites with controlled nanostructures. The storage modulus of the magnetically aligned nanocomposites was as high as 45 GPa. The nanocomposites tube loading can range from 20w/w% to 60w/w%. Both the random and aligned buckypapers and nanocomposites consisted of good dispersed tube networks and tube alignment.

The molecular interactions between SWNTs and the resin molecules were also explored using molecular dynamics (MD) simulation. A molecular model of a SWNT/EPON 862 nanocomposite was developed to predict the interfacial bonding by simulating a single tube pullout. The functionalization of oxidization and molecular wraps of the SWNTs for enhancing dispersion and interfacial bonding were also studied. The mechanical property predictions of the individually dispersed SWNT and nanotube rope nanocomposites compared well with the experimental observations. A demonstration sandwich wing structure was successfully developed to demonstrate the feasibility of using buckypaper/resin nanocomposite for structural applications. The results of this research demonstrate the effectiveness of using the buckypaper/resin infiltration method to manufacture nanocomposites with controlled tube dispersion, orientation and high tube loading, which are critical for developing high performance SWNT-reinforced structural and multifunctional nanocomposites, as well as SWNT-based devices.

All planned research tasks have been conducted and documented in this report. Chapter 1 introduces the project. Chapter 2 discusses the nanocomposites manufacturing process of buckypaper/resin infiltration. Chapters 3 and 4 explain the processing techniques for random and magnetically buckypapers, respectively. Chapter 5 presents the mechanical, electrical and thermal properties of the resultant materials. Chapter 6 explains the molecular interactions of the SWNTs/resin matrix molecules and composite interface by using MD simulation. The SWNT functionalization preliminary studies are presented in Chapter 7. Chapter 8 explores how buckypaper composites can be used for structural applications. Conclusions and acknowledgements are provided in Chapter 9.

AFRL MN & ML Directorates sponsored this research effort.

Keywords: Nanocomposites, SWNT, Manufacturing, Mechanical Properties and Alignment

Table of Contents

List of Figures

List of Tables

1. Introduction

1.1. Motivation and Objectives

Recent investigations have shown that single-walled nanotubes (SWNTs) possess remarkable mechanical properties exceeding those of any existing composites reinforcement materials. For example, both theoretical and experimental results have shown that SWNTs have a high elastic modulus in the range of 500 to 1,200GPa. The SWNTs' maximum estimated tensile strength is close to 200 GPa, which is 40 times greater than IM7 carbon fiber. Since many researchers consider SWNTs as the most promising reinforcement materials for the next generation of high performance structural and multifunctional composites, effective methods for developing SWNT reinforced nanocomposites are being sought.

Unlike conventional fibrous reinforcements, SWNTs are nanoscale dimensional materials with exceptional large surface areas (1,000~1,350 m^2/g), which result in strong interactions between the tubes due to the van der Waals forces, causing the SWNTs to form ropes or bundles. SWNT ropes also have the tendency to aggregate and exhibit intensive molecular interactions with resin matrix molecules. Nanocomposites produced by conventional methods of directly mixing the nanotubes and polymers in casting or utilizing injection processes do not yield acceptable uniform dispersion and high loading of SWNTs due to the aggregation tendency of SWNTs, high resin viscosity and the inability to control the formation of the SWNT network or nanostructure during composite consolidation. Consequently, a major challenge of nanotube composite processing is producing a nanotube network in polymeric matrix with the desired uniform dispersion, alignment and high loading. Functionalizing nanotubes to enhance tube dispersion and interfacial bonding is vital for developing high performance materials.

In this research, a novel processing approach was developed to fabricate bulk polymeric nanocomposites with controlled nanostructures, desired alignment and high tube loading,

which are critical for developing high performance and multifunctional nanotube-reinforced materials. Instead of directly mixing nanotubes and resin, a special resin infiltration method was used to impregnate buckypapers, which are thin preformed sheets of well-controlled, porous nanotube networks. Buckypaper preparation involves a multiple-step process for dispersion and filtration of nanotube suspensions. Magnetically aligned buckypapers were produced by in-situ filtrating well-dispersed nanotube suspensions in a high strength magnetic field. A special technique was developed to facilitate the resin infiltration through the buckypapers to achieve good nanotubes/epoxy resin impregnation. Multiple-layers of the resin impregnated random or aligned buckypapers were stacked together and cured to fabricate bulk solid composite samples. The influences of processing parameters on quality and tube alignment in magnetically aligned buckypapers were investigated. The molecular interactions between SWNTs and resin molecules were also explored using molecular dynamic (MD) simulation. The effects of tube functionalization on tube dispersion and material properties were explored. The research efforts of this project are summarized in Figure 1.1.

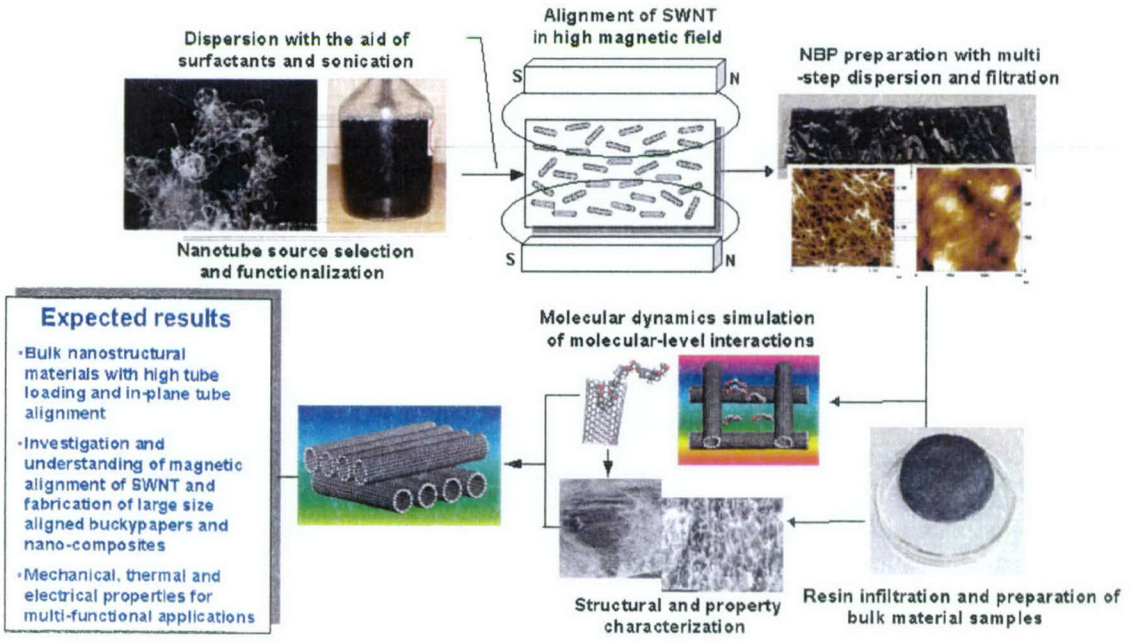

Figure 1.1 Flow chart of the research efforts

The essence of this proof-of-principle project was to systematically investigate and characterize the proposed technical approach and various physical properties of the resultant SWNT buckypaper-reinforced composites. The nanoscale processing-structure-property relationship was revealed both theoretically and empirically. The molecular interactions of SWNTs and resin molecules during processing and at nanocomposite interface were analyzed. The processing models and property predications were explored. The research team also conducted a preliminarily demonstration using buckypaper composites in structure applications. In summary, the goal of this research was two-fold: 1) improve the understanding of nanotube nanostructures and properties, and 2) populate a processing and property database of innovative buckypaper composite materials that have the future potential to be engineered and deployed.

In this report, the research objectives and major technical approaches, as well as a brief introduction of nanotubes and their composites, are provided in Chapter 1. Chapter 2 discusses the nanocomposites manufacturing process of buckypaper/resin infiltration. Chapters 3 and 4 describes the processing techniques of random and magnetically buckypapers, respectively. Chapter 5 presents the mechanical, electrical and thermal properties of the resultant materials. The investigation of the molecular interactions of SWNTs/resin matrix molecules and nanocomposite interface by using molecular dynamics (MD) simulation are discussed in Chapter 6. Preliminary studies of SWNT functionalization are examined in Chapter 7. Structural application demonstrations of using buckypaper composites are presented in Chapter 8. Conclusions and acknowledgements are provided in Chapter 9 and 10.

1.2. Background

Carbon nanotubes exhibit exceptional material properties. Their small dimension, exceptional strength and remarkable physical properties make them unique reinforcements for polymer nanocomposites. This brief literature review presents recent advances in carbon nanotubes and their use in composites. Particular emphasis is given to nanotube growth, mechanical and functional properties, nanocomposite processing and characterization, nanotube alignment, and functionalization.

1.2.1. Atomic Structure of carbon nanotubes

The first observation of carbon nanotubes in 1991 [1] stimulated many theoretical and experimental studies on the structure of carbon nanotubes. Basically, two kinds of nanotubes exist: SWNTs having one atomic layer in thickness and MWNTs (multi-walled carbon nanotubes) composed of concentric SWNTs. The unique atomic structure of carbon nanotubes can be defined in various ways. One way is to define a SWNT as a graphene sheet rolled into a cylindrical shape. Three important vectors – the chiral vector, translational vector and symmetry vector – determine the nanotubes' structure. Details of these three vectors can be found in references [2-3]. The structure of a SWNT is specified by the chiral vector $\mathbf{C}_h = n\boldsymbol{\alpha}_1 + m\boldsymbol{\alpha}_2$, which corresponds to a section of the nanotube perpendicular to the nanotube axis. The diameter, d_t, and chiral angle, θ, of nanotube are determined by the chiral vector.

$$d_t = C_h / \pi = \sqrt{3}\alpha_{C-C}(m^2 + mn + n^2)^{1/2} / \pi \tag{1.1}$$

$$\theta = \tan^{-1}[\sqrt{3}m/(m+2n)] \tag{1.2}$$

Different types of nanotube are uniquely determined by the values of n and m. Based on the chiral angle θ, three categories of nanotubes can be defined: zig-zag nanotubes ($\theta = 0°$), armchair nanotubes ($\theta = 30°$) and chiral nanotubes ($0° < \theta < 30°$).

Experimental observations showed that SWNTs tend to assemble into ropes due to the van der Waals interactions between individual nanotubes within the ropes. The isolated SWNT (10, 10) is approximately 1.36 nm in diameter. The first carbon nanotubes discovered were MWNTs, which were nested shell structures with an interlayer spacing of ~ 0.34 nm.

1.2.2. Synthesization of nanotubes

Carbon nanotubes have unique mechanical properties that should make them ideal reinforcements in composite materials. However, practical application requires manufacturing inexpensive, high quality nanotubes. Growing nanotubes by arc discharge

and laser vaporization methods have been actively pursued in the past decade. In 1991, Iijima [1] first observed MWNTs synthesized from the arc discharge technique. In 1992, Ebbesen and Ajayan [4] achieved a breakthrough in MWNT growth using the arc discharge by growing and purifying high quality MWNTs at the gram level. Synthesized MWNTs are about 10 mm long, with diameters in the range of 5-30 nm. To grow SWNTs, a metal catalyst is needed in the arc discharge system. The first success in producing substantial amounts of SWNTs by arc-discharge was achieved by Bethune and his coworkers in 1993 [5].

Laser vaporization was first used for the initial synthesis of fullerenes. Over the years, this technique has been improved to allow for the production of SWNTs. Smalley and coworkers synthesized high quality SWNTs at 1-10 gram scale by using laser vaporization [6]. Under a scanning electron microscope (SEM), the material appeared as a mat of ropes 10-20 nm in diameter and up to 100 μm or more in length, as shown in Figure 1.2(a). Under transmission electron microscope (TEM) examination as shown in Figure 1.2(b), each rope was found to consist primarily of a bundle of SWNTs aligned along a common axis with a diameter of ~1.4 nm. By varying the growth temperature, the catalyst composition and other growth parameters, the average nanotube diameter and the diameter distribution could be varied.

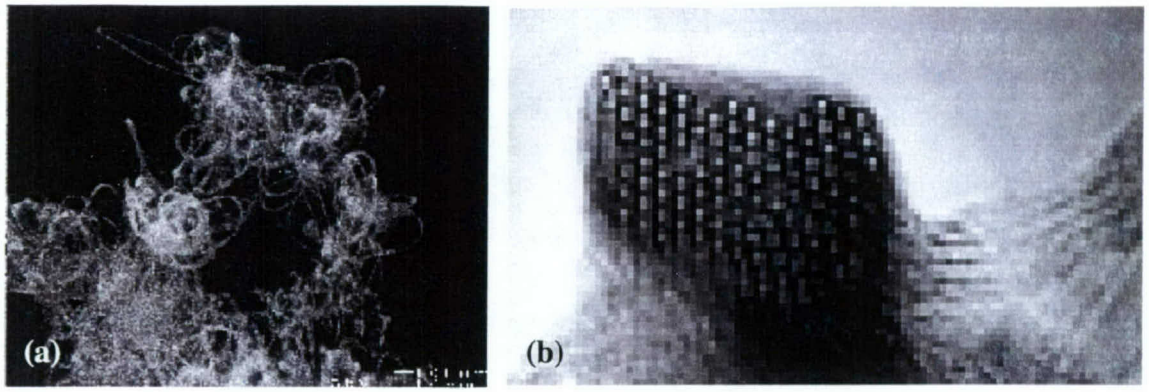

Figure 1.2 Single-walled nanotubes grown by laser vaporization [6]

Both the arc discharge and laser vaporization techniques are limited in regards to the production volume. In addition, subsequent purification steps are necessary to separate the nanotubes from unwanted by-products. These limitations have motivated the development of gas-phase techniques, including gas-phase catalytic growth from carbon monoxide and chemical vapor deposition (CVD) from hydrocarbons. These processes offer the greatest potential for large-scale production of carbon nanotubes.

Smalley *et al.* [7] developed a gas phase catalytic process to grow bulk quantities of SWNTs. The carbon feedstock is carbon monoxide (CO) and the growth temperature is in the range of 800-1,200°C. Carbon monoxide is a very stable molecule that does not produce unwanted amorphous carbonaceous materials at high temperatures. However, CO is not an efficient carbon source for nanotube synthesis. To enhance the CO carbon feedstock, Smalley and his co-workers have used high pressures of CO (up to 10 atm) to significantly speed up the disproportionation of CO molecules into carbon, and thus enhance the growth of SWNTs. The so-called HiPco (high-pressure conversion of carbon monoxide) process has been commercialized for a large-scale production of high-purity SWNTs.

Another method for producing carbon nanotubes is chemical vapor deposition (CVD) of hydrocarbon gases. This growth process involves heating a catalyst material to 500-1,000°C in a tube furnace and blowing a hydrocarbon gas through a tube reactor. The general nanotube growth mechanism in a CVD process involves the dissociation of

hydrocarbon molecules catalyzed by the transition metal, and dissolution and saturation of carbon atoms in the metal nanoparticle. The precipitation of carbon from the saturated metal particles leads to the formation of tubular carbon solids in an sp^2 structure. CVD methods have great potential for scaled-up nanotube materials synthesis. MWNTs have already been produced commercially from kilograms to tons. Nevertheless, these MWNTs tend to contain high densities of defects, such as pentagons and heptagons on the sidewalls of the nanotubes. Growing perfect MWNTs by CVD still remains a challenge.

With conventional CVD techniques, tangled carbon nanotubes are grown in a tube furnace. Synthesizing aligned arrays of carbon nanotubes with controlled diameter and length has sparked recent research activities in CVD nanotube growth. The synthesis of well-aligned, straight carbon nanotubes on a variety of substrates has been accomplished by using plasma enhanced chemical vapor deposition (PECVD). The plasma could be excited by a direct current or a microwave source. Ren *et al.* [8] achieved straight carbon nanotube arrays using a substrate coated with a layer of nickel catalyst. Acetylene gas is used as the carbon source and high-purity ammonia gas (NH3) is the catalytic gas and dilution gas. A direct current power generates the required plasma, and a deeply carbonized tungsten filament assists the dissociation of the reactive gases and supplies heat to the substrate. Control over the nanotube length and graphitization is accomplished by changing the growth time and temperature. Bower *et al.* [9] showed that in microwave plasma-enhanced CVD (MPECVD), alignment of carbon nanotubes results from the self-bias that is imposed on the surface of the substrate from the microwave plasma.

Fan *et al.* [10] obtained ordered MWNT structures by CVD on catalytically patterned substrates. MWNTs can self-assemble into aligned structures during CVD growth. Squared iron patterns on porous silicon substrates are employed for the growth. Regularly positioned arrays of nanotube towers exhibit very sharp edges and corners with no nanotubes branching away from the blocks. MWNTs within each block are well aligned along the direction perpendicular to the substrate surface.

Growing SWNTs into structures with well-controlled orientations is a challenge. Franklin *et al.* [11] reported that ordered SWNTs could be directly grown by methane CVD catalytically patterned substrates. Suspended SWNT networks with directionality on substrates containing lithographically patterned silicon pillars have been grown. Contact printing is used to transfer catalyst materials onto the tops of pillars selectively. CVD of methane using the substrates leads to suspended SWNTs forming nearly ordered networks with the nanotube orientations directed by the pattern of the pillars. Nanotubes are nucleated on the tops of the pillars and length from there as they grow. The methane flow keeps the nanotube floating and waving in the "wind" since the flow velocity near the bottom surface is substantially lower than that at the level of the tower tops. This prevents the SWNTs from being caught by the bottom surface. The nearby towers provide fixed points for the growing tubes. If the waving SWNTs contact adjacent towers, the tube-tower van der Waals interactions will catch the nanotubes and hold them aloft. SWNTs as long as 0.2 mm in length have been grown. Recently, researchers from Rensselaer Polytechnic Institute with collaborators at Tsinghua University have improved the CVD process to directly synthesize long, continuous, hair-like strands of SWNT rope that are up to eight inches in length by adding sulfur containing compound and hydrogen, as shown in Figure 1.3 (a). Figure 1.3 (b) shows the SEM micrograph of SWNT ropes, in which SWNTs are well ordered and are self-assembled during the growth process [12].

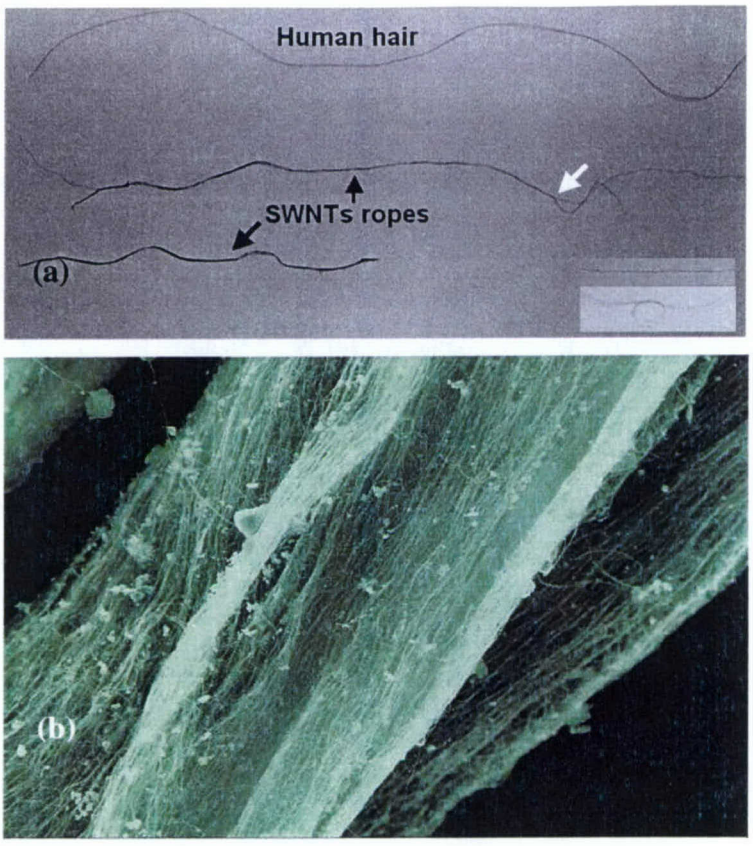

Figure 1.3 Hair-like single-walled nanotube ropes [12]

Understanding and modeling nanotube growth mechanisms for various synthesis methods are still undergoing studies. Production of large quantity and consistent quality SWNTs with affordable cost is still a challenging task for the scientific and engineering communities.

1.3. Mechanical Properties of Carbon Nanotubes

Carbon nanotubes are unique for their nearly perfect cylindrical structure of seamless graphite, nanoscale diameter and high aspect ratio. These novel materials are potentially 30 to 100 times stronger than steel, yet one-sixth the weight of steel and manifest remarkable flexibility. The unique mechanical properties of carbon nanotubes have been the subject of experimental and theoretical studies. The following is a brief summary of the mechanical properties of carbon nanotubes, which were either measured by experiments or calculated with theoretical models.

1.4. Experimental Studies

A growing body of experimental evidence indicates that carbon nanotubes have extraordinary mechanical properties. However, the technical difficulties involved in the manipulation of these nanoscale materials make determining their mechanical properties a rather challenging task. Challenges in characterizing the nanotubes properties include (a) lack of micro-mechanical characterization techniques for direct property measurements, (b) tremendous limitations in specimen size, (c) uncertainty in data obtained from indirect measurements, (d) inadequacy in test specimen preparation techniques, and (e) lack of control in nanotube alignment and distribution.

The mechanical properties of SWNTs and ropes were measured using various methods. Krishman *et al.* [13] succeeded in measuring the Young's modulus of SWNTs by observing their freestanding vibrations at room temperature under a transmission microscope. Micrographs of 27 SWNTs in the diameter range of 1.0-1.5 nm were measured to obtain the average Young's modulus of 1.25TPa.

SWNTs are mostly arranged in ropes with a close-packed stacking. Salvetat *et al.* [14] first measured the elastic properties of crystalline SWNT ropes by depositing them onto a membrane having 200 nm pores. By positioning the AFM tip directly on the midpoint of the carbon nanotube spanning the pore and applying an indentation force, the deflection versus force measurements were obtained to determine the elastic properties. They concluded that the elastic and shear moduli of individual SWNT rope to be on the order of 1 TPa and 1 GPa, respectively. Walters *et al.* [15] further investigated the elastic strain of nanotube ropes using atomic-force microscope (AFM). The ropes were observed to become deformed as elastic strings with tension proportional to elongation. The maximum strain observed, 5.8±0.9%, gave a lower bound of 45±7 GPa for the tensile strength, which is over 20 times the yield strength of typical high-strength steels. Yu *et al.* [16] studied the tensile-loading experiments of the SWNT rope. The SWNT rope had a strong attachment at one end to the sample surface. The free end of the SWNT rope was then approached and attached to an AFM tip. The AFM tip stretched the SWNT rope to the breaking point and served as the force sensor to measure the applied force. The stress

versus strain curves obtained from these tensile-loading experiments showed that they broke at strain values of 5.3% or lower. The force-strain data were entered in a model that assumed the load is carried by the SWNTs on the perimeter of each rope. This model provides an average breaking strength of SWNTs on the perimeter of each rope. The values are in the range of 1-52 GPa (mean 30 GPa). Based on the same model, the determined average Young's modulus values ranged from 320-1470 GPa (mean 1002 Pa).

The mechanical properties of MWNTs were also characterized. Treacy *et al.* [17] conducted the earliest experimental measurements of elastic modulus of MWNTs by measuring intrinsic thermal vibration using transmission electron microscopy. They obtained an average value of 1.8±0.9 TPa. Direct measurements of the stiffness and strength of individual structurally isolated carbon nanotubes were made with an (AFM). Wong *et al.* [18] were the first to directly measure the stiffness and strength of individual, structurally isolated MWNTs using AFM. They reported a mean of 1.28±0.59 TPa for the elastic modulus. The maximum bending strength determined for MWNTs examined was 28.5 GPa; however, the average bending strength measured was 14.2±8 GPa. Using a new testing stage based on a nanomanipulation tool operating within a SEM., Yu *et al.* [19] measured the response to axial tensile loading of an individual MWNT. The tensile-loading experiment was prepared and observed entirely within the microscope and recorded on video. The MWNTs broke in the outermost layer ("sword-in-sheath" failure), and the tensile strength of this layer was 11-63 GPa for the set of 19 MWNTs that were loaded. Analysis of the stress-strain curves for individual MWNTs indicated that the Young's modulus E of the outermost layer was 270-950 GPa.

1.5. Theoretical Prediction

Recent experiments have contributed to confirming that both MWNTs and SWNTs have exceptional mechanical properties. Similar conclusions have also been reached through computational or theoretical predictions.

Lu [20] studied the elastic properties of SWNTs. He adopted a force constant model, which has been successfully adopted in calculating the phonon spectrum and elastic properties of graphite. The predicted Young's modulus (~1 TPa), shear modulus (~0.45

TPa) and bulk modulus (~0.74 TPa) are comparable to those of diamond. The elastic moduli were concluded to be insensitive to the size and the chirality of SWNTs. Hernandez *et al.* [21] calculated the structural and elastic properties of SWNTs using tight-binding methods. Their calculations predict that carbon nanotubes have slightly higher values of ~1.24 TPa for the Young's moduli.

Theoretical studies have also investigated the mechanical properties of SWNT ropes. Lu [20] studied the elastic properties of crystalline ropes. These ropes consist of 100-500 SWNTs of uniform size arranged in hexagonal order. The calculated elastic moduli of ropes are ~0.6 TPa. They concluded that a crystalline rope is very anisotropic in its elastic properties-soft on basal plane and stiff along the axial direction. Popov *et al.* [22] studied the elastic properties of triangular crystal lattices formed by SWNTs by using analytical expressions based on a force constant lattice dynamics model. They calculated various elastic constants of nanotube crystals for nanotube types, such as armchair and zigzag. The elastic modulus, Poisson's ratio and bulk modulus clearly exhibited strong dependence on the tube radius. The bulk modulus was found to have a maximum value of 38 GPa for crystals composed of SWNTs with ~0.6 nm radius. Nardelli *et al.* [23] used the mechanical properties of SWNTs under uniaxial tension using quantum molecular dynamics simulations. In strained nanotubes, the spontaneous formation of double pentagon-heptagon defect pairs was observed. Tubes containing these defects are highly preferred to uniformly stretched tubes at strains greater than 5%. These defects act as nucleation centers for the formation of dislocations in the original ideal graphitic network and constitute the onset of further deformations of the carbon nanotube.

MWNTs are composed of a number of concentric SWNTs held together by relatively weak van der Waals forces. Lu [20] calculated the elastic properties of many MWNTs formed by single-layer tubes. The predicted Young's modulus of ~1TPa and shear modulus of ~0.45TPa are essentially insensitive to the number of walls. Both SWNTs and MWNTs have a large anisotropy in elastic properties. Ru [24] used the elastic-shell model to study the effects of van der Waals forces on the axial buckling of a double-walled carbon nanotube. The analysis showed that the van der Waals forces do not increase the critical axial buckling strain of a double-walled nanotube. Ru [25, 26]

proposed a multiple column model that considers the interlayer radial displacements coupled through the van der Waals forces. This model was used to study the effects of interlayer displacements on column buckling, concluding that the effect of interlayer displacements could not be neglected unless the van der Waals forces were extremely strong. Kolmogorov *et al.* [27] investigated the interlayer interaction in double-walled nanotubes, demonstrating that the tightly constrained geometry of MWNTs could produce an extremely smooth solid-solid interface. The energetic barrier to interlayer sliding in defect-free nanotubes can be comparable to that of a single unit cell of crystalline graphite.

1.6. Functional Properties of Carbon Nanotubes

Besides their outstanding mechanical properties, carbon nanotubes also offer a broad range of exceptional electronic, electrical, magnetic and thermal properties. These remarkable functional properties indicate broad potential applications of carbon nanotubes as multifunctional materials.

1.6.1. Electronic properties

The electronic properties of SWNTs have been studied in a number of theoretical works. All models show that the electronic properties vary in predictable ways from metallic to semi-conducting with the variation of diameter and chirality. The chirality and diameter are uniquely specified by the chiral vector, $\mathbf{C}_h = n\boldsymbol{\alpha}_1 + m\boldsymbol{\alpha}_2$. Depending on their precise molecular symmetry, some nanotubes are semiconducting, while others exhibit metallic conductivity. This behavior, coupled with their nanoscale geometry, makes them ideal candidates for wires and devices for molecular electronics.

Saito *et al.* [2] investigated the electronic structure of SWNTs as a function of the diameter and chirality using energy dispersion relationship, showing that all armchair (n, n) nanotubes are metallic; however, only a third of zigzag nanotubes are likely metallic, which is also true for chiral nanotubes.

Figure 1.4 shows this variation. These surprising results can be understood on the basis of the electronic structure of two-dimensional graphite, which is a zero gap semiconductor

with bonding and anti-bonding bands that degenerate at the K-point (zone corner) of the hexagonal Brillouin zone. The periodic boundary conditions permit only a few wave vectors to exist in the circumferential direction. If one of these wave vectors passes through the K-point in the Brillouin zone where the valence and conduction bands of two-dimensional graphite are degenerate, then metallic conduction results.

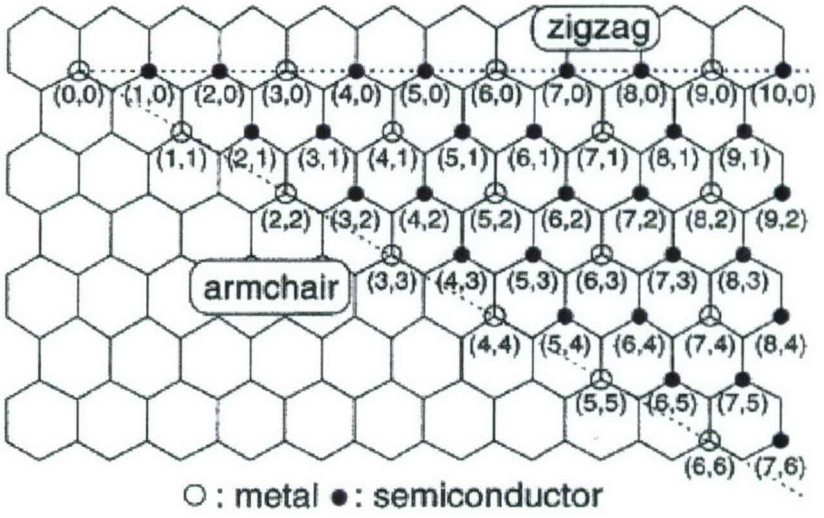

Figure 1.4 Metallic and semi-conducting behavior of carbon nanotubes [2]

1.6.2. Electrical properties

Carbon nanotubes can be metallic or semi-conducting depending on their folding angle and diameter. Metallic nanotubes present exceptionally high current carrying capabilities before breakdown and very low resistance, resulting from a weak electron-phonon coupling in this system. Thess *et al.* [6] studied the electrical conductivity of the SWNT ropes (10,10), which consist of 100 to 500 SWNTs with a lattice constant of 17Å. The rope had a resistivity on the order of 10^{-4} Ω-cm at 300K, which was determined by measuring the resistivity directly using a four-point technique. Frank *et al.* [28] reached a current density in the nanotube greater than 10^7 A/cm^2. Wei *et al.* [29] studied the current-carrying capacity of MWNTs under high current densities. They concluded that MWNTs could carry high current densities up to 10^9-10^{10} A/cm^2 and remain stable for extended periods at higher temperature. Later, Phaedon suggested that stable current

densities of nanotubes could be pushed as high as 10^{13} A/cm^2. The conductivity of nanotubes changed significantly as a result of doping with electron acceptors or donors. Another interesting characteristic is the pronounced dependence of nanotubes' electrical conductivity on the magnetic field [30,31].

1.6.3. Magnetic properties

An important parameter characterizing the magnetic properties of a material is its magnetic susceptibility. The SWNTs are predicted to have an anisotropic magnetic susceptibility. The comparison of the magnetic susceptibilities of SWNTs with various elements is shown in Table 1.1. Such a substantial magnetic susceptibility provides a possibility for aligning nanotubes in a liquid suspension.

Table 1-1 Comparison of magnetic susceptibilities

Substance	Magnetic susceptibilities ($\times 10^{-6}$ emu(mol C)$^{-1}$)
Single-walled nanotube	+85.4
Diamond	-5.9
Graphite	-6.0
Aluminum	+16.5
Copper	-5.46
Iron	+3586.0

Calculations reveal that the metallic SWNTs, such as the (n, n) variety, are paramagnetic in the direction of their long axis and tend to align parallel to the ambient magnetic field. Other varieties of SWNTs are diamagnetic, but their diamagnetic susceptibilities are normally negative in the direction perpendicular to the direction of an ambient field. The alignment energies for both varieties of SWNTs are comparable. The calculated susceptibilities of SWNTs predict that at room temperature, fields on the order of 10T will produce an observable alignment in a liquid suspension of SWNTs [32].

1.6.4. Thermal properties

Thermal conductivity and expansion of carbon nanotubes are also fundamentally interesting and technologically important. Hone *et al.* [33] found that the thermal conductivity was temperature dependent, and the thermal conductivity for a SWNT rope at room temperature could vary between 1800 and 6000 W/m-K. Che *et al.* [34] numerically calculated the thermal conductivity of a nanotube (10, 10) to approach 2980 W/m-K as the current applied was increased. Recently, Berber *et al.* [35] confirmed the prediction of Hone by suggesting an unusually high value of 6600 W/m-K for the thermal conductivity at room temperature. They theorized that these high values were due to the large phonon mean free paths. All these values are comparable to diamond, which has the highest measured thermal conductivity of any material.

The thermal expansion of carbon nanotubes differs in a fundamental way from carbon fibers and graphite. Ruoff [36] discussed the thermal conductivity and thermal expansion of carbon nanotubes, concluding that the thermal conductivity could be highly anisotropic, but the thermal expansion of carbon nanotubes is essentially isotropic. In other words, the radial thermal expansion coefficient could be identical to the on-axis thermal expansion coefficient.

1.7. Nanotube-Reinforced Composites

Based on these studies, developing nanotube-reinforced composites has become a major goal. The following sections review the relevant work in this area and discuss the challenges that are associated with the development of these new composites.

1.7.1. Processing and characterization of nanotube-reinforced composites

A number of nanotube-reinforced composites have been fabricated by melt blending/injection or extrusion and direct mixing/solution casting methods [37-44]. In melt blending process, thermoplastic polymers and nanotubes were mixed and then compressed at a high temperature using a hydraulic press to produce composite films, or an injection molding method was used to produce composite samples. The solution casting process may have several steps: (a) dissolving matrix polymers into an

appropriate solvent to make the solution; (b) dispersing nanotubes into the solvent to make the suspension; (c) mixing the solution and the suspension; and (d) casting the mixture to allow the solvent to evaporate to produce final nanocomposites. In direct mixing process, the nanotube dispersions are added dropwise to the matrix polymer solution, followed by subsequent casting. In all the processes, uniform dispersion within the polymer matrix and improved wetting and adhesion are critical to fabricate nanocomposites. When processing nanocomposites with a high-weight fraction of nanotubes, the dispersion of nanotubes becomes extremely difficult. Better dispersion of nanotubes in the matrix polymers could be achieved with high-energy sonification and surfactant-assisted process. Gong *et al.* [43] fabricated carbon nanotube/epoxy nanocomposites by curing mixtures of carbon nanotubes and bisphenol A epoxy resin in the presence of the surfactant. DMA analysis showed that the addition of only 1wt % carbon nanotube in the composite increased the glass transition temperature from 63°C to 88°C using a surfactant as the processing aid. The elastic modulus also increased by more than 30%. However, the addition of carbon nanotubes without the surfactant only had moderate effect on the glass transition temperature and on the mechanical properties, indicating that the surfactant played an important role in improving dispersion and modifying the interfacial bonding in carbon nanotube/polymer interface. In such a processing method, carbon nanotubes are randomly distributed in the matrix polymers when processing nanocomposites. No effective methods exist to control the nanostructure of carbon nanotubes in the final nanocomposite in these direct mixing and molding approaches.

1.7.2. Investigation of nanotube/resin matrix

The assessing the mechanical properties of nanotube-based composites remains controversial. Depending on the polymer matrix used and processing conditions, the measured properties show significant variations. The micro-Raman spectroscopy and Kelly-Tyson approach have been used to measure the interfacial shear stress.

Several previous studies suggested strong carbon nanotube-polymer adhesion. Qian *et al.* [38] employed a simple solution evaporation method, assisted by high-energy sonication,

to prepare uniform MWNT-Polystyrene (PS) composite samples. With only the addition of 1% by weight (about 0.5% by volume), they achieved between 36-42% increase in the elastic stiffness and 25% increase in the tensile strength of the resultant nanocomposites. Further, TEM studies investigated the interface of the tube/resin matrix. The results showed that the load transfer across the nanotube-polystyrene interface was operative into the plastic deformation regime of the composite film. Although some MWNTs fractured by either a sword-in-sheath mechanism or transverse shear fracture, most of the MWNTs eventually debonded at the MWNT-polymer interface and subsequently were pulled out of the matrix. Wagner *et al.* [39, 40] examined stress-induced fragmentation of the MWNTs/Urethane composite system. TEM observations revealed that nanotubes that were approximately parallel to the direction of testing undergo a progressive fragmentation process. Based on the Kelly-Tyson model, the MWNTs-matrix stress transfer efficiency was estimated to be 500 MPa, which was an order higher than that of conventional advanced composites. This higher strength of nanotube-polymer interface may result from a mechanism similar to the "2+2" cycloaddition reaction. The strong curvature, as well as the presence of multiple concentric graphene planes, is likely to strongly enhance the reactivity of carbon nanotubes towards double-bonds contacting polymeric chains. Later, Lourie and Wagner [41] investigated the strength of SWNT/epoxy resin interface by observing the fracture of a SWNT rope in real-time with transmission electron microscopy. The expansion of elliptical holes in the polymer matrix resulted in a tensile force in bridging nanotubes. The polymer matrix at both ends of the ropes deformed extensively under the tension force, and fractures of the nanotubes occurred under tension within the polymer hole region rather than in shear within the gripping polymer region at the ends of the ropes. This provided evidence of significant SWNTs-epoxy wetting and interfacial adhesion. Cooper *et al.* [42] prepared composite specimens by applying an epoxy-resin/nanotube mixture to the surface of an epoxy beam. Stress transfer between the polymer and the nanotubes was detected by a shift in the G′ Raman band (2619 cm^{-1}) to a lower wave number.

However, poor load transfer between nanotubes and polymers has also been reported. Schadler *et al.* [44] studied the mechanical behavior of MWNT/epoxy composites in both

tension and compression. They observed a 6 cm^{-1} shift in MWNTs in compression and no shift in tension, implying that load transfer in tension to the MWNTs was negligible. This was attributed to the fact that the inner tubes were sliding within the outer tubes so the load was not efficiently transferred to all the layers in the coaxial MWNT assembly. This may also occur due to the extremely low interfacial shear stresses between MWNTs and matrix arising from poor interfacial bonding. Using SEM and micro-Raman spectroscopy, Ajayan *et al.* [45] studied the failure of SWNT/epoxy composite loaded axially in tension and compression and obtained similar conclusions. No shift of Raman peak in compression and only a slight trend to lower wave numbers in tension was seen. They suggested poor interfacial load transfer between nanotubes and matrix polymers due to tube sliding within the rope.

1.7.3. Alignment of carbon nanotubes

Both theoretical and experimental investigations revealed that most of the properties of carbon nanotubes are highly anisotropic. The orientations of nanotubes have a significant influence on the bulk properties of nanotube-reinforced composites. However, most carbon nanotubes produced by arc-discharge, laser vaporization or chemical vapor deposition methods are randomly oriented. Many potential nanotube applications are hindered by the lack of alignment. To fully utilize their anisotropic properties, carbon nanotubes must be aligned in composites.

Ajayan *et al.* [46, 47] first observed aligned nanotubes in composites. They fabricated a composite with carbon nanotubes randomly dispersed inside an epoxy matrix and found that slicing the composite caused partial alignment of the nanotubes on the cut surface. Most of the longer and thinner tubes were aligned, while the shorter and thicker nanotubes were not oriented. Jin *et al.* [48] showed that aligned nanotube composites could be achieved by mechanically stretching the composite above the glass transition temperature of the polymer. X-ray analysis performed on the composites showed the degree of alignment could be varied with the stretching ratios. However, degree of alignment was the same at a given stretching ratio, regardless of the sample thickness. Haggenmueller *et al.* [49] showed that melt spinning of SWNTs in fiber form could also

create well-aligned nanotube composites. Walters *et al.* [50] achieved an aligned buckypaper of SWNTs by introducing a SWNTs suspension to a strong magnetic field to align the tubes and filter the suspension. Good tube alignment was observed in the magnetically aligned buckypapers.

1.8. Functionalization of Nanotubes

Due to their excellent mechanical properties, SWNTs show exceptional promise for composite reinforcement applications. However, the van der Waals attraction among SWNTs, causing them to bond together and form bundles and ropes, creates problems in tube dispersion and tube-to-tube sliding under tension [46, 51, 52]. The intrinsic smooth surface and chemical stability also result in poor interfacial bonding between SWNTs and matrix. This also causes load transfer problems. SWNTs will pull out from the matrix instead of fracturing [53]. Functionalization is considered a solution to these problems.

Schadler *et al.* [54] modified the surface of MWNTs by using small molecules and polymer chains. Carboxylic acid was attached to the MWNTs surface as small molecules by refluxing MWNTs in HNO_3. Quantitative analysis of the carboxylic acid concentration using titration confirmed the presence of carboxylic groups on the surface and showed a concentration of $1.9e^{-4}$ moles COOH per 1g nanotubes for MWNTs treated for 90 minutes. The longer carboxylation times resulted in a high tube solubility in water or resin for composites application.

Further modifications of carboxylated nanotubes included their reaction with butyl glycidyl ether (BGE). The elastic modulus of the carboxylated and BGE modified MWNT/polycarbonate composites indicated that the BGE modified MWNT/polycarbonate composites showed a significant improvement in the modulus compared to the carboxylated MWNT/polycarbonate composites. The 5wt% BGE modified MWNT/polycarbonate composites had almost twice the modulus of the pure polycarbonate, which indicated an improved load transfer after functionalization. Zhu *et al.* [55] functionalized SWNTs by using an optimized H_2SO_4/HNO_3 acid treatment and subsequent fluorination. The functionalized SWNTs were then dissolved in dimethylformamide and mixed with the epoxy resin. Samples of 1wt% SWNTs were

produced. The functionalized nanotubes were observed to be well dispersed and integrated in the epoxy resin matrix, which is shown in Figure 1.5. The mechanical properties were enhanced by a 30% increase in modulus and 18% increase in tensile strength. The pristine SWNTs reinforced composites only increased 5% in modulus and decreased slightly in tensile strength, as shown in Table 1.2. This may be because the functionalized SWNTs were integrated into epoxy composites through the formation of strong covalent bonds in the course of epoxy ring-opening esterification and curing chemical reactions.

Table 1-2Young's modulus and tensile strength of SWNT composites

epoxy composite formulation	Young's modulus E (MPa)	tensile strength σ (MPa)
neat resin 862/W	2026	83.2
1% BuckyPearl SWNTs	2123	79.9
1% F-SWNT-COOH	2632	95.0

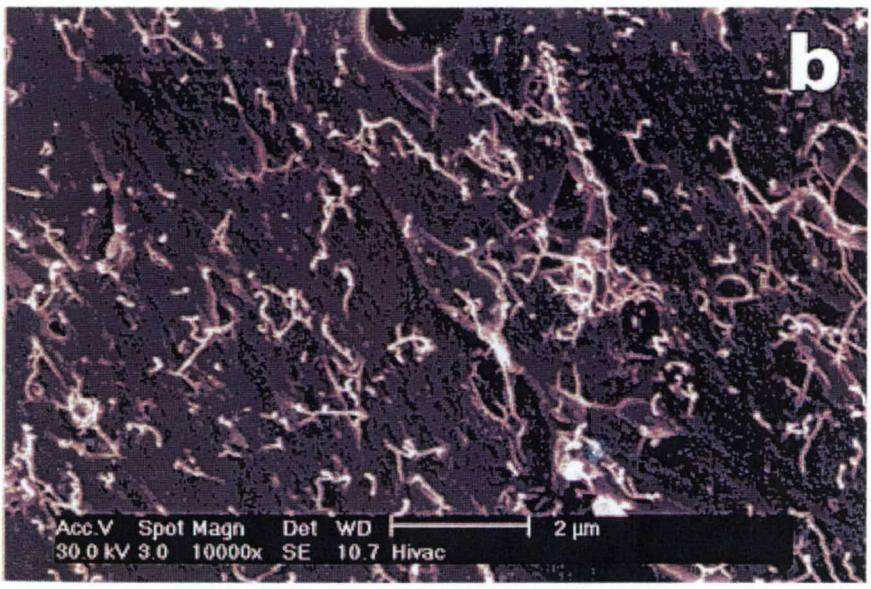

Figure 1.5 Improved tube dispersion in epoxy resin of functionalized SWNTs

To improve the interfacial interaction of SWNT/polymer composites, Gong *et al.* [56] used Polyoxyethylene 8 lauryl, $(CH_3\text{-}(CH_2)_{11}(OCH_2CH_2)_7OCH_2CH_3)$ or $C_{12}EO_8$ as surfactant to disperse the SWNT into polymer. The storage moduli and glass transition

temperature of the neat resin and carbon nanotube composite samples are listed in Table 1.3. Using surfactants as processing aids was found to improve the thermomechanical properties of carbon nanotube/polymer composites. The addition of only 1 wt % carbon nanotubes in the composite increased the glass transition temperature from 63°C to 88°C. The elastic modulus also increased by more than 30%. In contrast, the addition of carbon nanotubes without the surfactant only had moderate effects on the glass transition temperature and the mechanical properties. The SEM image shown in Figure 1.6 indicates that the addition of the surfactant, greatly improved the dispersion of SWNTs in the epoxy .

Table 1-3 Storage moduli and glass transition temperature of neat resin and carbon nanotube composites sample

samples	G' (GPa)			T_g (°C)	
	−60 °C	−20 °C	20 °C	tan δ	G''
(a) epoxy	1.90	1.65	1.43	63	50
(b) epoxy+$C_{12}EO_8$	1.53	1.38	1.20	62	47
(c) epoxy + 1% tube	2.12	1.90	1.60	72	53
(d) epoxy + $C_{12}EO_8$ + 1% tube	2.54	2.18	1.80	88	64

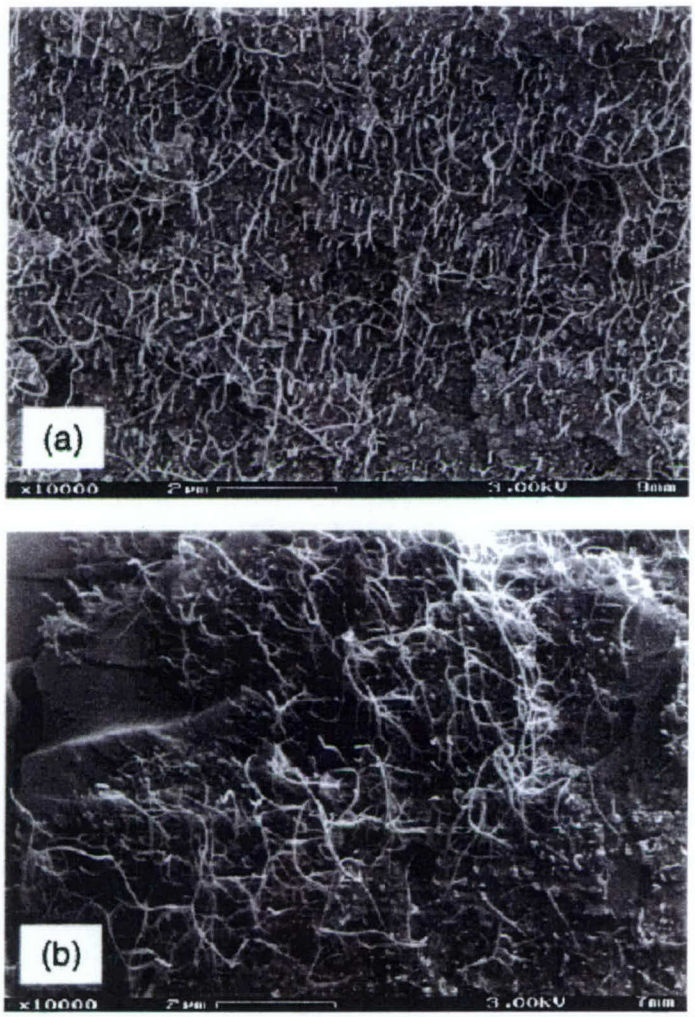

Figure 1.6 SEM photographs of carbon nanotubes on fracture surfaces of the composite samples: (a) with $C_{12}EO_8$ and (b) without $C_{12}EO_8$

1.9. Conclusions

There are two types of carbon nanotubes, SWNTs and MWNTs. SWNTs tend to self-assemble into ropes due to the van der Waals force between individual SWNTs. Carbon nanotubes can be synthesized using various methods, including arc discharge, laser vaporization and chemical vapor deposition. The CVD process offers the best known potential for large-scale production of carbon nanotubes. Further, CVD can synthesize carbon nanotubes with controlled diameter, length and alignment. Both experimental and theoretical studies show that carbon nanotubes, particularly SWNTs, have outstanding mechanical and functional properties, such as electronic, electrical, magnetic and thermal

properties. The composite community considers nanotubes as one of the most promising reinforcements for the next generation polymer composite materials.

Currently, nanotube based composites fabricated by directly mixing the nanotubes with polymers do not yield acceptable properties due to non-uniform dispersion, lack of orientation of nanotubes, and weak interface between nanotubes and polymer matrix. Consequently, the resultant composites fail to live up to the quality anticipated. Yet, developing of innovative processing techniques are ongoing to properly handle and optimize the nanoscale process to realize the full potential of nanotubes. A more comprehensive literature review report has been submitted to AFRL as part of this project's deliverables [57].

1.10. References

[1] Iijima, S. "Helical Microtubles of Graphite Carbon," *Nature*, Vol. 354, No. 6348, 1991, pp. 56-58.

[2] Saito, R., Dresselhaus, G., and Dresselhaus, M. S., *Physical Properties of Carbon Nanotubes*, 1998, London, Imperial College Press.

[3] Saito, R., Fujita, M., Dresselhaus, G., and Dresselhaus M. S., "Electronic Structure of Chiral Graphene Tubules," *Applied Physics Letters*, 1992, Vol. 60, No. 18, pp. 2204-2206.

[4] Ebbesen, T. W. and Ajayan, P. M., "Large-scale Synthesis of Carbon Nanotubes," *Nature*, 1992, Vol. 358, pp. 220-222.

[5] Bethune, D. S., Kiang, C. H., de Vries, M. S., Gorman, G., Savoy, R., Vazquez, J., and Beyers, R., "Cobalt-catalyzed Growth of Carbon Nanotubes with Single-atomic-layer Walls," *Nature*, 1993, Vol. 363, pp. 605-607.

[6] Thess, A., Lee, R., Nikolaev, P., Dai, H J., Robert, J., Xu C. H., Lee, Y. H., Kim, S. G., Rinzler, A. G., and Colbert, D. T., "Crystalline Ropes of Metallic Carbon Nanotubes," *Science*, 1996, Volume 273, No. 5274, pp. 483-487.

[7] Nikolaev, P. Bronikowski, M. J., Bradley, R. K., Colbert, D. T., Smith, K. A., and Smalley, R. E., "Gas-phase Catalytic Growth of Single-walled Carbon Nanotubes from Carbon Monoxide," *Chemical Physics Letters*, 1999, Vol. 313, pp. 91-97.

[8] Ren, Z. F., Huang, Z. P., Xu, J. W., Wang, J. H., Bush, P., Siegal, M. P., and Provencio, P. N., "Synthesis of Large Arrays of Well-aligned Carbon Nanotubes on Glass," *Science*, 1998, Vol. 282, No. 6, pp. 1105-1107.

[9] Bower, C., Zhu, W, Jin, S., and Zhou, O., "Plasma-induced Alignment of Carbon Nanotubes," *Applied Physics Letters*, 2000, Vol. 77, No. 6, pp. 830-832.

[10] Fan, S. S., Chapline, M. G., Franklin, N. R., Tombler, T. W., Cassell, A. M., and Dai, H. J., "Self-oriented Regular Arrays of Carbon Nanotubes and Their Field Emission Properties," *Science*, 1999, Vol. 283, pp. 512-514.

[11] Franklin, N. R. and Dai, H. J. "An Enhanced CVD Approach to Extensive Nanotube Networks with Directionality," *Advanced Materials*, Vol. 12, No. 12, pp. 890-893.

[12] Zhu, H. W., Xu, C. L., Wei B. Q., Vajtai, R., and Ajayan, P. M., "Direct Synthesis of Long Single-Walled Carbon Nanotube Strands," *Science*, 2002, Vol. 296, pp. 884-886.

[13] Krishman, A. "Young's Modulus of SWNTs," *Physical Review B*, 1998, Vol. 58, No. 20, pp. 14013-14019.

[14] Salvetat, J. P., Briggs, G. A. D., et al., "Elastic and Shear Moduli of Single-Walled Carbon Nanotube Ropes," *Physical Review Letters*, 1999, Vol. 82, No. 5, pp. 944-947.

[15] Walters, D. A., Ericson, L. M., Casavant, M. J., Liu, J., Colbert, D. T., Smith, K. A., and Smalley, R. E., "Elastic Strain of Freely Suspended Single-wall Carbon Nanotube Ropes," *Applied Physics Letters*, 1999, Vol. 74, No. 25, pp. 3803-3805.

[16] Yu, M. F., Files, B. S., Arepalli, S., and Ruoff, R. S., "Tensile Loading of Ropes of Single Wall Carbon Nanotubes and Their Mechanical Properties," *Physical Review Letters*, 2000, Vol. 84, No. 24, pp. 5552-5555.

[17] Trecacy, M J., Ebbesen, T. W., and Gibson, T. M., "Exceptionally High Young's Modulus Observed for Individual Carbon Nanotubes," *Nature*, 1996, Vol. 381, pp. 680-687.

[18] Wong, E. W., Sheehan, P. E., and Liebert, C. M., "Nanobeam Mechanics: Elasticity, Strength, and Toughness of Nanotods and Nanotubes," *Science*, 1997, Vol. 277, pp. 1971-1975.

[19] Yu, M. F., Lourie, O., Dyer, M. J., Moloni, K., Kelly, T. F., and Ruoff, R. S., "Strength and Breaking Mechanism of Multiwalled Carbon Nanotubes Under Tensile Load," *Science*, 2000, Vol. 287, pp. 637-640.

[20] Lu, J. P., "Elastic Properties of Carbon Nanotubes and Nanoropes," *Physical Review Letters*, 1997, Vol. 79, No. 7, pp. 1297-1300.

[21] Hernandez, E., Goze C., Bernier, P., and Rubio, A., "Elastic Properties of C and $B_xC_yN_z$ Composite Nanotubes," *Physical Review Letters*, 1998, Vol. 80, No. 20, pp. 4502-4505.

[22] Popov, V. N., Doren, V. E. V., and Balkanski, M., "Elastic Properties of Crystals of Single-walled Carbon Nanotubes," *Solid State Communications*, 2000, Vol. 114, pp. 395-399.

[23] Nardelli, M. B., Fattebert, J. L., Orlikowski, D., Roland, C., Zhao, Q., and Bernholc, J., "Mechanical Properties, Defects and Electronic Behavior of Carbon Nanotubes," *Carbon*, 2000, Vol. 38, pp. 1703-1711.

[24] Ru, C. Q., "Effect of van der Waals Forces on Axial Buckling of a Double-walled Carbon Nanotube," *Journal of Applied Physics*, 2000, Vol. 87, No. 10, pp. 7227-7231.

[25] Ru, C. Q., "Column Buckling of Multiwalled Carbon Nanotubes with Interlayer Radial Displacements," *Physical Review B*, 2000, Vol. 62, No. 24, pp. 16962-16967.

[26] Ru, C. Q., "Degraded Axial Buckling Strain of Multi-walled Carbon Nanotubes due to Interlayer Slips," *Journal of Applied Physics*, 2001, Vol. 80, No. 6, pp. 3426-3433.

[27] Kolmogorov, A. N. and Crespi, V. H., "Smoothest Bearings: Interlayer Sliding in Multiwalled Carbon Nanotubes," *Physical Review Letters*, 2000, Vol. 85, No. 22, pp. 4727-4730.

[28] Frank, S., Poncharal, P., Wang, Z. L., and de Heer W. A., "Carbon Nanotube Quantum Resistors," *Science*, 1998, Vol. 280, pp. 1744-1746.

[29] Wei, B. Q., Vajtai, R., and Ajayan, P. M. "Reliability and Current Carrying Capacity of Carbon Nanotubes," *Applied Physics Letters*, 2001, Vol. 79, No. 8, pp. 1172-1174.

[30] Eletskiĭ, A. V., "Carbon Nanotubes," *Physics-Uspekhi*, 1997, Vol. 40, No. 9, pp. 899-924.

[31] Langer, L., Bayot, V., Grivei, E., and Issi, J. P., "Quantum Transport in a Multiwalled Carbon Nanotube," *Physical Review Letters*, 1996, Vol. 76, No. 3, pp. 479-482.

[32] Lu, J. P., "Novel Magnetic Properties of Carbon Nanotubes," *Physics Review Letters,* 1995, Vol. 74, pp.1123-1126.

[33] Hone, J., Whittney, M., and Zettle, A., "Thermal Conductivity of Single-walled Carbon Nanotubes," *Synthetic* Metals, 1999, Vol. 103, pp. 2498-2499.

[34] Che, J. W., Cagin, T., and Goddard III, W. A., "Thermal Conductivity of Carbon Nanotubes," http://www.foresight.org/Conferences/MWNT7/Papers/Che/index.html

[35] Berber, S., Kwon, Y. K., and Tomànek, D., "Unusually High Thermal Conductivity of Carbon Nanotubes," *Physics Review Letters*, 2000, Vol. 84, No. 20, pp. 4613-4616.

[36] Ruoff, R. S. and Lorents, D. C. "Mechanical and Thermal Properties of Carbon Nanotubes," *Carbon*, 1995, Vol. 33, No. 7, pp. 925-930.

[37] Lozano, K., Rios, J. B., and Barrera, E. V., "A Study on Nanofiber-Reinforced Thermoplastic Composites (II): Investigation of the Mixing Rheology and Conduction Properties," *Journal of Applied Polymer Science*, 2001, Vol. 80, pp. 1162-1172.

[38] Qian, D., and Dickey, E. C., "In-situ transmission Electron Microscopy Studies of Polymer-carbon Nanotube Composite Deformation," *Journal of Microscopy*, 2001, Vol. 204, pp.39-45.

[39] Wagner, H. D., Lourie, O., Feldman, Y., and Tenne, R., "Stress-induced Fragmentation of Multiwall Carbon Nanotubes in a Polymer Matrix," *Applied Physics Letters*, 1998, Vol. 72, No. 2, pp. 188-190.

[40] Lourie, O., Cox, D. M., and Wagner, H. D., "Buckling and Collapse of Embedded Carbonn Nanotubes," *Physical Review Letters*, 1998, Vol. 81, No. 8, pp. 1638-1641.

[41] Lourie, O. and Wagner, H. D., "Transmission Electron Microscopy Observations of Fracture of Single-wall Carbon Nanotubes Under Axial Tension," *Applied Physics Letters*, 1998, Vol. 73, No. 24, pp. 3527-3529.

[42] Cooper, C. A., Young, R. J., and Halsall, M., "Investigation into the Deformation of Carbon Nanotubes and their Composites through the Use of Raman Spectroscopy," *Composites Part A:* Applied *Science and Manufacturing*, 2000, Vol. 32, pp. 401-411.

[43] Gong X. Y., Liu J., Baskaran S., Voise R. D., and Young J., "Surfactant-Assisted Processing of Carbon Nanotube/Polymer Composites," *Chemistry of Materials*, 2000, Vol. 12, pp. 1049-1052.

[44] Shaffer, M. S. and Windle, A. H., "Fabrication and Characterization of Carbon Nanotube/Poly(vinyl alcohol) Composites," *Advanced Materials*, 1999, Vol. 11, No. 11, pp. 937-941.

[45] Schadler L. S., Giannaris S. C., and Ajayan P. M., "Load Transfer in Carbon Nanotube Epoxy Composites," *Applied Physics Letters*, 1998, Vol. 73, No. 26, pp. 3842-3844.

[46] Ajayan P. M., Schadler L. S., Giannaris C., and Rubio A., "Single-walled Carbon Nanotube-polymer Composites: Strength and Weakness," *Advanced Materials*, 2000, Vol. 12, No. 10, pp.750-753.

[47] Ajayan, P. M., Stephan, O., Colliex, C., and Trauth, D., "Aligned Carbon Nanotube Arrays Formed by Cutting a Polymer Resin-nanotube Composite," *Science*, 1994, Vol. 265, pp. 1212-1214.

[48] Jin, L., Bower, C., and Zhou, O., "Alignment of Carbon Nanotubes in a Polymer Matrix by Mechanical Stretching," *Applied Physics Letters*, 1998, Vol. 73, No. 9, pp. 1197-1199.

[49] Haggenmueller, R., Gommans, H. H., Rinzler, A. G., Fischer, J. E., and Winey, K. I., "Aligned Single-wall Carbon Nanotubes in Composites by Melt Processing Methods," *Chemical Physics Letters*, 2000, Vol. 330, pp. 219-225.

[50] Walters, D. A., Casavant, M. J., Qin, X. C., Huffman, C. B., Boul, P. J., Ericson, L. M., Haroz, E. H., O'Connell, M. J., Smith, K., Colbert, D. T., and Smalley, R. E., "In-plane-aligned Membranes of Carbon Nanotubes," *Chemical Physics Letters*, 2001, Vol. 338, pp. 14-20.

[51] Qian D., Dickey E. C., Andrews R., Rantell T., "Load transfer and deformation mechanisms in carbon nanotube-polystyrene composites ", Appl. Phys. Lett., Vol.76, pp.2868-2870, 2000.

[52] Schadler L. S., Giannaris S. G., Ajayan P. M., Appl. Phys. Lett., 73(1998), 3842.

[53] Lourie O, Wagner H. D., "Transmission electron microscopy observations of fracture of single-wall carbon nanotubes under axial tension" Appl. Phys. Lett., Vol.73, pp.3527-3529, 1988.

[54] Linda S. Schadler, Kulyang Jiang, Rodney Andrews, Ami Eitan, "Nanotube reinforced polymer composites: tailoring the interface for improved mechanical properties", Internal report RPI.

[55] Jiang Zhu, JongDae Kim, Haiqing Peng, John L. Margrave, Valery N. Khabashesku, Enrique V. Barrera, Nano Lett., Vol.3, pp.1107, 2002.

[56] Xiaoyi Gong, Jun Liu, Suresh Baskaran, Roger D. Voise, James S. Young, "Surfactant-Assisted Processing of Carbon Nanotube/Polymer Composites", Chem. Mater, Vol.12, pp.1049-1052, 2000.

[57] Ben Wang, Literature Review Report: Comprehensive Property Characterization of Nanotube Buckypaper-Reinforced Composite Materials", submitted to AFRL, July, 2002.

2. New Manufacturing Process for SWNT-Reinforced Nanocomposites with Controlled Nanostructure and High Tube Loading: Buckypaper/Resin infiltration

Typically, SWNTs reinforced composites were fabricated by directly mixing SWNTs into polymers [1-6], followed by casting or injection molding techniques. However, SWNTs have a strong tendency to form bundles by aggregating together because of their large surface area and their strong van der Waals interaction. Their nanoscale dimension, stable chemical characteristics and smooth surface make efficiently dispersing SWNTs into a polymer matrix and controlling the final nanostructure of the composites during the processing difficult, if not impossible, particularly for high SWNT loading composites. Some researchers chemically modified the nanotube surface to improve the nanotubes dispersion in polymer matrix [7, 8]. However, these chemical modifications may destroy the pristine structure of the SWNTs and decrease maximum modulus and strength of the SWNTs [9]. Therefore, other dispersion methods that would avoid tube structure damage are required. Park *et al.* tried an in-situ polymerization method to effectively disperse as-pristine SWNT bundles into polyimide with the aid of sonication [10]. Besides the dispersion issue, the rapidly increasing viscosity of the polymer/tube mixture during processing made fabrication of high SWNT loading in composites difficult. The reported SWNT loading of the composites was usually less than 10~15% by weight.

In this research, a new processing technical approach was developed to manufacture the SWNT-reinforced composites with controlled nanostructure, desired tube alignment and high tube loading, which are critical for developing high performance nanocomposites. In this new buckypaper/resin infiltration process, SWNTs are first dispersed into water with the aid of surfactant and sonicated to form a stable suspension. The SWNT suspension is filtrated to form buckypapers, which are thin sheets composed of uniform SWNT rope networks. A diluted low viscosity resin solution infiltrates the buckypaper to impregnate the SWNT rope networks. A compressive molding process is then used to cure and make the final composite from the multilayered resin-impregnated buckypapers. Tube alignment of the composites can be achieved by magnetically aligning the SWNTs in the

buckypapers in a high magnetic field. This chapter describes this unique composite manufacturing process of buckypaper/resin infiltration. The manufacture of random orientated and magnetically aligned buckypapers are discussed in Chapters 3 and 4, respectively. The mechanical, electrical and thermal property properties of the resultant materials are presented in Chapter 5.

2.1. Raw Materials

The SWNTs used in this study were produced by Carbon Nanotechnologies Inc. (CNI) under the brand name "BuckyPearls^{TM}." According to the technical sheet provide by CNI, the individual tube is about 0.8-1.2 nm in diameter and 100-1000 nm long. The BuckyPearls were purified SWNTs product, as shown in Figure 2.1. The main impurities are metal catalyst particles (10~12 w/w%) and amorphous carbon. The bulk density of the BuckyPearls is 0.4g/cm^3. The TEM image of the SWNTs is given in Figure 2.2. The SWNTs were directly used without further purification.

Figure 2.1 BuckyPearls from CNI

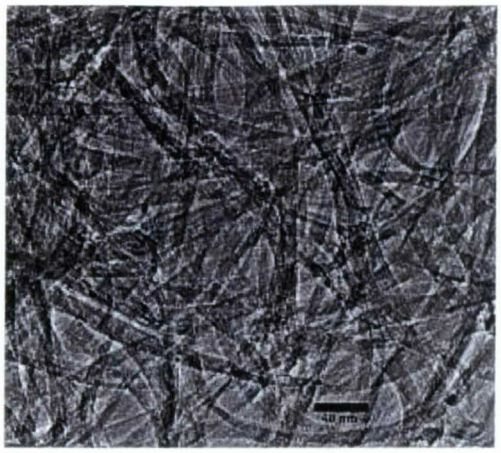

Figure 2.2 Clear SWNT ropes in BuckyPearls

Shell Chemical produced the epoxy resin system used in this study. EPON 862 is a low-viscosity, liquid epoxy resin manufactured from epichlorohydrin and Bisphenol-F (DGEBPF). This resin contains no diluents or modifiers. When cross-linked with appropriate curing agents, superior mechanical, adhesive, electrical and chemical resistance properties can be obtained. The epoxide equivalent weight of EPON 862 is 166-167. The viscosity of EPON 862 at 25C is 2700cp. The hardener EPI Cure W is a type of DETDA hardener or curing agent. The resin and curing agent molecules are shown in Figure 2.3.

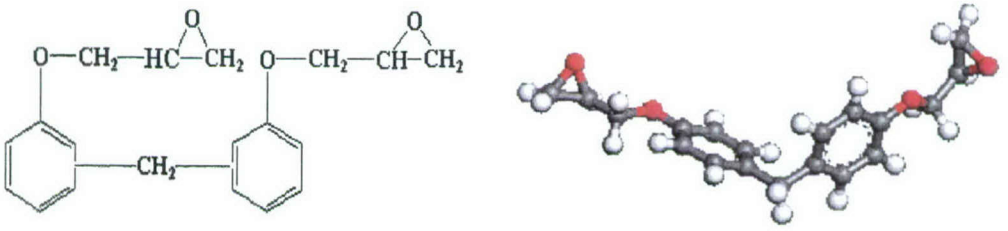

(a) Chemical structure and molecular model of EPON 862

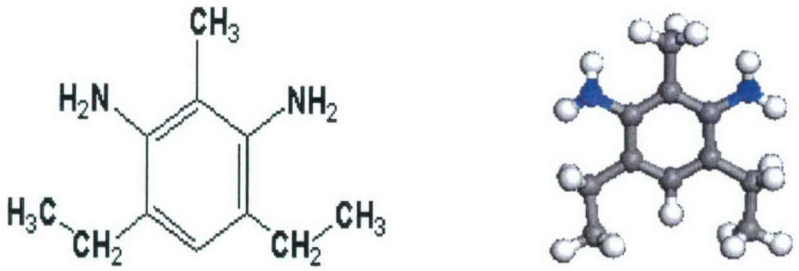

(b) Chemical structure and molecular model of DETDA

Figure 2.3 Molecular models of an EPON 862 epoxy resin and curing agent (DETDA)

2.2. Buckypaper/Resin Infiltration Process

Buckypapers are thin (10~50 μm) membranes of nanotube networks produced by multiple-step process of tube dispersion and suspension filtration. Since aqueous suspension and a number of different water-based surfactants can be used, relatively good tube dispersion can be expected in the buckypapers. The formed tube networks in the buckypapers can be retained in the composite fabrication operation and transferred into the final solid nanocomposites. In other words, the buckypaper can provided a preformed nanotube reinforcement structure for the final nanocomposites.

2.2.1. Preparation of buckypapers of randomly orientated SWNTs

In this research, buckypapers of random oriented SWNTs were produced by filtrating SWNT suspensions. The concentration of the aqueous SWNT suspension was 40mg SWNTs/L. Triton X-100 (Fisher Scientific) was used as surfactant. The buckypaper was prepared using the following procedure:

a) Weigh 40mg SWNTs (BuckyPearls);

b) Grind SWNTs with a small amount water (~10ml) using a mortar and pestle;

c) Add 20ml water into the mortar and sonicate 5min (Sonicator 3000, Misonix Inc.) to form a black thick paste;

d) Add 4g surfactant Triton X-100 into the paste and transfer paste into 250ml deioned water;

e) Sonicated 30 minutes using the sonicator with full power

f) Transfer this suspension into 500ml deioned water and sonicate another 30 minutes;

g) Add additional 500ml deioned water and sonicate 30 minutes to form a stable ink-like suspension;

h) Filtrate resultant suspension through a nylon filter membrane (47mm diameter and 0.45 μm pore size) with the aid of vacuum;

i) Wash the buckypaper separately with water and iso-propanal to thoroughly wash away the Triton X-100;

j) Peel off buckypaper from the nylon membrane and dried overnight under room temperature and then dried in vacuum oven at 80°C.

The filtration process takes 8-12 hours due to the small pore size of the filter membranes. The resultant buckypapers are shown in Figure 2.4. The produced buckypapers are thin black membranes less than 50μm thick. The buckypaper were strong and flexible to allow for handling similar to traditional glass fiber mats.

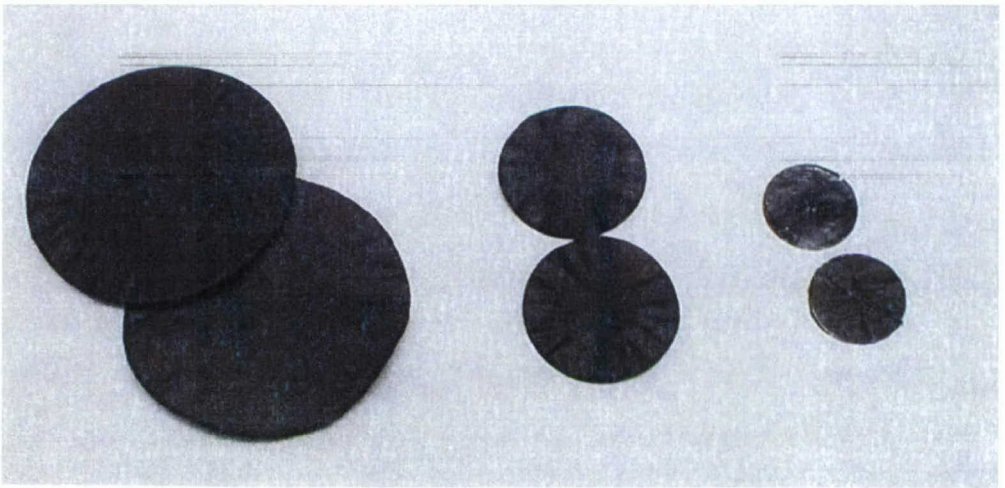

90 mm 47 mm

Figure 2.4 Buckypapers

2.2.2. Characterization of nanostructure of the buckypapers

The nanostructures of the produced buckypaper and buckypaper/epoxy nanocomposites were characterized using Scanning Electron Microscope (Joel 6400F, Joel Co.) and Atomic Force Microscope (Dimension 3000, Digital Instrument Co.). SEM and AFM images of the SWNT buckypapers are shown in Figure 2.5 and Figure 2.6, respectively. The buckypaper showed porous network structures composed of "continuous" SWNT ropes. These "continuous" ropes were the result of tube self-assembly by van der Waals force during buckypaper filtration. The rope size and porous structure were uniform, which indicates very good dispersion of the nanotubes in the suspension. The rope diameter was 15-60 nm. The images show the nanoscale porous structures of the buckypapers with pore sizes around 100-200 nm, which is much smaller than in the traditional glass fiber and carbon fiber fabrics or mats, indicating that the wetting and resin infiltration of buckypaper-based composites will occur at nanoscale, and a significant impact of the intense molecular interactions can be expected. More detailed descriptions and analysis of buckypaper manufacturing process are provided in Chapter 3.

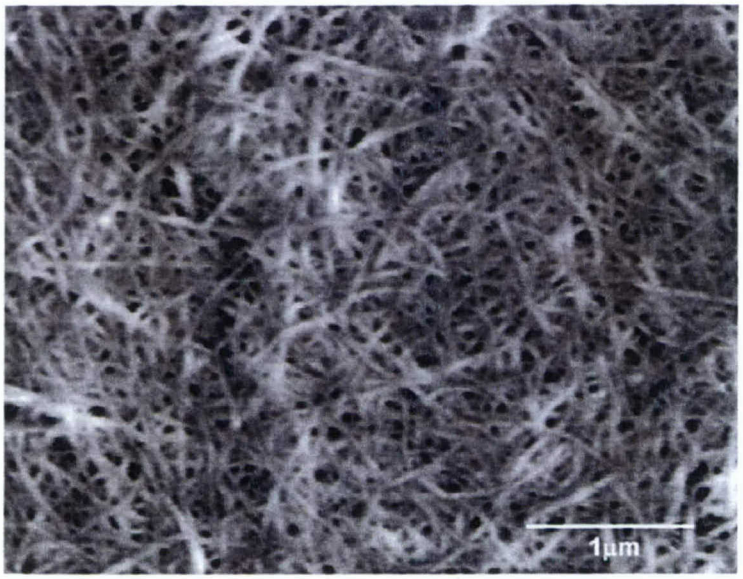

Figure 2.5 SEM image of the random buckypaper nanostructure

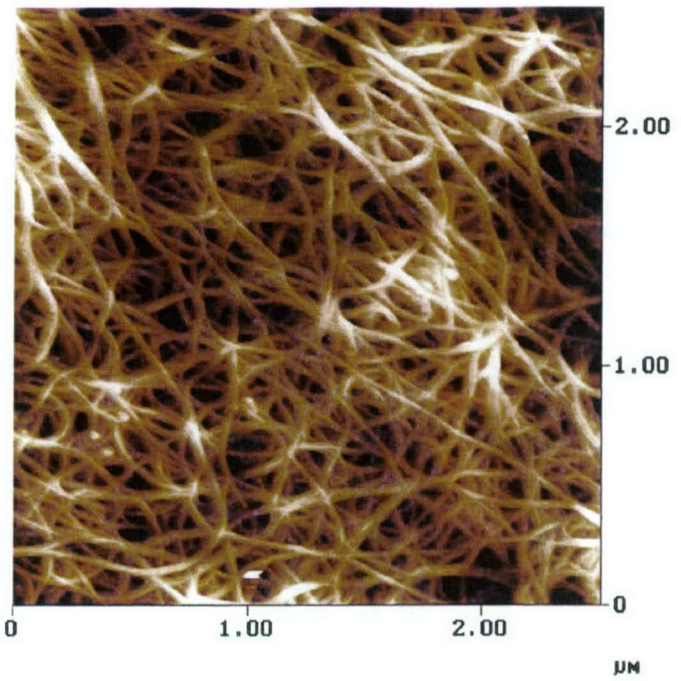

Figure 2.6 AFM image of the random buckypaper

2.2.3. Molecular interactions within buckypapers

When the liquid epoxy resins are infused through the nanoscale porous structures of the buckypaper, the molecular interactions between the resin molecules and carbon nanotubes in the porous structure are important for nanocomposite processing. These molecular interactions significantly influence the processing properties of the manufacturing process, which in turn determines the mechanical properties of the resultant nanocomposites.

A wide variety of factors influences the molecular interactions in the porous environment, such as the affinities of epoxy resins for carbon nanotubes, the pore structures and related processing conditions. However, detecting and determining the molecular behavior inside the nanoscale pores are difficult. Therefore, computational methods provide predictions of the molecular interactions in the nanoscale pores (nanopores). Some of the assumptions were made due to the restrictions on the computational efficiency. The first assumption was on the pores, which were constructed with four individual SWNTs,

without considering the SWNT ropes. Secondly, only the small pore size was considered although the actual buckypaper pore size is around hundred nanometers. With these assumptions, predicting the molecular interactions in the buckypaper pore structure becomes possible by using MD simulation. The more detailed discussion of MD simulation can be found in Chapter 6.

In the MD simulations, a model of buckypaper pore was used to examine the molecular interactions in the nanopore. A square nanopore was constructed with four (10,10) SWNTs with a length of 97 Å. The resulting pore width was 6 nm × 6 nm and 3 nm thick. The molecular model of the nanopore is shown in Figure 2.7. When processing buckypaper/epoxy nanocomposites, the EPON 862 epoxy resin was infused into the buckypaper after mixing with the curing agent. The liquid resin consisted of EPON 862 epoxy resin and DETDA curing agent with a weight ratio of 100:26.4. The ratio of the resin molecule number to the curing agent molecule number was about 2:1, which was used in the simulation. The simulation model contained 7,145 atoms.

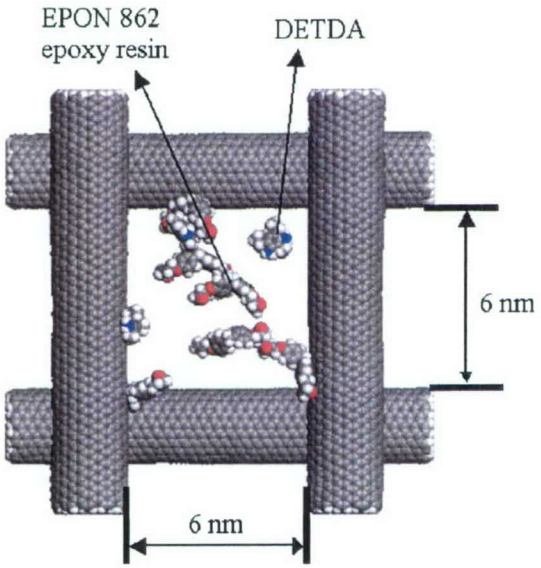

Figure 2.7 Molecular model of resin flowing though a small nanotube pore

Snapshots of MD simulation results are shown in Figure 2.8. Initially, the EPON 862 epoxy resin and curing agent molecules were placed near the opening of the pore (some slightly inside the pore, some well outside the pore). The simulation showed that during

the initial 10 ps, the resin molecules changed their orientation and moved towards the nanotubes. After a long equilibration period of 80 ps, the resin molecules close to a nanotube eventually moved closer and wetted the nanotube due to their attractive interaction. However, the resin molecules in the middle of the pore remained in the same location due to the resin molecules' weak interactions with the nanotubes. Considering a large quantity of such nanoscale pore structures exit in the buckypaper, the influences of tubes/resin molecular interactions during composite manufacturing can be expected, which are usually ignored in the conventional fiber/resin composite processing. Further research is needed to reveal the influence of molecular interactions on resin flow with nanoscale pore structures of buckypaper.

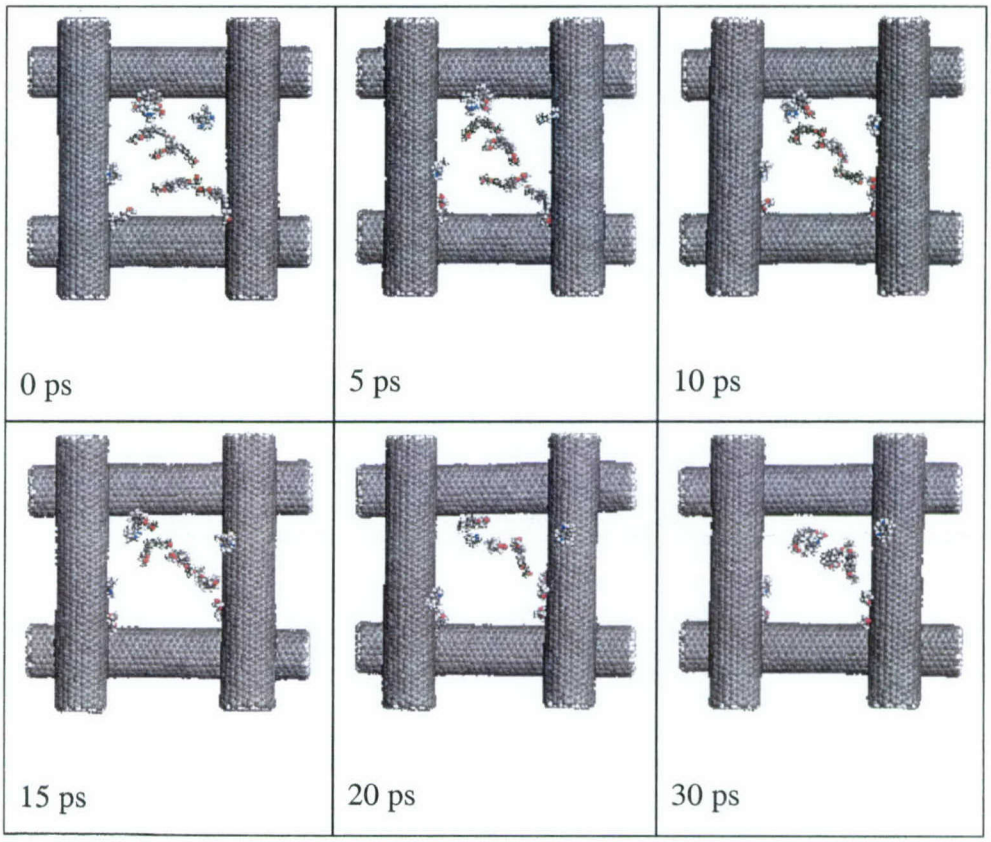

(a) Side view of the MD simulation results

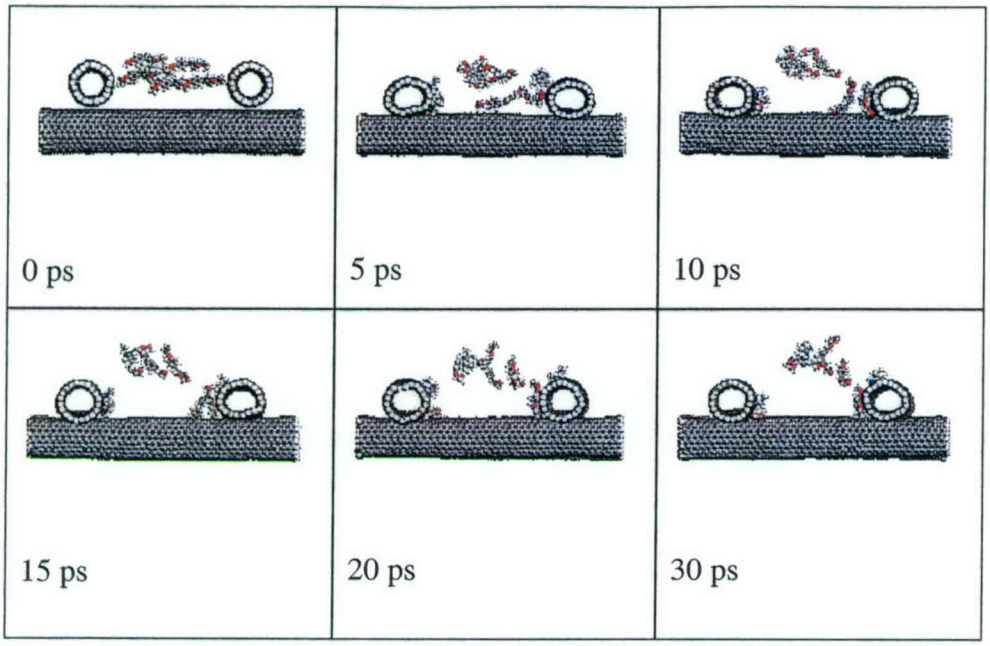

(b) Cross sectional view of the MD simulation results

Figure 2.8 MD simulation snapshots of the molecular interactions in a buckypaper pore structure

2.2.4. Permeability of buckypapers

Through thickness (z-direction) permeability of the produced buckypaper was measured to estimate the resin infiltration time along the thickness direction. Water was used as the fluid in the permeability test. The experiment was carried out with a filtration system. A buckypaper was placed inside the filter and sealed. The buckypaper acted as a filter membrane in this test. The water was added and flowed through the buckypaper along the thickness direction with the aid of a vacuum. The water flow rate, buckypaper thickness, buckypaper surface area and vacuum pressure were recorded to calculate the permeability. Under this experimental condition, the permeability in the z-direction of a buckypaper of 20-50μm thickness and the nanoscale pore structure was measured. The z-direction permeability K_z was calculated using the following equation derived from Darcy's Law:

$$K_z = \frac{Q\eta L}{AP} \tag{2.1}$$

where: Q is the flow rate;

η is the viscosity of water;

L is the thickness of buckypaper;,

P is the vacuum pressure;

and A is the surface area of buckypaper.

The permeability test results are listed in Table 2.1. The average value of the buckypaper's z-direction permeability was about $2\times10^{-19}m^2$. Compared to normal glass fiber reinforcement fabrics or mats, the permeability of the buckypaper was 8-10 order lower. The small in-plane permeability of buckypaper can also be expected due to its small pore sizes. Therefore, allowing the resin flow and infuse the buckypaper in the in-plane direction as for conventional RTM and VARTM processes would be extremely difficult due to the thinness (20-50μ) of the produced buckypaper, as well as very low permeability.

Table 2-1 Kz of the buckypapers

Buckypaper Thickness (μm)	25.4	31.2	35.7
z-Permeability (m^2)	3.36×10^{-19}	1.11×10^{-19}	1.44×10^{-19}
Average z-Permeability (m^2)	1.97×10^{-19}		

To allow the resin system to completely impregnate the entire thickness direction of the buckypaper, the minimum infiltration time can be calculated by equation 2, which is also derived from 1D Darcy's Law.

$$t = \frac{\eta L^2}{K_z P} \tag{2}$$

where: K_z is the z-direction permeability of buckypaper;

η is the viscosity of resin;

L is the thickness of buckypaper;

and P is the vacuum pressure for resin infusion.

The viscosity of EPON 862/EPI Cure W (DETDA) system is 2700cp at room temperature, which means that under a full vacuum, complete impregnation through a 40um thickness buckypaper at room temperature will take more than 60 hours. During such a long period, the EPON 862/EPI Cure W system will partially gel, which will increase the viscosity and require an even longer time to impregnate, making the process not feasible. Therefore, decreasing the viscosity of EPON 862/EPI Cure W system was necessary. Acetone was used to dilute the resin system and decrease the viscosity. In our experiments, the content of acetone was properly controlled such that enough resin was left within the final nanocomposites after the evaporation of the acetone. The chosen weight ratio of the EPON 862/EPI Cure W system EPON to acetone was 10:7. The viscosity of the diluted resin solution was 25cp at room temperature. A 5-hour infiltration time was chosen to ensure the buckypaper was completely impregnated, which was indicated by observing a liquid resin layer appearing on the opposite surface of the buckypaper during resin infiltration.

2.2.5. Resin infiltration of the buckypapers

Resin infiltration was performed under the same experimental setup as the permeability test. Instead of water, epoxy resin was used as the fluid. The EPON862 and EPI Cure W were mixed at a weight ratio of 100:26.4. The mixed resin and curing agent were diluted with acetone at the weight ratio of 10:7 to decrease the viscosity. To properly impregnate the SWNTs, the diluted resin system was allowed to flow through the buckypaper along its thickness direction for 5 hours. Figure 2.9 illustrates the buckypaper before and after resin infiltration, showing that the resin completely infiltrated though and impregnated

the buckypaper. After infiltration, the impregnated buckypaper was soaked into EPON 862 resin system overnight. The acetone was vaporized in the vacuum oven, and made ready for use.

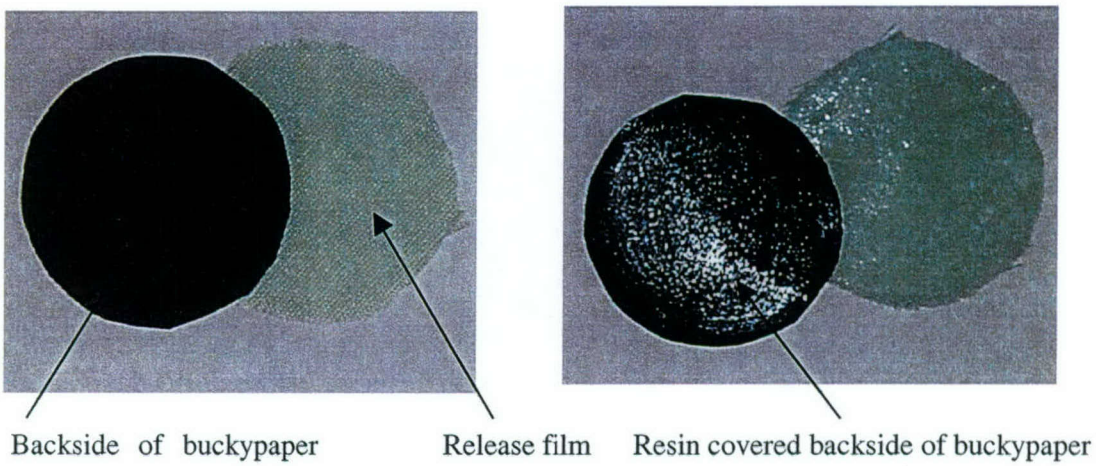

Figure 2.9 Buckypapers before and after resin infiltration

2.2.6. Fabrication of SWNT buckypaper/epoxy nanocomposites

SWNT buckypaper/epoxy resin nanocomposites were prepared using the compression molding technique. The hot press machine used in this research was manufactured by Carver (Mode. #3925). Several resin-impregnated buckypapers were stacked to fabricate relatively thick (0.2-0.5mm) bulk composite samples. The mold assembly is shown in Figure 2.10. Silicon rubber 0.5 mm thick was used to evenly distribute the pressure since the buckypaper was too thin. The thickness control film was the PTFE coating film (0.12mm thickness) with a central hole the diameter slightly larger than that of the composites to be molded. This film was used to control the thickness of the final composites. Another two PTFE films served as the release films and control the surface quality of the nanocomposite. The pressure was 10kg/cm^2. The curing process followed the instructions from the Shell Chemical: cure at 177°C for 2.5 hours under pressure; cool to room temperature; post cure in an oven for another 2 hours at 177°C and cool to room temperature inside the oven.

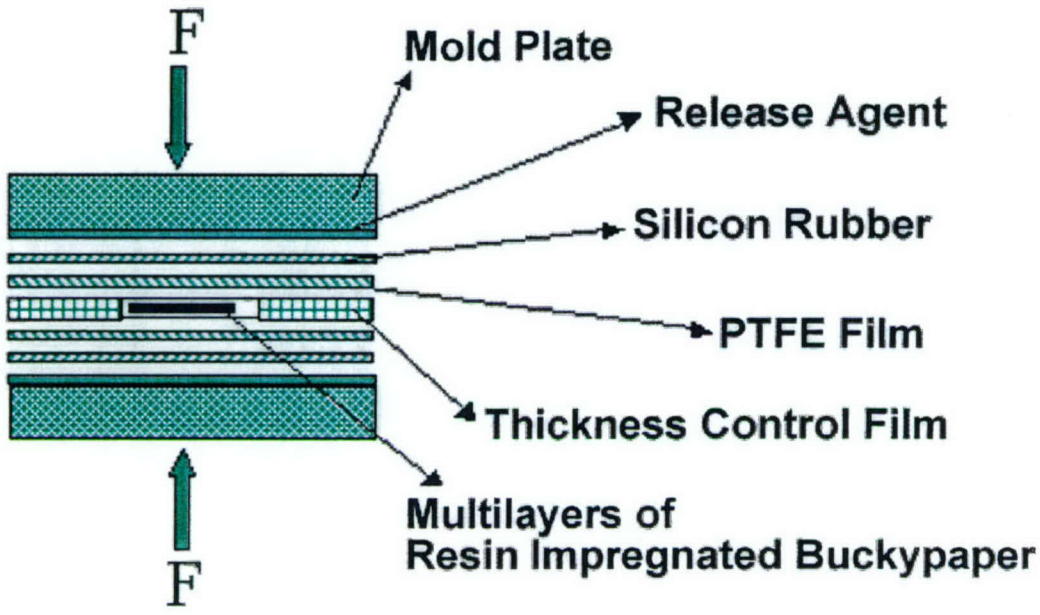

Figure 2.10 Mold assembly of hot press

The manufactured random buckypaper-reinforced composites are listed in Figure 2.1. The composites have a diameter of 47mm. In conventional processing techniques of directly mixing resin with SWNTs, even less than 1wt% loading of SWNTs mixed in resin will result in extremely high viscosity. High viscosity causes dispersion problems and makes manufacturing the composites difficult, if not impossible. Using the proposed method, the high viscosity issue has been completely avoided and the SWNT loading of the resulting composites can be as high as 39wt%.

Table 2-2 Random buckypaper nanocomposites

Sample No.	No. of Buckypaper Layers	Composites Thickness (mm)	SWNT Content (wt%)
A	5	0.198	28.1
B	3	0.114	31.3
C	3	0.220	37.7
D	3	0.246	39.1

2.2.7. Nanostructures of the produced buckypaper/epoxy composites

Figure 2.11 is the SEM image of the fracture surface of the SWNT composite samples of more than 30w/w% tube loading. These samples were fractured under tensile force. Figure 2.11 (a) shows the cross-section of the nanocomposite sample, indicating that the epoxy resin completely impregnated throughout the cross section of the buckypaper-reinforced composites. The fracture surface was coarse, as shown in Figure 2.11(b), which may indicate that the composite has good toughness because the SWNT tubes are flexible that increases not only the stiffness but also the toughness. Figure 2.11(c) and (c) show that the SWNT ropes were distributed across the surface and show a continuous and evenly distributed network. Good tube/resin wetting was also observed. The striking observation was the morphology of SWNT ropes, which were surrounded by cured epoxy resins, as shown in Figure 2.12 (AFM images). These could be contrasted from the SWNT ropes in the buckypaper before resin infiltration, as shown in Figure 2.5 and Figure 2.6. The porous structure of the original nanotube network of the buckypapers was replaced by the epoxy resin.

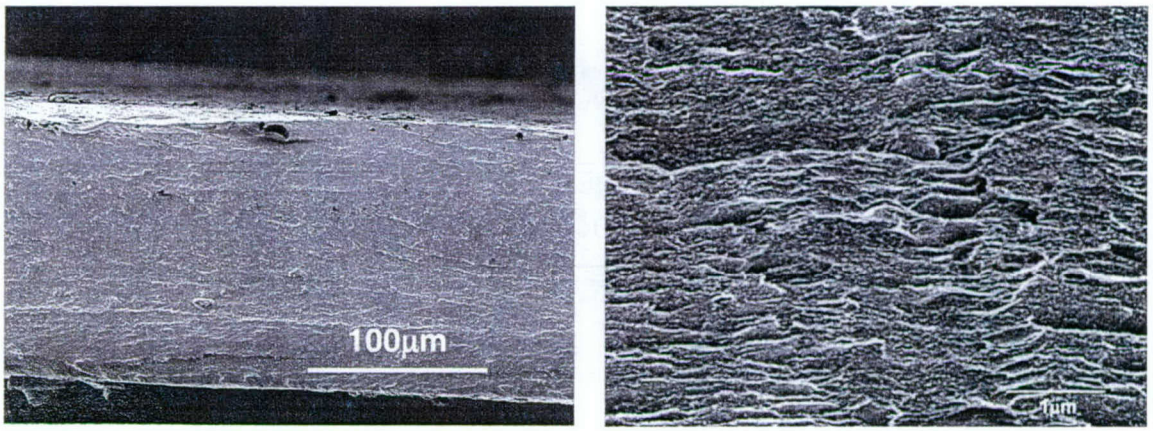

(a) Good resin/buckypaper impregnation (b) Rough fracture surface

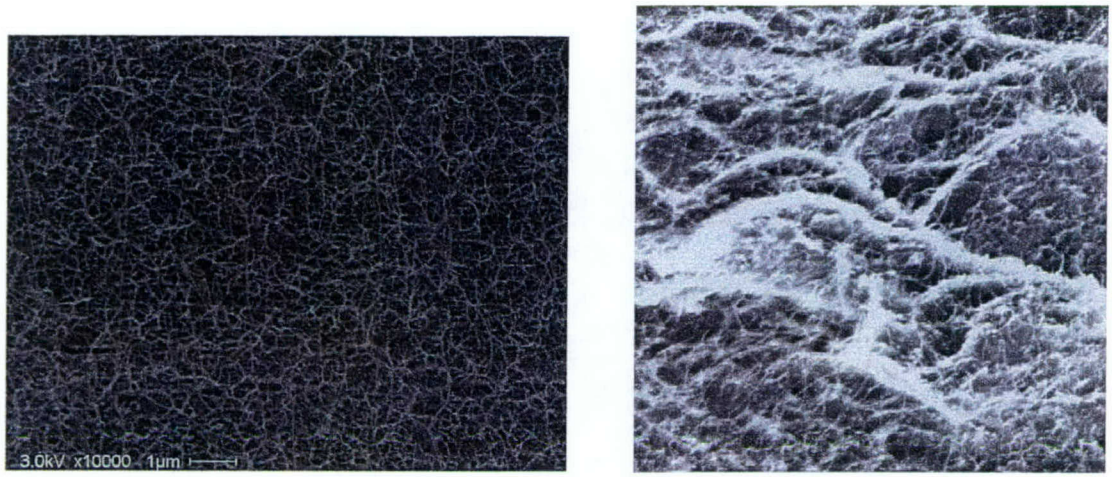

(c) SWNT network in the composites (d) SWNT network in the composites (x30K)

Figure 2.11 SEM images of the fracture surface of buckypaper composites

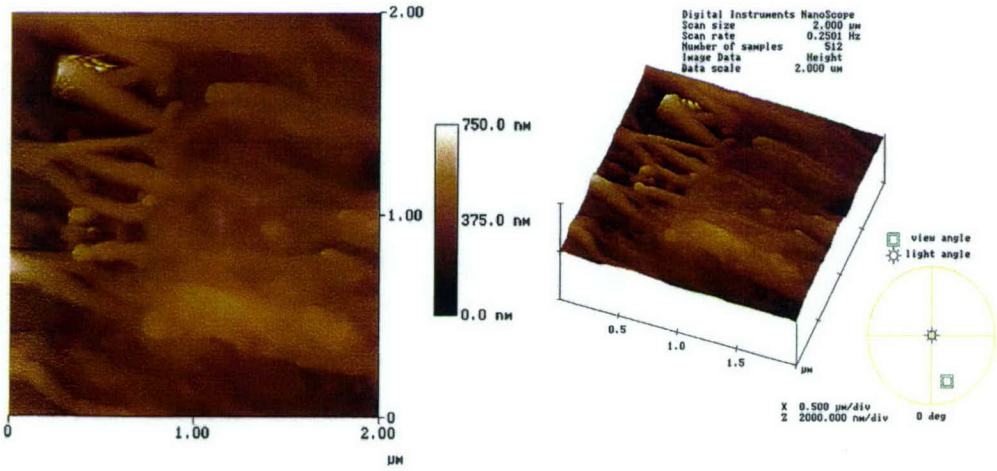

Figure 2.12 AFM images of tube/resin wetting in buckypaper composites

2.3. Nanocomposites of Magnetically Aligned Buckypaper Nanocomposites

Due to their nanoscale dimension, extra-large surface area and strong molecular interactions, SWNTs have the tendency to form ropes that aggregate together making direct manipulation of large quantity of nanotubes difficult for achieving desired alignment during nanocomposite processing [11-20]. Several efforts have been attempted to control tube alignment in composites. Ajayan and his colleagues observed tube alignment during cutting polymer/nanotube samples [21]. Stretch-induced alignment,

which involves mechanically stretching the SWNTs/PMMA composites at an elevated temperature of 90°C, has also been attempted [22, 23]. Nanotube alignment has been reportedly achieve through spinning or spooling a mixture of nanotubes/resin into fibers or strip forms, which is called flow-induced alignment. However, these methods are considered ineffective since only local and relatively low degree of orientation can be randomly achieved. Possible reasons for the inability of aligning tubes in composites are high resin viscosity, tube aggregation and strong tube/polymer resin molecular interactions after resin/tube mixing.

In this project, nanocomposites with controlled tube alignment and high tube loading were fabricated by using the magnetically aligned buckypapers/resin infiltration approach. Detailed preparation of magnetically aligned buckypapers is discussed in Chapter 4. By using the same resin infusion approach and curing parameters as outlined in Section 2.3, composite samples of six-layer magnetically aligned buckypaper/epoxy were successfully produced, as shown in Figure 2.13. In the composite processing, all six aligned buckypapers were stacked along the same alignment direction to produce quasi-unidirectional SWNT-reinforced nanocomposites. The curvature of the composite samples, as shown in Figure 2.13, also indicates good tube alignment. The parameters of the produced aligned buckypaper composites are provided in Table 2.3. Since SWNTs are more closely packed in the magnetically aligned buckypapers, the tube content of the composites is relatively high than that of the random buckypaper composites. The composite samples could have diameters of 25-90 mm and thickness of 40-200 μm depending on the number of layers of impregnated buckypapers used.

Figure 2.13 Curvature of magnetically aligned buckypaper composite

Table 2-3 Parameters of magnetically aligned buckypaper nanocomposites

Sample	Magnetic field* (T)	SWNT content in nanocomposites (w/w%)
Aligned Nanotube/Epoxy 1	17.3	47.3
Aligned Nanotube/Epoxy 2	17.3	63.7
Aligned Nanotube/Epoxy 3	17.3	54.5

*Magnetic strength for fabricating aligned buckypapers (see Chapter 4)

Figure 2.14 and Figure 2.15 show the cross-sections of the aligned buckypaper composites, which indicates that the tube alignment in the magnetically aligned buckypaper was successfully transferred into the bulk solid composite samples. The SWNTs and resin matrix can be seen to have achieved good impregnation throughout the cross-section in the nanocomposites. The results indicate that the proposed processing approach is effective for manufacturing nanocomposites with high loading and controlled tube alignment nanocomposites.

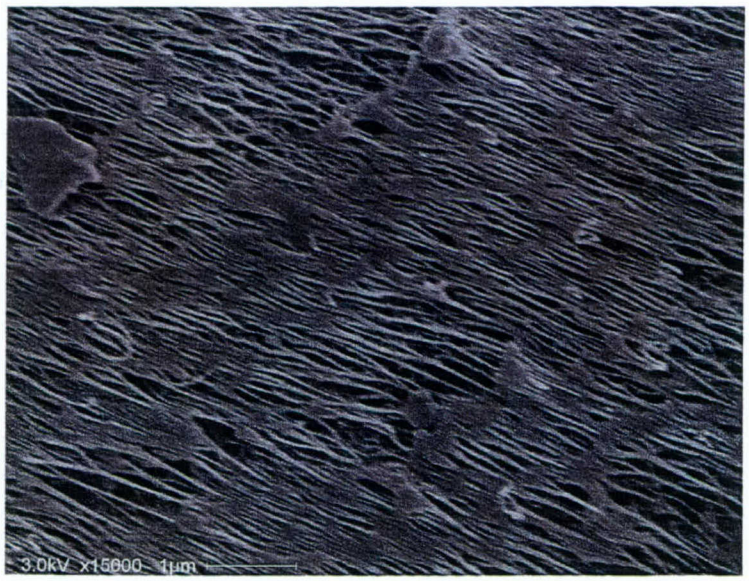

Figure 2.14 Tube alignment in magnetically aligned buckypaper/epoxy resin

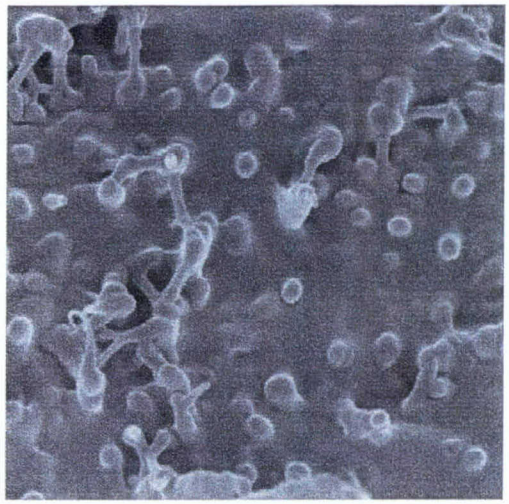

Figure 2.15 Cross-section of magnetically aligned buckypaper/epoxy composite (X12, 000)

2.4. Conclusions

The research developed a novel processing technique for producing buckypapers of preformed SWNT network/resin infiltration to fabricate SWNTs-reinforced nanocomposites with controlled nanostructure, desired tube alignment and high tube loading, which are very difficult to achieve by using conventional methods of directly mixing nanotube with resin matrix. The experimental results show that both random and oriented SWNT nanocomposites can be produced with high tube loading (23~60w/w%). Uniformly dispersed SWNT networks and good nanotube/resin impregnation were observed in random buckypaper/epoxy composite samples. Significant tube alignment in the magnetically aligned buckypaper nanocomposite was also demonstrated. This unique processing technique is an effective method for developing SWNTs-reinforced nanocomposites for high performance structures, thermal management and electrical conducting applications

2.5. References

[1] Satish Kumar, Thuy D. Dang, Fred E. Arnold, Arup R. Bhattacharyya, Byung G. Min, Xiefei Zhang, Richard A. Vaia, Cheol Park, W. Wade Adams, Robert H.

Hauge, Richard E. Smalley, Sivarajan Ramesh, and Peter A. Willis, "Synthesis, structure and properties of PBO/SWNT composites," *Physics*, 2002, 35, 9039.

[2] M. J. Biercuk, M. C. Llaguno, M. Radosavljevic, J. K. Hyun, and A. T. Johnson and J. E. Fischer, "Carbon nanotube composites for thermal management," *Applied Physics Letters*, 2002, 20, 15.

[3] Marc in het Panhuis, Amitesh Maiti, Alan B. Dalton, Albert van den Noort, Jonathan N. Coleman, Brendan McCarthy, Werner J. Blau, "Selective interaction in a polymer-single-walled carbon nanotube composites," 2003, 107, 478.

[4] Kin Liao, Sean Li, "Interfacial characteristics of a carbon Nanotube-polystyrene composite system", 2001, 79, 4225.

[5] J. Sandler, M.S.P. Shaffer, T. Prasse, W. Bauhofer, K. Schulte, A.H. Windle, "Development of a dispersion process for carbon nanotubes in an epoxy matrix and the resulting electrical properties," 1999, 40, 5967.

[6] B.C. Rosen and L. Jin, "Single-walled carbon nanotube-polymer composites: electrical, optical and structural investigation," *Synthetic Metals*, 2002, 127, 59.

[7] Jiang Zhu, Jong Dae Kim, Haiqing Peng, John L. Margrave, Valery N. Khabashesku, Enrique V. Barrera, "Improving the dispersion and integration of single-walled carbon nanotubes in epoxy composites through Functionalization", *Nano. Letters*, 2003, 3, 1107.

[8] E.T. Mickelson, C.B. Human, A.G. Rinzler, R.E. Smalley, R.H. Hauge and J.L. Margrave, "Fluorination of single-wall carbon nanotubes," *Chemical Physics Letters*, 1998, 296, 188.

[9] A. Garg and S.B. Sinnott, "Effect of chemical functionalization on the mechanical properties of carbon nanotubes," *Chemical Physics Letters*, 1998, 295, 273.

[10] C. Park, Z. Ounaies, K.A.Watson, R.E. Crooks, J. Smith Jr., S.E. Lowther, J.W. Connell, E.J. Siochi, J.S. Harrison and T.L. St. Clair, "Dispersion of single wall carbon nanotubes by in situ polymerization under sonication," *Chemical Physics Letters*, 2002, 364, 303.

[11] E.T. Thostenson, Z.F. Ren, and T.W. Chou, *Composites Science and Technology*, 61, 1899 (2001).

[12] R. Saito, G. Dresselhaus and M.S. Dresselhaus. *Physical properties of carbon nanotubes*. 1st ed. London: Imperial College Press, 1999.

[13] K.T. Lau and D. Hui, Composite Part B, 33, 263 (2002).

[14] P.M. Ajayan, *Progress Crystal Growth and Characterization*, 34, 37 (1997).

[15] P.M. Ajayan, L.S. Schadler, C. Giannaris, and A. Rubio, *Advanced Materials*, 12 (10) 750 (2000).

[16] M.F. Yu, B.S. Files, S. Arepalli and R.S. Ruoff, *Physical Review Letters*, 84 (24), 5552 (2000).

[17] L.S. Schadler, S.C. Giannaris and P.M. Ajayan, *Applied Physics Letter*, 73 (26): 3842 (1998).

[18] Z.X. Jin, K.P. Pramoda, G.Q. Xu, and S.H. Goh, *Chemical Physics Letters*, 337, 43 (2001).

[19] K. Lozano, J. Rios and E.V. Barrera, *Journal of Applied Polymer Science*, 80, 1162 (2001).

[20] M.L. Shofner, R. Vaidyanathan, C. Green, C. Condon, *Proceeding of ICCE/9*, 719 (2002).

[21] P.M. Ajayan, O. Stephan, C. Colliex, D. Trauth, *Science*, 265, 6 (1994).

[22] J.R. Wood, Q. Zhao and H.D. Wagner, *Composites Part A: Applied Science and Manufacturing*, 32, 391 (2001).

[23] W.Z. Li, S.S. Xie, L.X. Qian, B.H. Chang, *Science*, 274, 1701 (1996).

3. Investigation of Buckypaper Fabrication Process

Developing an effective fabrication process for SWNT buckypapers is a crucial step to realizing the concept of the novel buckypaper/resin infiltration process, since nanotube dispersion and distribution characteristics will be preformed during this stage and then directly transferred into the final composite products. Therefore, the quality of buckypaper significantly influences the various properties of the nanocomposites. This chapter details the design of experiment (DOE) approach employed to investigate the influences of the selected processing parameters on the quality of the produced randomly orientated buckypapers. A buckypaper process model was also established based on the results.

Since multiple steps are involved in buckypaper manufacturing and quality characterization, all relevant operations for consistency must be standardized. With such standardization, we can obtain more consistent and reliable results for building process models. Therefore, investigating the buckypaper manufacturing and characterization is classified into three successive steps: 1) manufacturing process, 2) SEM/AFM image acquisition, and 3) image analysis and measurement. In the manufacturing stage, procedures were standardized to minimize time variations and the same supply of raw materials was used throughout all the experiments. The processing parameter for each step was clearly defined, so that all experiments were conducted by following standard procedures. In the image acquisition stage, two types of microscopes were used to observe microstructures and nanostructures of the buckypapers. The procedures for structural observation were also standardized. In the measurement stage, rules of measurement were established and techniques of image processing were introduced. With such standardization, buckypaper samples were characterized on the same basis, and the quality of buckypaper was measured consistently for analysis.

3.1. Manufacturing Process

The manufacturing process was standardized so that each buckypaper sample was produced using the same procedure. The standard manufacturing process is shown in Figure 3.1. The bold fonts were factors considered important to the quality of buckypaper, which are set according to the DOE analysis. All experiments used the nanotubes from the same batch of BuckyPearls, purchased from CNI (Carbon Nanotechnologies Inc.), so that unknown variance from different material batches could be at least minimized, if not eliminated.

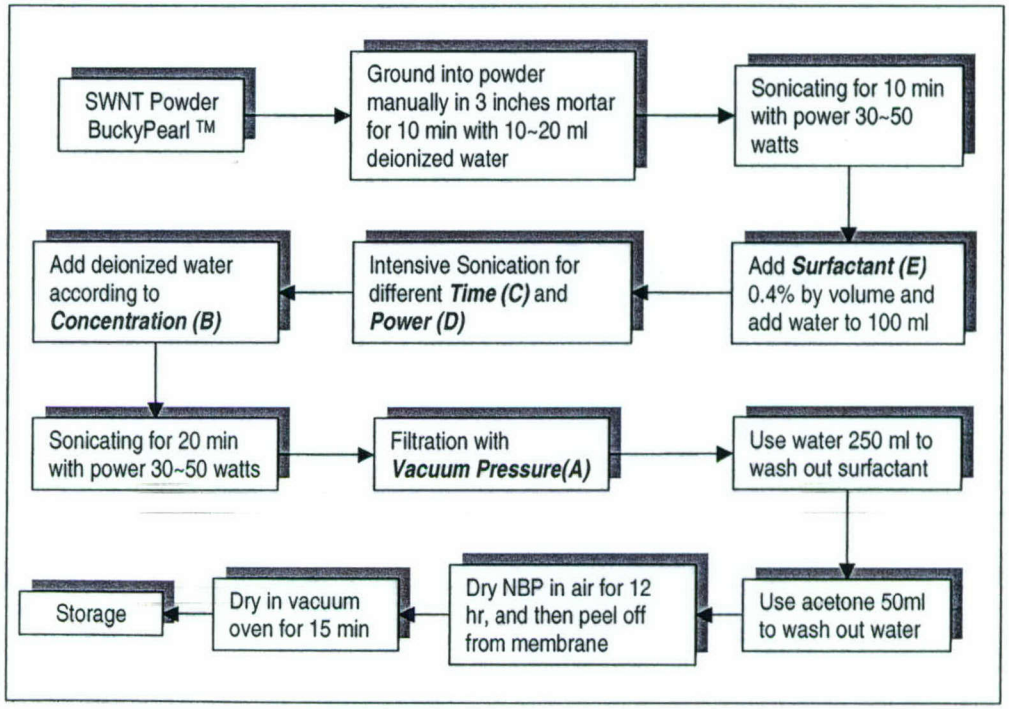

Figure 3.1 Standardized buckypaper manufacturing process

3.2. Procedure for SEM/AFM Image Acquisition

The nanostructures of the produced buckypapers were observed by Scanning Electron Microscopy (SEM) and Atomic Force Microscopy (AFM). SEM scans the buckypaper surface, starting with low magnification ($\times$ 500~ $\times$ 2,000) and increases to higher magnifications ($\times$5,000~$\times$70,000). From the observation at low magnification, effects of the selected surfactants on surface quality can be easily identified. Based on these

observations, the locations of more representative areas for further observations at high magnification are determined. To explain representative areas of the sample, a standard procedure of structure observation was developed for the project, as shown in Figure 3.2. The figure provides multiple images of a buckypaper sample under different magnifications. Figure 3.2 (a) shows the sample surface under low magnification, from which large particles deposited on the surface can be observed. The area was enlarged into Figure 3.2(b), showing flat areas among the large particles. The flat areas were observed under increased magnification. Figures 3.2(c) and (d) are two observed areas with the same magnification from the marked squares in Figure 3.2(b), showing that ropes are evenly distributed in these two different areas, which means a representative area can be found within these regions. With increased magnifications, the network of SWNTs was gradually explored, as shown in Figures 3.2(e) and (f). Magnification was increased until clear rope distribution could be found and measured, as shown in Figure 3.2(g). The AFM can only scan in a small (several microns) region that was selected as representative area in microcopy. In AFM images, the local rope distribution can be clearly observed.

3.4 Measurement of Buckypaper Nanostructure

Based upon previous findings, the measurement methods were modified to obtain more accurate and consistent measurements. Two criteria, rope size and pore size, were used to analyze and evaluate the dispersion effects of the SWNTs in the buckypapers. The averaged rope size represents the dispersion ability of breaking tube tangles and aggregations, and the standard deviation of rope size evaluates the uniformity of dispersion ability. The pore sizes and their standard deviation examine the uniformity of how evenly the nanotubes were distributed in the buckypaper.

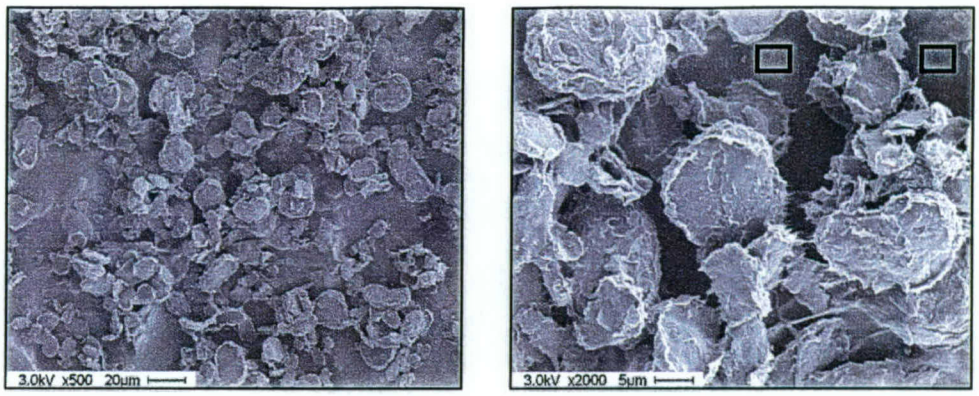

(a) (b)

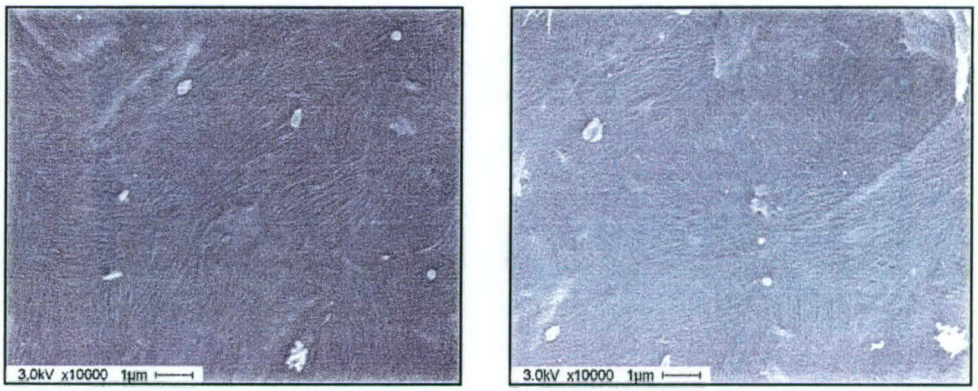

(c) (d)

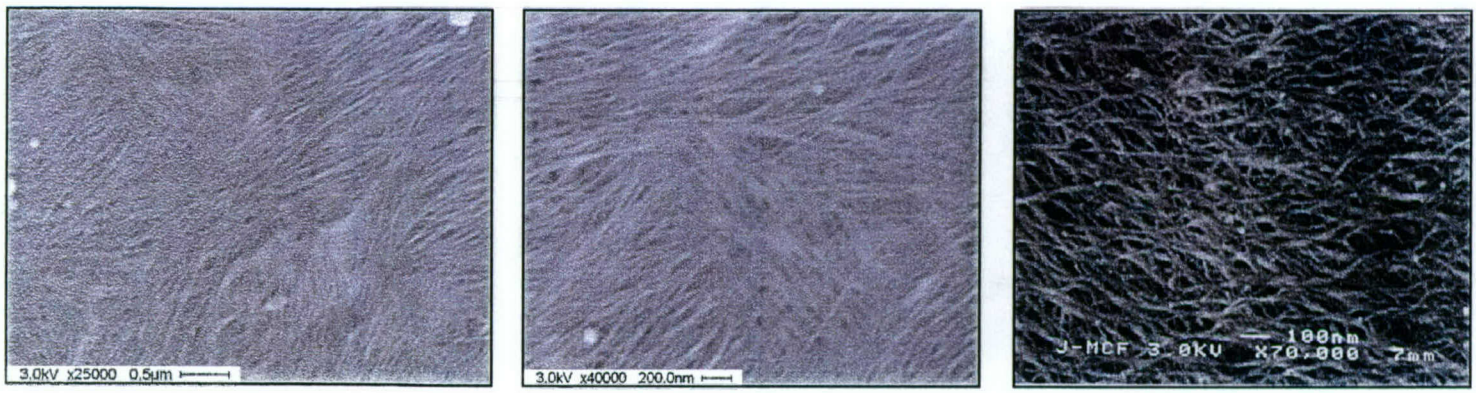

(e) (f) (g)

Figure 3.2 Standard procedure of structure observation

3.2.1. Measurement of SWNT rope size

After taking the SEM/AFM images, image processing software packages, including NanoScope and Photoshop, were utilized to measure rope diameters. A multitude of ropes were distributed in the image and no available image processing software was available for such an analysis. Therefore, defining standard rules for measurement was required so that the measurements of ropes were consistent and representative based on limited measurements. Rules were established so that the measurements were made by following the same procedures for all images. SEM pictures and AFM images were analyzed as follows:

- A SEM image was divided into three equal sections, and a diagonal line was drawn through the picture. In each section, ten nanotubes were randomly selected for measurement. Only those nanotubes that passed through the diagonal line were be measured, as shown in Figure 3.3.
- AFM images have a smaller scale than SEM images. Therefore, three images were taken for each sample to obtain more general information. A diagonal line was drawn in each image and ten ropes passing through the diagonal line were selected for measurement. An example of AFM image is shown in Figure 3.4.

The diameter of the rope is defined as the length perpendicular to the longitudinal of the rope direction, which is shown in Figure 3.5. Only those individual ropes that pass through the diagonal were measured. Ten ropes were randomly selected from each section, based on a random number table. The average and standard deviations of the diameters were calculated.

Diagonal

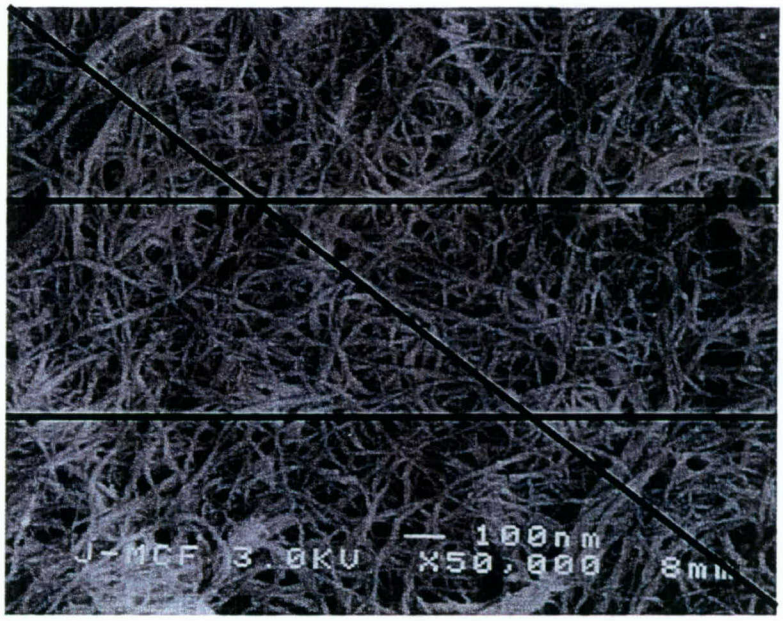

Figure 3.3 SEM image analysis

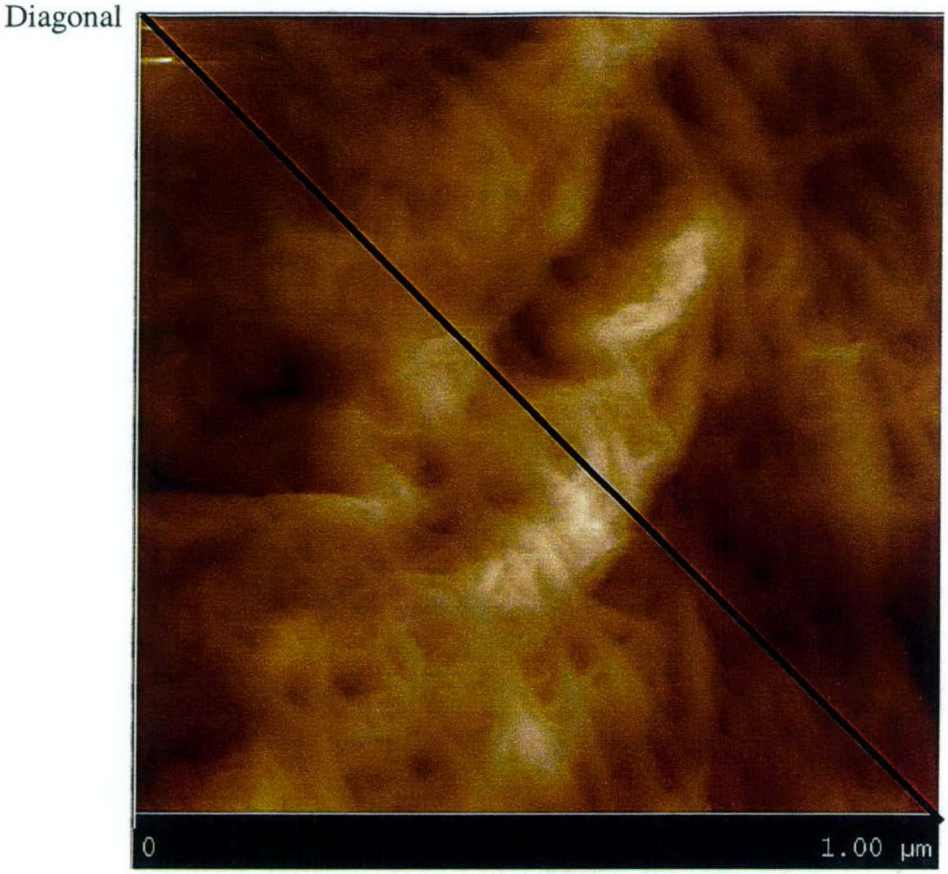

Figure 3.4 AFM image analysis

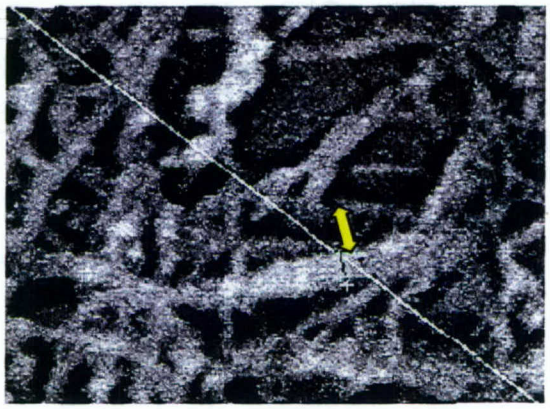

Figure 3.5 Measurement of rope diameter

3.2.2. Measurement of pore size in buckypapers

A pore in buckypaper is defined as the space between ropes. The pore size is an important criterion to evaluate the uniformity of rope distribution and processing

properties for the resin infiltration and impregnation of buckypapers. The measurement of the pore size was based upon SEM images. The pore size was analyzed by a Matlab image processing analyzer. These images were compressed into two dimensions then leveled, monochrome and digitalized, as shown in Figure 3.6.

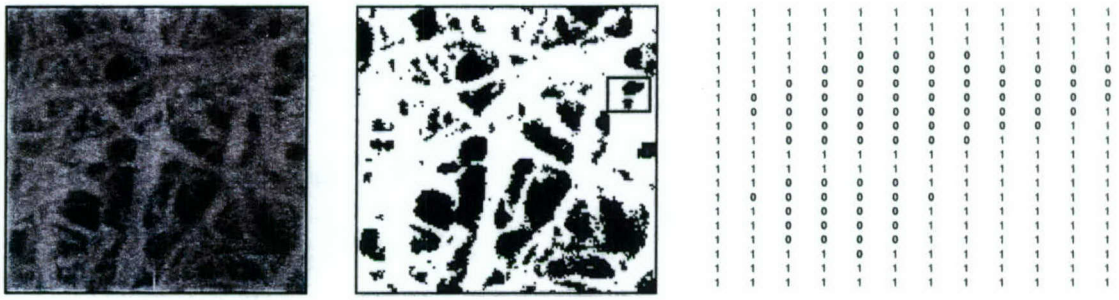

(a) (b) (c)

Figure 3.6 Image processing of pore size measurement: (a) original image, (b) leveled and monochrome image, (c) digital matrix of selected region in (b)

The procedure for pore size measurement is described as follows,

Step 1: Load image. Read image, and convert into a digital matrix.

Step 2: Estimate the background. Estimate the background illumination to eliminate unbalanced brightness.

Step 3: Subtract the background from the original image. Remove background to create an image with more uniform background.

Step 4: Increase the image contrast. Adjust the contrast of the image.

Step 5: Create binary image. Convert a binary version of the image.

Step 6: Collect basic pore information. Measure the number and area of pores.

Step 7: Compute statistical properties of pore size. Generate statistics including mean and standard deviation.

3.3. Experimental Design of Buckypaper Process Investigation

Five processing factors that impact buckypaper quality were chosen for manufacturing process investigation and model building. These factors were suspension concentration, sonication level, sonication time, vacuum pressure and surfactant type. The concentration of suspension represents the content of nanotubes suspended in water. Theoretically, the more nanotubes included, the harder the bundles to be broken. However, a sufficient quantity of nanotubes to rapidly produce high quality buckypapers was also a concern in process efficiency [1]. It is believed that high power and long sonication time can effectively break nanotubes, but over-sonication will result in broken tubes pieces and reduce the effectiveness of the nanotubes [2]. A Sonicator 3000 was used as for sonication. Using tip sonication method, the ultrasonic motion can break nanotube bundles into individual nanotubes. The vacuum pressure applied during filtration determines the filtration time. A shorter the filtration time allows the suspension to remain stable and dispersed [3]. The all surfactants selected demonstrated good dispersion effects in nanotube suspensions. However, only Triton X-100 has been used to make buckypapers [4,5], and the effects of NaDDBS and SDS are still unknown. The level settings of these factors were uncertain, and DOE helped determine what factors are statistically influential, how the factors influence, and the level setting.

Since these five factors are considered crucial to the quality of buckypapers, we used the current processing parameters as the center point, and the possible operating region was used as the range of factor levels in the design of experiments. Four of the factors were quantitative factors with two levels. Only the surfactant type was a qualitative factor with three levels. To conduct the experiments efficiently, half fraction of experiments were conducted. The resulting design was a mixed-level design ($2^{4-1} \times 3^{1}$) with three half fractional factorial designs for three surfactants. The results of the experimental design are given in Table 3.1. The bold lines indicated the central point of the DOE in the Table.

Table 3-1 DOE experiment list

Standard Number	Run Number	A Vacuum Pressure (Hg/inch)	B Suspension Concentration (mg/l)	C Sonicate Level (level)	D Sonicate Time (min)	E Surfactant Type
1	20	9	10	6	20	NaDDBS
2	23	29	10	6	100	NaDDBS
3	2	9	70	6	100	NaDDBS
4	27	29	70	6	20	NaDDBS
5	13	9	10	10	100	NaDDBS
6	12	29	10	10	20	NaDDBS
7	11	9	70	10	20	NaDDBS
8	25	29	70	10	100	NaDDBS
9	**10**	**19**	**40**	**8**	**60**	**NaDDBS**
10	**14**	**19**	**40**	**8**	**60**	**NaDDBS**
11	15	9	10	6	100	Triton X-100
12	21	29	10	6	20	Triton X-100
13	18	9	70	6	20	Triton X-100
14	28	29	70	6	100	Triton X-100
15	8	9	10	10	20	Triton X-100
16	7	29	10	10	100	Triton X-100
17	1	9	70	10	100	Triton X-100
18	29	29	70	10	20	Triton X-100
19	**4**	**19**	**40**	**8**	**60**	**Triton X-100**
20	**22**	**19**	**40**	**8**	**60**	**Triton X-100**
21	17	9	10	6	100	SDS
22	30	29	10	6	20	SDS
23	6	9	70	6	20	SDS
24	9	29	70	6	100	SDS
25	3	9	10	10	20	SDS
26	26	29	10	10	100	SDS
27	5	9	70	10	100	SDS
28	19	29	70	10	20	SDS
29	**16**	**19**	**40**	**8**	**60**	**SDS**
30	**24**	**19**	**40**	**8**	**60**	**SDS**

3.4. Fabrication of the Buckypaper for DOE Investigation

Based on Table 3.1 of DOE sample design, thirty randomly oriented buckypapers were produced using the standardized manufacturing procedure, as defined in Section 3.2. Figure 3.7 shows the produced buckypapers.

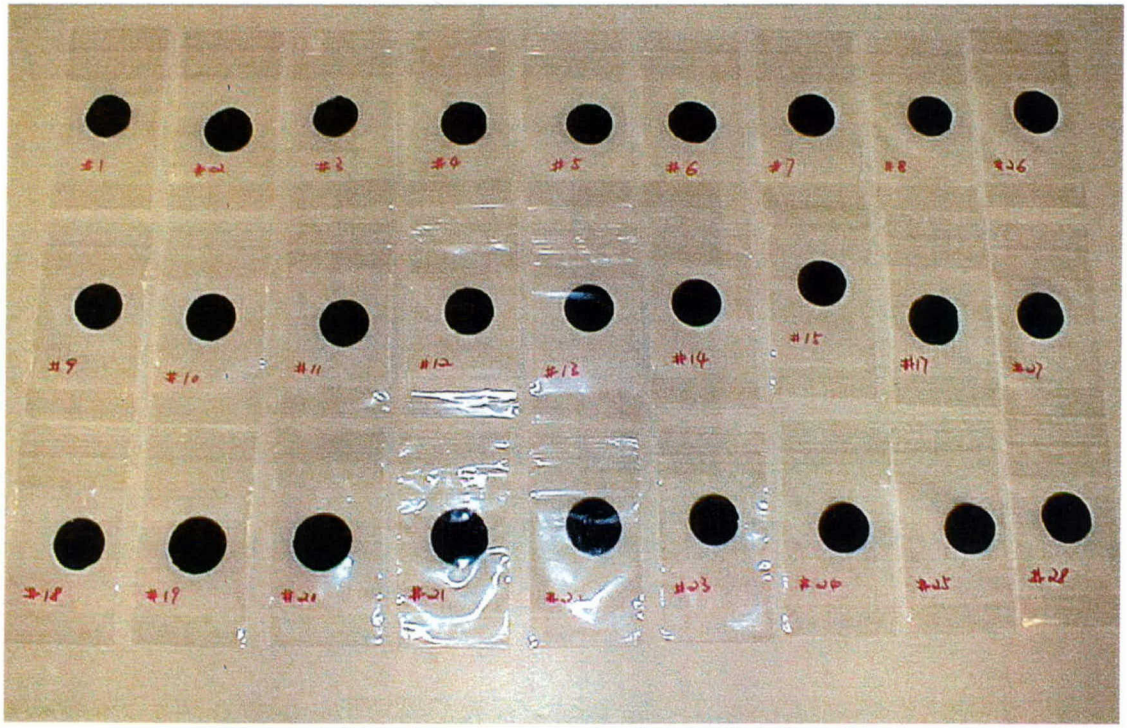

Figure 3.7 Buckypaper samples for the DOE analysis

3.5. Measurement of the Buckypapers for DOE

The standardized measurement defined in Figure 3.4 was used to measure all the produced buckypapers. Considering the possible variations of the nanostructure measurements of the buckypapers, two operators measured the rope size of each sample twice. The purpose of this arrangement was to test the repeatability of the measurement rules and also evaluate the impact of measurements. As a result, we built four blocks to evaluate the effect of measurement. The first block included the first measurements made by operator 1, and the second block contained the repeated measurement by the same operator. The third and fourth blocks contained the two repeated measurements made by operator 2, which only contained center points. Sample 19 of Table 3.1, one of the two

central point of Triton X-100 surfactant buckypaper, will be used as an example to illustrate the measurement procedure and data collection used in this project.

The processing parameters of Sample 19 are given in Table 3.2. The SEM images of the sample are shown in Figure 3.8 (a), (b), and (c). The surface of the sample is rough at low magnifications, but uniform rope networks can be seen at higher magnifications. The original SEM image used to measure tube rope size is shown in Figure 3.9 (a), and Figure 3.9 (b) shows the histogram of rope size distribution from the measurement. The rope distribution was near a normal distribution with the mean of 16.95 nm, with a standard deviation of 3.76 nm. Table 3.4 lists the four repeated measurements of rope size by two operators. These four measurements were averaged and the standard deviation is provided. Figure 3.10 illustrates the image processing for pore size analysis. The histogram of pore size distribution is shown in Figure 3.11 (a), which is near an exponential distribution with the mean of 4126.73 nm^2, and a standard deviation of 5617.16 nm^2. Figure 3.11 (b) shows the cumulative pore size distribution, indicating that 90% of pore sizes are smaller than 15,000 nm^2. In conclusion, sample No. 19 had a fair surface quality with good dispersion. The average rope size was 16.95 nm, standard deviation was 3.76 nm, the average pore size was 4126.73 nm^2, and the standard deviation of pore size was 5617.16 nm^2.

Table 3-2 Processing parameters and measurement results of sample 19

Factors	**Vacuum Pressure (Hg/inch)**	**Concentration (mg/l)**	**Sonication Power (level)**	**Sonication Time (min)**	**Surfactant Type**
	19	40	8	60	Triton X-100
Responses	**Surface Quality**	**Average Rope Size (nm)**	**Standard Deviation of Rope Size (nm)**	**Average Pore Size (nm^2)**	**Standard Deviation of Pore Size (nm^2)**
	Fair	16.95	3.76	4126.73	5617.16

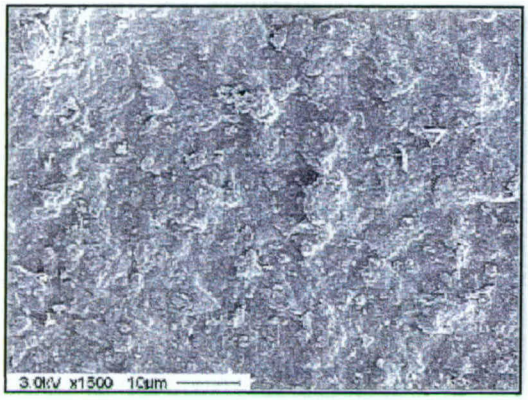

(a) x 1,500

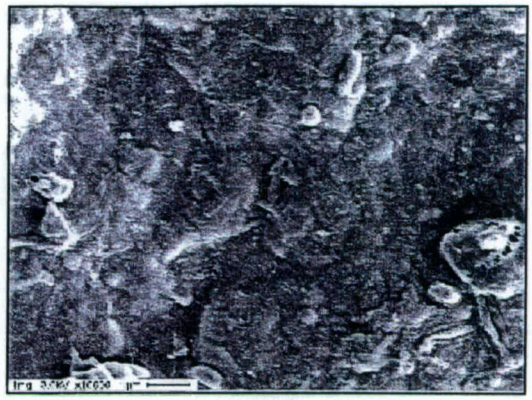

(b) x 10,000

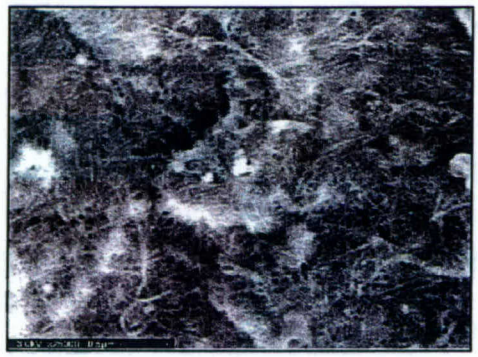

(c) x 30,000

Figure 3.8 SEM images of sample 19

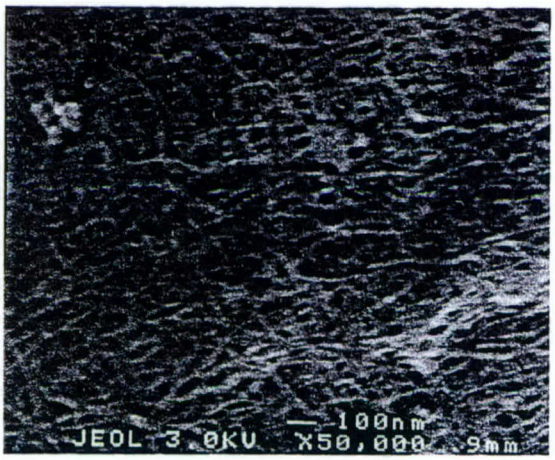

(a) Original image

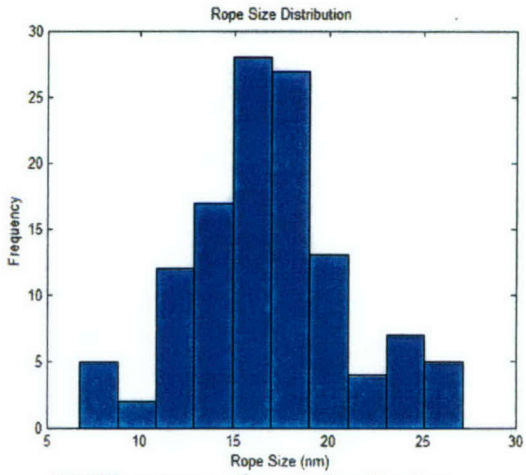

(b) Histogram of rope distribution

Figure 3.9 Measurement of rope size

Table 3-3 Measurement results of SWNT ropes in sample 19

	First Measurement			Second Measurement			Third Measurement			Fourth Measurement		
	a	b	c	a	B	c	a	b	c	a	b	c
1	11.86	16.95	18.64	11.86	15.25	13.56	22.41	18.97	18.97	20.69	15.52	15.52
2	15.25	16.95	18.64	13.56	15.25	18.64	18.97	20.69	20.69	22.41	20.69	20.69
3	13.56	20.34	16.95	10.17	18.64	15.25	17.24	24.14	24.14	22.41	18.97	20.69
4	11.86	20.34	15.25	8.47	20.34	15.25	17.24	20.69	15.52	15.52	18.97	15.52
5	13.56	16.95	18.64	15.25	18.64	16.95	15.52	20.69	18.97	12.07	18.97	18.97
6	13.56	18.64	16.95	11.86	18.64	16.95	13.79	22.41	18.97	15.52	24.14	13.79
7	10.17	25.42	13.56	11.86	23.73	16.95	25.86	24.14	17.24	17.24	24.14	18.97
8	13.56	15.25	11.86	11.86	16.95	11.86	12.07	20.69	24.14	25.86	17.24	18.97
9	25.42	6.78	13.56	27.12	8.47	13.56	13.79	13.79	13.79	17.24	13.79	12.07
10	8.47	18.64	15.25	8.47	13.56	15.25	12.07	17.24	20.69	13.79	15.52	15.52
Average Rope Size	**16.95 nm**											
Standard Deviation of Rope Size	**3.76 nm**											

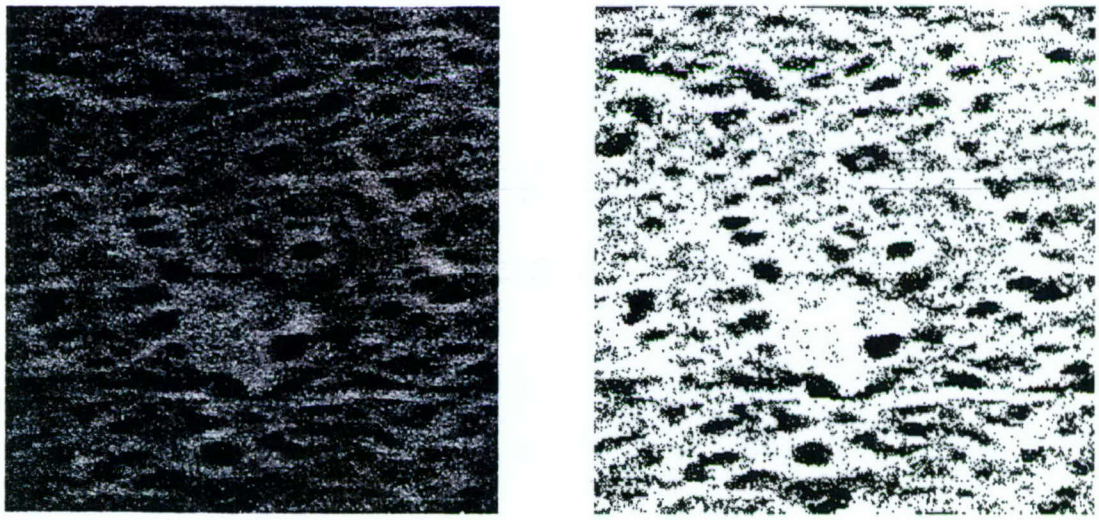

(a) Original image (56,666nm x 58,421nm) (b) Black and white scale image

Figure 3.10 Image processing of pore size

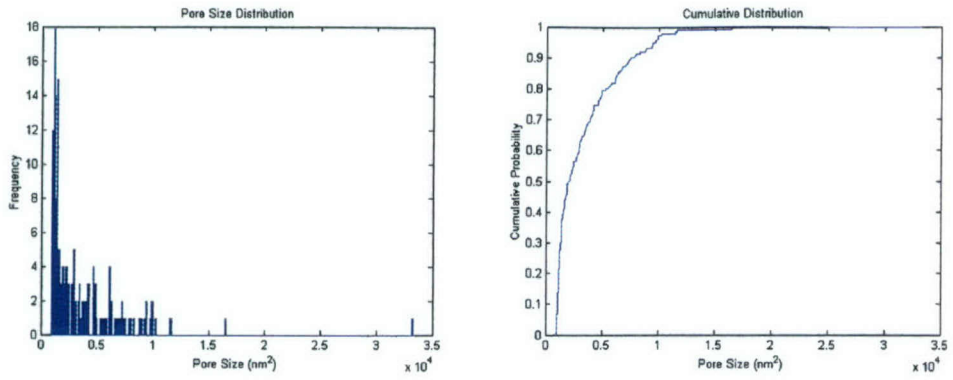

(a) Pore size distribution (b) Cumulative distribution

Figure 3.11 Histogram of pore size distribution of Sample 19

The same procedure was used for characterizing all 30 samples. Table 3.4 summarizes the results of rope size measurement. The notation "O1M1" denotes the first measurement made by operator 1, which is the first block in the design. "O1M2" indicates the second measurement made by the same operator, which is the second block. "O2M1" and "O2M2" only apply to the six center points, which form the third and forth blocks. The blocking was only built for average rope size and standard deviation of rope size, in which measurements were taken manually. The pore size was analyzed by Matlab image processing analyzer, which is repeatable. No block was built to evaluate the repeatability of pore size measurement [6,7]. In this project, the blocking method was used to evaluate the variability transmitted from repeated measurements and different operators.

Table 3-4 Measurement results of 30 buckypaper samples

Standard Number	Run Number	Average Rope Size (nm)				Standard Deviation of Rope Size (nm)				Robust C.V. of Pore Size (%)
		O1M1	O1M2	O2M1	O2M2	O1M1	O1M2	O2M1	O2M2	
1	20	21.91	20.47			6.89	4.76			51.35%
2	23	31.73	33.29			10.44	9.94			76.92%
3	2	28.43	26.18			6.49	9.72			53.03%
4	27	43.21	44.8			22.3	18.81			64.56%
5	13	106.62	96.02			29.37	22.47			62.34%

6	12	41.61	35.93			14.73	13.6			70.24%
7	11	19.72	19.44			7.79	5.68			56.82%
8	25	21.94	22.39			7.48	6.9			64.18%
9	**10**	**13.33**	**12.66**	**13.06**	**13.85**	**3.33**	**3.07**	**2.78**	**2.87**	**58.93%**
10	**14**	**20.8**	**20.03**	**25.03**	**26.59**	**5.93**	**6.31**	**7.01**	**7.61**	**51.72%**
11	15	24.94	23.39			7.82	8.68			65.91%
12	21	25.03	22.72			8.06	6.43			71.01%
13	18	34.5	33.28			15.09	11.32			60.98%
14	28	17.37	17.07			4.35	4.05			44.44%
15	8	22.36	20.51			7.24	6.65			59.32%
16	7	17.63	16.02			7.43	5.03			76.83%
17	1	17.76	15.34			6.8	5.57			58.93%
18	29	26.43	26.61			7.71	6.87			69.32%
19	**4**	**15.76**	**15.14**	**18.85**	**18.05**	**3.91**	**3.85**	**3.66**	**3.62**	**69.35%**
20	**22**	**12.77**	**12.49**	**13.45**	**12.82**	**3.05**	**2.94**	**3.57**	**3.54**	**52.48%**
21	17	20.69	18.28			7.25	8.5			64.04%
22	30	24.63	23.84			6.53	5.39			64.65%
23	6	18.8	19.99			7.72	8.6			81.25%
24	9	24.89	21.52			8.36	8.45			71.43%
25	3	35.97	34.21			10.44	7.62			80.79%
26	26	14.22	14.67			4.46	4.44			61.82%
27	5	20.69	19.88			10.03	0			67.12%
28	19	28.65	26.75			7.59	8.33			47.27%
29	**16**	**17.53**	**17.24**	**15.06**	**16.16**	**4.49**	**4.4**	**3.23**	**3.24**	**50.00%**
30	**24**	**30.11**	**30.83**	**31.3**	**32.44**	**9**	**9.9**	**8.19**	**8.53**	**50.00%**

In Table 3.4, the average rope size indicates the dispersion effect of the process, while the standard deviation of rope size measures the uniformity of the rope distribution. The rope sizes are considered the most important responses in buckypaper processing, since they are directly related to the mechanical and functional properties of the resultant composites. The pore size has relatively less importance compared to the rope size. Therefore, we simplified the evaluation of pore size to one response, robust coefficient

variance (robust C.V.) of pore sizes [8]. The robust C.V. standardizes the deviation with the median to compare sample to sample on the same basis.

$$RobustC.V. = \frac{MAD}{Median} \tag{3.1}$$

where MAD (Median Absolute Deviation) provides a scale estimate based on the median absolute deviation. The actual value calculated is

$$MAD = (median(abs(x - median(x)))) \tag{3.2}$$

The results of the robust C.V. values of all buckypaper samples are also given in Table 3.4.

3.6. Analysis of the DOE Experimental Results

The measurement results were analyzed by Design Expert, a DOE software package. The statistically analysis of average rope size is shown in Figure 3.12. The results show that the main effects and two factor interactions are highly significant, except the D and AE terms. On the other hand, the mean square error was 18% of the mean square model in the design without blocking, but the ratio was reduced to 8.2% in the design with four blocks, which indicates the blocking effect could separate the noise from the error, so the error can clarify the significance of the factors and their interactions. However, the blocking effect was larger than expected, which was 2.8 times the mean square of the residual. This suggests the necessity of variability analysis to find the largest source of variability. It should be noted that the curvature was significant, indicating a higher order model may be more appropriate than the current linear model. The models of the three surfactant influences are shown in Figure 3.13, which can be used to predict rope size in manufacturing buckypapers.

Response: Avg rope size

ANOVA for Selected Factorial Model

Analysis of variance table [Partial sum of squares]

Source	Sum of Squares	DF	Mean Square	F Value	Prob > F	
Block	422.62	3	140.87			
Model	12443.80	18	691.32	14.03	< 0.0001	significant
A	*193.65*	*1*	*193.65*	*3.93*	*0.0530*	
B	*475.21*	*1*	*475.21*	*9.64*	*0.0032*	
C	*210.02*	*1*	*210.02*	*4.26*	*0.0443*	
D	*3.848E-003*	*1*	*3.848E-003*	*7.810E-005*	*0.9930*	
E	*1723.23*	*2*	*861.61*	*17.49*	*< 0.0001*	
AB	*1152.88*	*1*	*1152.88*	*23.40*	*< 0.0001*	
AC	*1281.96*	*1*	*1281.96*	*26.02*	*< 0.0001*	
AD	*2266.64*	*1*	*2266.64*	*46.00*	*< 0.0001*	
BC	*2215.15*	*1*	*2215.15*	*44.96*	*< 0.0001*	
BD	*1297.90*	*1*	*1297.90*	*26.34*	*< 0.0001*	
BE	*1171.54*	*2*	*585.77*	*11.89*	*< 0.0001*	
CD	*557.84*	*1*	*557.84*	*11.32*	*0.0015*	
CE	*708.17*	*2*	*354.08*	*7.19*	*0.0018*	
DE	*1342.53*	*2*	*671.26*	*13.62*	*< 0.0001*	
Curvature	910.81	1	910.81	18.49	< 0.0001	significant
Residual	2414.33	49	49.27			
Lack of Fit	*1734.19*	*37*	*46.87*	*0.83*	*0.6867*	*not significant*
Pure Error	*680.14*	*12*	*56.68*			
Cor Total	16191.57	71				

Std. Dev.	7.02	R-Squared	0.8375
Mean	24.97	Adj R-Squared	0.7778
C.V.	28.11	Pred R-Squared	0.6976

Figure 3.12 Analysis of variance

Surfactant NaDDBS

Avg rope size =

-64.00220

+2.39192 * Vacuum Pressure

+0.57089 * Suspension Concentration

+10.85096 * Sonication Level

+0.35520 * Sonication Time

+0.017327 * Vacuum Pressure * Suspension Concentration

-0.27407 * Vacuum Pressure * Sonication Level

-0.018222 * Vacuum Pressure * Sonication Time

-0.12009 * Suspension Concentration * Sonication Level

-4.59615E-003 * Suspension Concentration * Sonication Time

+0.045198 * Sonication Level * Sonication Time

Surfactant X-100

Avg rope size =

-36.05130

+2.39192 * Vacuum Pressure

+0.94012 * Suspension Concentration

+6.18504 * Sonication Level

+0.071736 * Sonication Time

+0.017327 * Vacuum Pressure * Suspension Concentration

-0.27407 * Vacuum Pressure * Sonication Level

-0.018222 * Vacuum Pressure * Sonication Time

-0.12009 * Suspension Concentration * Sonication Level

-4.59615E-003 * Suspension Concentration * Sonication Time

+0.045198 * Sonication Level * Sonication Time

Surfactant SDS

Avg rope size =

-45.91502

+2.39192 * Vacuum Pressure

+0.89616 * Suspension Concentration

+7.99879 * Sonication Level

+0.077815 * Sonication Time

+0.017327 * Vacuum Pressure * Suspension Concentration

-0.27407 * Vacuum Pressure * Sonication Level

-0.018222 * Vacuum Pressure * Sonication Time

-0.12009 * Suspension Concentration * Sonication Level

-4.59615E-003 * Suspension Concentration * Sonication Time

+0.045198 * Sonication Level * Sonication Time

Figure 3.13 Average size models of different surfactants for buckypaper processing

From a practical practice, the five factors selected were all highly significant to the average rope size of buckypapers, as was the interactions between factors. The sonication time (factor D) was not contributive by itself, but the effect was interactive with others, like the sonication power. Surfactant type (factor E) contributed most in terms of the highest significance. All three types of surfactants demonstrated good dispersion effects in the SWNT suspensions, as proven by other scientists [3,4], but only Triton X-100 has been frequently used to produce buckypapers. However, the statistical analysis results in Figure 3.12 show the selection of surfactant does influence the average rope size. The tube rope size and pore structure database of the buckypapers generated in this research is valuable for design and optimization of buckypaper/resin infiltration process.

3.7. References

[1] Zhi Wang, Zhiyong Liang, Ben Wang, Chuck Zhang and Leslie Kramer, "Processing and property investigation of single-walled carbon nanotube (SWNT) buckypaper/epoxy resin matrix nanocomposites." *Composites Part A: Applied Science and Manufacturing*, Volume 35, Issue 10, October 2004, Pages 1225-1232.

[2] Jihua (Jan) Gou, "Single-wall Carbon Nanotube Buckypaper/Epoxy Composites: Molecular Dynamics simulation and Process Developments." 2002 PhD dissertation.

[3] T.V. Sreekumar, Tao Liu, Stish Kumar, Lars M. Ericson, Robert H. Hauge, and Richard E. Smalley, "Single-Wall Nanotube Film." *Chem. Mater.* 2003, 15, 175-178.

[4] A.G. Rinzler, J. Liu, H. Dai, P. Nikolaev, C.B. Huffman, F.J. Rodriguez-Macias, P.J. Boul, A.H. Lu, D. Heymann, D.T. Colbert, R.S. Lee, J.E. Fischer, A.M. Rao, P.C. Eklund, R.E. Smalley, "Large-scale purification of single-wall carbon nanotubes: process, product, and characterization." *Appl. Phys. A* 67, 29-37 (1998).

[5] Rajdip Bandyopadhyaya, Einat Nativ-Roth, Oren Regev, and Rachel Yerushalmi-Rozen. "Stabilization of Individual Carbon Nanotubes in Aqueous Solutions." *Nano letters* 2002 Vol.2, No.1 25-28.

[6] Douglas C. Montgomery, *Design and Analysis of Experiments*. Fifth edition, A Wiley-Interscience Publication. John Wiley & Sons, Inc.

[7] Raymond H. Myers, Douglas C. Montgomery, *Response Surface Methodology*. Second edition, A Wiley-Interscience Publication. John Wiley & Sons, Inc.

[8] Box, G.E. P., and R.D. Meyer, "An Analysis of Unreplicated Fractional Factorials" *Technometrics*, Vol. 28, pp.11-18.

4. Magnetically Aligned Nanotube Buckypapers

Controlled SWNT alignment is critical for both structural and multifunctional applications of SWNTs-reinforced nanocomposites. Randomly aligned buckypapers and composites have very good tube dispersion; however, tube alignment does not occur during manufacturing. The literature review indicates that the molar susceptibilities for a (10, 10) SWNT (armchair) is $+85.4 \times 10^{-6}$ emu (mol C)$^{-1}$ when parallel to B (magnetic vector), and -21.0×10^{-6} emu (mol C)$^{-1}$ when perpendicular to B. Theoretical predictions show that for a (10, 10) SWNT with a length of 300nm, a magnetic field of 10-25 Tesla (T) can align SWNTs suspended in a very low viscous solution. Dr. Richard Smalley's team experimentally demonstrated the effectiveness of aligning SWNTs in buckypapers within high magnetic fields of greater than 8 T [1-3]. By using such magnetically aligned buckypaper materials, we can achieve nanotube alignment in buckypaper/resin infiltration nanocomposites.

In this project, the research team further modified the filter design and processing parameters to produce high quality and relatively large buckypapers for making nanocomposites with orientated SWNTs. The influences of suspension concentration and magnetic strength on tube alignment were investigated. The research team used the high magnetic fields at the National High Magnetic Field Laboratory (NHMFL), Tallahassee, Florida to carry out the nanotube alignment experiments.

SWNTs have been predicted to have an anisotropic magnetic susceptibility [4]. Table 2.1, which compares the magnetic susceptibilities of SWNTs with various elements, shows that SWNTs have a relatively low magnetic susceptibility. Hence, under a sufficiently strong magnetic field, SWNTs should orient in the direction of magnetic field if the tubes are free to rotate in liquid suspension. Calculations reveal that the metallic SWNTs, such as the (n, n) variety, are paramagnetic in the direction of their long axes and tend to align parallel to the ambient magnetic field. The other varieties of SWNTs are diamagnetic, but their diamagnetic susceptibilities are mostly negative in the direction perpendicular to the

direction of an ambient field. The alignment energies for varieties of SWNTs are comparable.

In 1998, in order to test whether magnetic fields with a strength of 10T would result in substantial alignment of suspended SWNTs, Walters and Smalley *et al.* passed polarized light through a suspension of SWNTs in dimethylformamide (DMF) and the transmitted light was collected. A magnetic field was applied perpendicular to the propagation direction of the light. The transmittance was monitored as a function of the incident polarization angle ϕ, the angle between the incident light electric field vector and the magnetic field, as shown in Figure 4.1. Solid lines were sinusoidal fits to the measured transmitted light intensities. As the field was increased from zero, a significant modulation of the light intensity (up to 37% peak-to-peak) was developed, as shown in Figure 4.2. Minimum transmittance occurred when the incident light was polarized parallel to the direction of magnetic field. Therefore, the SWNTs were aligned along the magnetic field direction. Significant tube alignment was observed when the field strength was greater than 8 Tesla.

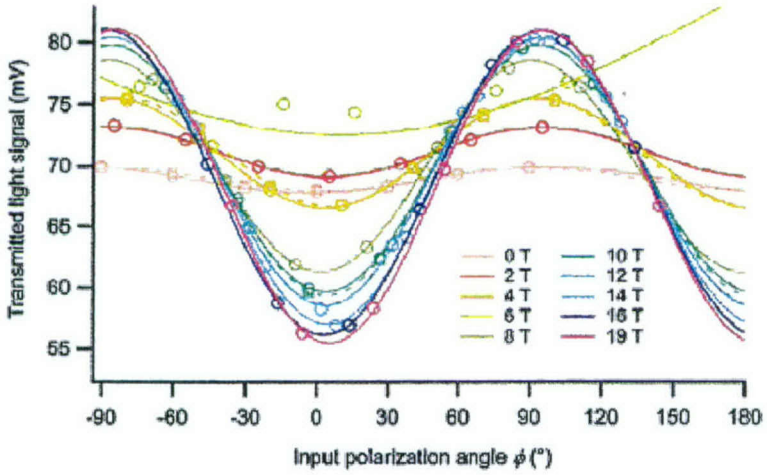

Figure 4.1 Transmitted light signal (mv) pass through the SWNT suspension as a function of magnetic field strength (Dr. Smalley's group)

Dr. Smalley and his group also experimentally demonstrated the effectiveness of aligning SWNTs in water/Triton-X solutions under high magnetic field for producing magnetically aligned buckypapers. By in-situ filtering well-dispersed SWNT suspensions

in a high strength magnetic field, his team carefully produced buckypapers of magnetically aligned SWNTs, called magnetically aligned buckypapers, as shown in Figure 3.2. Further, Raman spectroscopy measurements indicated that the alignment of carbon nanotubes of the produced buckypapers in the direction of the magnetic field had an axial orientation within 17±1°C of magnetic field axis. The SEM observations also confirmed good tube alignment in the magnetically aligned buckypapers.

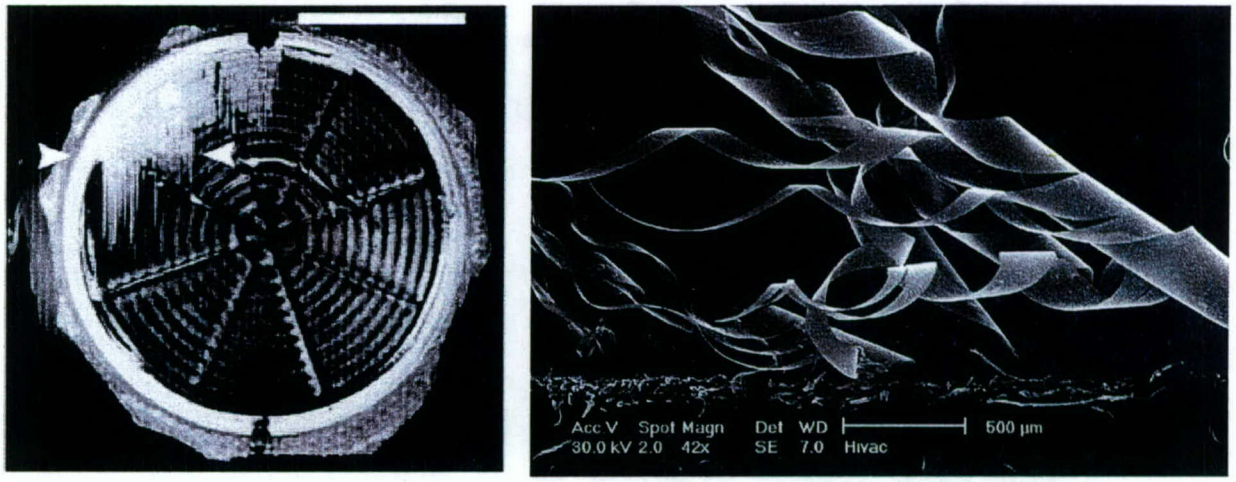

(a) Magnetically aligned buckypaper of 25 mm in diameter

(b) Heavy curvatures of the peeling-off strips indicating tube alignment in the buckypaper

Figure 4.2 Magnetically aligned buckypaper (Dr. Smalley's group)

4.1. Fabrication of Magnetically Aligned Buckypapers Using Syringe Filters

The research team first fabricated small samples following Dr. Smalley's method and setup to validate the effectiveness of nanotube alignment in magnetically aligned buckypapers. The Millipore Millex-GN syringe filters of 25 mm in diameter and 0.45 µm pore size were used in the experiments. The experiment flowchart is shown in Figure 4.3. The filter was placed inside the bore of the magnet, which generates the magnetic field. The magnets used in our experiments were at the NHMFL. The bore sizes of the magnets were 50 mm outer diameter (O.D) for the 25 T magnet and 195 mm O.D for the 20 T magnet. When the tube suspension passed through the filter, the nanotubes aligned in the direction of the magnetic field and deposited on the membrane of the filter to form the buckypaper of aligned tube networks. The SWNT suspension preparation procedure is

the same as mentioned in Section 3.2. After cleaning and drying, the produced magnetically aligned buckypapers were peeled from the filter membrane.

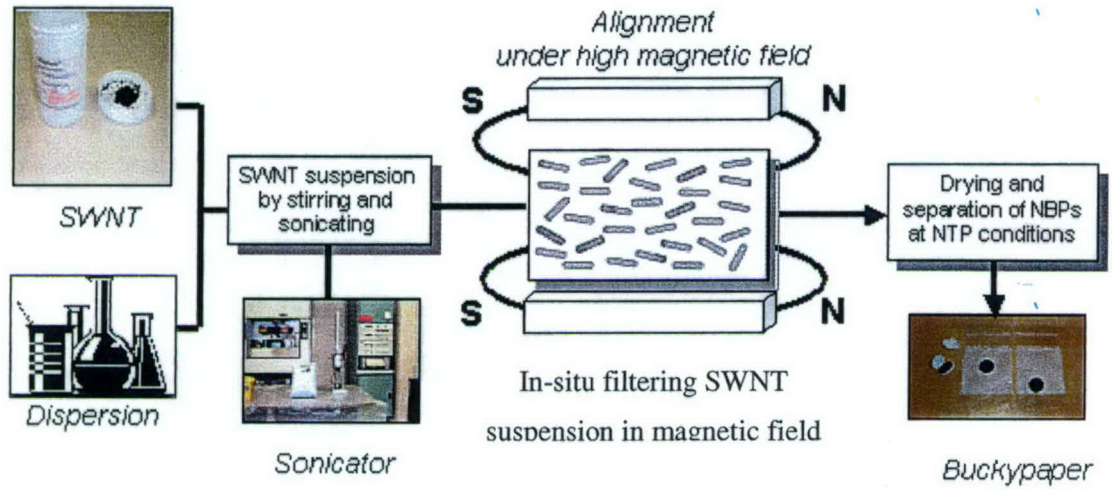

Figure 4.3 Schematic diagram for preparation of magnetically aligned buckypaper

4.1.1. Experimental set-up

The experimental setup consisted of a separatory funnel, a peristaltic pump, a 25 mm O.D. nylon Millex-GN syringe Millipore filter of pore size 0.45 μm and a conical measuring cylinder, as shown in Figure 4.4. The separatory funnel, which holds the suspension, was connected to the nylon filter through a peristaltic pump, which provided pressure to the suspension. This nylon filter was placed inside the bore of the magnet with the help of a "Plastic T" assembly. The surface of the filter membrane was kept parallel to the magnetic field. The direction of alignment was marked on the filter using a permanent marker, which indicated tube alignment direction. The suspension passed through the filter and the clear solution that came from the filter was collected in a measuring jar.

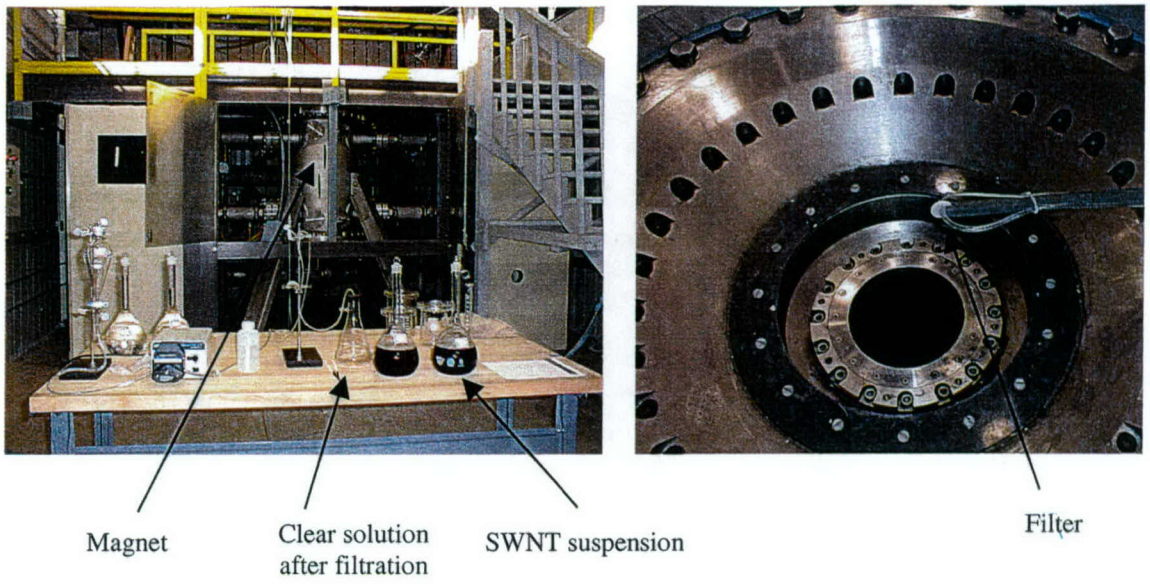

Figure 4.4 Experimental setup for fabricating magnetically aligned SWNT buckypaper using small syringe filter

4.1.2. Experiments

An aqueous solution with 0.4 % surfactant, Triton X-100, passed through the nylon filter kept in the bore of a resistive coil magnet in a magnetic field of 25T. The aqueous solution cleaned the tubes and filter, removing any contamination. The SWNT suspension was then pumped through the filter at a pressure of 138-172kPa (20-25psi) under the selected magnetic strength. After a desired amount of suspension passed through the filter, isopropyl alcohol was passed through the filter to wash the surfactant Triton X-100. The filter was then removed from the magnetic field and kept in a vacuum oven at 63.5-76.2cmHg (25-29inHg). This facilitated the drying of the buckypaper.

After drying, the filter was cut using a milling machine to remove the magnetically aligned nanotube buckypaper, as shown in Figure 4.5. The produced buckypapers resulted in the heavy curvatures in the torn strips indicated significant alignment of the SWNTs, as confirmed by AFM images, as shown in Figures 4.6 and 4.7. Nine alignment experiments were repeated under 15~25 T magnetic fields and all showed good nanotube alignment in the resultant buckypapers.

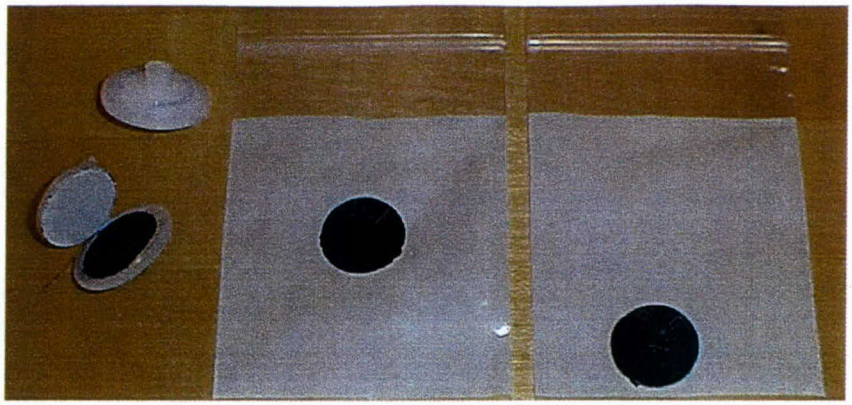

Figure 4.5 Magnetically aligned nanotube buckypapers.

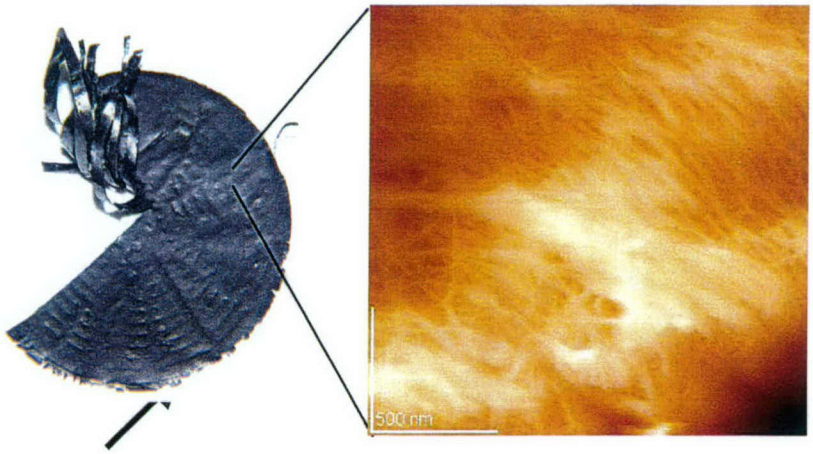

Figure 4.6 Magnetically aligned nanotube buckypaper and AFM image

These experimental results further validated Dr. Smalley's method of magnetically aligning SWNTs and demonstrated the effectiveness of orienting SWNTs in the magnetically aligned buckypapers. However, this setup was limited for efficiently producing buckypapers for nanocomposite research and applications. Each buckypaper 25mm diameter took approximately 1.5~2 hrs to achieve a thickness around 6~10 μm with the suspension concentration between 10~100 mg/L. Therefore, we developed a new method for producing relatively large aligned buckypapers for nanocomposite research.

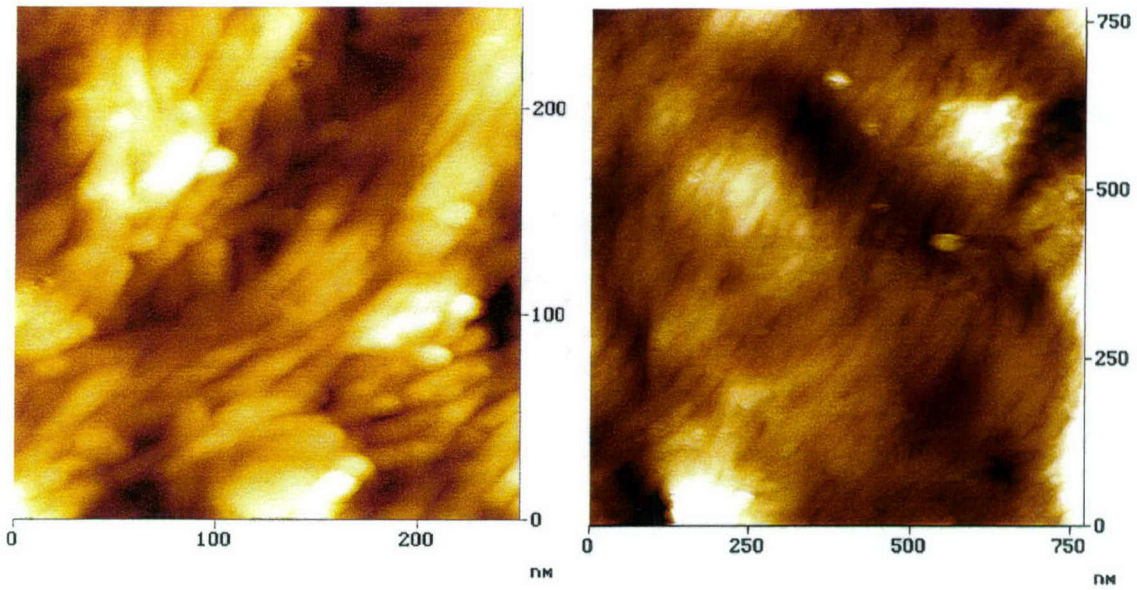

Figure 4.7 Good tube alignments in magnetically aligned buckypaper under 25T field

4.2. Fabrication of Large Magnetically Aligned Buckypaper Using Custom-Made Cylinder Filters

Millex-GN syringe Millipore filters were used in the experiments described in Section 4.2. They were very small and did not yield enough samples for further testing and nanocomposite fabrication. The filter only had a diameter of 25 mm (0.984 in) and an area of 4.9 cm^2 (0.969 in^2). To make a larger magnetically aligned buckypaper, a tubular filter was custom designed to make buckypapers of approximately 38 cm (15 in) long and 10 cm (3.94 in) wide, resulting in an area of 387 cm^2 (60 in^2).

4.2.1. Cylindrical filter design

Non-magnetic materials were required for all parts of the custom-designed filter since it was used inside the high strength magnet of 5~25 Tesla. Any magnetic materials, such as steel, can cause damage to the filter apparatus, as well as the magnet. Aluminum was used for making the filter. The design requirements for the filter were constrained by the size of the magnet bore and area covered by the magnetic field in Cell 5 at the NHMFL. The diameter of the magnet bore was 190 mm. The depth of the bore was 1,165.2 mm and the magnetic field was centered at 582.6 mm. Allowing for clearance, the maximum

diameter of the filter assembly was less than 172 mm (6.75 in). The total length of the filter could vary but the membrane remained within 76 mm (~3.0 in) from the magnetic center, which maintained good uniformity of magnetic strength. A total filter length of 152 mm (~6.0 in) was used.

The blueprint of the assembled filter design is shown in Figure 4.8. The filter can be divided into external and internal assemblies, which can be assembled to form a watertight seal filter. The magnetically aligned buckypaper was formed on the surface of the filter membrane during filtration.

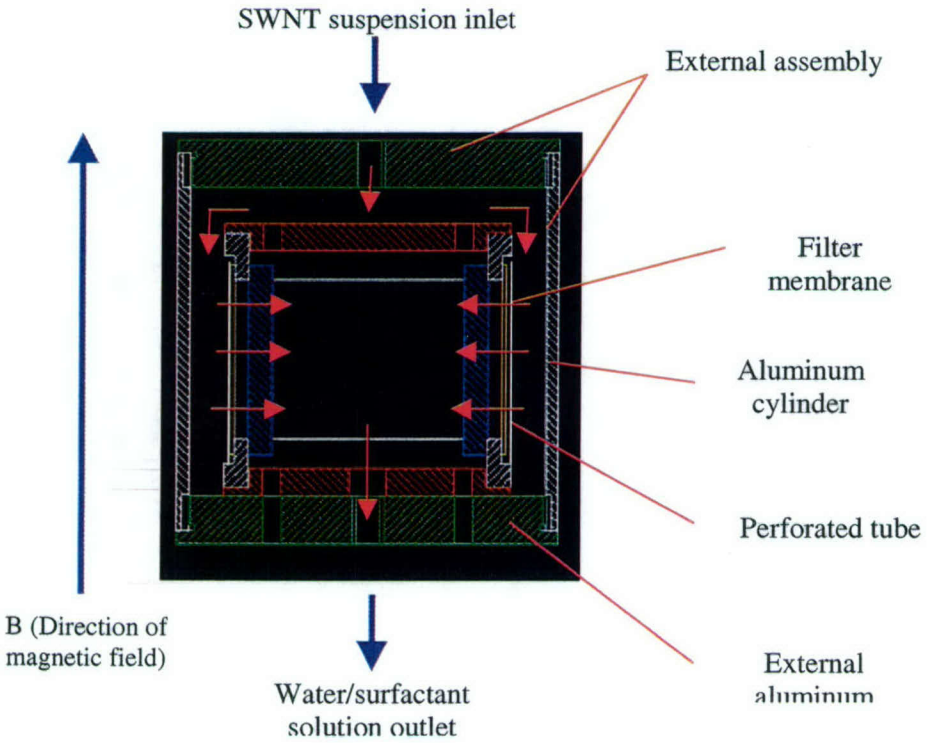

(The arrows indicate the flow direction of SWNT suspension during filtration)

Figure 4.8 Cylinder filter design

The detailed filter design is provided in Figure 4.9. Three parts made up the external filter assembly: End Cap A, End Cap B and the External Cylinder. Five parts made up the internal filter assembly: Internal Cap C, Internal Cap D, Flange C, Flange D and the rolled perforated tube, as shown in Figure 4.9. When these components were assembled, they formed the structure upon which the Millipore filter membrane of 0.45 μm pore size

was attached to the surface of the preformed tube surface. A 5/16"-18 threaded rod bolted the internal filter assembly together. End Cap B was then bolted to the External Cylinder and formed a watertight chamber.

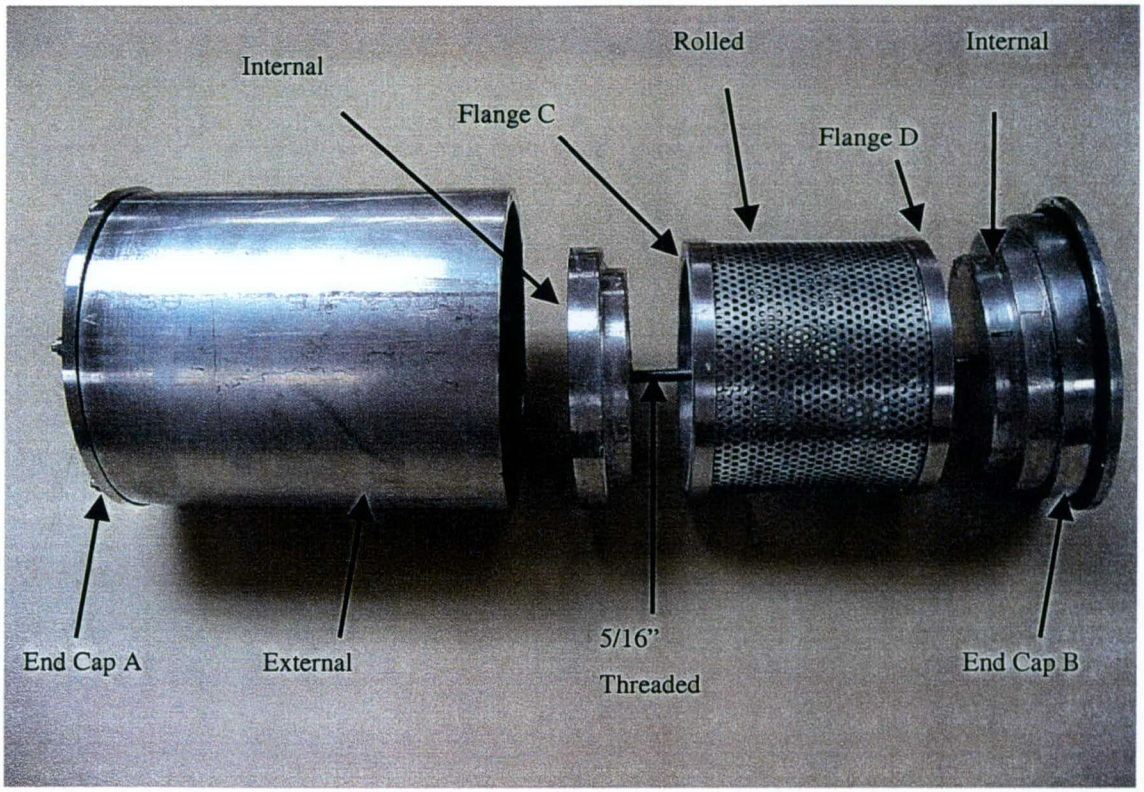

Figure 4.9 Complete cylindrical filter assembly

4.2.2. Assembly of the filter

The nylon membrane of 0.45μm pore size, made by the Millipore Corporation, comes at a standard width of 15 cm and a length of 300 cm (Product ID: INYU00010). Once the flanges C and D were attached to the rolled and perforated tube, the length of the inner (internal) filter assembly became approximately 13.5 cm. The membrane was cut so that the length of the membrane was 5 cm more than the circumference internal filter assembly. The filter membrane was wrapped onto the inner filter assembly and a layer of double sided permanent tape was applied on the inner side of the membrane. The membrane was sealed with West System fast cure epoxy glue. The outer edges of the membrane were stuck to the flanges C and D using the double-sided permanent tape. A

silicone gasket was placed on the internal cap C. Silicone glue was uniformly applied on the outer periphery of the inner filter assembly and was then placed on the internal cap C. A silicone gasket was placed on the internal cap D and silicone glue was applied on the gasket. The internal cap D was then placed onto the inner filter assembly. The end cap D was placed on flange D and tighten using a nut and bolt. The inner assembly, external cylinder, the end cap A and B were then attached using nuts and bolts. The filter was then ready to use. The assembled filter used in the magnetic field is as shown in Figure 4.10.

Filter membrane on the surface of the perforated tube

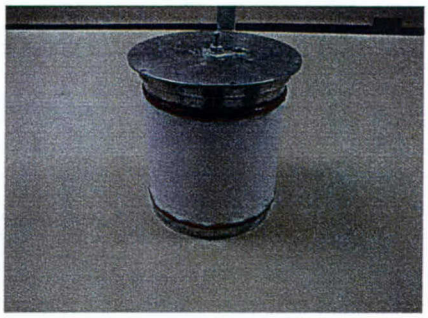

Complete assembly of the internal parts

Filter assembly

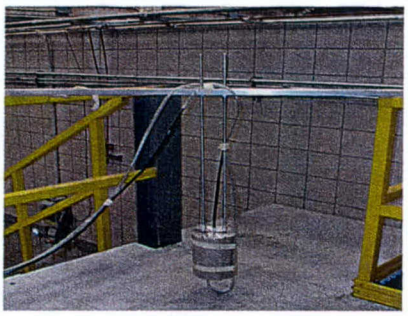

Final filter assembly with suspension supply and outlet tubes

Figure 4.10 Various phases of filter assembly

4.2.3. Fabrication of large magnetically aligned buckypapers

The assembled filter was used to fabricate large magnetically aligned buckypapers. During the experiments it was found that suspension frequently broke due to the peristaltic motion of the SWNT suspensions because of the peristaltic pump. To ensure

that a stable suspension could pass through the filter, an in-situ sonication system was provided in subsequent experiments. In this way, the suspension was resonicated just before entering the filtration system, ensuring good tube dispersion and stable suspension. Figure 4.11 shows the experimental setup for fabricating the large aligned buckypapers at the NHMFL. After fabrication, the produced buckypapers were also cleaned and dried using the same procedure described in Section 4.2.

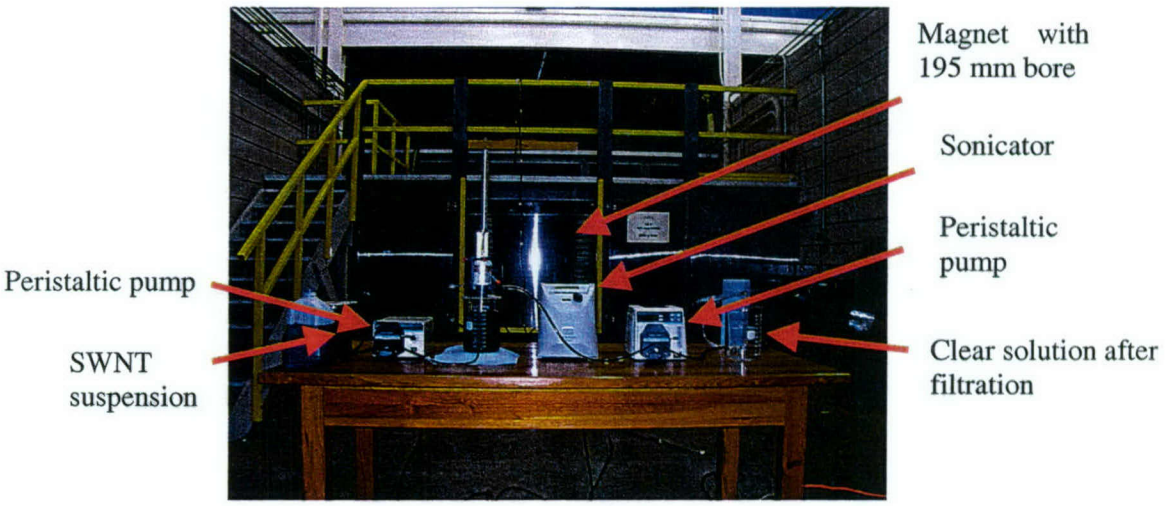

Figure 4.11 Modified experimental set-up for producing large magnetically aligned nanotube buckypapers

The world's largest magnetically aligned buckypapers were successfully produced in the project, as shown in Figure 4.12. The produced buckypapers have a working area more than 387 cm^2 (60 in^2) with a thickness around 15~ 30 μm. Good tube alignment was observed in the produced buckypapers The successful development of this large aligned buckypaper fabrication approach provides the possibility for producing bulk nanocomposite samples with in-plane controlled tube orientation.

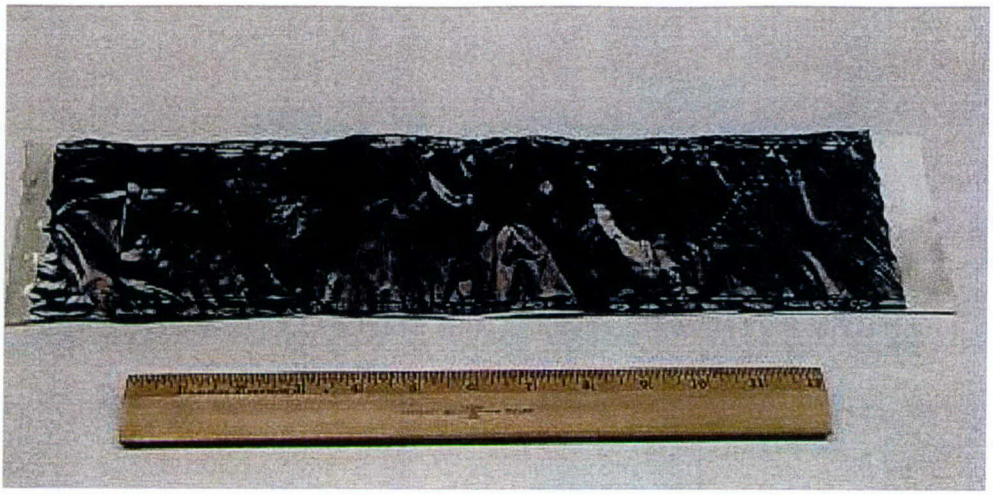

(40mg/L SWNT suspension concentration and 17.3 Tesla magnetic field)
Figure 4.12 World's largest magnetically aligned buckypaper

4.3. Investigation of SWNT Alignment in Magnetically Aligned Buckypapers

The alignment of SWNTs in high magnetic fields for fabricating aligned buckypapers is a result of complicated interactions of nanotube anisotropic magnetic susceptibility, strength of magnetic field, tube dispersion, surfactant, tube self-assembly and temperature, as well as filtration flow rate. Among these impact factors, concentration of tube suspension and strength of magnetic field are the most important parameters for achieving a high degree of alignment and efficiency for producing magnetically aligned buckypapers, which are critical for controlling tube alignment quality and reducing electrical consumption of the process. To more systematically reveal the influences of both suspension concentration and magnetic field strength, we conducted a series experiments to produce large magnetically aligned large buckypapers (60in^2 working area) with different tube concentrations (10mg/L, 20mg/L, 40mg/L and 100mg/L) and varying magnetic strengths (5 Tesla, 10 Tesla and 17.3 Tesla). The anisotropy ratios of the electrical resistivity of the resultant buckypapers were characterized using the four-probe method with a special designed fixture, which can be used as a good indicator of tube alignment. We also examined the nanostructures of the produced buckypapers to understand the relationships between tube alignment and electrical resistivity.

4.3.1. Experimental Parameters

The experimental parameters used to produce large buckypapers are provided in Table 4.1. The produced buckypapers are shown in Figure 4.13.

Table 4-1 Parameters for producing large magnetically aligned buckypapers

Magnet: Cell 5/195mm Membrane: Nylon

Flow pressure: 30-35 psi Surfactant: 0.4% Triton-X

Number	Suspension Conc. SWNT (mg/l)	Pore size of filter (μm)	Suspension volume (l)	Filtration time (hrs)	Magnetic field (T)
1	10	0.45	16	2.5	17.3
2	20	0.45	12	6.5	17.3
3	40	0.45	12	7	17.3
4	100	0.45	7	1.16	17.3
5	40	0.45	14	5.5	10
6	40	0.45	12	4.33	5
7	40	0.45	16	2.5	0

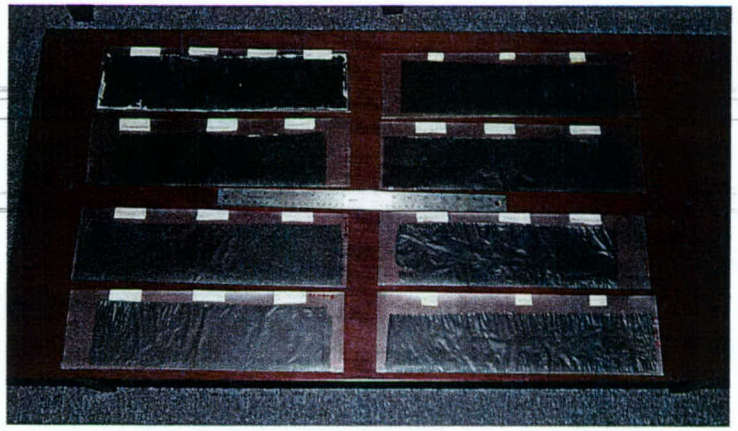

Figure 4.13 Large aligned buckypapers produced using various processing parameters

4.3.2. Anisotropy ratios of electrical resistivity

To investigate nanotube alignment in the resultant buckypapers, an electrical resistivity measurement was conducted. Since the thickness of these aligned buckypaper was only 15-30μm, a special fixture of four-probe electrical resistivity measurement was designed

and fabricated to ensure good contact between the buckypaper samples and the very fine silver probes.

Setup of electrical resistivity measurement. The four-probe resistivity method is the standard test procedure to accurately determine the electrical resistivity of samples. In this method, the resistance of the sample is determined by passing a known direct current (I), measuring the resulting voltage drop (DV) and performing the division to get R=DV/I. To calculate the sample resistance, the value of the current must be known. To establish a constant current through the sample, a known voltage (power supply), E, is connected to a series circuit consisting of the sample buckypaper resistor R and a known resistor, R_B, as shown in Figure 4.14.

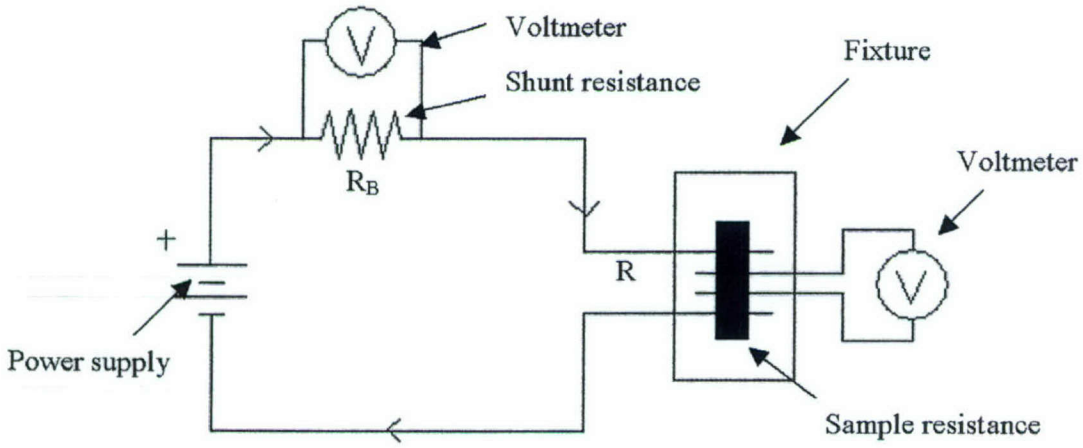

Figure 4.14 Principle of four-probe resistivity measurement

The resistance, R_B, is chosen in such a way that $R_B >> R$. Hence, the constant current is taken as $I \cong E/R_B$. Resistivity, ρ of the sample is then calculated using the formula,

$$R = \frac{\rho \times A}{L} \tag{4.1}$$

where,

L = sample length,

A = cross-sectional area of the sample,

Since the nanotubes are aligned, the buckypaper also becomes anisotropic. The electrical resistivity anisotropy of the aligned buckypaper sample can be calculated as follows,

$$\text{ElectricalResistivity Anisotropy} = \frac{\text{Resistivity perpendicular to B}}{\text{Resistivity parallelto B}} \tag{4.2}$$

where B is the magnetic field direction

In the project, the experimental setup consists of an HP power supply connected in series with a shunt resistance and the sample resistance (buckypaper). Two Keithley 2002 MEM multimeters were connected in parallel to each resistance as shown in Figure 4.15. These multimeters were connected to the computer containg the data acquisition software, LabView 6.1, and a GPIB interface card from National Instruments. The LabView records the voltage drop across the resistance for the applied current range. Silver probes were used to connect the samples to multimeters, since they offer the least resistance to the current flow. Table 4.2 shows the various equipments used for the resistivity measurements.

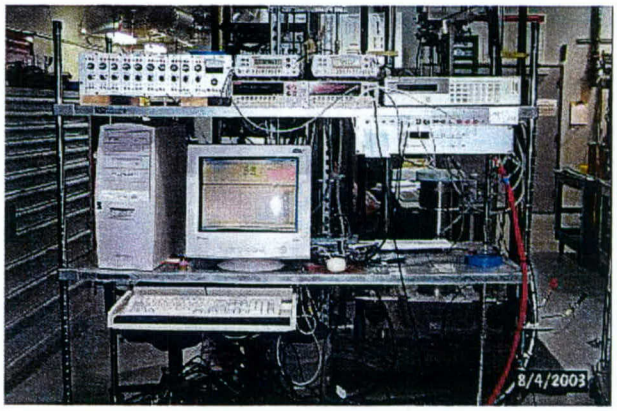

Figure 4.15 Experimental setup for the resistivity measurements

Table 4-2 List of equipments and materials for the resistivity measurements

Facilities/Materials	Description
DC Power supply 0-8V/10A	Supplier: Hewlett Packard, www.hp.com
Digital Multimeter (10nV accuracy)	Supplier: Keithley Instruments www.keithley.com
GPIB 488.2 interface Card	Supplier: National Instruments www.ni.com
Lab view 6.2	Supplier: National Instruments www.ni.com
Silver probes (No. 100234)	Supplier: Digikey Inc. www.digikey.com
Silicone rubber (1mm thick)	Supplier: Air tech www.airtech.com
Plastic film (50μm thick)	Supplier: Fisher scientific www.fishersci.com
Shunt resistance	Supplier: Digikey Inc. www.digikey.com

The fixture for testing the resistivity was custom made as shown in Figures 4.16 and 4.17. Since the buckypaper samples are thin and delicate, it is important to ensure proper contact between the probes and the sample. The fixture consists of two plates that attach to each other with nuts and screws. The top plate was made up of G-10 and had silicon rubber glued to it. A small plastic sheet was then attached to this silicon rubber. The four probes were placed on the bottom plate made up of Plexiglas and attached with the help of epoxy glue at the glass edge. Most four probes resistivity fixture had 1 mm separation distance, but the distance between the probes was selected as 3 mm for our fixture. Since the distance was increased between the probes, the accuracy of testing accuracy was increased. The inner probes were the voltage probes and the outer probes were the current probes. These probes were placed at an equal distance from each other. The sample was placed on these probes as shown in Figure 4.16 and then the fixture was closed with G-10, as shown in Figure 4.17. The silicon rubber helped the sample to take the shape of probes. The plastic sheet helped the sample to not stick on the silicon rubber.

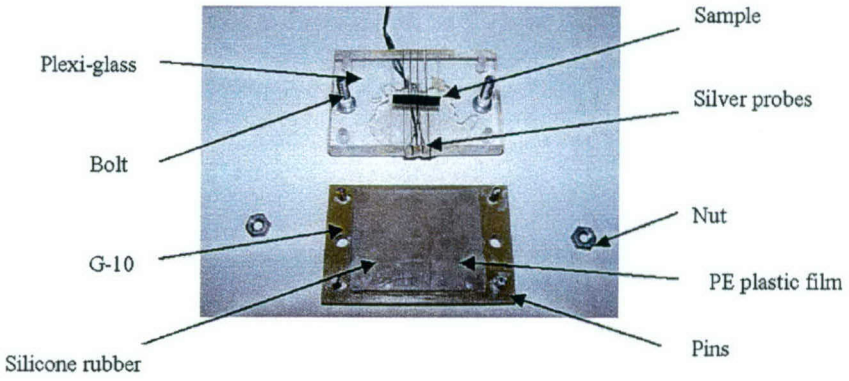

Figure 4.16 Fixture for the resistivity measurements

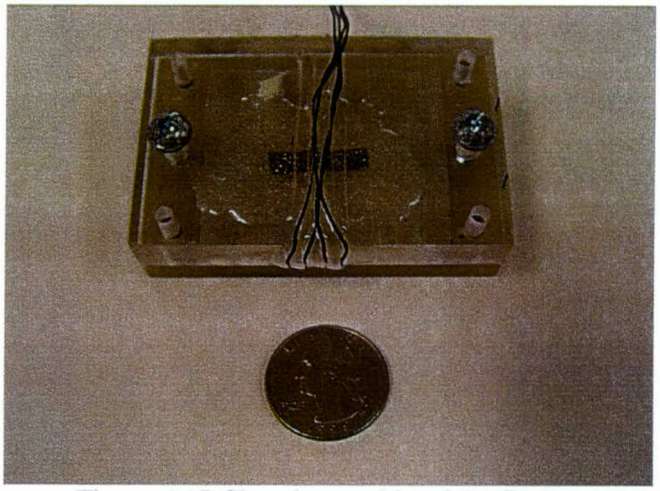

Figure 4.17 Closed assembly of the fixture

Measurement of electrical resistivity. Appropriate settings were chosen for filter, speed and accuracy for the multimeters. The probes in the fixture were short by placing a silver wire for calibration. A small amount of current was passed and the multimeters were calibrated to zero. The voltage for the power supply was set to 8V. The sample measured was first weighed and the dimensions of the sample were noted. For the aligned samples whose resistivity was measured in parallel direction to B, the multimeters were set at a higher accuracy range of 200mV, and for samples whose resistivity was measured in perpendicular direction to B, the multimeters were set at a medium accuracy range of 2V. The resistivity of the sample in perpendicular direction to B was high, so the voltage

around 200mV provided very low current. Therefore, we could not acquire many data points to obtain the slope of voltage by current. Hence, we decreased the accuracy range to 2V. The sample tested was placed on the fixture and a 0.0001A current was passed from the power supply. Once the current was passed across the sample, LabView automatically recorded the voltage across the shunt resistance and the sample in the computer. The current was then increased gradually to obtain the potential difference for at least 100 different current values. Then, the resistivity of the sample was calculated. The setup was also calibrated using a thin copper foil with a known resistivity.

4.4.3 Resistivity analysis for the aligned buckypapers

Resistivity was measured for all the aligned and random buckypapers as listed in Table 4.1. For each aligned buckypaper, six samples were tested. Of these six samples, the resistivity of three samples was measured in a parallel direction to the magnetic field and the other three samples were measured in a perpendicular direction to the magnetic field. Resistivity was measured for both sides for each sample. The actual length, width and thickness were measured using a caliper. Since buckypapers are a porous structure made of SWNT networks, we cannot account for the measured volume of the buckypaper from a caliper in Equation 4.1. Hence, we use the effective thickness (t_{eff}), which is defined as the measured mass per unit area divided by density of SWNT ropes (1.33 gm/cm^3), as suggested by Dr. Smalley's group. Figures 18 and 19 show the slope of voltage and current for the aligned buckypaper fabricated using nanotube suspension of 40mg/L concentration and the 17.3 Tesla magnetic field (Sample 3). Since the slope was linear in all the graphs, it can be concluded that the resistance measured was constant for the given current range. Table 4.3 shows the measurement of the resistivity and anisotropy of sample 3. Since a slight variation in resistivity existed in different samples from the same buckypaper, the mean and standard deviation were also calculated. In this case, six samples were measured in parallel direction to B ($\parallel$) and another six samples were measured in perpendicular direction to B ($\perp$). The anisotropy of these samples was as high as 9.46, which indicated significant tube alignment in the buckypaper. Other samples' resistivity and anisotropy ratios were also measured and calculated in the project.

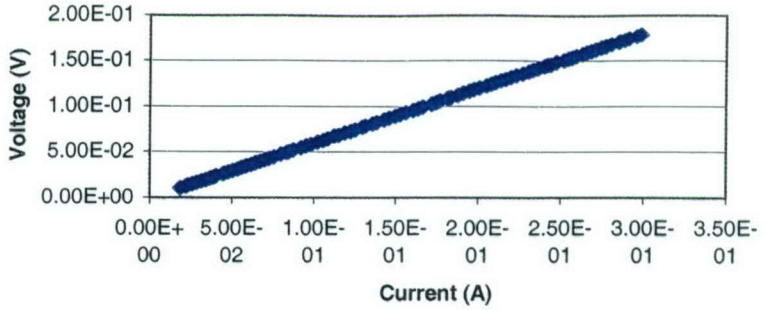

(Resistivity measured in parallel direction to B)
Figure 4.18 Voltage vs. current of sample 3

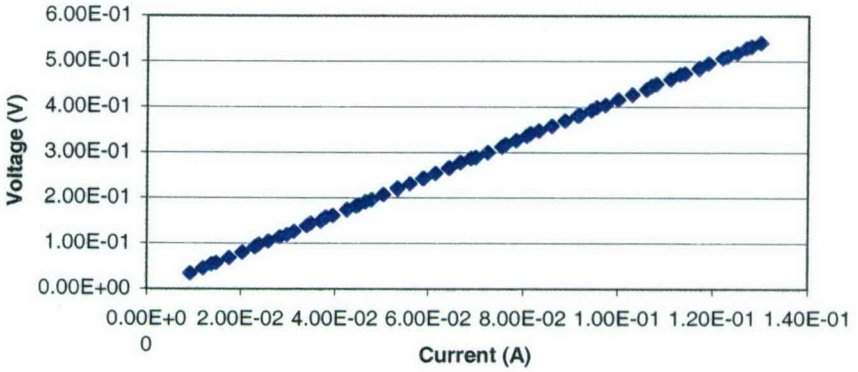

(Resistivity measured in perpendicular direction to B)
Figure 4.19 Voltage vs. current of sample 3

Table 4-3 Resistivity measurements of Sample 3

(a) Resistivity parallel to tube alignment direction

Sample No.	Direction	Resistivity (Ω-cm)	Average (Ω-cm)	Mean (Ω-cm)	Std. Dev. (Ω-cm)
Sample 3-1	||	6.70E-04	6.74 E-04	6.21E-04	9.18E-05
Sample 3-1	||	6.77E-04			
Sample 3-2	||	6.89E-04	6.82 E-04		
Sample 3-2	||	6.74E-04			
Sample 3-3	||	5.17E-04	5.16 E-04		
Sample 3-3	||	5.15E-04			
Sample 3-4	||	6.21E-04	6.23 E-04		
Sample 3-4	||	6.25E-04			
Sample 3-5	||	5.01E-04	5.04 E-04		
Sample 3-5	||	5.06E-04			
Sample 3-6	||	7.25E-04	7.26 E-04		
Sample 3-6	||	7.26E-04			

(b) Resistivity perpendicular to tube alignment direction

Sample No.	Direction	Resistivity (Ω-cm)	Average (Ω-cm)	Mean (Ω-cm)	Std Dev. (Ω-cm)
Sample 3-7	⊥	6.90E-03	6.95E-03	5.89E-03	6.56E-04
Sample 3-7	⊥	7.00E-03			
Sample 3-8	⊥	6.09E-03	6.07E-03		
Sample 3-8	⊥	6.04E-03			
Sample 3-9	⊥	6.02E-03	5.98E-03		
Sample 3-9	⊥	5.93E-03			
Sample 3-10	⊥	5.22E-03	5.22E-03		
Sample 3-10	⊥	5.22E-03			
Sample 3-11	⊥	5.91E-03	5.97E-03		
Sample 3-11	⊥	6.02E-03			
Sample 3-12	⊥	5.14E-03	5.16E-03		
Sample 3-12	⊥	5.18E-03			

4.3.3. Influences on tube alignment

Influences of Suspension Concentration. Figure 4.20 shows the influences of the suspension concentration on the anisotropy ratios of the magnetically aligned buckypapers, which were produced with a 17.3 Tesla magnetic field. The figure shows that the anisotropy of the buckypaper is fairly constant for the samples made with

suspensions of concentration from 10 to 40 mg/l; however, the anisotropy ratio of the buckypaper sharply decreased with an increase in the concentration of the SWNT suspension from 40mg/L to 100mg/L. The SEM observations indicate obvious differences between nanotube networks of 40mg/L and 100mg/L buckypapers, as shown in Figures 4.21 and 4.22. The preferred tube orientation along the magnetic force direction (white arrow) and tight tube packing can be seen in buckypapers made with the 40mg/L suspension. In the buckypaper made with the 100mg/L suspension, the formed tube network is random and relatively loose, which may be because the tubes cannot move easily and align due to poor tube dispersion and intensive tube-tube interactions in high concentration suspensions.

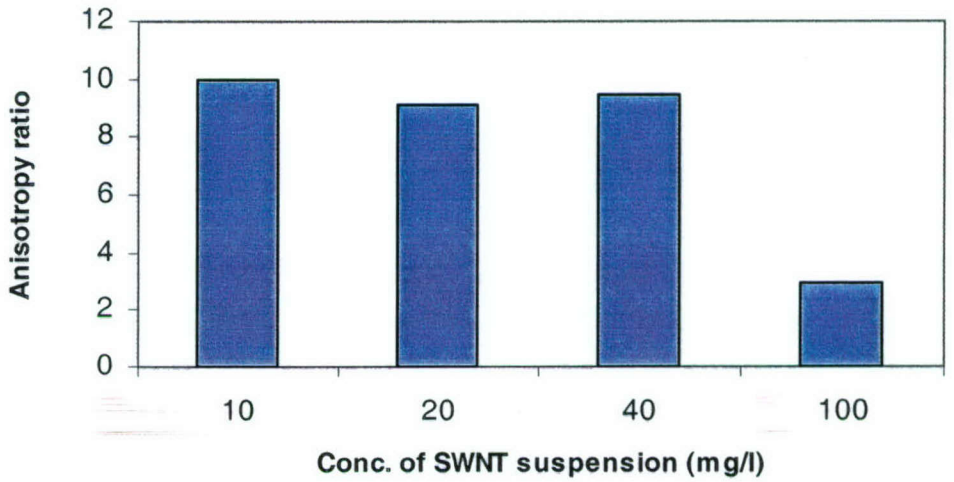

Figure 4.20 Influences of suspension concentration on anisotropy ratios of magnetically aligned buckypapers under 17.3 Tesla magnetic field

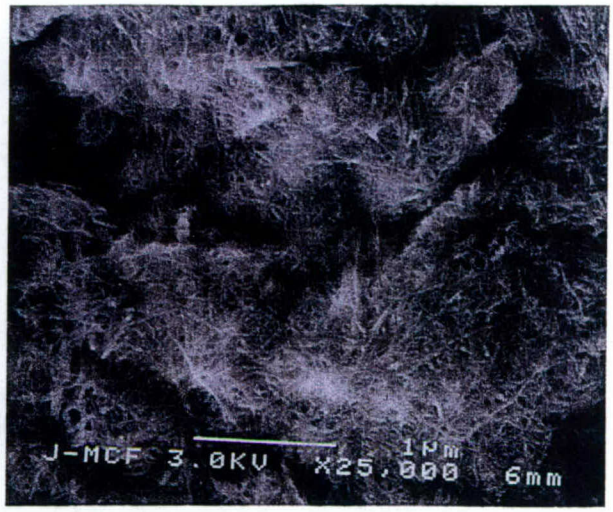

Figure 4.21 Aligned buckypaper of 40mg/L Figure 4.22 Aligned buckypaper of 100mg/L

Influences of magnetic field strength. Figure 4.23 shows the influences of magnetic field strength on the anisotropy ratios of the magnetically aligned buckypapers, which were produced with the suspension concentration of 40mg/L. The results illustrate that the applied magnetic field strength has a direct impact on tube alignment in the produced buckypapers. The anisotropy ratios increase almost linearly with the increase of magnetic field strength.

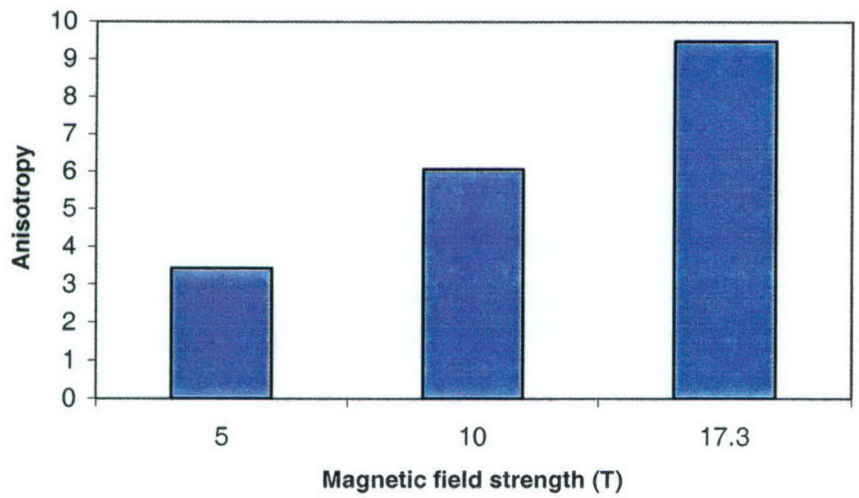

Figure 4.23 Influences of strength of magnetic field on anisotropy ratios of magnetically aligned buckypapers using 40mg/L suspension

Figures 4.24 and 4.25 show the nanostructures of the aligned buckypaper produced using 5 Tesla and 10 Tesla fields, respectively. Figures 4.24, 4.25 and 4.21 show an increase of tube rope diameter and alignment with the increase of field strength during the aligned buckypaper processing. Figure 4.24 shows almost random networks of fine tube ropes, whereas relatively large and continuous tube ropes with alignment can be seen in Figure 4.21.

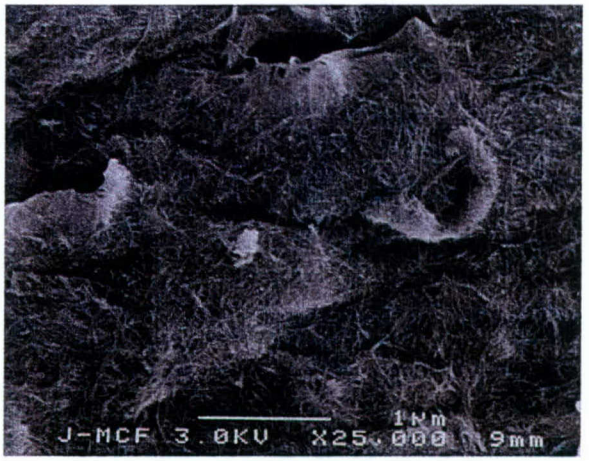

Figure 4.24 SEM of the aligned buckypaper produced using 5 Tesla magnetic field

Figure 4.25 SEM of the aligned buckypaper produced using 10 Tesla magnetic field

Figure 4.26 shows the significant tube alignment in the internal layer by peeling the aligned buckypaper produced with the 17.3 Tesla field.

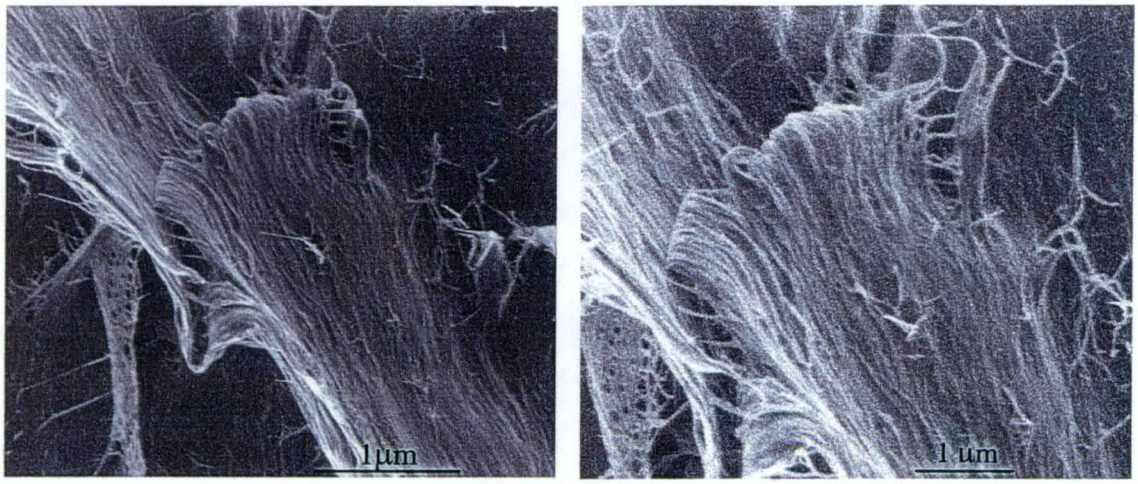

(a) (b)

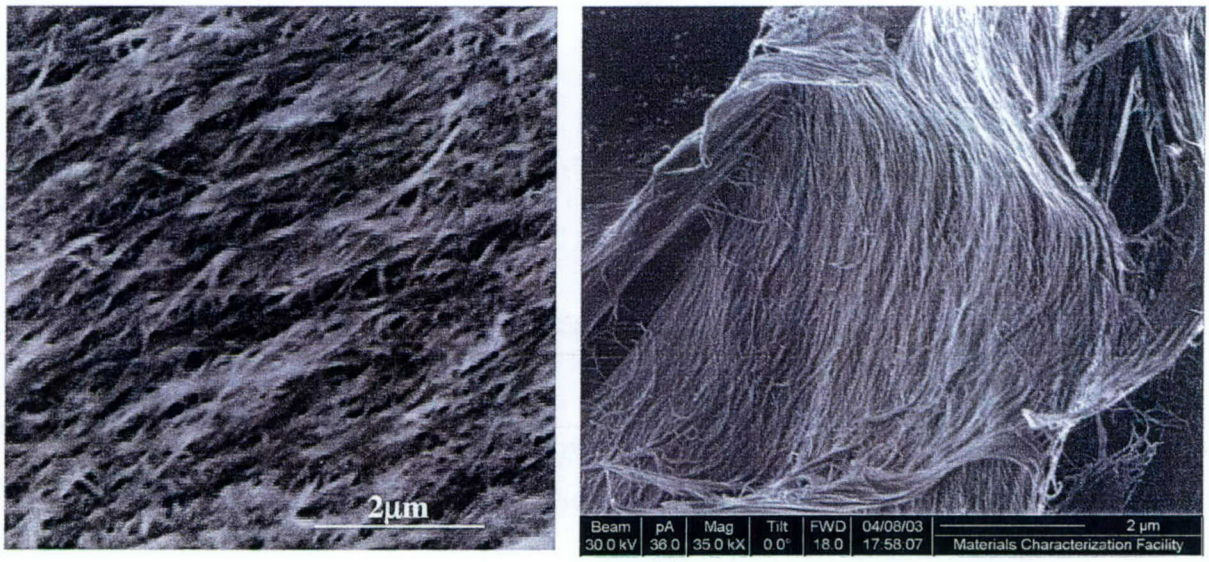

(c) (d)

Figure 4.26 Significant SWNT alignment in the buckypaper produced by using 40mg/l suspension and 17.3 Tesla magnetic field

4.4. Conclusions

By in-situ filtration of well-dispersed SWNT suspension inside high magnetic fields, aligned buckypapers can be fabricated, in which SWNTs are aligned along the direction of the magnetic field. In this project, a custom-made cylinder filter was designed and fabricated to produce large magnetically aligned buckypapers at the NHMFL. The

world's largest magnetically aligned buckypapers, with a working area of 60 in^2,were successfully manufactured and significant tube alignment was observed by SEM and AFM analysis. The anisotropy ratios of electrical resistivity measurements of the produced buckypapers were as high as 9.46 along and perpendicular to the direction of tube alignment direction, which indicated good tube alignment in the resultant buckypapers. The research also revealed the influences of suspension concentration and magnetic field strength on the nanotube alignment. The results show that significant tube alignment can be achieved in the buckypapers made with 40mg/L suspension and the 17.3 Tesla magnetic field. The success of producing large magnetically aligned buckypapers with significant tube alignment provides the possibility for using buckypaper/resin infiltration process to fabricate nanocomposites with controlled tube orientation. The descriptions of mechanical and thermal properties of the resultant magnetically aligned buckypaper are given in Chapter 5.

4.5. References

[1] A. Walters, M. J. Casavant, X. C. Qin, C. B. Huffman, P. J. Boul, L. M. Ericson, E. H. Haroz, M. J. O'Connell, K. Smith, D. T. Colbert and R. E. Smalley, "In-plane-aligned membranes of carbon nanotubes," *Chemical Physics Letters*, Vol.338, No.1, pp.14-20, 2001.

[2] J. E. Fischer, W. Zhou, J. Vavro, M.J. Casavant, D.E Walters and R. E. Smalley, "Magnetically aligned single wall carbon nanotubes films: Preferred orientation and anisotropic transport properties," *Journal of Applied Physics*, Vol. 93, No. 4, 99. 2157-2163, 2003.

[3] J. Hone, M. C. Llaguno, N. M. Nemes, A. T. Johnson, D. A. Walters, M. J. Casavant, J. Schmidt, and R. E. Smalley, "Electrical and thermal transport properties of magnetically aligned single wall carbon nanotube films," *Applied Physics Letters* Vol. 77, No. 5, 666-668, 2000.

[4] J. P. Lu, "Novel magnetic properties of carbon nanotubes," *Physics Review Letters*, Vol.74, pp.1123-1126, 1995.

5. Mechanical Properties and Thermal Conductivities of Buckypaper and Buckypaper/Epoxy Nanocomposites

The mechanical properties and thermal conductivity of the produced buckypapers and buckypaper/resin infiltration nanocomposites were characterized. Dynamical mechanical analysis (DMA) was used for characterizing the mechanical properties of the nanocomposites. The thermal conductivity of the produced buckypaper and nanocomposites was measured using a comparative method. The tensile moduli of both individually dispersed SWNTs and SWNT rope nanocomposites were predicted by the Halpin-Tsai model for discontinuous reinforcement composites. The predicted results were also compared with the experimental results.

5.1. Dynamic Mechanical Properties of the Buckypaper Nanocomposites

The dynamic mechanical properties and damping behaviors of the nanocomposites were tested with a dynamic mechanical analyzer (DMA2980, TA Instrument Co.). The test was conducted in the tensile (film) mode. The sample was heated to 350°C at 5°C/min at a frequency of 1Hz.

5.1.1. Random buckypaper/epoxy nanocomposites

The storage modulus results of the random buckypaper nanocomposites listed in Table 2.2 are shown in Figure 5.1 and Table 5.1. The storage moduli of the resulting nanocomposites dramatically increased by 349% to 492%, compared to the neat resin modulus. However, the storage moduli of the composites were significantly less than predicted by the rule of mixtures for random orientation individual SWNT-reinforced composites. We believe that the poor load transfer between the nanotubes in the ropes and between the nanotubes and resin matrix was the major reason. The formation of large tube ropes in the composites could significantly decrease the load transfer in the composites. For example, Salvetat *et al.* experimentally showed that when the SWNT rope diameters increased from 3 to 20 nm, the elastic and shear modulus of single-walled carbon nanotube ropes could be decreased from 900 GPa to around 100 GPa due to

possible tube slippage in the ropes [1]. Therefore, the actual nanotube rope-reinforced composites may demonstrate poor mechanical properties. To realize individual tube dispersion in the buckypaper and composites for better load transfer is an ongoing research effort for this project. Another notable phenomenon observed from the DMA results is that there is no obvious influence of tube loading on the storage modulus. We believe that the nanostructures and mechanical properties of the nanotube-reinforced composite are highly dependent on tube dispersion, which directly influences molecular interactions of tube/tube and tube/resin in the materials. Such molecular interactions will play a critical role in load transfer and interfacial bonding that determine mechanical properties of the nanocomposites. The variations in tube dispersion in the resultant composites could be the major reason for this phenomenon.

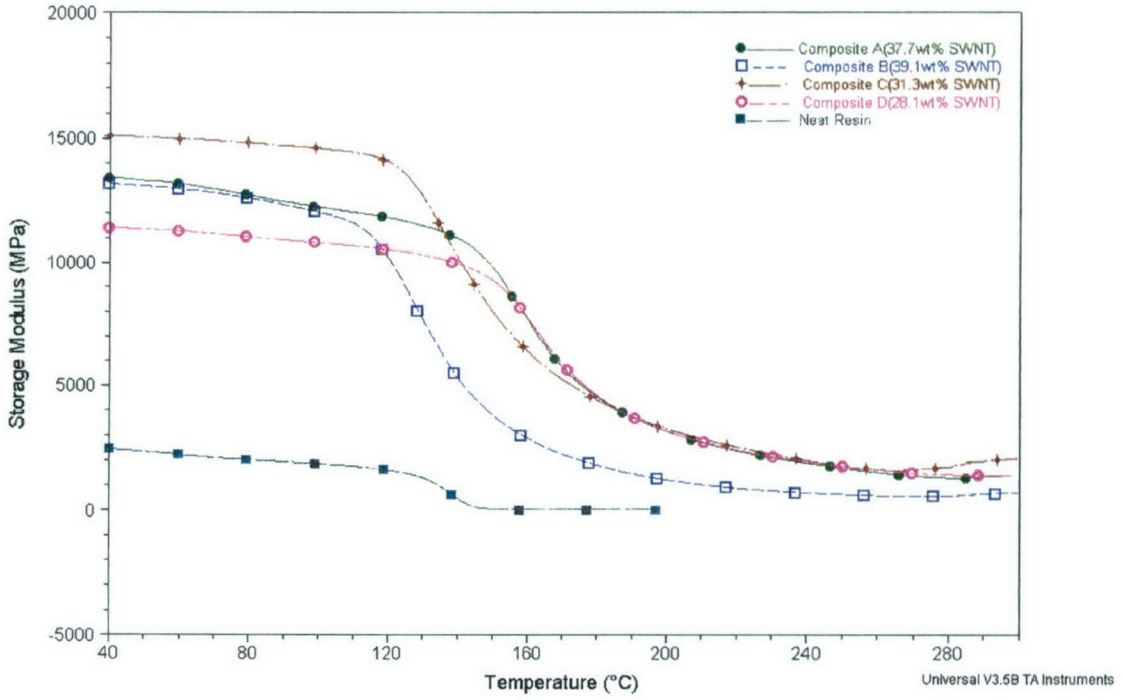

Figure 5.1 Storage modulus curves of the random nanocomposites

The DMA tgδ (Tan Delta) curves in Figure 5.2 show that the Tgs of the resultant nanocomposites did not significantly change. The damping behavior of the buckypaper-reinforced nanocomposites is different from that of the traditional fiber-reinforced

composite. There is no obvious Tg peak on the tgδ curve. After glass transition, the tgδ continuously increases rather than going back to the base line. The damping behavior reflects the energy dissipation of molecular movement and interaction. For cured resin, usually below the Tg, the resin molecule segment cannot completely move. A low tgδ value indicates no significant energy loss. During the glass transition, the molecule segment absorbs enough energy and begins to move; however, the moving space inside the polymer is too tight, so more energy is required to move the molecules. A temperature higher than Tg results in enough free space inside the resin to allow the molecule segments move freely, causing the tgδ to again decrease.

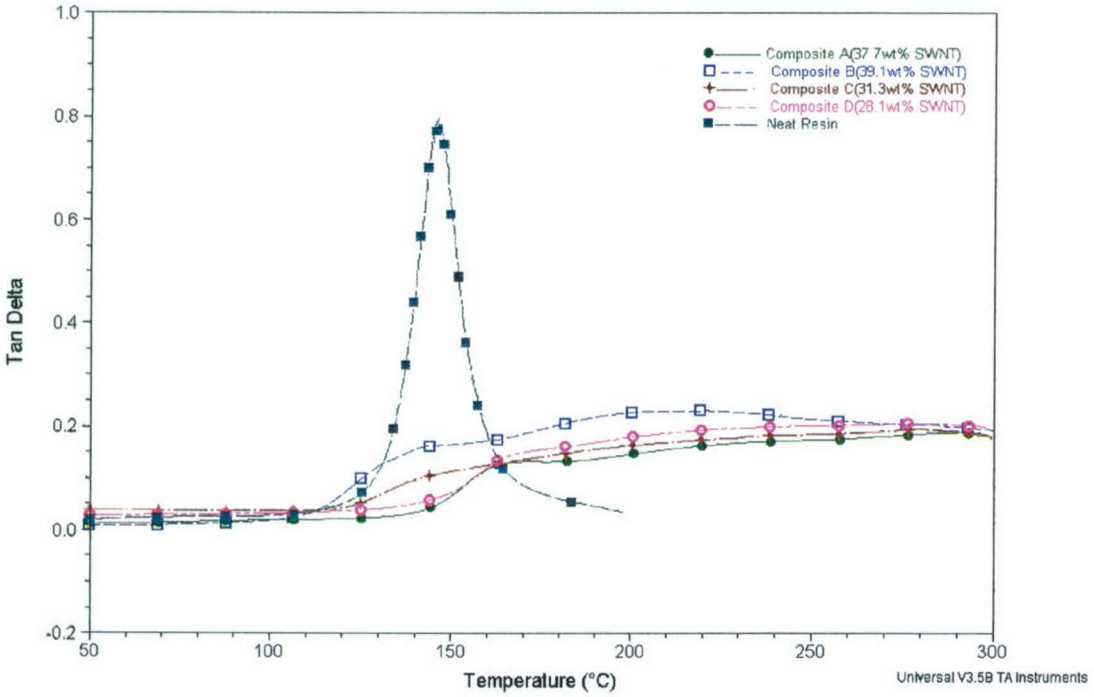

Figure 5.2 tgδ curves of the random nanocomposites

For traditional carbon fiber and glass fiber reinforced composites, both fiber and porous structures are at microscale and only a very small portion of the resin molecules are able to directly interact with reinforcement. The damping behavior of the carbon fiber and glass fiber reinforced composites are almost the same as that of the neat resin. However, for the buckypaper-reinforced composite, SWNTs have extremely large surface area and

are at the same scale of the resin molecules. Interactions between tubes and resin molecules are expected to be intense. Therefore, the resin molecule segment movement may intensely interact with the SWNTs and consume energy. These intensive molecular-level interactions may be the major reason for the high tgδ in the buckypaper-reinforced composites.

Table 5-1 Storage modulus results of the random buckypaper composites

Sample No.	SWNT Loading (wt%)	Storage Modulus (GPa)	Increase (%)
Neat Resin	0	2.55	0
A	28.1	11.45	349
B	31.3	15.10	492
C	37.7	13.49	429
D	39.1	13.24	419

5.1.2. Magnetically aligned buckypaper/epoxy nanocomposites

The storage modulus results along the tube alignment direction of the magnetically aligned buckypaper nanocomposites listed in Table 2.3 are shown in Figure 5.3 and Table 5.2. The storage modulus of the aligned buckypaper nanocomposites can be as high as 45.0 GPa, which is more than 16.5 times increase compared to that of the neat epoxy resin. In comparison with the random buckypaper composite, the storage modulus of aligned buckypaper composite is about 3 times higher. This increase in storage modulus indicates highly anisotropic stiffness, with the maximum in the magnetic field direction of the magnetically aligned buckypaper composite. The nanotube loading is also increased comparing the random to aligned buckypaper composite due to the tube alignment and tight packing of SWNTs in the aligned buckypapers and their composites. The nanotube loading increased from 28-40% by weight for the random buckypaper composite to 47-64% by weight for the aligned buckypaper composite. The results show that the tube alignment significantly impacts the mechanical properties of the SWNT-reinforced nanocomposites. The changes of the Tgs and tgδ in the aligned buckypaper nanocomposite are the same as those in the random buckypaper nanocomposites.

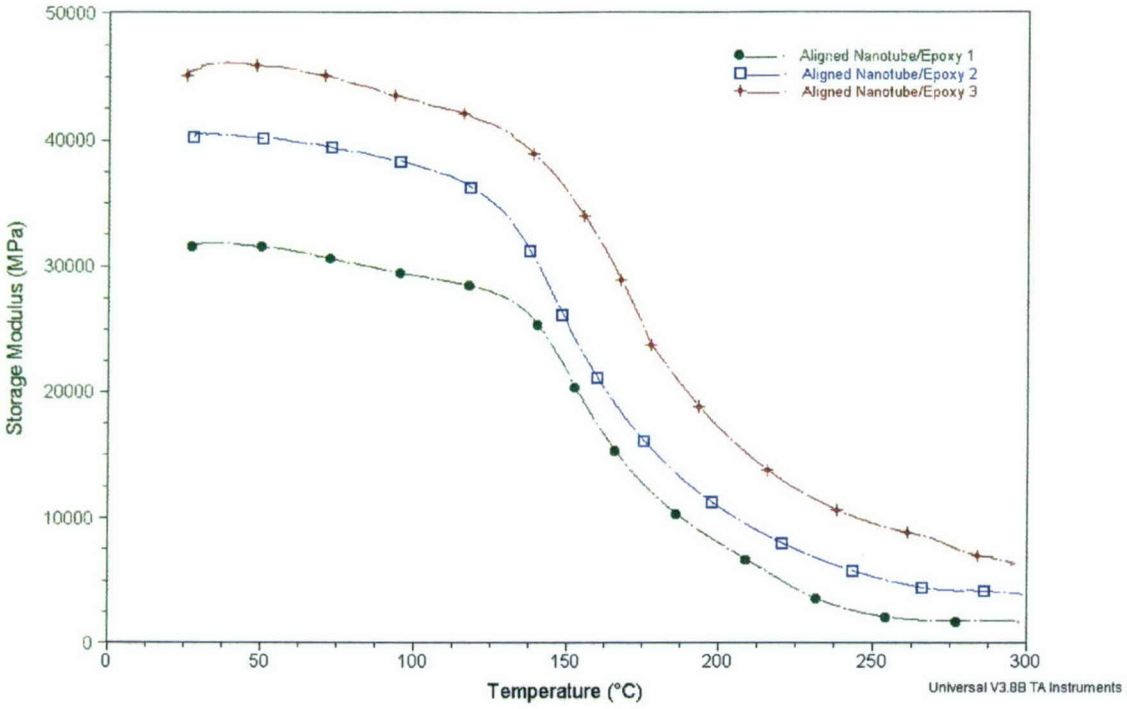

Figure 5.3 Storage modulus curves of the magnetically aligned nanocomposites

Table 5-2 Storage modulus results of the magnetically aligned buckypaper composites

Sample	Magnetic Field (T)	SWNT Loading (wt%)	Storage Modulus (GPa)	Increase (percentage)
Neat Resin	0	0	2.55	0
Aligned Nanotube/Epoxy 1	17.3	47.3	31.0	1,116
Aligned Nanotube/Epoxy 2	17.3	63.7	45.0	1,665
Aligned Nanotube/Epoxy 3	17.3	54.5	40.5	1,488

5.2. Mechanical Property Predication of SWNT-Reinforced Nanocomposites

In this project, we investigated the influences of tube dispersion, loading and orientation on the mechanical properties of SWNT reinforced composites. Random and aligned discontinuous reinforcement models for composites predicted the tensile moduli of both individually dispersed SWNTs and SWNT rope based nanocomposites. The parameters

used in the calculation models were determined based on our experimental observations. Theoretical estimates were compared with experimental results.

Since many researchers consider SWNTs as one of the most promising reinforcement materials for the next generation of high performance structural and multifunctional composites, a keen interest exists in developing SWNT reinforced composites.

Unlike conventional fibrous reinforcements, SWNTs have strong interactions between each other due to van der Waals forces, causing the SWNTs to form ropes or bundles. SWNT ropes also have the tendency to aggregate together due to their molecular interactions. Therefore, nanoscale dimension and formation of SWNT ropes make accurate theoretical predictions of nanotube composite properties difficult.

In this project, property predictions of SWNT-reinforced composites were conducted to theoretically reveal the influences of tube dispersion, loading and orientation on the composite properties based on our experimental observations. Since the SWNT were shorter than the length of the composites in the experiments, they were discontinuous in the composites. Therefore, these nanotube composites can be considered as short reinforcement composites. In this case, the composite properties will strongly depend on the aspect ratio of the nanotubes, the elastic properties of nanotube and matrix, and the interfacial shear between the nanotube and matrix. Both random and aligned discontinuous reinforcement models of composites were used to predict the tensile moduli of individually dispersed SWNTs and SWNT rope reinforced nanocomposites. The parameters used in the models were determined based on our experimental observations.

5.3. Calculation Models

For unidirectional short fiber composites, elastic properties, such as tensile modulus, can be calculated by Halpin-Tsai equations [2]. The Halpin-Tsai method is a simple and effective model or a set of empirical relationships that enable the properties of a composite material to be expressed in terms of the properties of the matrix and reinforcing phases, together with their proportions and microstructure geometry. These

equations were validated by experimental measurements. To theoretically predict the mechanical properties of nanotube-reinforced composites, these equations were assumed to be valid for predicting nanotube-reinforced nanocomposites since nanotubes can also be considered as short-reinforcements in the resin matrix. Good wet-out and interfacial bonding were assumed to exist between the nanotubes and the matrix. Based on our experimental observations of the produced buckypaper and nanocomposites, the nanotubes in the composites were also assumed to be straight. The composite modulus for aligned discontinuous SWNT/epoxy in the longitudinal and transverse direction were calculated from the following equations:

$$E_{11} = \frac{1 + 2(l_{NT} / d_{NT})\eta_L V_{NT}}{1 - \eta_L V_{NT}} E_{EP} \tag{5.1}$$

$$E_{22} = \frac{1 + 2\eta_T V_{NT}}{1 - \eta_T V_{NT}} E_{EP} \tag{5.2}$$

$$\eta_L = \frac{(E_{NT} / E_{EP}) - 1}{(E_{NT} / E_{EP}) + 2(l_{NT} / d_{NT})} \tag{5.3}$$

$$\eta_T = \frac{(E_{NT} / E_{EP}) - 1}{(E_{NT} / E_{EP}) + 2} \tag{5.4}$$

where,

E_{11}= Composite modulus of aligned discontinuous SWNT/epoxy in longitudinal direction

E_{22}= Composite modulus of aligned discontinuous SWNT/epoxy in transverse direction

l_{NT} = Length of the nanotubes

d_{NT} = Diameter of the nanotubes

V_{NT} = Volume fraction of the nanotubes

E_{EP} = Elastic modulus of the epoxy resin

E_{NT} = Elastic modulus of the nanotubes

For the modulus of a randomly oriented discontinuous SWNT/epoxy nanocomposites, E_{CR}, planar isotropy was assumed. Using the equations provided by Halpin and Pagano [2], the in-plane tensile modulus of a composite containing two-dimensional randomly orientated nanotubes were calculated,

$$E_{CR} = \left[\frac{3}{8}E_{11} + \frac{5}{8}E_{22}\right] \tag{5.5}$$

where E_{11} and E_{22} are the moduli of the aligned discontinuous SWNT/epoxy in longitudinal direction and transverse direction of the nanocomposites with same tube content, respectively, which were calculated from equations 5.1 to 5.4.

5.3.1. Model parameters of individually dispersed nanocomposites

Figure 5.4 shows the molecular model of the nanocomposites of individually dispersed and unidirectional aligned SWNTs. The following assumptions were made to calculate the composite modulus of random and aligned discontinuous SWNT/EPON 862 resin composites:

- Only individual nanotubes were present in the SWNT/epoxy composite;
- The SWNTs were assumed to be individually and uniformly dispersed in the resin matrix; and
- The presence of only one type of SWNTs, (7,7) SWNTs, was considered in the nanocomposites and these nanotubes had a diameter of 1 nm, which was almost the same as that of the SWNTs used in our experiment. (See BuckyPearl properties in Section 2.2).

Based on the molecule structure of (7,7) SWNT, we calculated E_{NT} and the effective radius R_{NT} of the nanotube [3],

$$E_{NT} = \frac{4\sqrt{3}\pi b Y \Lambda \nu}{3b^2\Lambda^2 + 2\sqrt{3}\pi\Lambda\nu + \pi^2\nu^2} \tag{5.6}$$

$$R_{NT} = \frac{b}{2\pi}\sqrt{3}\Lambda + \frac{\nu}{2} \tag{5.7}$$

$$\Lambda = \sqrt{(n^2 + m^2 + m^2 + nm^2)} \tag{5.8}$$

where,

n and m are chiral vector integer pairs of SWNT;

b is the C-C bond length in SWNT;

ν is equilibrium separation distance of SWNTs and resin matrix; and

Y is the in-plane Young's modulus of the graphene sheet.

Using the above equation, the effective radius of (7,7) SWNT was 0.645 nm and effective diameter was 1.29 nm. The modulus of (7,7) SWNT was 801.37GPa. The elastic modulus of EPON 862 resin was 2.72 GPa. The length of individual tube used in our experiments was ~100-1000 nm.

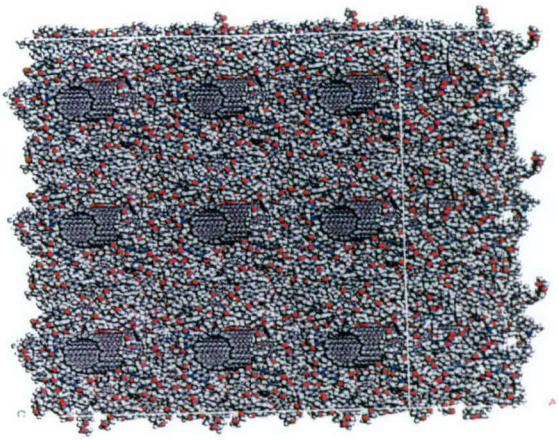

Figure 5.4 Molecular model of aligned individual SWNT-reinforced nanocomposites

5.3.2. Properties of individually dispersed SWNT-reinforced nanocomposites

Using the above models and parameters, E_{CR} and E_{11} were calculated for both random and aligned nanotube composites with 40% SWNT volume content. These properties with respect to aspect ratio are shown in Figures 5.5 and 5.6. The results show that the aspect ratio plays a significant role in changing the modulus of the composite. Results also indicate that in both random and aligned cases, the maximum properties can be achieved when the SWNT aspect ratio is larger than 1,000.

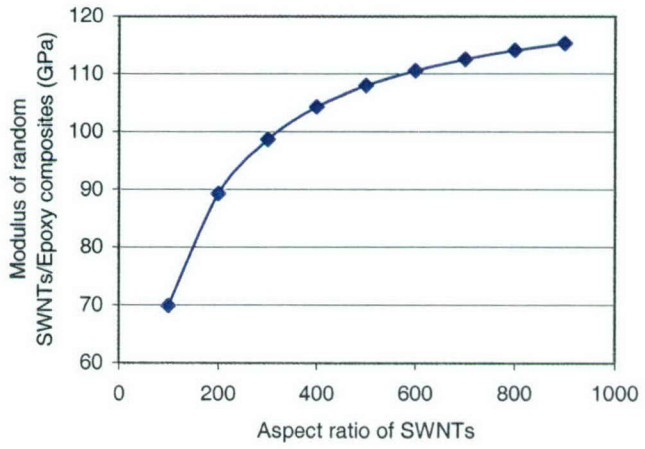

Figure 5.5 E_{CR} vs. tube aspect ratio of random individually dispersed SWNT/epoxy nanocomposites

Figures 5.7 and 5.8 show E_{CR} and E_{11} for both random and aligned nanotube composites with an increase in nanotube volume. Here the length of SWNT is assumed as 1 μm to calculate upper-boundary properties of the nanocomposites in the experiments. The results show that the nanotube content in the composite plays a significant role in changing the modulus of the composite.

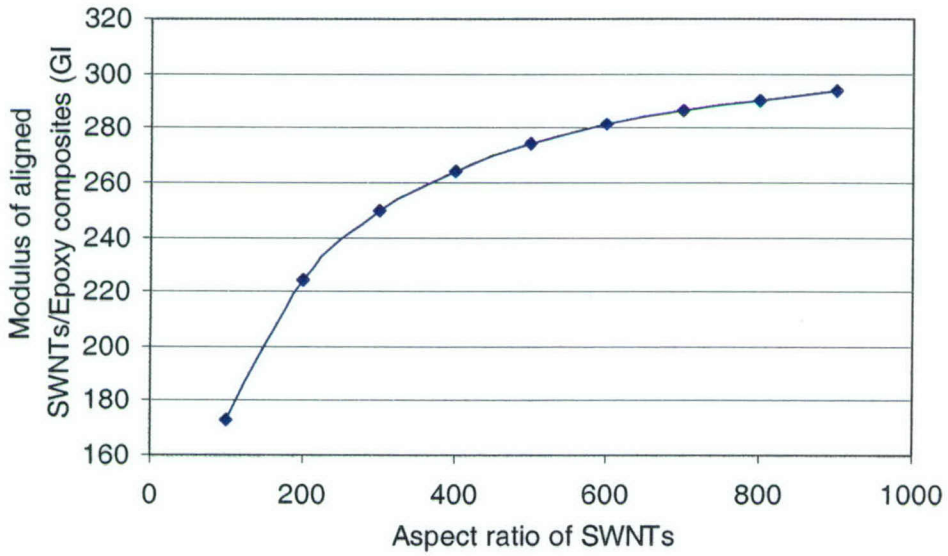

Figure 5.6 E_{11} vs. tube aspect ratio of random individually dispersed SWNT/epoxy nanocomposites

Figures 5.7 and 5.8 also show a linear increase in modulus for random and aligned discontinuous SWNT/epoxy composites with respect to nanotube content. As shown in Figure 5.7, for random nanocomposites, the modulus is 177 GPa when the tube volume fraction is 0.6, which is closed to a unidirectional carbon fiber composite with the same fiber volume fraction. As shown in Figure 5.8, for aligned nanocomposites, the composite modulus could be as high as 448 GPa when the tube volume fraction is 0.6, which is about 2.5 times higher than that of the random discontinuous SWNT/epoxy nanocomposite. These results indicate the importance of nanotube alignment for developing high performance SWNT nanocomposites.

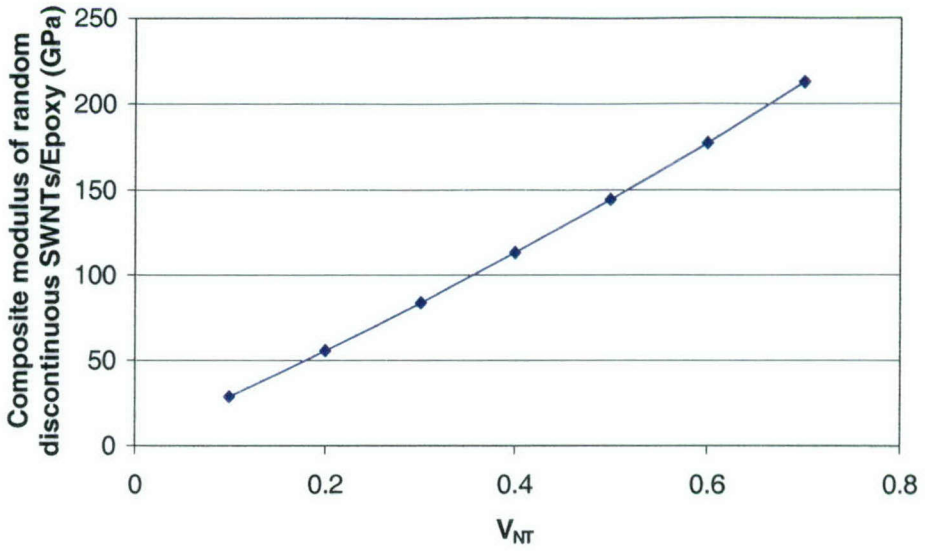

Figure 5.7 E_{CR} vs. nanotube volume fraction (V_{NT}) of random individually dispersed SWNT nanocomposites

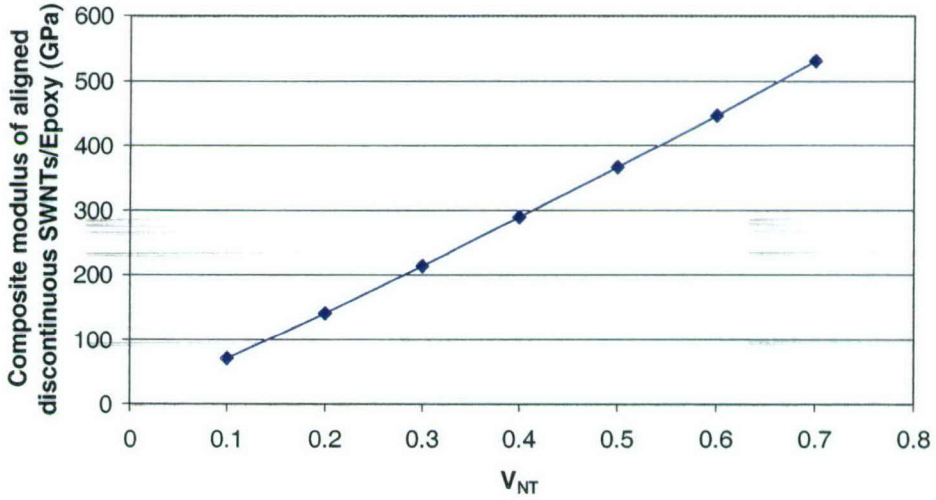

Figure 5.8 E_{CR} vs. nanotube volume fraction (V_{NT}) of aligned individually dispersed SWNT nanocomposites

5.3.3. Properties of SWNT rope-reinforced nanocomposites

The predicted properties of individually dispersed SWNT-reinforced nanocomposites are exceptionally high compared to our current experimental results and available data in literature. SWNTs usually form ropes or bundles in the buckypapers and composites, as shown in Figures 2.2, 2.5 to 2.6. Figures 2.14, 2.15, 4.7 and 4.25 show the oriented

nanotube ropes in the magnetically aligned buckypaper and its composites, respectively. The diameter of these ropes varies from 20 to 100 nm. Due to self-assembly phenomena of the ropes, SWNT ropes appear to be endless in microscopic images for both buckypapers and nanocomposites (see Chapters 2, 3 and 4).

The reported mechanical properties of the nanotube ropes are far less than that of individual SWNTs due to the possible slippage and structural defects existing in the ropes [1]. Salvetat *et al.* experimentally measured the modulus of SWNT ropes using AFM. The results, shown in Figure 5.9, indicate that the moduli of tube ropes dramatically decreased as the rope diameters increased. Therefore, the actual SWNT rope properties should be able to predict the mechanical properties of the SWNT buckypaper-reinforced nanocomposites.

Based on the observations of SWNT rope geometry in the buckypaper and composites (See Chapters 2, 3 and 4), the diameter of the ropes was assumed to be 20 nm, and from Figure 5.9, the modulus for a 20 nm rope diameter was 67GPa ±50%. These values were used to re-calculate the nanocomposite properties based on equations 5.1~5.5. The predicted results of both the random and aligned nanotube SWNT rope-reinforced nanocomposites are provided in Figures 5.10 to 5.13. The predicted results were compared with experimental results for validation.

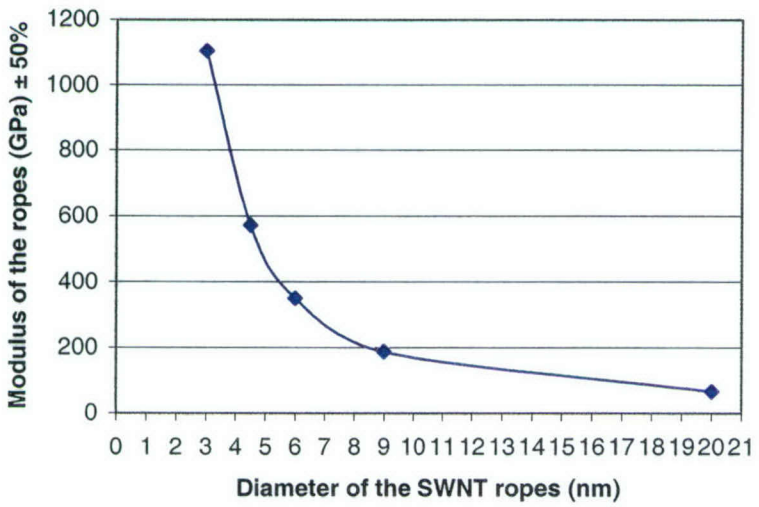

Figure 5.9 Modulus decreases with increase of SWNT rope diameters [1]

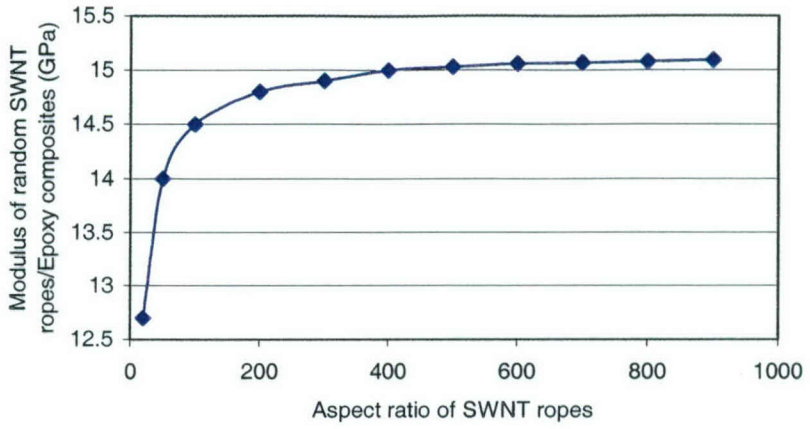

Figure 5.10 E_{CR} vs. tube rope aspect ratio of random SWNT rope/epoxy nanocomposites

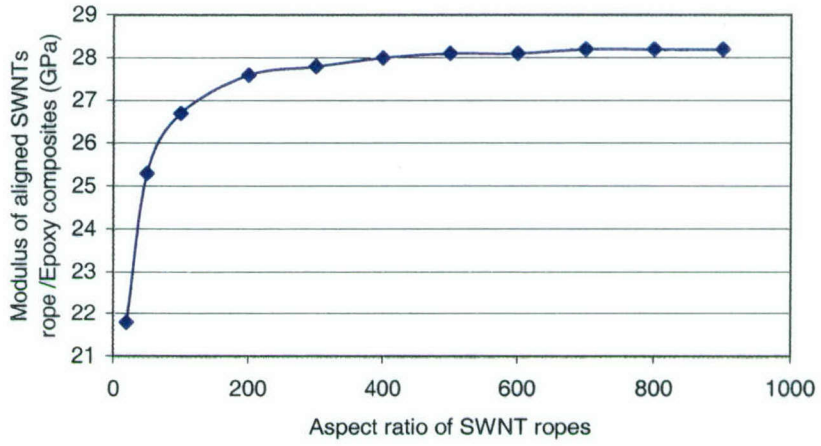

Figure 5.11 E_{CR} vs. tube rope aspect ratio of aligned SWNT rope/epoxy nanocomposites

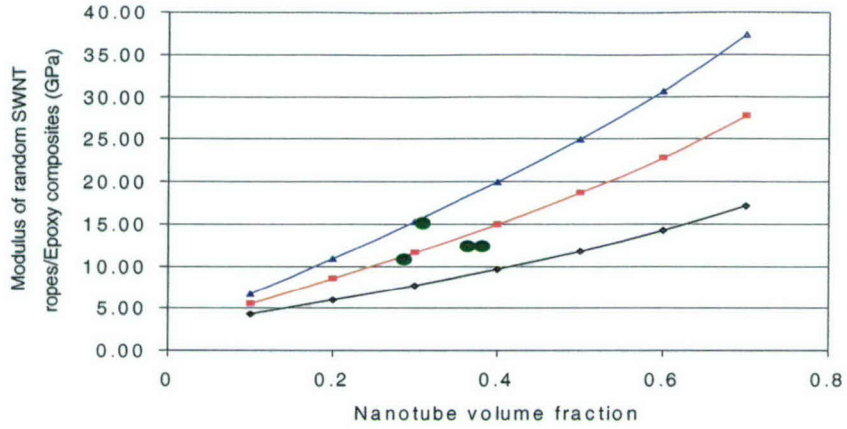

Figure 5.12 E_{CR} vs. nanotube volume fraction of random SWNT rope nanocomposites

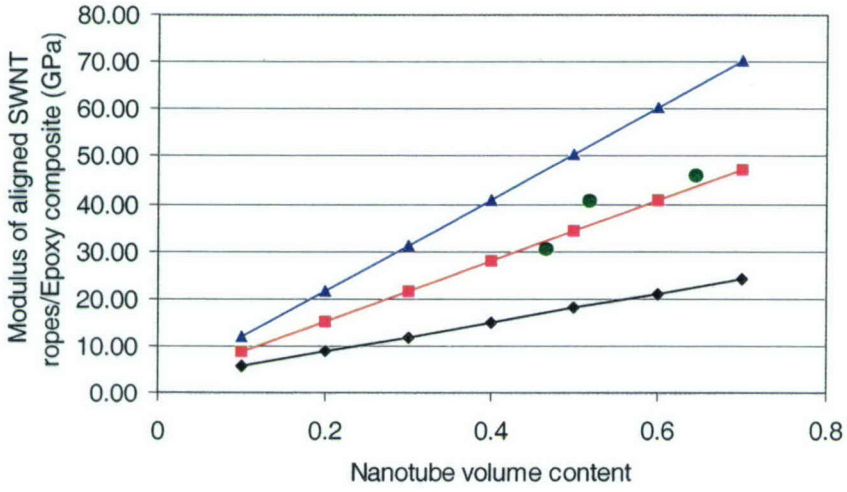

Figure 5.13 E_{11} vs. nanotube volume fraction of aligned SWNT rope nanocomposites

Figures 5.10 and 5.11 show the composite moduli of the random and aligned SWNT ropes/epoxy increased with respect to increase in aspect ratio, where the rope volume content was 40%. The results show that the composite modulus remained nearly constant for both random and aligned discontinuous SWNT ropes/epoxy composite after the rope aspect ratio reached 400. Hence, for subsequent calculations, the length of the nanotube ropes was chosen to be 8 μm since the ropes appear endless in the available microscope images for the buckypapers and their composites. However, the rope length is believed to be significantly less than the size of the nanocomposites used in the project (25-47 mm in diameter). Therefore, the discontinuous reinforcement models of 8 μm rope length were used to predict the upper-boundary properties of the buckypaper composites. Figures 5.12

and 5.13 show an almost linear increase in modulus of random and aligned SWNT ropes/epoxy composites with respect to an increase in nanotube weight content. Furthermore, considering the large variation of the measured properties of SWNT ropes [1], the upper-boundary (upper line), middle (middle line) and lower-boundary (bottom line) composite properties are also shown in the Figures by using 110.5, 67.0 and 33.5 GPa modulus of the SWNT ropes in the prediction, respectively.

5.3.4. Comparison of the predicted and experimental results

Unlike the direct mixing of nanotubes in the resin, the buckypaper/resin infiltration process can produce nanocomposites with uniform nanotube dispersion and high tube loading. More importantly, the desired in-plane nanotube alignment in the nanocomposites was achieved by using the aligned buckypapers made in high magnetic fields. The experimental results of the storage moduli of both random and aligned buckypaper nanocomposites listed in Tables 5.1 and 5.2 are also shown in Figures 5.12 and 5.13, respectively. The dots in Figures 5.12 and 5.13 represent the actual experimental values of the random and aligned buckypaper/epoxy nanocomposite moduli. These storage modulii were tested with a DMA 2980, using the tensile mode at 1 Hz frequency, which was close to the Young's moduli testing condition for the nanocomposites. The aligned samples were tested in the direction of tube alignment. Since the density of the SWNT ropes was close to that of the neat resin, it was assumed that the rope volume content fraction was the same as the weight fraction in the produced composite samples. It can be seen that the predicted results agreed well with the experimental results, which indicates that the formation of SWNT ropes in the composites has a significant influence on the mechanical properties.

5.4. Thermal Conductivity of Buckypaper and Buckypaper Nanocomposites

SWNTs have exceptionally high mechanical properties and thermal conductivity. For example, MD simulations revealed that the thermal conductivity of SWNTs could be as high as 6600 W/mK at room temperature. Many scientists and researchers believe that SWNTs are among the most promising reinforcement materials or functional agents for developing high performance structural and multifunctional nanocomposites. Strong

interests exist in developing high thermal conducting nanomaterials using SWNTs [4-12]. Due to the highly anisotropic nature of nanotube thermal conductivity, existing manufacturing techniques cannot effectively produce controlled nanotube alignment in SWNT nanocomposites, which is critical for developing SWNT-based thermal conducting materials.

In the buckypapers and buckypaper-reinforced nanocomposites, SWNTs can form dense networks (see Chapter 2, 3 and 4). Therefore, a high thermal conductivity is expected. Particularly, in-plane tube alignment and high tube content can be achieved in magnetically aligned buckypaper-reinforced nanocomposites, which are important for developing high performance thermal management materials using SWNTs. In this project, thermal conductivity of both magnetically aligned buckypapers and their composites were measured using a comparative method. The results were analyzed, and two models were studied to predict the thermal conductivity of the nanocomposites. These results provide a deeper understanding on thermal properties of both buckypapers and their nanocomposites.

Dr. Smalley's group first investigated the thermal properties of buckypaper materials [12-14]. Hone *et al.* measured the thermal conductivity of random and aligned buckypapers. They observed a quasi-linear temperature relationship of the buckypaper thermal conductivity from 50 K to room temperature. In this project, the research team measured the thermal conductivity of the large buckypapers and nanocomposites described in Chapters 2, 3 and 4.

5.4.1. Fixture of the measurements

The thermal conductivity of the produced buckypapers and nanocomposites was measured using a comparative method. This method can be used for evaluating materials with moderate to high conductivity (between 0.02 and 250 W/mK) and requires very small samples. The method conforms to ASTM E1225-99: Standard Test Method for Thermal Conductivity of Solids by Means of the Guarded-Comparative-Longitudinal Heat Flow Technique.

Figure 5.14 shows the schematic of the comparative method. The principle of the measurement lies with passing the heat flux through a known sample and an unknown sample and comparing the respective thermal gradients, which are inversely proportional to their thermal conductivities. Typically, the measured sample is sandwiched between two known samples, known as the references, to further account for heat losses that are difficult to eliminate during measurement.

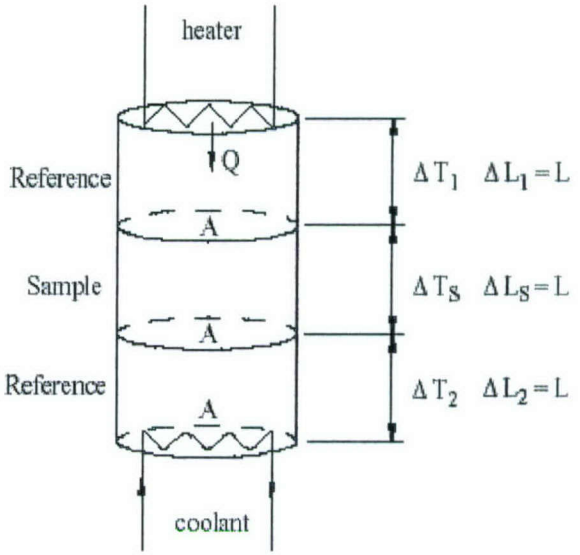

Figure 5.14 Schematic of the comparative method principal

The following equation was used to calculate the sample thermal conductivity,

$$\frac{Q}{A} = K_S \frac{\Delta T_S}{L} = K_R \frac{\Delta T_1 + \Delta T_2}{2} \frac{1}{L} \tag{5.9}$$

where K_S is the thermal conductivity of the sample and K_R the thermal conductivity of the references.

The reference used is constantan. The material, purchased as a foil made by Goodfellow, was selected according to the geometry of the buckypapers. Its thickness was 0.02 mm, which is comparable with the thickness of buckypapers. The composition of this alloy

was Cu55/Ni45. The thermocouples, purchased from Omega, were realized from chromel and constantan wires with a diameter of 0.0005 inch (0.0127 mm).

Figure 5.15 shows the fixture design used for the measurements. Several improvements in the fixture were needed to decrease the signal noise and the heat loss by radiation across the sample. A rectangular piece of copper was used as support for the experiment and to control the temperature of the fixture. Isolated wires were fixed on the rectangular support to provide the electricity for the heater of the sample and collect the voltage produced by the different thermocouples. The heater was a small chip resistor suspended in the air by the wires on which it was connected at one end of the rectangular piece of copper.

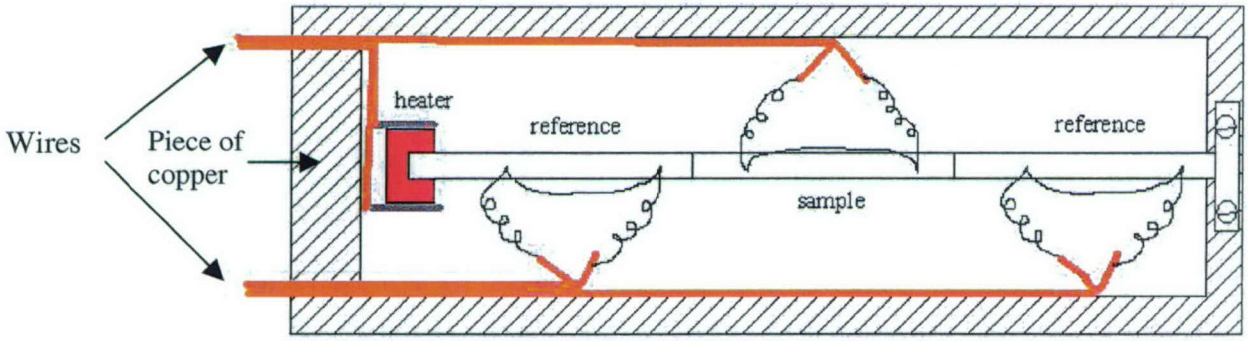

Figure 5.15 Schematic of the fixture

To measure the temperature dependence of the sample, a system to control the sample temperature was developed based on the cold finger technique. A copper rod with a diameter close to the size of the fixture width was screwed on the fixture to maintain a large contact surface between the cold finger and the fixture, as shown on Figure 5.16. GE Vanish, a manganin heater wire, was pasted on a copper rod. A small hole was drilled in the copper rod to place a thermometer and estimate the temperature of the fixture. To reduce heat loss, the cold finger was placed on the side of the heater. The temperature of the cold finger was assumed to be the same as the temperature of the fixture due to the high conductivity of copper. After the time required to reach thermal equilibrium, the Manganin wire was plugged with the thermometer to a temperature controller. The

temperature controller set the current in the manganin wire to reach the temperature desired.

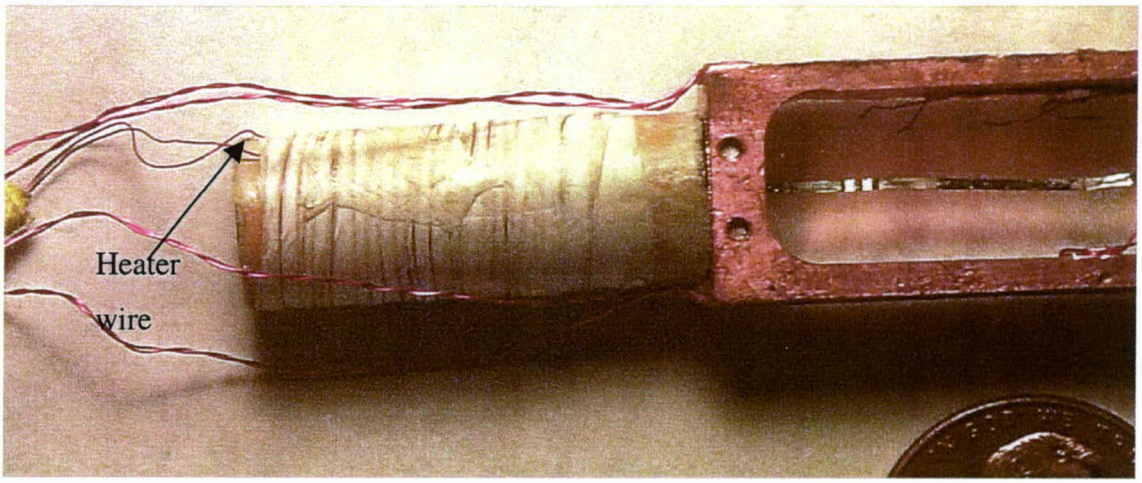

Figure 5.16 Cold finger for temperature control

The thermocouples were differential ones made with chromel and constantan wires of 0.0005 inch in diameter. The junction was made in a nitrogen atmosphere by electric contact with a gold foil. The set up is presented in Figure 5.17. Nitrogen was used to remove the oxygen and prevent oxidation during the melting of the junction. The wires were twisted together and the electric current was applied on the twist to melt it and ensure a good junction between the chromel and the constantan wires.

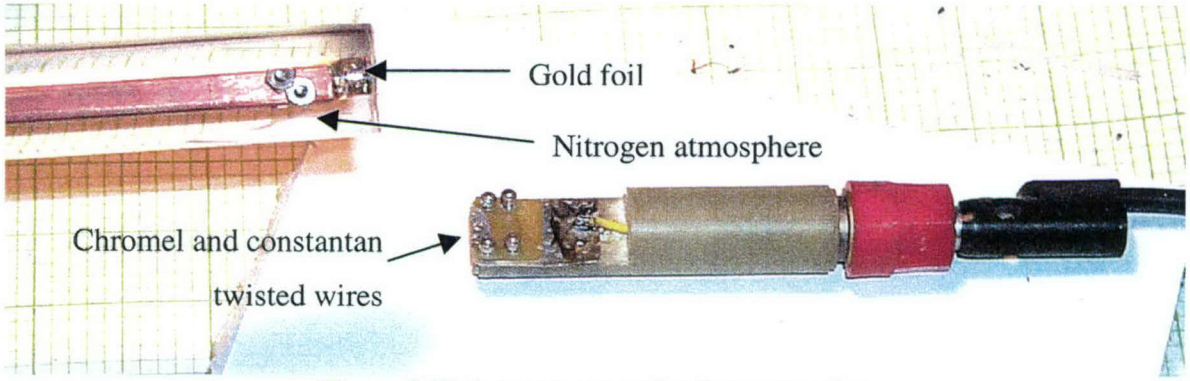

Figure 5.17 Apparatus to make thermocouples

A coil was formed on each wire after making the junction to increase the length of the wires and to decrease the space occupied by the thermocouples. The extremities of the thermocouples were then bonded by silver paste on the wires.

5.4.2. Experimental setup

In the rectangular fixture support, the first reference was glued to the heater using the GE Vanish. The sample was then bonded on the other side of the reference using a thin layer of silver paste and a second reference was similarly bonded on the other end of the sample. The second reference was mechanically pressed at the end of a piece of copper to ensure a good thermal contact between the end of the reference and the fixture support. Since the cross section area was small due to the small thickness of the sample (around 0.008 mm^2 for the buckypaper samples), the contact between the reference and the sample was achieved on the sample surface using diluted silver paste to ensure the conduction of heat flow, as shown in Figure 5.18. The surface contact was considered large enough when the contact surface was at least 10 times bigger than the cross section area.

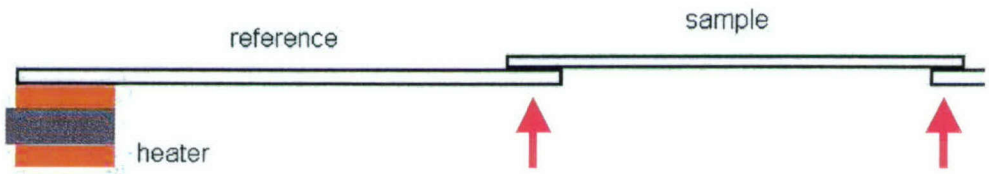

Figure 5.18 Schematic of the contact between sample and references

Since the reference and the sample were electrically conductive, some electrical isolation was required between the material and the thermocouples. If electrical contact occurred between the junctions of the thermocouples, the electrical signal produced by the difference of temperatures between the two junctions would change and the measurements would be impossible. For the reference, a layer of thermal epoxy with high thermal conductivity was applied on the surface where the junctions of the thermocouples were bonded. For the sample, a layer a GE Vanish was similarly applied. The junctions were placed on the reference and the sample so that the distance between the junctions of the thermocouples was almost the same for each thermocouple. As the contact between the reference and the sample were on the surface, the junction was placed some distance from the contact in the direction of the heat flow, as shown in Figure 5.19.

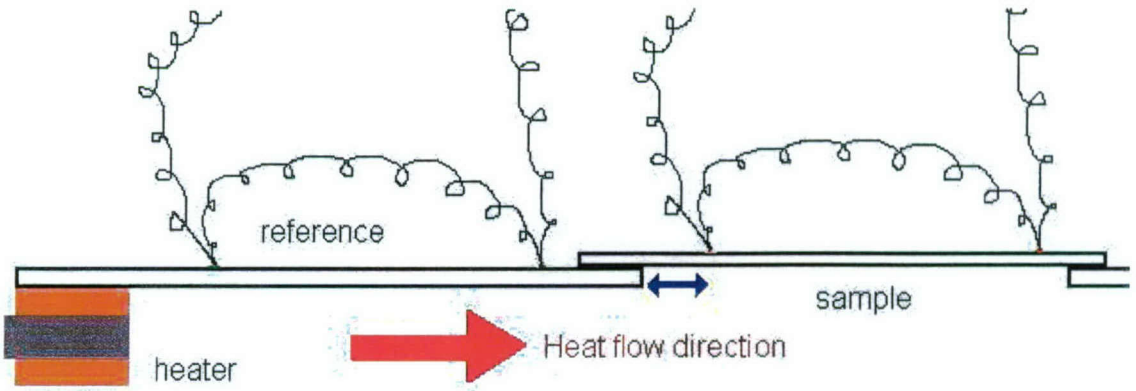

Figure 5.19 Schematic of thermocouples on sample and references

5.4.3. Radiation shield

The last component of the fixture was the radiation shield. A thermal shield of a high conductive polymer sheet was rolled around the fixture to decrease the heat loss. The shield was held on the fixture with Teflon tape, as shown in Figure 5.20. The radiation shield was positioned after the setup of the experiment since it enclosed the fixture. The wires were then connected to a probe, and the probe was sealed in a vacuum can.

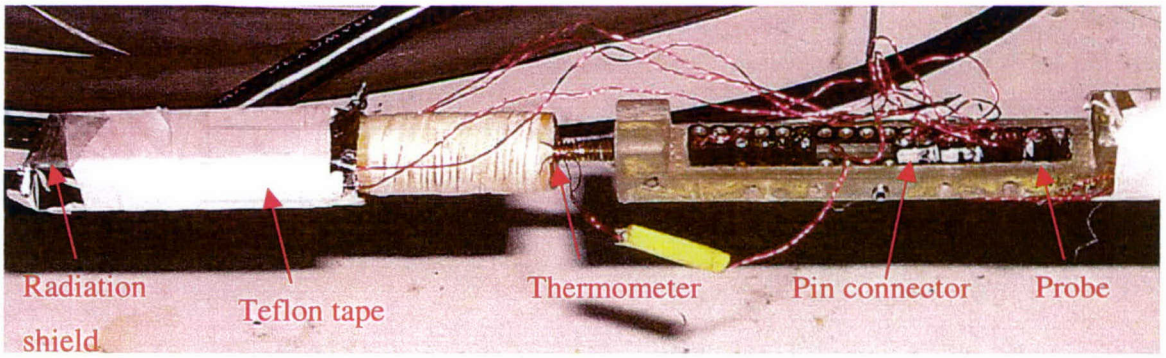

Figure 5.20 The fixture with thermal shield plugged on the probe

Finally, the thermocouples and the heater were plugged into the probe with pin connectors, and the signals were carried to the instruments. The signal from the thermocouples was measured by nanovoltmeters as their voltage required a precision of 10 nV. The heater on the fixture support was powered with a programmable power supply, and the heater of the cold finger and its thermometer was connected to the temperature controller. All instruments (nanovoltmeters, power supply and temperature

controller) were also connected to the computer with GPIB cables and were used with a LabView program to conduct the experiment control.

5.4.4. Experimentation

Before conducting the experiment, the GE Vanish applied to bond the thermocouples on the sample has to be completely dry. In natural conduction, the curing time is 6 hours. However, to reduce the time needed for each experiment, the fixture was placed under the heat of a light bulb for one hour.

After checking the thermocouples bonds, the fixture was heated using the cold finger to 50°C for 30 minutes. The vacuum was set with a diffusion pump that could reach 10^{-6} torr. Upon reaching room temperature, measurements were taken. The LabView program monitored the voltage of the thermocouples. Measurements were taken at a number of current increase steps: a current step was applied to the heater on the reference in order to create a temperature difference between each end of the reference. This temperature difference can be interpreted as a heat flow that was conducted from the first reference, to the sample and then to the second reference, which was kept at a constant temperature by contact with the fixture. After a time step of few seconds, the equilibrium should have been reached, and the voltage produced by each thermocouple was taken to produce a point in the measurement. The measurements were in a steady state, since the equilibrium was reached before the value was saved. Once the values were saved, a step was added to the current applied to the heater on the reference to increase the temperature of the heater. The current step was a parameter on LabView that was sent on the programmable power supply until the temperature maximum was reached. Another heat flow was again produced and a second set of values was saved to make a point in the measurements. This cycle continued until the sum of difference of temperatures reached a defined maximum temperature. The current step and the maximum temperatures were related parameters. They both contributed to the number of measurements for each test. The current step had to be large so that the temperature difference was large enough for a measurement in the experiments, as shown in Figure 5.21. However, if the current step was too high, the temperature maximum would be reached in two or three steps. A good measurement must

contain five to ten sets of values that are averaged to register data points in the test. When the maximum temperature was reached, the thermal conductivity was computed according to the comparative technique. The heat flow taken into account for the sample was the average of the heat flow measured on each reference to estimate the heat loss. This assumption was possible by keeping the same distance for each thermocouple with the same geometry and lengths for the references and the samples.

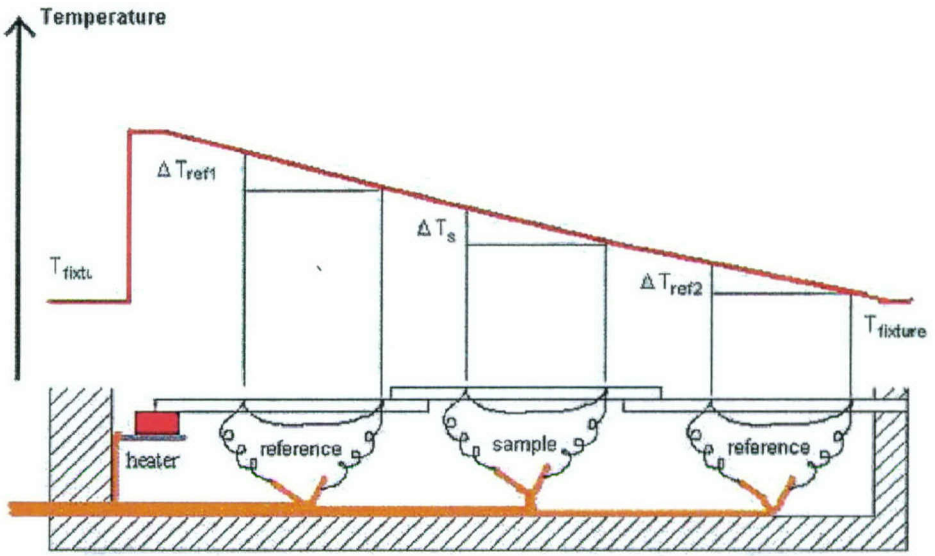

Figure 5.21 Schematic of heat loss during a measurement

5.4.5. Measurement analysis

The first measurements were taken at room temperature by keeping the vacuum can at ambient temperature (circled in Figure 5.22). The vacuum can was then dipped into liquid nitrogen and the temperature was set with the temperature controller. The time to set the temperature was kept long enough to ensure stability in the temperature, varying from 20 minutes to 90 minutes for lower temperatures, where cooling took longer as the difference of temperature between liquid nitrogen and the fixture decreased.

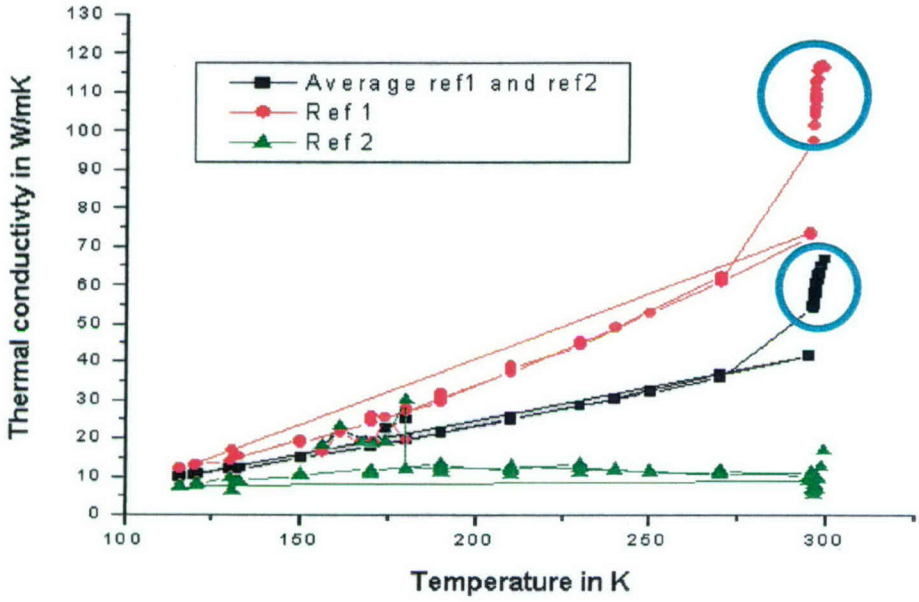

Figure 5.22 Temperature dependence of the thermal conductivity for buckypaper in the aligned direction

The values presented in Figure 5.22 are the results for an aligned buckypaper in the aligned direction. The aligned buckypapers were made with a 17.3 T using a suspension concentration of 20 mg/L and Triton X100 as the surfactant. The buckypaper thickness was 0.02mm. Three sets of values represent the thermal conductivity of the sample calculated using the heat flow measured on the first reference, the heat flow measured on the second reference and an average of the heat flow of both references. The points represent the actual values measured and the lines join at the point in the consecutive order of measurement. The first measurements are the circled values at room temperature. Then the vacuum can was dipped in the liquid nitrogen and the temperature was set at 270K. The measurements continued during cooling by different steps in temperatures until 120K and then a value at room temperature was measured by heating the fixture with the cold finger to 300K. The last value was the correct value for room temperature, since it matched the linear temperature dependence described in the literature.

The difference between the values of reference 1 and reference 2 represents the heat losses. Their values decreased with temperature, which proved that these losses are due to

radiation. As the temperature of the fixture was closer to the temperature of liquid nitrogen, the radiation decreased. This system was particularly sensitive to radiation because of the high surface to volume ratio, due to the small thickness of the samples. The average value is the one that is to be kept as the measured value of the thermal conductivity of all the samples in this project.

5.4.6. Results and analysis

The thermal conductivity test results of the buckypaper and buckypaper/epoxy nanocomposites are presented in Figure 5.23. As expected, the thermal conductivity of the aligned buckypaper in the alignment direction was the highest at all temperatures. The thermal conductivity of the random buckypaper and the aligned one in the perpendicular direction are in the same order, although a higher value for the random could have been expected. This may be the result in the difference of the sample, such as the quality of the nanotubes or the size of the ropes or even some local variations in the buckypaper since the size of the samples are very small. The linear temperature dependence is more obvious for the aligned direction and the random buckypapers than for the perpendicular direction where a curvature in the values is visible.

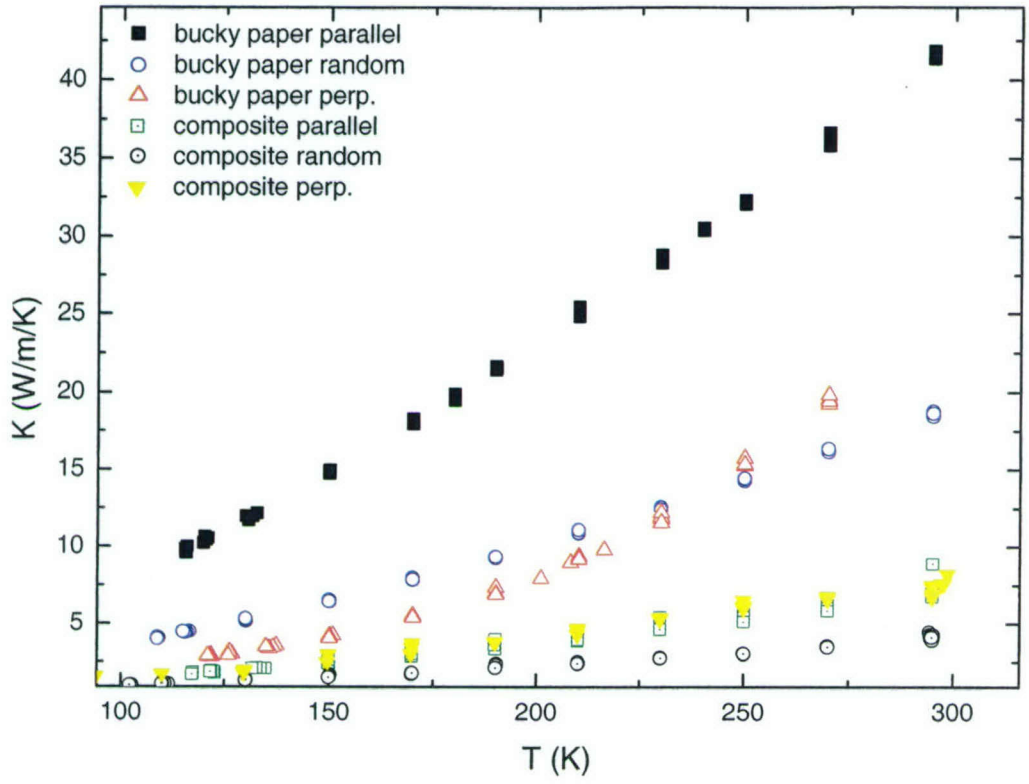

Figure 5.23 Thermal conductivities and temperature dependence of buckypapers and buckypaper composites

The buckypaper thickness was 0.02 mm, while the composite was 0.15 mm for the aligned nanocomposites samples and 0.2 mm for the random one. As expected, the thermal conductivity along the SWNT aligned direction of the magnetically aligned buckypaper provides the highest value and resembles the results of Fisher *et al.* We observed the same quasi-linear temperature relationship of the buckypaper thermal conductivity from 100K to room temperature. However, the temperature dependence of the aligned buckypaper in the perpendicular direction does not show the same monotonic dependence, but rather, exhibits an upturn in the slope at 200K. We also noticed that the buckypaper composite samples present the same quasi-linear temperature dependence, which may be due to the fact that the epoxy has a very low thermal conductivity that remains stable between 100K and room temperature. This may also suggest that the matrix does not influence the thermal transport across the buckypaper in the composites.

For the aligned composites, it appears that the values in the aligned and perpendicular directions are the same. This can be explained by the fact that the samples come from different composites (A-4-6C for the aligned direction and A-4-3C for the perpendicular direction) and may have different microstructures. The characteristics of the composite samples are listed in Table 5.3. This difference of results was already observed in the measurement of the storage modulus by DMA. A-4-6C has a storage modulus of 40 GPa, while A-4-3C has only 18 GPa.

Table 5-3 Characteristics of aligned nanocomposite samples

Name	Magnetic strength for the buckypaper	SWNT weight fraction	Storage modulus in the alignment direction (GPa)
Composite parallel	17.3	54.5 %	40
Composite perpendicular	17.3	47.9 %	18
Random composite	0	25 – 31 %	10~15

The measurements for the aligned buckypaper in the aligned and perpendicular direction came from the same buckypaper. The anisotropy for the composites was insignificant, but the anisotropy ratio for the buckypaper was calculated with the ratio of the thermal conductivity in the aligned direction by the value in the perpendicular direction, as shown in Figure 5.24. This anisotropy ratio was lower than expected and decreased as the temperature increased. This phenomenon agrees with the trend observed on the thermal conductivity of the buckypaper in the perpendicular direction. If this trend is the result of some heat loss, then the actual anisotropy of the sample is measured at the lower temperature where the heat losses are less important. The anisotropy was then 3.5 and less than half the measured value for that of the electrical conductivity reported in Chapter 4.

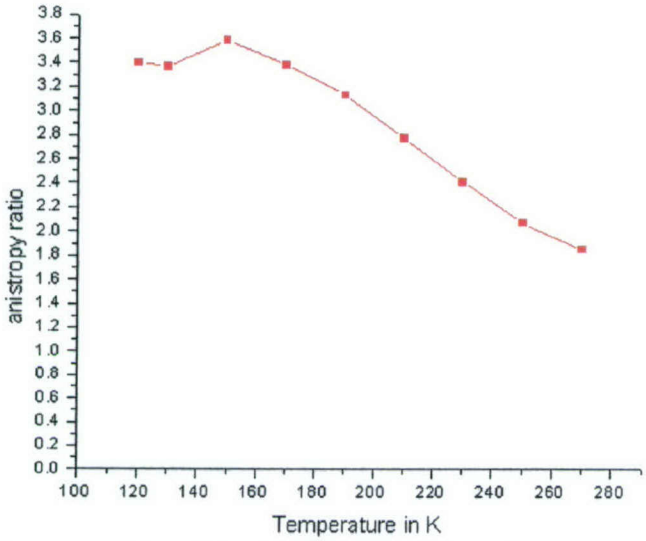

Figure 5.24 Anisotropy ratios of the thermal conductivity for the aligned buckypaper

5.4.7. Temperature dependence

To compare the temperature dependence of all samples, the values were normalized by their thermal conductivity at 270K. This temperature was chosen since the conductivity was higher at room temperature. The temperature dependence of the normalized thermal conductivity is presented in Figure 5.25. All samples, random or magnetically aligned buckypapers and nanocomposites, have almost the same quasi-linear relationship with temperature, except for the measurement of the aligned buckypaper sample in the perpendicular direction.

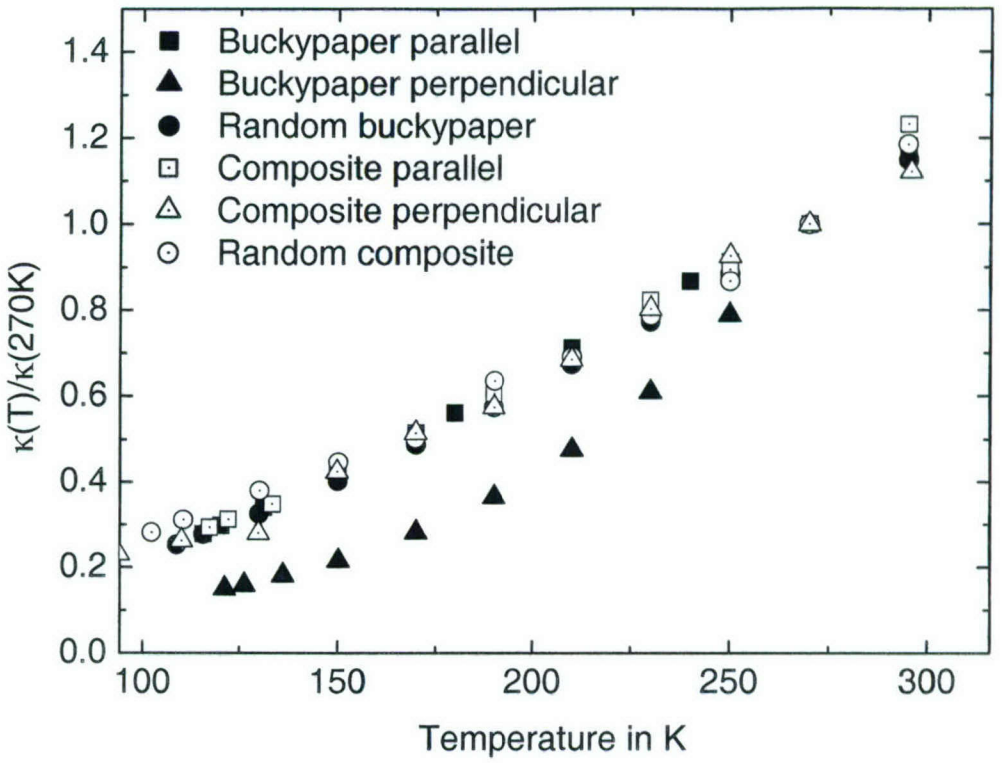

Figure 5.25 Normalized temperature dependence

Buckypapers and nanocomposites exhibited the same temperature dependence between 110K to room temperature, whether the nanotubes had been magnetically aligned or infused with resin. Only the absolute value of the thermal conductivity differed between them. So far, we can estimate the thermal conductivity of any buckypaper or buckypaper composite sample between 100K and room temperature from a single reading in this temperature range. The temperature dependence was characterized by fitting a polynomial in temperature T to an average of the quasi-linear regressions for all samples (except for the perpendicular thermal transport result), as shown in the following equation:

$$\frac{\kappa(T)}{\kappa(270)} = 4.74 \cdot 10^{-3} \times \mathrm{T} - 2.82 \cdot 10^{-1} \qquad (5.10)$$

where κ(T) is the thermal conductivity in W/mK, κ(270) is the value of the thermal conductivity at 270 K, and T is the temperature in Kelvin.

Equation 5.10 can be used to predict the thermal conductivity of buckypapers and buckypaper/EPON 862 composites from room temperature to 100K, with the measurement of the thermal conductivity at only one temperature.

5.4.8. Modeling and prediction

Several models were considered to describe the thermal conductivity of the buckypapers and their composites. Since the buckypapers formed a continuous SWNT network in the nanocomposite, the Rule of Mixture (Equation 5.11) could provide a good prediction.

$$\kappa_n = V_{SWNT}\kappa_b + (1 - V_{SWNT})\kappa_e \tag{5.11}$$

where κ_n is the thermal conductivity of the nanocomposite, κ_b is the thermal conductivity of the buckypaper used for the composites, κ_e is the thermal conductivity of the matrix, and V_{SWNT} is the volume fraction of SWNT in the composite.

The predicted results are shown in Figures 5.26 and 5.27 for random buckypaper-reinforced and aligned buckypaper-reinforced nanocomposites. However, this model apparently overestimates the thermal conductivity of the nanocomposites, especially for the aligned samples. This may be due to the negative effects of the nanotube contact with epoxy resin.

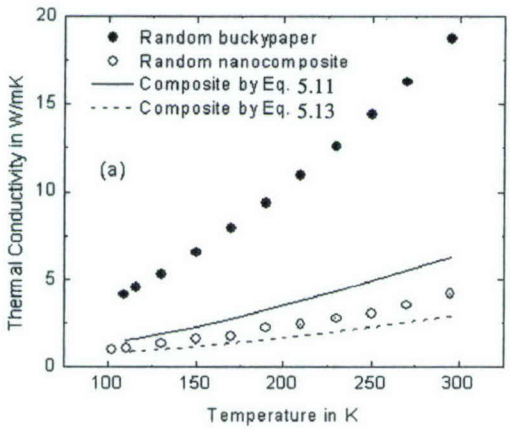

Figure 5.26 Thermal conductivity of the random buckypaper, its nanocomposites and model predictions

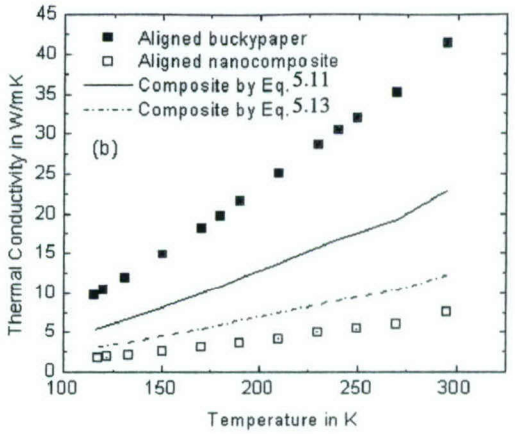

Figure 5.27 Thermal conductivity of the aligned buckypaper in the alignment direction, its nanocomposite and model predictions

The model for randomly oriented nanotubes in a composite presented by Nan et al. was also considered [15]:

$$K_n = \frac{3K_e + V_{SWNT}K_{SWNT}}{3 - 2V_{SWNT}} \tag{5.12}$$

where κ_{SWNT} is the thermal conductivity of an individual nanotube.

Even though this model was designed to predict the thermal conductivity of randomly dispersed nanotubes in a matrix, a modified form was considered to attempt to model the buckypaper composite behavior. The thermal conductivity (κ_{SWNT}) of isolated and individual nanotubes would greatly overestimate the conductivity of the resultant composite. The large interface-resistance to heat flow and interfacial contact in SWNT nanocomposites may explain the overestimation previously reported [4,36]. These effects could be taken into account by using the thermal conductivity of the buckypaper, since some tube-tube contact and interface resistance are already taken into account in the buckypaper thermal properties. Therefore, κ_{SWNT} is changed to κ_b in Equation 5.12 to obtain the following modified model:

$$K_n = \frac{3K_e + V_{SWNT}K_b}{3 - 2V_{SWNT}} \tag{5.13}$$

This model predicts a lower thermal conductivity than the simple Rule of Mixture model and more closely follows the experimental results.

In Figures 5.26 and 5.27, the experimental data and predictions from the theoretical models are shown and compared for the random and aligned nanocomposites. For random composites, the experimental thermal conductivity values are between two different theoretical predictions, while those of aligned composites are smaller by a factor of two or four.

5.5. Conclusions

The produced randomly oriented buckypaper nanocomposites had a SWNT loading up to 39%. The storage moduli of the resulting composites were as high as 15Gpa, which were 429% higher compared to the neat resin modulus. The DMA results showed that the presence of SWNTs significantly affects the damping properties of the composites due to possible intensive molecular interactions between the nanotubes and resin molecules. The storage moduli of the magnetically aligned buckypaper nanocomposites can be as high as 45.0GPa, which is one of the highest reported values found in the literature data.

The mechanical properties of SWNT-reinforced/epoxy nanocomposites were predicted based on the composite models of both random and aligned discontinuous reinforcements. The predicted tensile moduli of individual dispersed and aligned SWNTs-reinforced composites were higher compared to conventional unidirectional carbon fiber composites. These predicted results were also much higher compared to the experimental data found in literature. Considering the formation of SWNT ropes in the actual nanocomposites, the mechanical properties of the nanotube rope-reinforced/EPON 862 resin nanocomposites showed that the predicted results agreed with the experimental ones for both random and aligned SWNT rope-reinforced nanocomposites, indicating that the formation of SWNT ropes in the composites has a significant influence on the mechanical properties.

In the magnetically aligned buckypaper, the thermal conductivity was relatively high (42 W/m/K at room temperature) along the tube alignment direction, with an anisotropy kpara/kperp ~ 3.5. However, in the buckypaper/epoxy nanocomposites, the thermal conductivity dropped significantly by almost an order of magnitude, and became comparable to the value for the non-aligned (randomly oriented) nanocomposite. We found that the temperature dependence of both buckypapers and their composite systems all follow a quasi-linear temperature dependence characteristic of phonon scattering, except for the case of thermal transport perpendicular to the tube alignment direction of the aligned buckypaper sample.

5.6. References

[1] J.-P. Salvetat, G.A.D. Briggs, J-M. Bonard, R.R. Bacsa, A.J. Kulik, T. Stöckli, N.A. Burnham and L. Forró, Elastic and Shear Modulus of Single-Walled Carbon Nanotube Ropes. *Physical Review Letters*, 1999;82(5):944.

[2] P. K Mallick, *Handbook of fiber reinforced composites*, Second Edition, Marcel Dekker Inc., 1998.

[3] R. B. Pipes, S-J. Frankland, P. Hubert, and E. Saether, "Self-Consistent Properties of the SWCN and Hexagonal Arrays as Composite Reinforcements," *Composites Science and Technology*, 63(10):1349, 2003.

[4] R. S. Ruoff, D. C. Lorents, "Mechanical and Thermal properties of carbon nanotubes," *Carbon*, Vol. 33, No. 7, 925-930, 1995.

[5] J. Hone, B. Batlogg, Z. Benes, A. T. Johnson, J. E, Fischer, "Quantized Phonon Spectrum of Single-Wall Carbon Nanotubes," *Science*, Vol. 289 8/9, 1730-1733 2000.

[6] S. Berber, Y.-K. Kwon, D. Tománek, "Unusually High Thermal Conductivity of Carbon Nanotubes," *Physical Review Letters*, Vol. 84, No. 20, 4613-4616, 2000.

[7] M. A. Osman, D. Srivastava, "Temperature dependence of th thermal conductivity of single-wall carbon nanotubes" *Nanotechnology* 12, 21-24, 2001

[8] E.T. Thostenson, Z.F. Ren and T.W. Chou, "Advances in the Science and Technology of Carbon Nanotubes and Their Composites: a Review," *Composites Science and Technology*, 61:1899, 2001

[9] K.T. Lau and D. Hui, "The Revolutionary Creation of New Advanced Materials-Carbon Nanotube Composites," *Composites Part B*, 33:263, 2002.

[10] M. J. Biercuk, M. C. Llaguno, M. Radosavljevic, J. K. Hyun, and A. T. Johnson and J. E. Fischer, "Carbon Nanotube Composites for Thermal Management," *Applied Physics Letters*, 20(15):15, 2002.

[11] R. Saito, G. Dresselhaus and M.S. Dresselhaus, *Physical Properties of Carbon Nanotubes*, Imperial College Press, London, 1998.

[12] J. Hone, M. Whitney, C. Piskoti, A. Zettl and R. E. Smalley, "Thermal conductivity of single-walled carbon nanotubes," *Physical Review B*, Vol.59, No. 4, 1999, 2514-16.

[13] J. Hone, M.C. Llaguno, N.M. Nemes, A. T. Johnson, J. E. Fischer, D. A. Walters, M. J. Casavant, J. Schmidt and R. E. Smalley, "Electrical and thermal transport properties of magnetically aligned single wall carbon nanotube films," *Applied Physics Letters*, Vol. 77, No. 5, 2000, 666-668.

[14] J.E. Fischer, W. Zhou, J. Vavro, M.C. Llaguno, C. Guthy, R. Haggenmueller, M.J. Casavant, D.E. Walters and R.E. Smalley, "Magnetically aligned single wall carbon nanotube films: Preferred orientation and anisotropic transport properties," *Journal of Applied Physics*, Vol. 93, No 4, 2003, 2157-63.

[15] C-W. Nan, Z. Shi, Y. Lin, "A simple model for thermal conductivity of carbon nanotube-based composites," *Chemical Physics Letters* Vol. 375, pp 666, 2003.

6. Molecular Dynamics Simulations of Molecular Interactions in Nanocomposite Processing and Composite Interface

When processing SWNT/epoxy nanocomposites, the liquid epoxy resin interacts with the nanotubes at nanoscale and intense molecular interactions can be expected. These interactions play critical roles in processing, determining nanostructures, as well as forming interface of final nanocomposites. This chapter reports on the molecular dynamics (MD) simulations conducted to examine and understand the molecular interactions in processing and interface of SWNTs/EPON 862 nanocomposites.

Good wetting between single-walled nanotubes (SWNTs) and resin matrix molecules is extremely important during SWNT/polymer composites processing and applications. Compared to fibers in conventional carbon fiber reinforced composites, SWNTs might be expected to have different wetting characteristics due to their considerably smaller diameters and curvature, extra-large surface area and unique electronic structure [1-4]. For example, Dujardin *et al.* [3] found that a given liquid material with the surface tension of 40-80 mJ/m would spread well on the surface of individual SWNT to achieve good wetting. According to this result, most of liquid polymeric resins used in conventional carbon fiber composite processing with a surface tension of 30-60 mJ/m [5, 6] should result in good wetting with SWNTs. In a number of efforts for developing nanotube composites, both epoxy resins and thermoplastic polymers were used as the matrix polymers to produce both MWNT and SWNT composites [7-12]. However, these studies have shown that the current nanotube-based composites do not demonstrate their much-anticipated performance. In recent research cases, the surfaces of the pullout nanotubes or nanotube ropes from the polymeric composites were usually smooth and showed no signs of adhered resin remaining on the tube surfaces. Poor wetting and interfacial bonding are among the major technical issues for developing nanotube-reinforced composite materials. Unfortunately, there is a lack of fundamental understanding of nanoscale wetting and interfacial bonding mechanisms between SWNTs and resin molecules, due to the nanoscale dimensions involved, lack of effective test methods, as well as the high cost for experiments.

In this project, MD simulation investigated the molecular interactions in processing and interface of the SWNT/EPON 862 nanocomposites. The simulations were carried out using Materials Studio, a commercial software package developed by Accelrys, Inc. on a SGI–Octane 2 workstation. The molecular dynamics simulation was performed long enough to observe several cycles of thermal vibrations. The interval of each molecular dynamics simulation step was typically 1 or 2 femto seconds (fs). All calculations were carried out at the initial temperature 300K using NVT ensembles (constant number of particles, constant volume and constant temperature). A summary of the MD simulation conditions is listed in Table 6.1. The simulation results were also compared with our experimental observations and results in Chapters 2, 5 and 7.

Table 6-1 Conditions for the MD simulation setup

Simulation condition	Setup
Hardware	SGI-Octane 2
Software	Materials Studio 2.0
Force field	COMPASS
Time step	1 or 2 fs
Initial temperature	300 K
Ensemble	NVT

Molecular dynamics deal with the time-dependent processes of moving molecules. MD simulations evaluate the forces on a particle and use these forces to determine the particle's acceleration. A particle's initial velocity is usually determined by a random distribution according to the Maxwell-Boltzmann distribution at a given simulation temperature. Once an initial velocity is chosen, it is updated using the calculated accelerations. In a MD simulationa, the classic equations of motion are used to approximate the positions, velocities and accelerations of all the atoms and molecules.

$$\frac{dE}{dR} = m\frac{d^2R}{dt^2} \tag{6.1}$$

where E is the potential energy, R is the coordinates of atoms, and m is the mass of atoms. However, an analytical solution for the accelerations would be quite complicated for all but simple systems, so a numerical solution must be used.

At the heart of a MD simulation is the force field, which is the main set of approximations used to represent the molecular system examined. A force field is an analytical expression that gives the potential energy of a molecular system in terms of the atomic coordinates. The condensed phase optimization molecular potentials for atomistic simulation studies (COMPASS) module in the Materials Studio software was used to conduct force field computations. The COMPASS was parameterized, tested and validated for most of the common organic and inorganic materials [13-15]. This method was parameterized from *ab initio* computations of model compounds and optimized using condensed-phase properties of polymers and low-molecular-weight compounds.

The total potential energy calculated by the COMPASS can be broken down into the following terms:

$$E_{pot} = E_{valence} + E_{nonbond} \tag{6.2}$$

$$E_{valence} = E_{diagonal} + E_{coupling} \tag{6.3}$$

$$E_{diagonal} = E_{bond} + E_{angle} + E_{torsion} + E_{out-of-plane} \tag{6.4}$$

$$E_{nonbond} = E_{elec} + E_{vdW} \tag{6.5}$$

The valence component, $E_{valence}$, is decomposed into diagonal terms, $E_{diagonal}$, and the off-diagonal cross coupling terms, $E_{coupling}$. The diagonal terms, $E_{diagonal}$, can be further decomposed into the bond stretching energy, E_{bond}, angle energy, E_{angle}, torsion energy, $E_{torsion}$, and out-of-plane deformation energy, $E_{out-of-plane}$, given as follows:

$$E_{bond} = \sum_{b} \left[{}^{2}K_b (b - b_0)^2 + {}^{3}K_b (b - b_0)^3 + {}^{4}K_b (b - b_0)^4 \right] \tag{6.6}$$

$$E_{angle} = \sum_{\theta} \left[{}^{2}K_\theta (\theta - \theta_0)^2 + {}^{3}K_\theta (\theta - \theta_0)^3 + {}^{4}K_\theta (\theta - \theta_0)^4 \right] \tag{6.7}$$

$$E_{torsion} = \sum_{\phi} \left[{}^{1}K_\phi (1 - \cos\phi) + {}^{2}K_\phi (1 - \cos 2\phi) + {}^{3}K_\phi (1 - \cos 3\phi) \right] \tag{6.8}$$

$$E_{out-of-plane} = \sum_{\chi} K_\chi \chi^2 \tag{6.9}$$

where ${}^{2}K$, ${}^{3}K$, ${}^{4}K$ are the quadratic, cubic and quartic force field parameter or force constant, respectively. For this equation, b is the bond length, b_0 is the reference value of the bond length, θ is bond angle, θ_0 is the reference value of the bond angle, ϕ is the torsion angle, and χ is an out-of-plane coordinate.

The off-diagonal cross coupling terms $E_{coupling}$ includes bond/bond, bond/angle, angle/angle, angle/torsion, central bond/torsion and terminal bond/torsion interactions:

$$\begin{aligned} E_{coupling} = & \sum_{b} \sum_{b'} K_{bb'} (b - b_0)(b' - b_0) \\ & + \sum_{b} \sum_{\vartheta} K_{b\theta} (b - b_0)(\theta - \theta_0) \\ & + \sum_{b} \sum_{\phi} K_{b\phi} (b - b_0)[F^{1}_{b\phi} (\cos\phi) + F^{2}_{b\phi} (\cos 2\phi) + F^{3}_{b\phi} (\cos 3\phi)] \\ & + \sum_{\theta} \sum_{\theta'} K_{\theta\theta'} (\theta - \theta_0)(\theta' - \vartheta_0') \\ & + \sum_{\theta} \sum_{\phi} (\theta - \theta_0)(F^{1}_{\theta,\phi} \cos\phi + F^{2}_{\theta,\phi} \cos 2\phi + F^{3}_{\theta,\phi} \cos 3\phi) \\ & + \sum_{\theta} \sum_{\theta'} \sum_{\phi} (\theta - \theta_0)(\theta' - \vartheta_0')(\phi - \phi_0) \end{aligned} \tag{6.10}$$

$E_{nonbond}$ is the nonbond energy between atoms in different molecules or between atoms separated by three or more bonded atoms, which is given by the sum of the Coulumbic

electrostatic interaction E_{elec} and the van der Waals energy E_{vdW} of the Lennard-Jones 9-6 function.

$$E_{elec} = \sum_{i,j} \frac{q_i q_j}{r_{ij}} \tag{6.11}$$

$$E_{vdW} = \sum_{i,j} \varepsilon_{ij} \left[2\left(\frac{r_{ij}^{\,0}}{r_{ij}}\right)^9 - 3\left(\frac{r_{ij}^{\,0}}{r_{ij}}\right)^6 \right] \tag{6.12}$$

where q_i and q_j are the atomic partial charges on atoms i and j, and r_{ij} is the distance between them. ε_{ij} and $r^0{}_{ij}$ are the negative of the minimum van der Waals energy and that distance between atoms i and j where the minimum occurs, respectively.

From the viewpoint of computational cost, nonbond interactions involve extensive calculations. To avoid heavy computations, some approximation methods are used to save computational expenses without sacrificing accuracy. For calculating the van der Waals interactions, an appropriate combination rule was used to improve computational efficiency. Any van der Waals interaction parameters that are actually defined for the heterogeneous atom pairs are called off-diagonal parameters. Off-diagonal parameters that are not available for such atom pairs are calculated by averaging those for each of the two atom types using the 6th-power combination rule. In the simulation, ε_{ij} and $r^0{}_{ij}$ are computed from the individual atomic parameters ε_i, ε_j, $r^0{}_i$ and $r^0{}_j$ by the Waldman-Hagler combination rules.

$$r^0{}_{i,j} = \left(\frac{\left(r^0{}_i\right)^6 + \left(r^0{}_j\right)}{2} \right)^{\frac{1}{6}} \tag{6.13}$$

$$\varepsilon_{i,j} = 2\sqrt{\varepsilon_i \cdot \varepsilon_j} \left(\frac{\left(r^0{}_i\right)^3 \cdot \left(r^0{}_j\right)^3}{\left(r^0{}_i\right)^6 + \left(r^0{}_j\right)^6} \right) \tag{6.14}$$

Meanwhile, the energy summation has a significant dependence on the number of atoms in the system. To reduce the computational efforts, nonbond interactions are simply calculated to a cutoff distance and interactions beyond this distance are ignored. In the simulations, the nonbond interaction was considered within a cutoff distance of 10 Å. The nonbond interaction beyond 10 Å was insignificant for the molecular system.

6.1. Single-walled Carbon Nanotubes

The calculation of potential energy of SWNTs/epoxy molecules requires the geometric model of a single-walled carbon nanotube, where the coordinates of atoms are known. Based on the coordinates of atoms, the bond and non-bonded distances and angles can be calculated. Meanwhile, the connection of atoms in the model also represents the chemical nature of the SWNT, which is used to determine some parameters in the potential energy model. This section describes the molecular model of SWNTs and force field atom type.

6.1.1. Molecular model of the single-walled nanotube

A SWNT can be described as a conformational mapping of a graphene sheet into a cylinder subjected to periodic boundaries both around the cylinder and along its axis. The geometry of a SWNT is determined by the chiral vector C_h, transnational vector $\mathbf{T}$, and symmetry vector $\mathbf{R}$. If the set of primitive lattice vector $\boldsymbol{\alpha}_1$ and $\boldsymbol{\alpha}_2$ are introduced, then $\mathbf{C}_h$ can be expressed as:

$$\mathbf{C}_h = n\boldsymbol{\alpha}_1 + m\boldsymbol{\alpha}_2 \equiv (n, m) \tag{6.15}$$

Each carbon nanotube can be labeled as a pair of integers (n, m). Various helical structures are possible, such as numerous different chiral, "Zigzag" $\mathbf{C}_h = (n, 0)$ and "armchair" $\mathbf{C}_h = (n, n)$ configurations.

In this research, the (10, 10) SWNT was considered. The main structural parameters of a SWNT are listed in Table 6.2. A segment of (10, 10) SWNT with a finite length of 9.7 nm was used to perform MD simulations. The computer graphics (CG) representation of

the nanotube in the longitudinal view is shown in Figure 6.1. The boundary effect is avoided by adding hydrogen atoms at the ends of carbon nanotube. The model has 400 carbon atoms and 40 hydrogen atoms. Each C-C bond length is 1.42Å and C-H bond length is 1.10 Å. The hydrogen atoms have charges of +0.1268 e and the carbon atoms connecting hydrogen atoms have charges of –0.1268 e, thus overall the carbon nanotube is neutrally charged.

Table 6-2 Structural parameters for (10,10) SWNT

Symbol	Name	Value
a	Length of unit vector (Å)	$a=\sqrt{3}b_{c-c}=2.49$
$\boldsymbol{\alpha}_1,\boldsymbol{\alpha}_2$	Primitive vector	$\left(\frac{\sqrt{3}}{2},\frac{1}{2}\right)a,\left(\frac{\sqrt{3}}{2},-\frac{1}{2}\right)a$
$\mathbf{C}_h$	Chiral vector	$\mathbf{C}_h=10\boldsymbol{\alpha}_1+10\boldsymbol{\alpha}_2\equiv(10,10)$
R	Radius (Å)	$r_t=\frac{a\sqrt{n^2+m^2+nm}}{2\pi}=6.8$
$\mathbf{T}$	Translational vector	$\mathbf{T}=t_1\boldsymbol{\alpha}_1+t_2\boldsymbol{\alpha}_2=\boldsymbol{\alpha}_1-\boldsymbol{\alpha}_2$ $t_1=\frac{2m+n}{d_R}=1,\ t_2=-\frac{2n+m}{d_R}=-1$
T	Length of $\mathbf{T}$ (Å)	$T=\lvert\mathbf{T}\rvert=\frac{\sqrt{3}L}{d_R}=2.49$
N	Number of hexagons in the unit cell	$N=\frac{2(n^2+m^2+nm)}{d_R}=20$
$\mathbf{R}$	Symmetry vector	$\mathbf{R}=p\boldsymbol{\alpha}_1+q\boldsymbol{\alpha}_2\equiv(p,q)=(1,0)$ $t_1q-t_2p=1$
τ	Pitch of $\mathbf{R}$ (Å)	$\tau=\frac{(mp-nq)T}{N}=\frac{MT}{N}=1.25$
ψ	Rotation angle of $\mathbf{R}$	$\psi=\frac{2\pi}{N}=0.314$

6.1.2. Force field atom type of SWNTs

To calculate potential energy, the force field atom type of each atom in the molecule system must be specified to determine which force field parameters to use. The force field atom types are related to the micro-chemical environment of atoms, such as the number and nature of connected atoms.

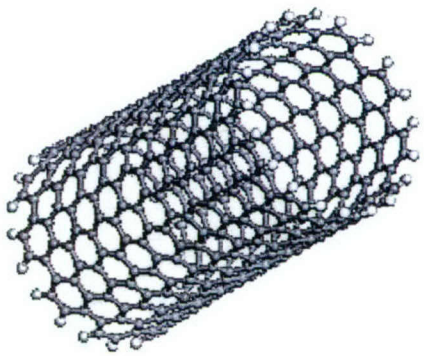

Figure 6.1 Molecular model of a (10, 10) SWNT segment

In the carbon nanotube, the bonding mechanism is similar to that of graphite because carbon nanotube can be thought of as a rolled-up graphene sheet. When carbon atoms combine to form graphite, sp^2 hybridization occurs. In this process, one s-orbital and two p-orbitals combine to form three hybrid sp^2-orbitals at 120° to each other within a plane. The in-plane bond is referred to as the σ-bond, which is a strong covalent bond that provides the carbon nanotube its high stiffness and strength. The remaining p-orbital is perpendicular to the plane of the σ-bonds and contributes mainly due to the inter-layered interaction, referred to as the π-bond, which interacts with the π-bonds on the neighboring layer. However, the inter-layer interaction of atom pairs on neighboring layers is much weaker than the σ-bond. Based on the electronic structure of carbon nanotube, the force field type of carbon atoms is sp^2. In calculating potential energy, all the parameters of carbon atoms in carbon nanotube are based on sp^2 structure.

6.2. Molecular models of EPON 862/DETDA epoxy system

Starting materials for the EPON 862 epoxy matrix (see Section 2.2) are low-molecular-weight organic liquid resins containing a number of epoxide groups, which are three-membered rings of one oxygen atom and two carbon atoms. EPON 862 epoxy resin is a low-viscosity, liquid epoxy resin manufactured from epichlorohydrin and Bisphenol-F. The chemical structure of Shell EPON 862 epoxy resin is shown in Figure 6.2.

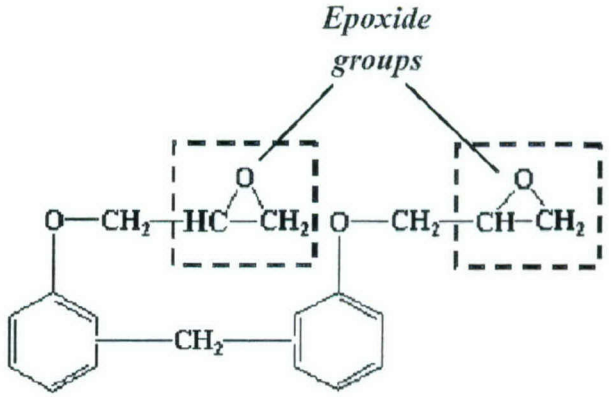

Figure 6.2 Chemical structure of Shell EPON 862 epoxy resin

Energy-minimization molecular mechanics were performed to find the morphology of EPON 862 epoxy resin. The chain of a simple molecule of Shell EPON 862 epoxy resin was twisted to achieve the low potential energy. Figure 6.3 clearly shows its configuration with minimum potential energy. With this energy, the simple molecule of EPON 862 epoxy resin has the molecular size of 23 Å × 9 Å ×6 Å.

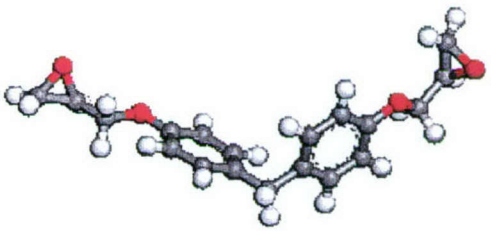

Figure 6.3 Molecular model of an EPON 862 epoxy resin under the minimum energy

To process the nanocomposites, EPON 862 epoxy resin and EPI-CURE W curing agent resin system were cured for 2.5 hours at 177° C, followed by a 177° C post cure for two additional hours to transform the liquid resin to a solid state. The principle ingredient of EPI-CURE curing agent is diethyl toluene diamine (DETDA). The nitrogen content in the curing agent was 15.7% by weight. The chemical structure of curing agent is shown in Figure 6.4 (a). Similarly, the energy-minimization molecular mechanics were also performed to find the morphology of curing agent molecule, as shown in Figure 6.4 (b). Under the minimum energy, the DETDA molecule has the molecular size of 6.7 Å × 6.5 Å × 1.8 Å

(a) Chemical structure (b) Molecular model under minimum energy

Figure 6.4 DETDA molecule

When processing nanocomposites, the liquid epoxy resin matrix consisted of EPON 862 resin and EPI-CURE W curing agent (DETDA) at a weight ratio of 100:26.4. The molecular interactions of EPON 862 epoxy resin and DETDA with the nanotube was examined respectively in the project.

6.3. Molecular Interactions between SWNTs and Resin Molecules

When processing SWNT/epoxy nanocomposites, sufficient wetting between the nanotubes and the matrix polymer is critical for coupling the inherent strength of the nanotube to the matrix polymer. Intense attractive interactions between carbon nanotubes and polymer molecules are essential for good wetting in the nanocomposites.

To analyze the molecular interactions of EPON 862 molecules and carbon nanotubes, a MD simulation was set up: an EPON 862 epoxy resin molecule was initially placed at the side of a nanotube. Snapshots of the MD simulation are shown in Figure 6.5. Initially, the chain of EPON 862 epoxy resin molecule was twisted severely. One end of the chain was put near the nanotube's wall, while the other end was placed away from the nanotube.

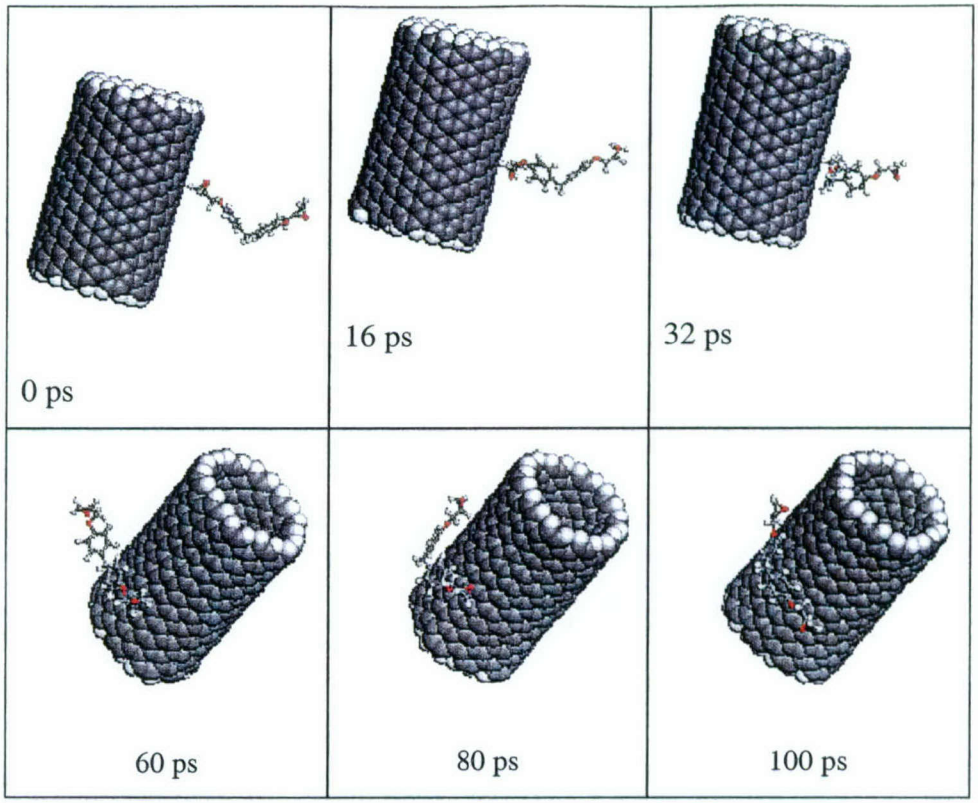

(a) Side view of the MD simulation results

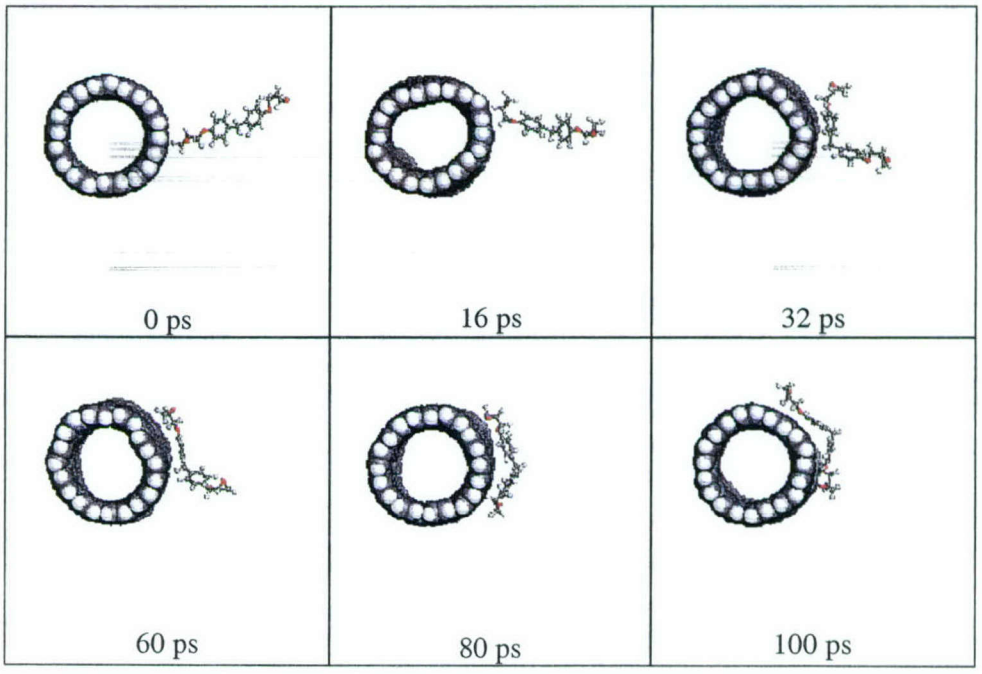

(b) Cross sectional view of the MD simulation results

Figure 6.5 MD simulation snapshots of the molecular interactions between EPON 862 molecule and (10,10) SWNT

The simulation shows that during the initial 16ps, the molecular chain of the EPON 862 resin stretched and moved toward the nanotube. All the atoms in the resin molecule gradually moved towards the nanotube's wall. After a long equilibration period of 100ps, the resin molecule chain eventually tended to spirally wrap on the surface of the nanotube. The nanotube maintained its overall shape, although some distortion of its cross section occurred during the interaction, as seen in Figure 6.5. Two aromatic rings of the molecule finally orientated to align their ring plane parallel to the SWNT surface. The negative interaction energy of the MD simulation indicates that the EPON 862 epoxy resin molecule moved towards the nanotube's surface due to an attractive force.

The dynamic interaction behaviors can be illustrated by tracking the interaction energy of the SWNT/EPON 862 epoxy resin system, as shown in Figure 6.6. The negative interaction energy indicated that the EPON 862 epoxy resin molecule moved towards the surface of nanotube due to an attractive force. Their interaction energy decreased until the system reached the equilibrium state. Consequently, the interaction energy of the SWNT and the EPON 862 epoxy resin molecule decreased by 25 kcal/mol.

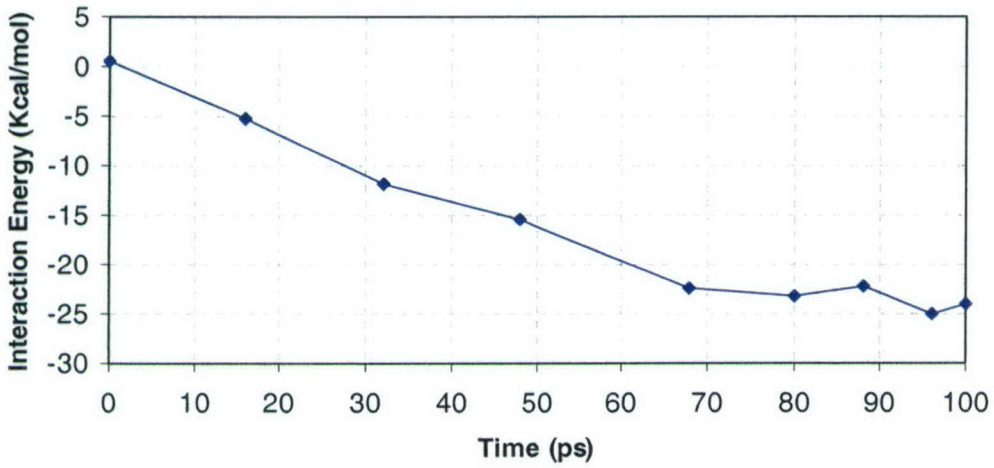

Figure 6.6 Interaction energy between SWNT and EPON 862 epoxy resin molecule

6.4. Molecular Interactions between (10, 10) SWNT and DETDA

MD simulations of the interactions between SWNT and DETDA molecule were conducted using the same procedure. The DETDA molecule was smaller than the EPON 862 epoxy resin molecule. The MD simulation of the tube/DETDA interactions was set up by placing a DETDA molecule near the nanotube wall. Snapshots of the MD simulation are shown in Figure 6.7(a) and (b). During the MD simulation, the DETDA molecule changed its orientation constantly and moved toward the nanotube due to their attractive force. The distance between the nanotube and the DETDA molecule decreased until they reached equilibration, which also resulted in a decrease of interaction energy of 25 kcal/mol, as shown in Figure 6.7(c). The simulation also indicated that the interaction of SWNT/DETDA achieved its equilibrium state faster than that of the SWNT/EPON resin interactions, due to the short molecular chain of DETDA.

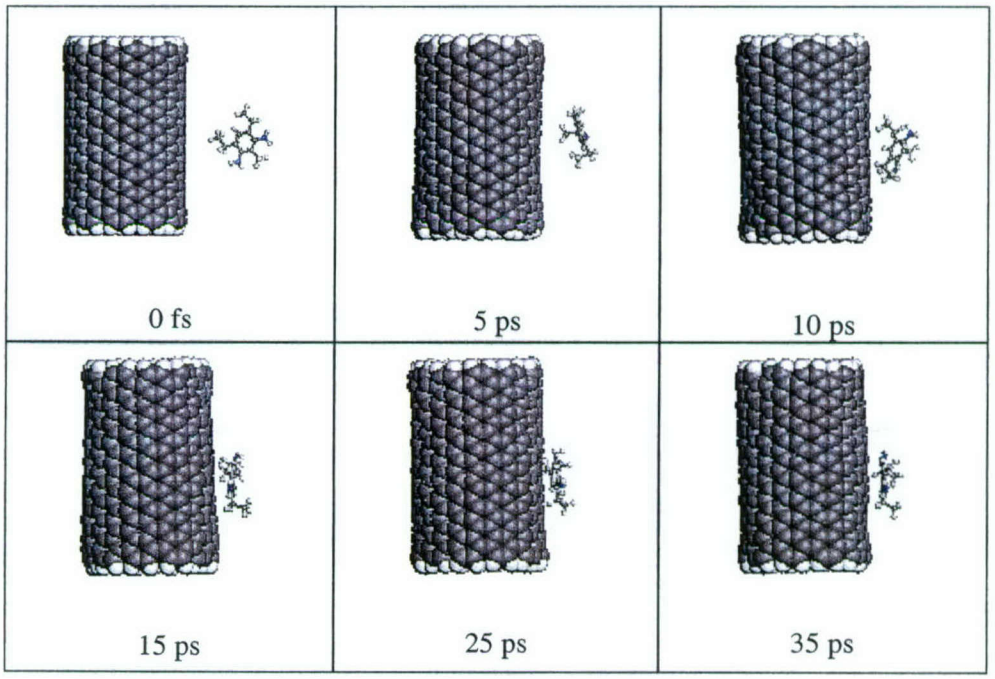

(a) Side view of the MD simulation results

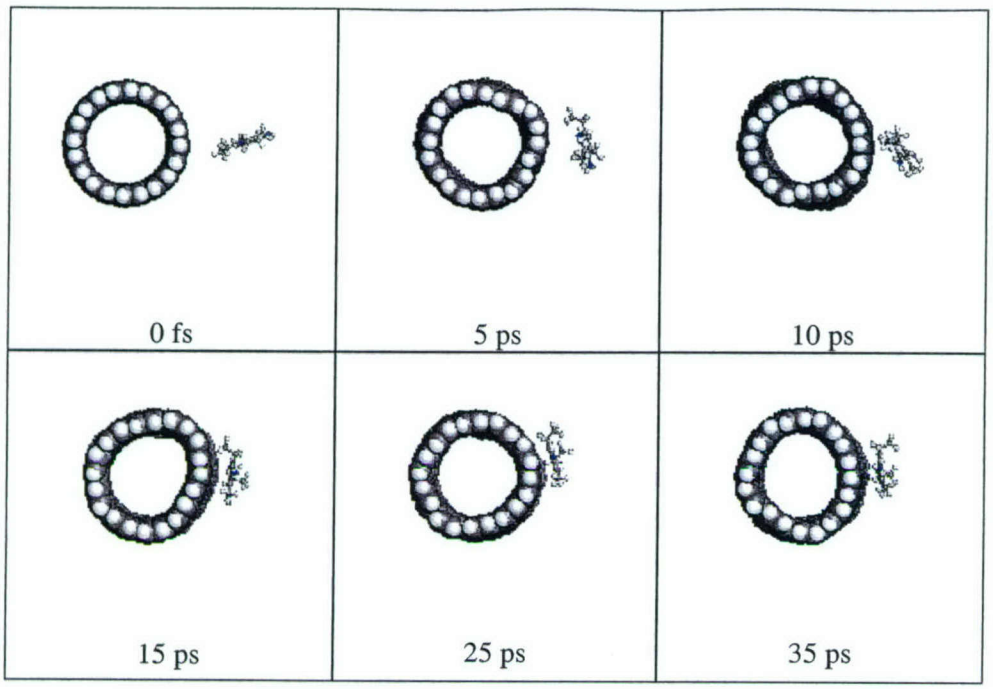

(b) Cross sectional view of the MD simulation results

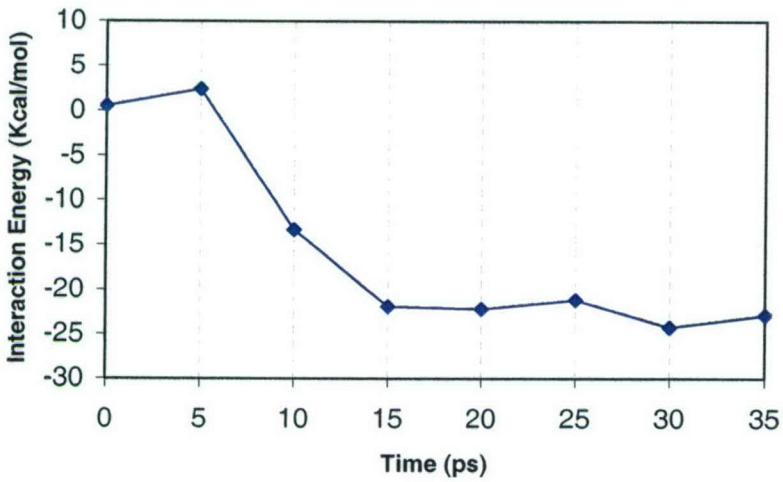

(c) Interaction energy between SWNT and DETDA

Figure 6.7 MD simulation of the molecular interactions between DETDA molecule and SWNT

The MD simulation clearly shows that both EPON 862 and DETDA molecules have attractive interactions with (10, 10) SWNT. Therefore, good wetting and interfacial bonding can be expected for (10, 10) SWNT and EPON 862/DETDA matrix composites. The good tube/resin matrix impregnation and wetting shown in Sections 2.3 and 2.4

agreed with that predicted results. The MD simulation was shown to be an effective tool to assess molecular interactions for developing nanotube-based composite materials.

6.5. MD Simulation of SWNT Pullout and Interfacial Bonding

In the development of nanotube composites, a major concern is the interfacial bonding between nanotubes and the polymer matrix. Interfacial bonding is critical to mechanical performance of SWNT-reinforced nanocomposite. A good interface is required to attain a satisfactory load transfer from the matrix to the nanotubes during loading. Load transfer depends on the interfacial shear stress between the fiber and the matrix. A high interfacial shear stress will effectively transfer the applied load to the SWNT over a short distance and take full advantages of high stiffness and strength of the SWNTs. However, the direct measurements of interfacial bonding or load transfer between SWNTs and polymer molecules are extremely difficult because of their nanoscale dimension.

In this project, a simplified SWNT pullout simulation was conducted to assess interfacial bonding properties between SWNT and EPON 862/DETDA matrix in term of system potential energy variation.

6.5.1. Molecular model of SWNT/EPON 862 nanocomposites

When processing the nanotube composites, EPON 862 epoxy resin and EPI-CURE W curing agent (DETDA) were cured for 2.5 hours at 177° C, followed by a 177° C post cure for additional two hours to transform the liquid resin to the solid state. MD simulations were performed on the cured epoxy resins. This section describes the molecular models of the cured epoxy resin and resultant nanocomposite.

In the curing reaction, the hydrogen atoms in the amine ($-NH_2$) groups of a DETDA molecule reacted with the epoxide groups of the epoxy resin. Initially, one epoxide group reacted with one curing agent molecule. The resulting molecule of the curing agent molecule further reacted with three other epoxy molecules at the site of -HN and another $-NH_2$, as show in Figure 6.8.

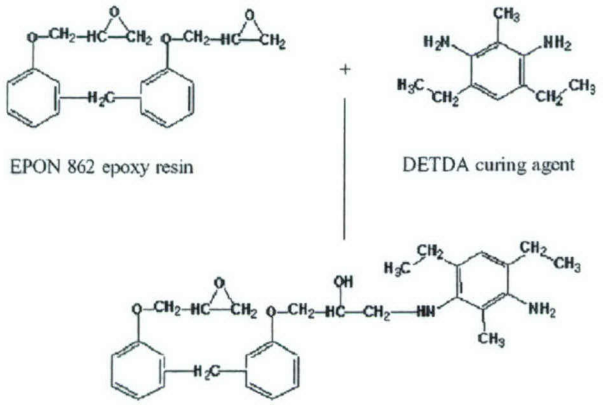

Figure 6.8 Reaction of an epoxide group with a curing agent molecule

Figure 6.9 shows the formation of a cross-link between epoxy resin and curing agent molecules. The curing agent molecule continued to react with another epoxy molecule at the site of HN and formed cross-link at the atom N. The resulting molecule could further react with two curing agent molecules at the two epoxide groups and two epoxy resin molecules at the site of NH_2. As the reaction continued, the epoxy resin and curing agent molecules generated more cross-links. The cross links expanded in all directions and formed a 3D cross-link network macromolecule, as shown in Figure 6.10.

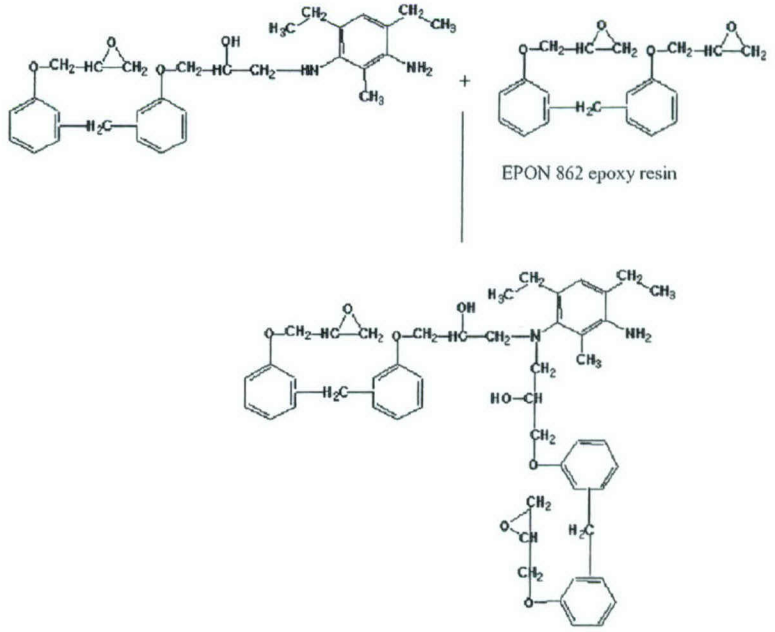

Figure 6.9 Formation of a cross-link between the epoxy resin and curing agent

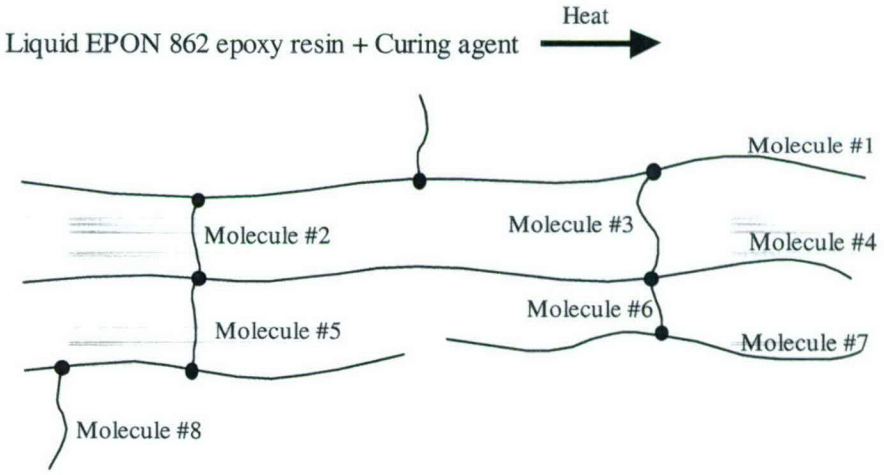

Figure 6.10 Formation of the cross-link of EPON 862/DETDA resin matrix

Based on the above analysis of the cross-link formation, a molecular model of a partial cross-link network of the resin matrix was constructed. The energy-minimization of the model was performed. Figure 6.11 shows a morphological conformation of the cured resin matrix model with minimum potential energy. With this energy, the cured epoxy

resin molecule had a molecular size of 50 Å × 29 Å × 16 Å, which is much larger than both individual resin and curing agent monomers as shown in Section 6.3.

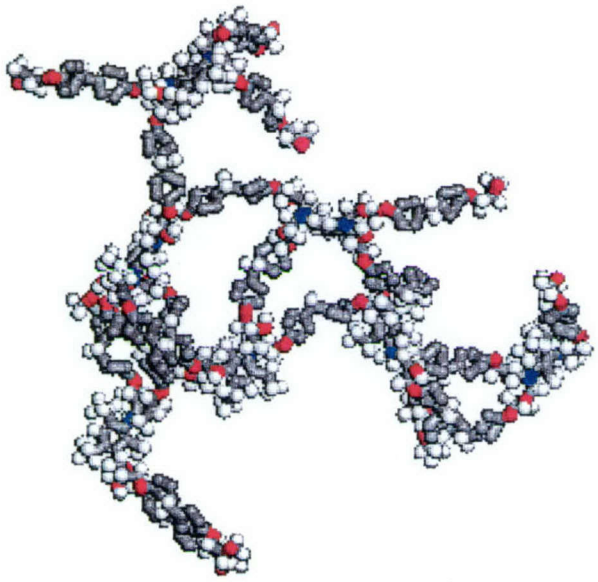

Figure 6.11 Molecular model of the cured epoxy resin under the minimum energy

In the MD simulations, the periodic model of the SWNT/EPON 862 nanocomposite system was used. Periodic boundary conditions refer to the simulation of models consisting of a periodic lattice of identical subunits. By applying periodic boundaries to simulations, the influence of bulk environments can be included, thereby improving the rigor and realism of a model. Therefore, the properties of a small, infinitely periodic system and the macroscopic system are essentially the same.

To simulate the interfacial bonding interactions between the nanotube and epoxy resin matrix, a nanocomposite model was composed of a fragment of SWNT (10, 10) totally embedded inside the amorphous polymer matrix of the cured epoxy resin, as shown in Figure 6.12. This molecular model of the nanocomposite includes 21,288 atoms, which consists of a supercell in the range of 50 Å × 50 Å × 100 Å. The configuration was initiated by randomly generating the cured epoxy resin molecules surrounding the SWNT using an initial density of 1.2 g/cm^3. The matrix polymer was then equilibrated for approximately 20 ps with a time step of 0.2 fs while holding the nanotube rigid. The

system was further equilibrated for 60 ps at a time step of 2 fs with a non-rigid nanotube. The energy of the SWNT/epoxy nanocomposite system was minimized during the calculations to achieve strongest bonding between the SWNT and the epoxy resin matrix.

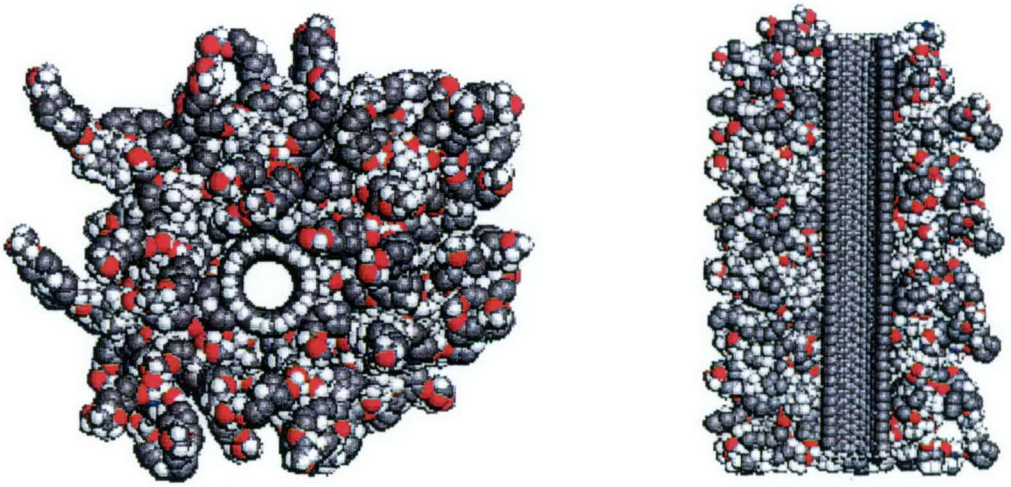

(a) top view (b) section view

Figure 6.12 Molecular model of the SWNT/epoxy nanocomposite

6.5.2. MD simulation of tube pullout of the nanocomposites

The final mechanical properties of nanotube-reinforced nanocomposites are known to strongly depend on the magnitude of interfacial shear stress between resin matrix to nanotubes. To characterize the interfacial shear strength of the SWNT/EPON 862 composites, a tube pullout simulation of the established nanocomposite model was performed. The SWNT was pulled out from the cured resin matrix along the tube axis direction Z. Snapshots of the pullout simulations are shown in Figure 6.13.

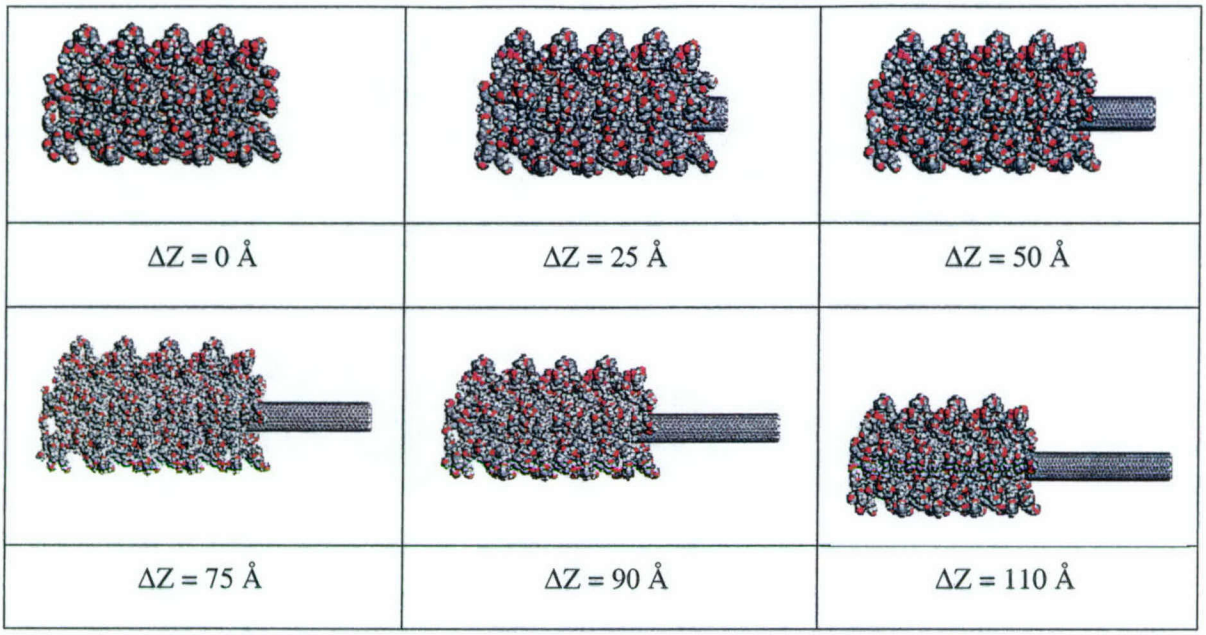

Figure 6.13 MD simulation snapshots of the SWNT pullout

The potential energy, interaction energy and interfacial bonding energy of the composite were plotted against the displacement of the SWNT from the epoxy resin, as shown in Figure 6.14. The potential energy of the SWNT-epoxy resin composite increased as the nanotube was pulled out of the epoxy resin, as shown in Figure 6.14 (a). The total potential energy increased faster at the early stage of pullout, whereas it went up slower in the subsequent pullout. In fact, the increase of pullout energy resulted from the decrease of the interaction energy of the tube/resin matrix during tube pullout. The interaction energy decreased due to the decrease of contact area during the pullout. The potential energy of the SWNT and the epoxy resins increased due to the change of their configurations during the pullout. However, the interaction energy changed with the displacement linearly, as shown in Figure 6.14 (b). This is due to the stable interfacial bonding interaction between the SWNT and epoxy resins. The interfacial bonding energy kept constant with a value of 0.1 kcal/mol·Å^2 during the pullout of the SWNT, as shown in Figure 6.14 (c).

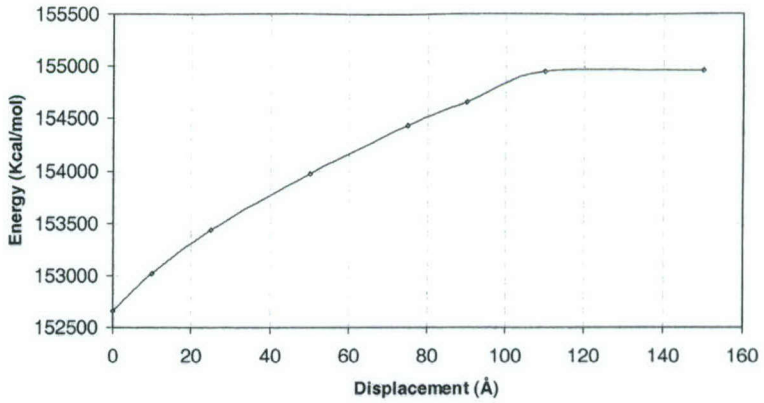

(a) Potential energy of the system

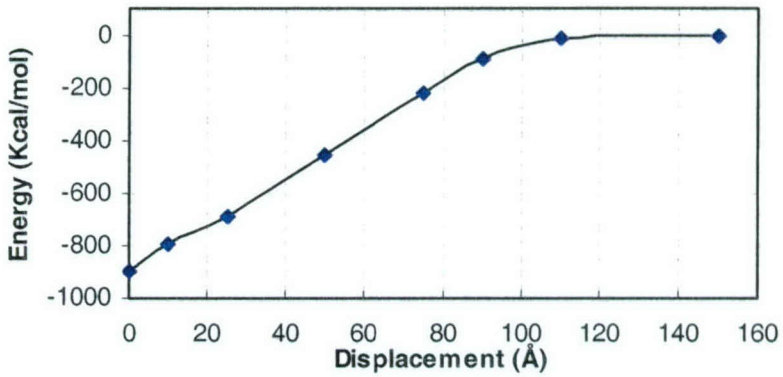

(b) Interaction energy of the SWNT and the resin matrix

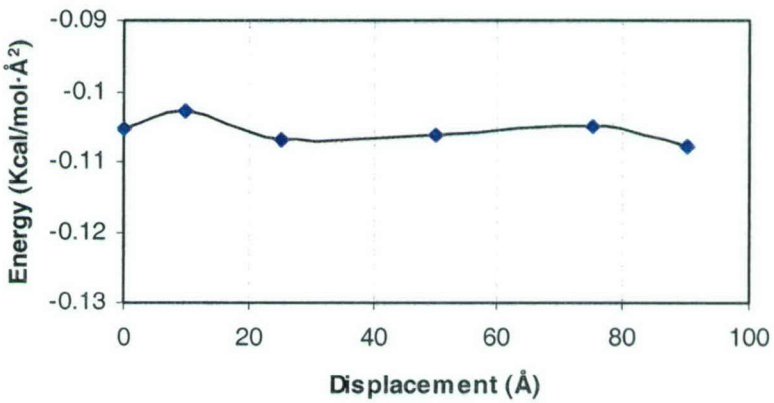

(c) Interfacial bonding energy

Figure 6.14 Energy plots during the pullout of the SWNT

6.5.3. Interfacial shear stress

The pullout energy, $E_{pullout}$, is defined as the energy difference between the fully embedded nanotube and the complete pullout configuration [16]. Pullout energy can be related to the interfacial shear stress, τ_i, by the following relation:

$$E_{pullout} = \int_0^L 2\pi r(L-x)\tau_i dx = \pi r \tau_i L^2 \tag{6.16}$$

$$\tau_i = \frac{E_{pullout}}{\pi r L^2} \tag{6.17}$$

where r and L are the radius and length of the nanotube, respectively, and x is the displacement of the nanotube. At the initial stage of pullout, the potential energy of the composite was 152,665 kcal/mol. After pullout, the potential energy increased to 154,951 kcal/mol. The interfacial shear stress estimated from the molecular simulation was about 75 MPa.

For comparison, the Kelly-Tyson model was used to approximate the interfacial shear strength [17-19]. By assuming that the applied stress was transferred to the nanotube via a nanotube-polymer interfacial shear mechanism at the molecular level, the nanotube-epoxy resin interfacial shear strength τ can be calculated as follows:

$$\tau = \left(\frac{\sigma_{NT}(l_c)}{2(l_c / D_{NT})}\right)\left(1 - \frac{d^2{}_{NT}}{D^2{}_{NT}}\right) \tag{6.18}$$

where $\sigma_{NT}(l_c)$ is the tensile strength of the nanotube of length l_c, d_{NT} and D_{NT} are the inner and outer diameters of the nanotube, respectively, l_c is the critical length of the nanotube, and l_c / D_{NT} is the critical aspect ratio of the composite. The interfacial shear stress was calculated with a critical aspect ratio of 1,000. The SWNT (10, 10) had an outer diameter of 1.36 nm and a wall thickness of 0.34 nm [16]. If assuming the strength value of SWNT to be 100~200 GPa, we found the stress transfer ability τ of the SWNT-

polymer interface should be in the range of 38~75 MPa. The interfacial shear strength value of 75 MPa from the MD simulations falls into the upper range of the Kelly-Tyson model.

The estimated interfacial shearing strength is also about 20%~80% higher than that of most carbon fiber reinforced composites. Such high interfacial shear stress could be attributed to high surface area/volume ratio of well-dispersed individual SWNTs embedded in the resin matrix. However, SWNTs try to form ropes or bundles of 20-50 individual tubes in current nanotube composites due to their smooth surface and van der Waals interactions (see Chapters 2, 3 and 4). This dramatically reduces resin/tube contact area in composites and largely reduces the shearing strength or load transfer between tubes and resin matrix.

6.6. Conclusions

In this study, MD simulations were used to understand and assess the molecular interactions during tube/resin wetting and interfacial bonding of the resultant SWNT/epoxy resin composites. The simulation results show that the molecules of EPON 862 and DETDA will change the molecular conformation and try to align their aromatic ring parallel to the surface of (10, 10) SWNTs. As a result, these molecules could stretch and wrap on the surface of the SWNTs. The simulation results show that the interfacial shear strength could be as high as 75Mpa for a single SWNT pullout from the cured resin matrix in the SWNT/EPON 862 resin nanocomposites due to only van der Waals interactions. Based on the MD simulations, good wetting and impregnation of SWNT/EPON 862 resin/EPI-CURE W curing agent system can be expected. The experimental results in Chapter 2 agreed with these predicted results, which preliminarily validated the MD simulation results.

6.7. References

[1] P. Cheol and J.S. Emilie, *Proceeding of ICCE/9*, pp. 599-600, 2002.

[2] C.F. Fan and T. Cagin, *Journal of Chemical Physics*, 103 (20), 9053 (1995).

[3] E. Dujardin, T.W. Ebbesen, H. Hiura, and K. Tanigaki, *Science*, 265, 1850 (1994).

[4] R. Saito, G. Dresselhaus and M.S. Dresselhaus. *Physical Properties of Carbon Nanotubes*, 1st ed. London: Imperial College Press, 1999.

[5] J.K. Kim and Y.W. Mai, *Engineered Interface in Fiber Reinforced Composites*, Elsevier Science Ltd., 1998.

[6] D. Hull and T.W. Clyne, *An Introduction to Composite Materials*, 2nd edition, Cambridge University Press, 1996.

[7] L.S. Schadler, S.C. Giannaris and P.M. Ajayan, *Applied Physics Letter*, 73 (26), 3842 (1998).

[8] D.L. Qian and E.C. Dickey, *Applied Physics Letters*, 76 (20): 2868 (2000).

[9] P.M. Ajayan, *Progress Crystal Growth and Characterization*, 34, 37 (1997).

[10] P.M. Ajayan, L.S. Schadler, and C. Giannaris, and A. Rubio, *Advanced Materials*, 12 (10), 750 (2000).

[11] Z.X. Jin, K.P. Pramoda, G.Q. Xu, and S.H. Goh, *Chemical Physics Letters*, 337, 43 (2001).

[12] K. Lozano, J. Rios, and E.V. Barrera, *Journal of Applied Polymer Science*, 80, 1162 (2001).

[13] Materials Studio, User's Manual, Version 1.2, Accelrys, Inc., San Diego, CA, 2001.

[14] H. Sun, *Journal of Computational Chemistry*, 15 (7), 752 (1994)

[15] J.R. Maple, M.J. Hwang, T.P. Stockfisch, U. Dinur, M. Waldman, C.S. Ewig, and A.T. Hagler, *Journal of Computational Chemistry*, 15 (2), 162 (1994).

[16] Liao, K. and Li, S., *Applied Physics Letters*, Vol. 79, No. 25, pp. 4225-4227.

[17] Wagner, H. D., Lourie, O., and Zhou, X. F., *Composites Part A: Applied Science and Manufacturing*, 1999, Vol. 30, pp. 59-66.

[18] Wagner, H. D., Lourie, O., Feldman, Y., and Tenne, R., *Applied Physics Letters*, 1998, Vol. 72, No. 2, pp. 188-190.

[19] Ajayan P. M., Schadler L. S., Giannaris C., and Rubio A., *Advanced Materials*, 2000, Vol. 12, No. 10, pp.750-753.

7. Functionalization of SWNTs for Enhancing Dispersion and Interfacial Bonding

Mechanical properties of current SWNT-reinforced nanocomposites are far below what we anticipated, possibly due to poor dispersion, lack of alignment and weak interfacial bonding between nanotubes and resin matrix, as mentioned in Section 1.2. Improving tube dispersion and interfacial bonding is becoming a critical issue for developing SWNT-reinforced nanocomposites.

Besides using solvents and surfactants, chemical modification and functionalization are reported to be feasible and effective methods for improving the solubility and dispersion of nanotubes in resin matrix. In addition, functionalized nanotubes can provide chemical bonding sites to polymer matrix so that the load can be transferred to the nanotubes through chemical bonding.

In this project, a preliminary study was conducted to investigate the functionalization of SWNTs for enhancing dispersion and interfacial bonding in casting composite samples. Two methods, oxidization and molecular wrap, were used in this project for functionalizing SWNTs.

7.1. Oxidation of SWNTs

By oxidizing SWNTs, the end-caps of SWNTs can be opened and terminated with the oxygenated functionalities including carboxylic, carbonyl and hydroxyl groups [1-4]. IR spectrum results also show the existence of carboxylic acid and quinone groups on the nanotubes surface prior to heating above 623K for the oxidized SWNTs in the air.

Oxidized nanotubes have better solubility and can form well-dispersed electrostatic stabilized colloids in water and ethanol. For functionalizing nanotubes, SWNT ropes were reported to be largely exfoliated into individual nanotubes with significantly improved solubility in organic solvents. Furthermore, carboxylic acid groups can undergo

easterification reactions with the epoxy. Some cross-link between tubes and resin matrix may take place during composites curing.

Oxidation treatment of nanotubes can be generally divided into two groups: gas phase and liquid phase oxidation [5-18]. Some examples of gas phase oxidation are listed in Table 7.1.

Table 7-1 Gas phase oxidization

Gas Phase	Procedure
O_2	Raw material of tubes was treated with O_2 gas at 300°C for 30 min to eliminate the carbon shell surrounding metal particles and oxidized tubes.
O_3	Carbon nanotubes were placed in a chamber. Ozone was generated and purified by special apparatus. O_3 can be used alone or mixed with O_2. Carbon nanotubes can be oxidized by O_3 for 30-90 min at room temperature or heated to 150-200°C.

H_2SO_4 and HNO_3 can be easily permeated through the graphene sheets to create defects or pores in graphene sheets. Some examples of liquid phase oxidization are summarized in Table 7.2.

Table 7-2 Liquid phase oxidization

Liquid Phase	Procedure
$KMnO_4/H_2SO_4$	SWNTs were first refluxed in alkalescent solution of potassium permanganate (0.2M $KMnO_4$ and 0.2 M NaOH). $Na2SO_3$ was added by stirring, followed by an addition of M $H2SO_4$. The obtained solution was filtered with a membrane under vacuum in dilute NaOH and then deionized water. In the final step rinsing, diluted HCl was added.
H_2O_2/H_2O_4	Carbon nanotubes were suspended in H_2O_2/H_2SO_4, then reacted at room temperature for 24 hours under stirring.
HNO_3	Purified SWNTs was refluxed in 2.6M HNO_3 for 48h. The solid was collected on a membrane and rinsed with deionized water.
HNO_3:H_2SO_4=1: 3	The raw carbon nanotubes were oxidized in a mixed solution of HNO_3 and H_2SO_4 (1:3 by volume), followed by filtering onto a glass filter and washing with distilled water, then the black product was heated.

The sidewalls of the SWNTs possess a chemical stability akin to that of the basal plane of graphite. The chemistry available for modifying the nanotube sidewalls without disrupting the tubular structure is significantly more restrictive. Using the technology developed in the fluorination of graphite and fullerences, some researcher reported the

chemical manipulation of the carbon nanotubes sidewalls by fluorinating and defluorinating process. The fluorination agent was the element fluorine in their experiments. For example, Mickelson *et al.* [19] placed approximately 1 mg of fluorinated nanotubes into a vial containing approximately 10 ml of alcohol solvent and sonicated for approximately 10 minutes. Sonication was performed by partially immersing the capped vial in an ultrasonic cleaner operating at 55kHz. The solved fluorotubes were then dispersed on a clean mica surface by means of a 3000 rpm rotary spinner and examined with AFM. They found fluorinated carbon nanotubes could form a stable solution in alcohol and solvated as individual tubes. This may be due to the formation of hydrogen bonding between the alcohol's hydroxyl hydrogen and the nanotube-bound fluorine. By using various defluorinating processes, other functional groups containing oxygen element can more easily be created on the sidewalls of SWNTs.

7.2. Noncovalently Functionalization

The use of polymer molecular wrapping on SWNTs is called noncovelent functionalization. Polymer wrapping functionalization usually use a type of conjugated polymer, such as poly(m-phenylenevinylene)-co-[(2,5-dioctyloxy-p-phenylene) -vinylene] (PmPV) [20,-21], poly(p-phenylenevinylene) (PPV) [41-42], poly(p-phenylenevinylene-co-2,5-dioctyloxy-m-phenylenevinylene) (PmPV-co-DOctOPV) [22], poly (vinylpyrrolidone), polystyrene sulfonate [23] and Gum Arabic [24]. These polymers have strong molecular interactions with carbon nanotubes that effectively break up the ropes into single tubes or make SWNTs soluble in suspensions. The loading transfer between tubes and resin matrix can also be improved if the wrapping molecules have strong interactions or form chemical bonding with the resin matrix. The advantage of such noncovalently functionalization of tubes is to avoid damaging the unique electronic and molecular structures of the tubes, which could harm the nanotube's mechanical, thermal and electronic properties.

7.3. Experiments of SWN Functionalization

In this project, oxidization and Gum Arabic wrapping of SWNT were conducted to enhance tube dispersion and interfacial bonding in EPON 862 resin matrix nanocomposites. The composite samples of the functionalized SWNTs were fabricated using the direct mixing and casting method.

7.3.1. Oxidization of nanotubes

To achieve a better bonding between nanotubes and matrix, the purified SWNTs BuckyPearls (see Chapter 2) were oxidized by chemically treating. Through oxidization, functional groups are expected to form around the end-cap of the SWNTs, as shown in Figure 7.1, which can enhance tube dispersion and form chemical bonding in epoxy resin matrix.

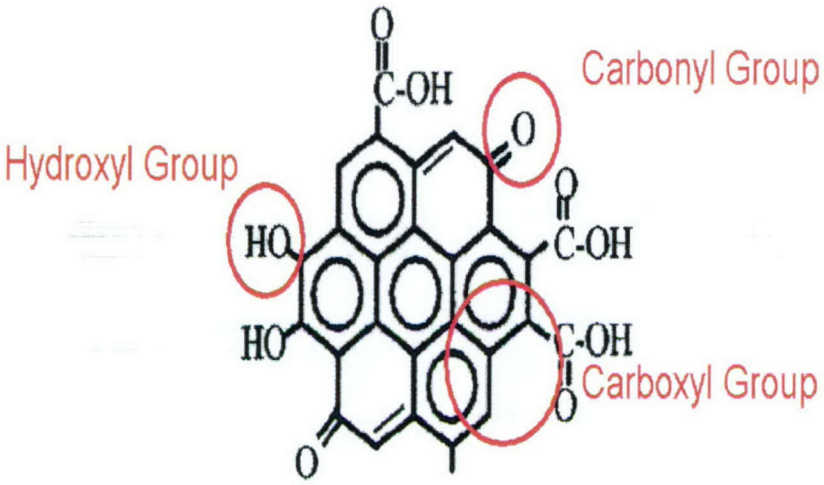

Figure 7.1 Possible functional groups formed during tube oxidization

To fabricate oxidized nanotubes, 500mg SWNTs were added to 250ml mixed solution of H_2SO_4 and HNO_3 (high concentration acids from Fisher Scientific Inc.) at a mixing ratio of H_2SO_4:HNO_3=3:1. The tube/acid suspension was stirred for 15 minutes and refluxed for 12 hours at room temperature. Then 100ml 1N HCl was added into the as-prepared suspension and stirred for 30 minutes. NaOH was added gradually until the solution achieved PH=5. A filter was used to filtrate the suspension to form a buckypaper, which

was then washed several times with distilled water to remove the residual chemicals and then dried in a vacuum at 80°C.

The AFM images of both pristine and oxidized SWNTs are shown in Figures 7.2 and 7.3, respectively. Compared to the pristine SWNTs, the oxidized SWNTs were "acid cut" after the oxidizations. The length is obviously shorter than pristine SWNTs. The Raman spectrums of pristine SWNTs and the oxidized SWNTs are shown in Figure 7.4. Those peaks below 350cm-1 are the key peaks for pristine SWNTs. They relate to the unique molecular structure of SWNTs. For the oxidized SWNTs, peaks A, B, C and D disappeared, indicating that the SWNTs were over oxidized in the experiment and the unique structure of SWNTs was damaged. This may greatly decrease the unique mechanical and electrical properties of SWNTs and decrease the reinforcement efficiency.

Modification of the oxidization procedure is needed. A modified oxidization procedure was used in the experiment for reducing oxidization time, as shown in Figure 7.5.

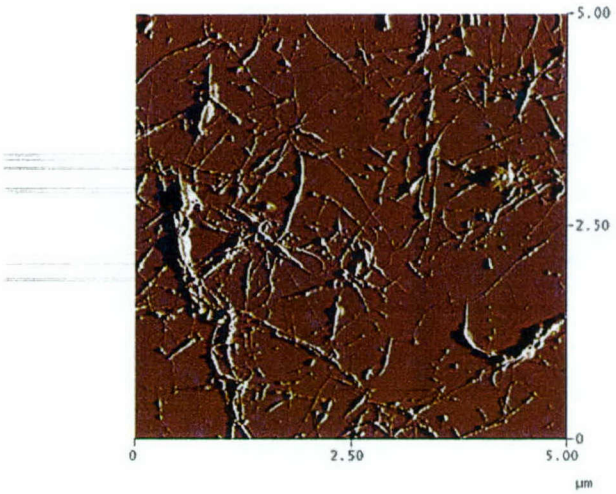

Figure 7.2 AFM images of the pristine SWNTs

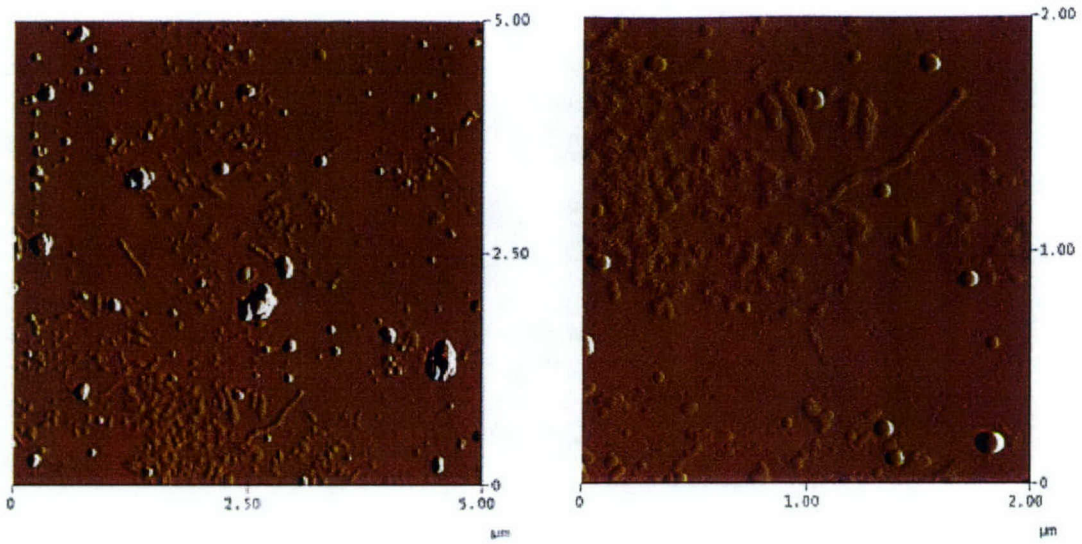

Figure 7.3 AFM images of the oxidized SWNTs

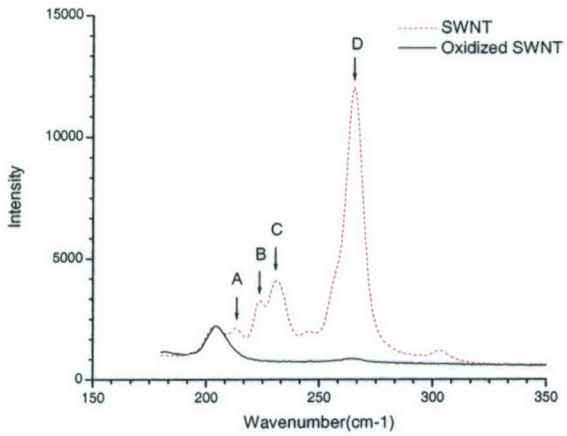

Figure 7.4 Raman spectrums of pristine SWNTs and oxidized SWNTs

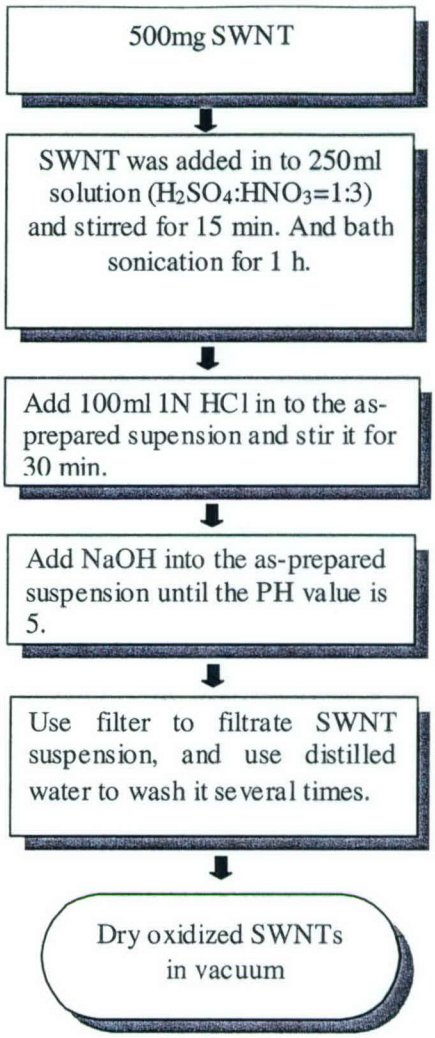

Figure 7.5 Modified procedure for SWNT oxidization

Figure 7.6 shows the Raman spectrum of the oxidized SWNTs using the improved procedure. All the peaks below 350 remain, yet had 5cm^{-1} shift to high wave number. This means the SWNTs structure underwent only a slight change because of oxidation. The AFM images of SWNTs oxidized by the improved procedure are shown in Figure 7.7, demonstrating the new oxidation method does not damage the SWNTs structure as occurred in the previous oxidation method. The improved oxidation method was used for preparing the oxidized SWNTs for the nanocomposite fabrication in this research.

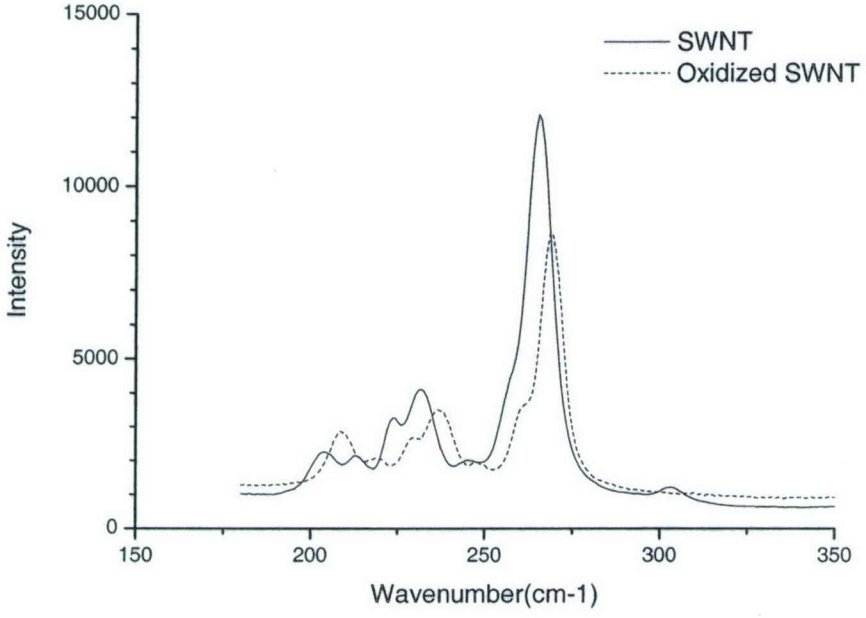

Figure 7.6 Raman spectrums of pristine SWNTs and oxidized SWNTs using modified procedure

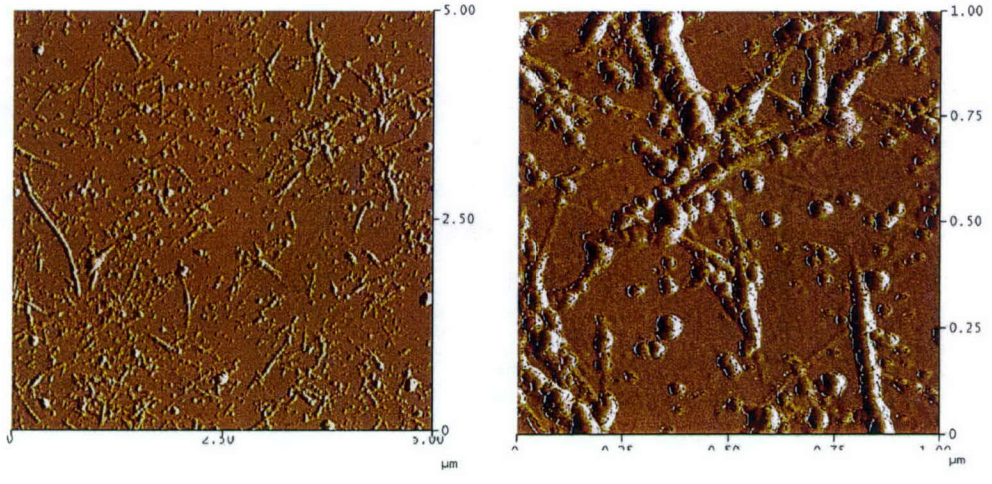

Figure 7.7 AFM images of the oxidized SWNTs using modified procedure

7.3.2. Gum Arabic wrapping SWNT

GA (Gum Arabic) polymer is a good surfactant for aqueous SWNT suspensions. This means that GA has strong interactions with SWNTs. The MWn of GA is about 250,00

and the MWw is about 580,000. Its DPn is about 1,550 and its DPw is about 3,600. GA molecules can wrap around the nanotubes. Gum Arabic is 75% Arabinogalactan and 20% is a Arabinogalactan-protein complex. The main function group of Arabinogalactan and protein is amine (-NH), which can react with epoxy function group. Therefore, GA molecular can form mechanical links with SWNTs and chemical links with epoxy resin. GA molecules may form a bridge between SWNTs and epoxy resin to improve tube dispersion and properties of SWNTs/epoxy composites.

Preparation of the GA wrapped SWNTs is relatively simple. In the experiment, SWNTs and Gum Arabic were added to distilled water. Gum Arabic was 5 times the weight of SWNTs. The suspension was sonicated for 24 hours with the Sonicator 3000 at 12W (see Chapter 2). The as-prepared solution was placed into an at 80° C oven to dry. Figure 7.8 shows the Raman spectrums of pristine SWNTs and GA wrapping SWNTs. All peaks shifted $2cm^{-1}$ to higher wave number. The relative height of peaks A and B also changed. For pristine SWNTs, peak A is obviously lower than peak B. For GA wrapped SWNTs, peaks A and B were almost the same height. The Raman results indicate that molecular interactions exist between GA and SWNTs. Figure 7.9 shows the SWNTs wrapped by GA molecules. The diameter of GA wrapping SWNTs was obviously larger than pristine SWNTs, as shown in Figure 7.2.

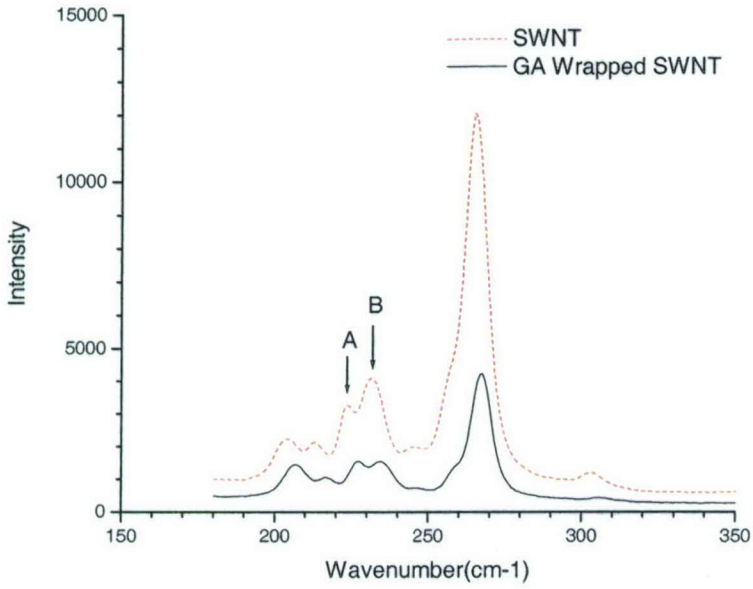

Figure 7.8 Raman spectrums of pristine SWNTs and GA wrapped SWNTs

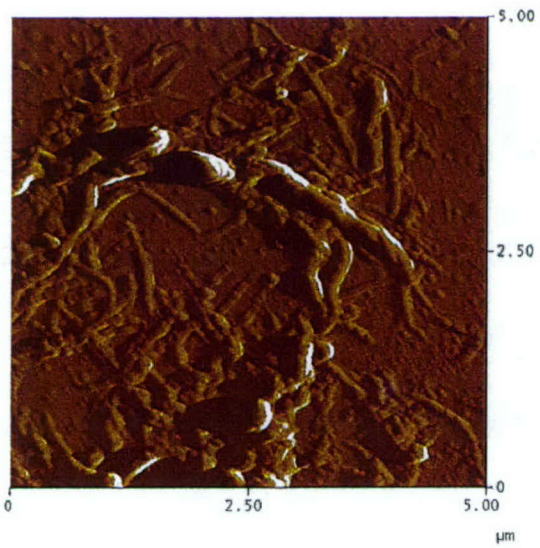

Figure 7.9 AFM image of GA wrapped SWNTs

7.4. Fabrication of the Functionalized SWNT-Reinforced Nanocomposites

Compression molding was used to fabricate the casted nanocomposite samples of the functionalized SWNTs. The procedure for manufacturing the samples is described as follows:

1. SWNTs were added into the hardener EPI Cure W, Shell Chemicals (see Section 2.2) and the mixture was sonicated at 12W using the Sonicator 3000, for 1.5 hours to disperse the tubes in the hardener.
2. EPON 862 resin was mixed with some acetone to reduce the viscosity of resin. Then the mixture of the SWNT and hardener was added into resin solution and sonicated at 66W for 1.5 hours to disperse the tubes in the resin/hardener mixture.
3. The produced mixture was put in a vacuum oven under full vacuum to evaporate the acetone and degas bubbles. The mixture was then cast into the sample mold and vacuumed again, with the temperature remaining at 60°C to reduce the viscosity of the mixtures for degassing.
4. The samples were cured at 355 °F (177 °C) for 2.5 hours under 145~200 psi.
5. The samples were post cured in the oven at 355 °F (177 °C) for 2.5 hours.
6. The nanocomposite samples of 1wt % functionalized SWNTs were produced for DMA and SEM testing. The control samples of the neat resin and pristine SWNT/EPON 862 were also manufactured in the research using the same procedure.

7.5. DMA and SEM Tests

Dynamic mechanical properties of the produced samples were characterized by using dynamic mechanical analyzer DMA2980 (see Section 5.1). The test mode was the film tension mode. Test temperature was from room temperature to 300°C at 5°C/min. The frequency was 1Hz. The nanostructure of the produced samples were characterized with Scanning Electron Microscope (Joel 6400F, Joel Co.)

7.6. Results and Discussions

The DMA results of the SWNT nanocomposiste and the neat resin samples are provided in Figure 7.10 and the results are summarized in Table 7.3. The SWNT loading of all nanocomposite samples was 1w/w%.

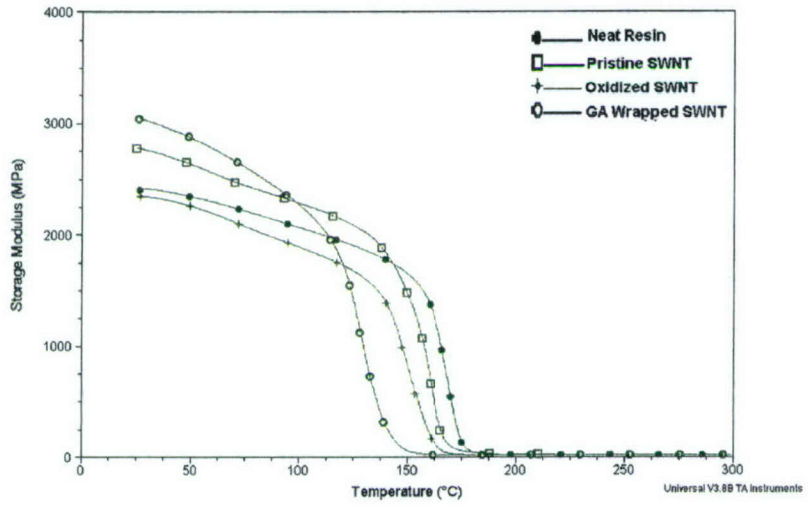

(a) Storage modulus

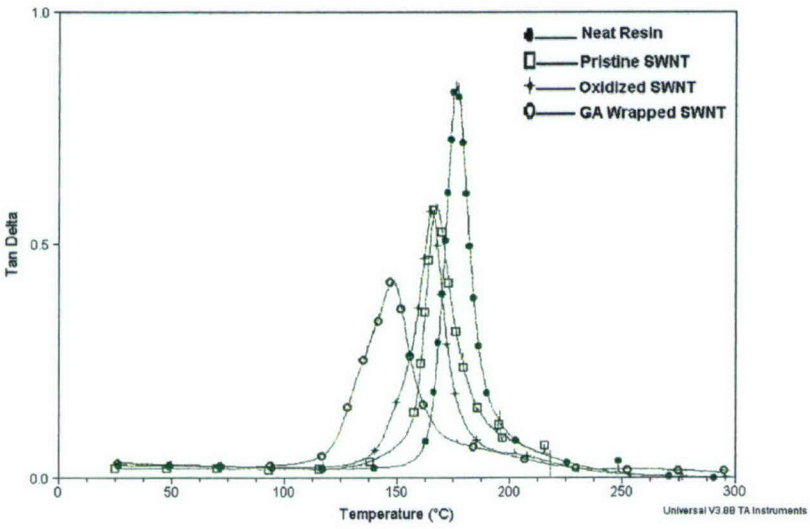

(b) Tan Delta and Tg

Figure 7.10 DMA results of the nanocomposites of the functionalized SWNTs

Table 7-3 DMA results of functionalized SWNT nanocomposites

Type of SWNTs	StorageModulus (MPa)	Tg (°C)	Modulus Increase (%)
Neat Resin	2498	176.28	-
Pristine SWNT	2782	167.65	11.37
Oxidized SWNT	2347	165.0	- 4.0
GA wrapped SWNT	3042	147.79	21.78

The nanocomposites of the GA wrapped SWNTs had the largest modulus increase, yet also had the largest Tg decrease. As described earlier, GA is a type of polymer molecule. GA molecules can wrap around tubes and enhance tube dispersion [24]. The main function group of GA is amine (-NH), which can react with epoxy function group to form a chemical bonding with the epoxy resin matrix. Therefore, GA in the nanocomposite can have strong molecular interactions with the SWNTs and can also chemically bond with the resin matrix. GA can be considered as load transfer bridge between the tubes and resin matrix. This will improve the interfacial bonding between SWNTs and epoxy resin and result in better load transfer efficiency. Better load transfer will lead to a higher mechanical properties of composites. The noncovalent functionalization of molecular wrapping can avoid tube damages. This also contributes to higher mechanical properties of the GA wrapped SWNT nanocomposites. However, the GA molecules also have long molecular chains, which wrap the surface SWNTs (see Figure 7.10) and may form a layer of plasticizer. This could result in a decrease in Tg.

The oxidized SWNT nanocomposites did not show any property improvements as expected. The further optimization of oxidization process for avoiding tube damage may be the key for nanocomposite applications. For the pristine SWNT-reinforced samples, a 11.37% storage modulus increase and a 9 °C Tg decrease was seen. The addition of the SWNTs, including both pristine and functionalized tubes, showed a negative effect on the Tgs of the samples.

Figure 7.11 shows the fracture surface of the EPON 862 neat resin sample. The fracture surface of the neat resin was smooth and presents the patterns of the quick crack propagation. It indicates the failure mode is a brittle fracture.

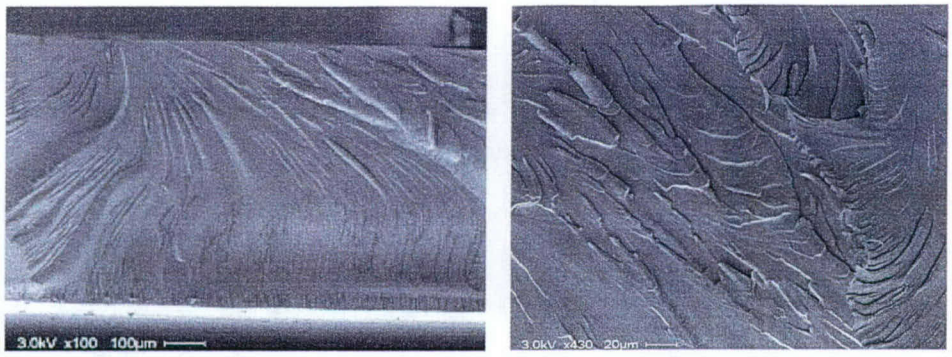

Figure 7.11 Fracture surface of the neat resin sample

Figure 7.12 shows the SEM images of 1%wt pristine SWNT/EPON 862 nanocomposites. The feature of "river-marking" was observed in the fracture surface. These river-markings occurred as a result of crack deflections and subsequent propagation on two slightly different fracture planes. Therefore, the fracture surface was rough. This may suggest that propagation of the cracks has been impeded and forced to frequently change directions. As a result, the fracture surface becomes rough, as shown in Figures 7.13 (a) and (b). This effect may enhance the fracture toughness of nanocomposites. This also indicates that the failure mode is a tough fracture. The pristine SWNTs were dispersed in the resin but some tube aggregations can still be seen, as shown in Figures 7.13 (c) and (d).

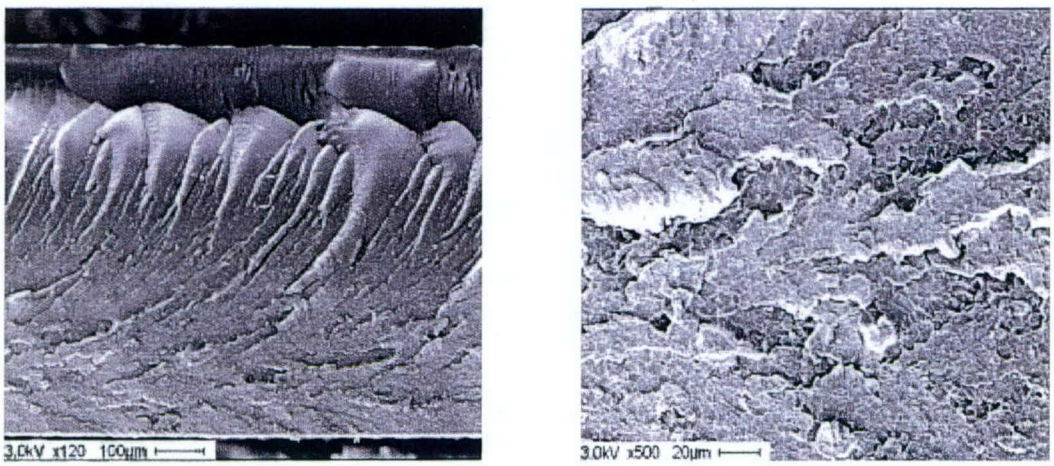

(a) (b)

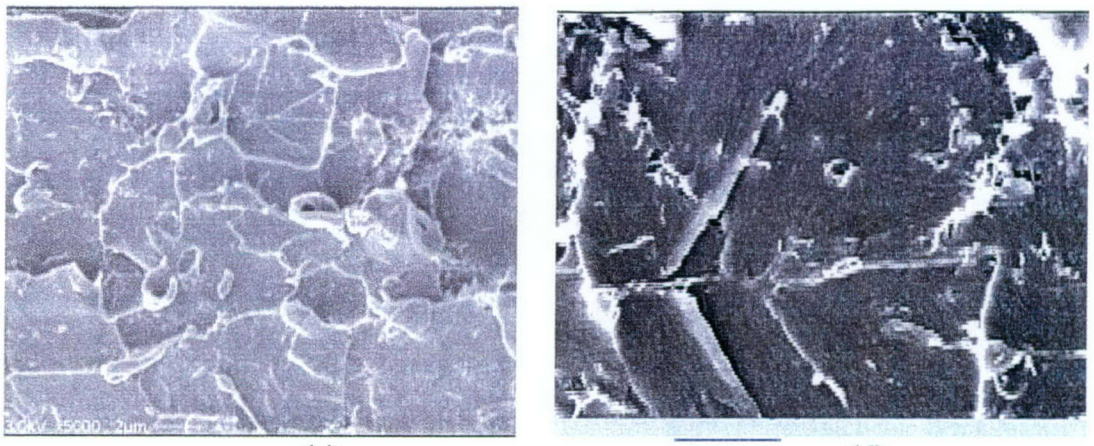

(c) (d)

Figure 7.12 Fracture surface and tube dispersion of 1wt% pristine SWNT/EPON 862 nanocomposites

The SEM images of 1%wt oxidized SWNT/EPON 862 nanocomposites are provided in Figure 7.13. From all images, the pattern of fracture surface has many parallel cracks, and the fracture surface does not look rough, as seen in Figure 12. This may be due to damage of the tubes or possible good interfacial bonding by functionalization of nanotubes. Neither tubes pullout nor aggregation could be observed. Only very short SWNTs (small white particles in the pictures) could be seen separately in the local region, which may indicate good tube dispersion by using the oxidized nanotubes. However, the smaller aspect ratio of the oxidized tubes may be the primary reason for lower mechanical properties of the resultant nanocomposites.

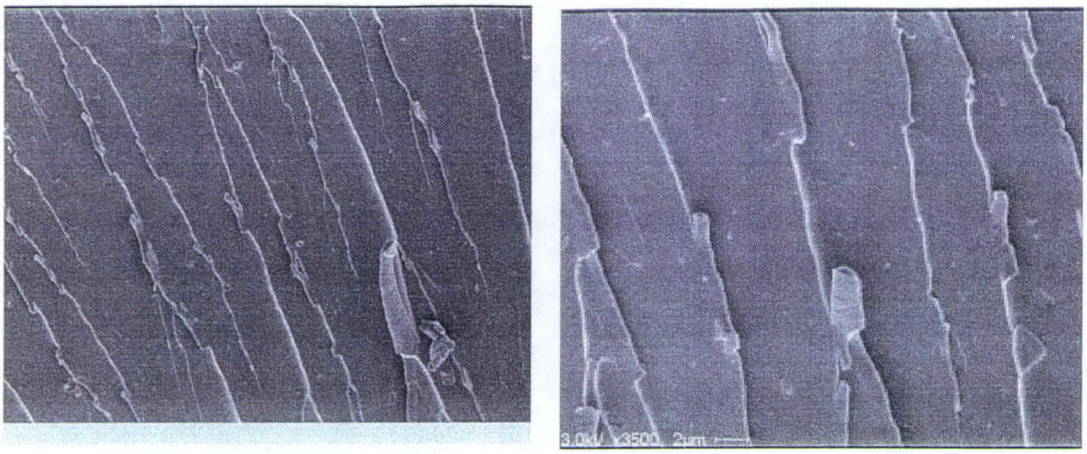

Figure 7.13 Fracture surface and tube dispersion of 1wt% oxidized SWNT/EPON 862 nanocomposites

Figure 7.14 shows the fracture surface of 1wt% GA wrapped SWNT/EPON862 nanocomposites. In Figures 7.14 (a) and (b), the fracture surface does not look very rough. Figure 7.14 (c) shows that the wrapped tubes were dispersed in the resin but some tube aggregation can still be seen. A large number of pullouts of tubes to bridge the cracks can be seen in Figure 7.14 (d), which is a strong indication of good tube bonding and load transfer in the resin matrix. As seen in Figure 7.14 (d), the GA wrapped SWNTs have good adhesion at the roots of the pullouts. This good interfacial bonding and elimination of tube damages from the tube functionalization of GA wrapping contribute to the visible increase of the nanocomposite mechanical properties in the research.

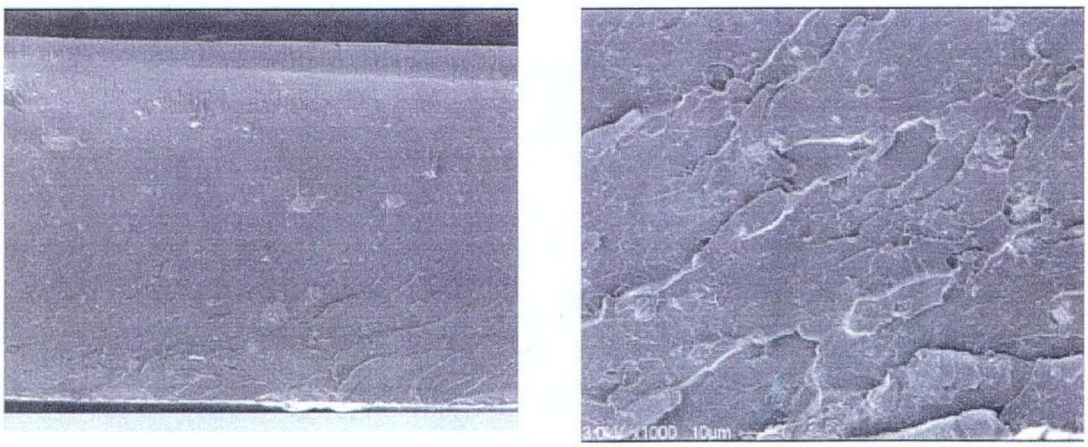

(a) (b)

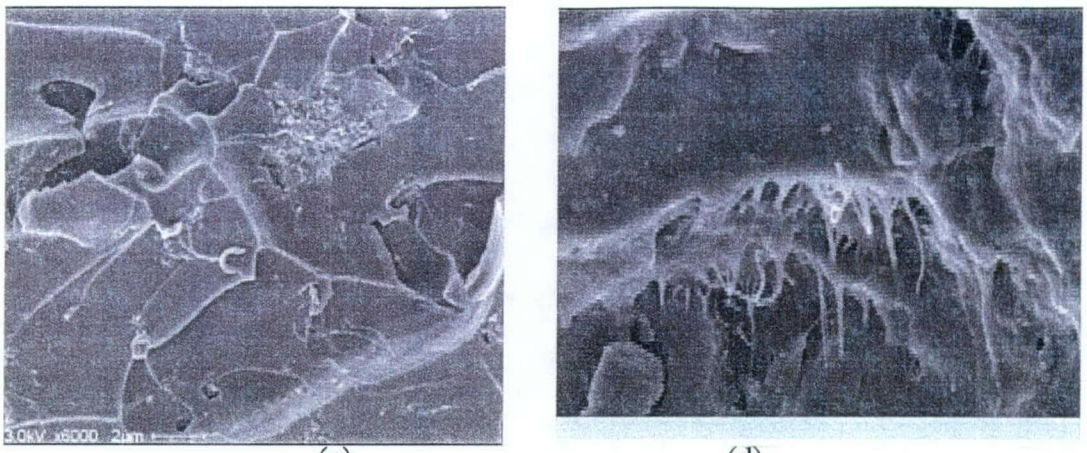

(c) (d)

Figure 7.14 Fracture surface and tube dispersion of 1wt% GA wrapped SWNT/EPON 862 nanocomposites

7.7. Conclusions

A preliminary study was conducted to investigate the functionalization of SWNTs for enhancing dispersion and interfacial bonding in casting composite samples. Two methods, oxidization and GA molecular wrapping, were used in this project for functionalizing the SWNTs. The influences of the functionalization on tube geometry and chemical structures were analyzed by AFM and Raman spectrum analysis. The damages of the tube structure during oxidization were observed. Casted nanocomposites of 1wt% pristine and functionalized tubes were produced. DMA results show that the storage moduli of the pristine and GA wrapped SWNTs nanocomposite increased 11.37% and 21.87%, respectively, compared to that of the neat resin sample. However, the oxidized nanotube composites showed a 4% storage modulus decrease. The influences of tube functionalization on dispersion and interfacial bonding were examined.

7.8. References

[1] P. Cheol and J.S. Emilie, *Proceeding of ICCE/9*, pp. 599-600, 2002.

[2] C.F. Fan and T. Cagin, *Journal of Chemical Physics*, 103 (20), 9053 (1995).

[3] M.S. Dresselhaus, D. Dresselhaus, R. Ratio, *Physical properties of carbon nanotubes*, Imperical College Press, London, 1999.

[4] Dresselhaus MS, Dresselhaus G, Eklund PC. *Science of fullerenes and carbon nanotubes*. San Diego: Academic Press, 1996.

[5] E.T. Thostenson, Z.F. Ren and T.W. Chou, "Advances in the Science and Technology of Carbon Nanotubes and Their Composites: a Review," *Composites Science and Technology*, 61:1899, 2001.

[6] K.T. Lau and D. Hui, "The Revolutionary Creation of New Advanced Materials-Carbon Nanotube Composites," *Composites Part B*, 33:263, 2002.

[7] Dillon, A.C., Jones, K.M., Bekkedahl, T.A., Kiang, C.H., Bethune, D.S.,Heben, M.J. "Storage of hydrogen in single-walled carbon nanotubes," *Nature*,Vol.386, pp.377-379, 1997.

[8] T.W. Ebbesen, P.M. Ajayan, H. Hiura, K. Tanigaki, "Purification of nanotubes" *Nature*, Vol.367, pp.519-521,1994.

[9] J.M.Kneller, R.J.Soto, S.E. Surber, T. Pietraβ, J.-F. Colomer, .A.Fonseca, J.B.Nagy, "TEM and laser-Polarized 129Xe NMR characterization of oxidatively purified carbon nanotubes," *J.Am. Chem. Soc.*, Vol.122, pp.10591-10597, 2000.

[10] I.W. Chiang, B.E. Brinson, A.Y. Huang, P.A. Willis, M. J. Bronikowski, J. L. Margrave, R.E. Smalley, and R.H.Hauge, "Purification and characterization of single-wall carbon nanotubes (SWNTs) obtained from the gas-phase decomposition of CO (HiPco Process)" *J. Phys. Chem.B*, Vol.105, pp.8297-8301, 2001.

[11] D.B. Mawhinney, V.Naumenko, A. Kuznetsova, J.T. Yates. Jr., J.Liu, R.E. Smalley, "Infrared spectral evidence for the etching of carbon nanotubes: ozone oxidation at 298 K," *J.Am. Chem. Soc.*, Vol.122, pp.2383-2384, 2000.

[12] G. Sipos-Nagy, A. Dombi, Ozone, "Decomposition of halogenated methanes in oxygen-free gas mixtures by the use of a silent electric discharge," *Sci. Eng.*, Vol.18, pp.141, 1996.

[13] Rinzler, A., Liu, J., Dai, H., Nikolaev, P., Huffman, C., Rodriguez Macias, F., Boul, P., Lu, A., Heymann, D., Colbert, D. T., Lee, R.S., Fischer, J., Rao, A., Eklund, P.C., Smalley, R.E., "Large-scale purification of single-wall carbon nanotubes: process, product, and characterization", *Appl. Phys. A*, Vol.67, pp.29-37, 1998.

[14] H. Hiura, T.W. Ebbesen, K. Tanigaki, "Enhancement of adsorption inside of single-walled nanotubes:opening the entry ports," *Adv. Mater.*, Vol.7, pp.275, 1995.

[15] E. Dujardin, T.W. Ebbesen, A. Krishnan, M.M.J. Treacy, "Purification of single-shell nanotubes," *Adv, Mater.* Vol.10, pp.611-613, 1998.

[16] K. Hernadi, A. Siska, L. Thien-Nga, L.Forro, I. Kiricsi, "Reactivity of different kinds of carbon during oxidative purification of catalytically prepared carbon nanotubes," *Solid State Ionics*, Vol.141, pp.203-109, 2001.

[17] Liu, J., Rinzler, A.G., Dai, H.J., Hafner, J.H., Bradley, R. K., Bol, P.J., Lu, A., Iverson, T., Shelimov, K., Huffman, C.B., Rodriguez Macias, F., Shon, Y.0S., Lee, T.R., Colbert, D.T., Smalley, R.E., "Fullerene pipes," *Science* Vol.280, pp.1253-1256. 1998.

[18] Anya Kuznetsova, Irene Popva, John T. Yates, Jr., "Oxygen-containing functional groups on single-wall carbon nanotubes: NEXAFS and vibrational spectroscopic studies," *J. Am. Chem. Soc.*, Vol. 123, pp.10699-10704, 2001.

[19] [35] Kneller, JM, RJ Soto, SE Surber, T. Pietraß, JF Colomer, A. Fonseca, J. B.Nagy, and Gv Tendeloo, "TEM and laser-polarized 129 Xe NMR characterization of oxidatively purified carbon nanotubes," *J. Am. Chem. Soc.*, Vol. 122, pp. 10591-10597, 2000.

[20] Kuznetsova, A., Mawhinney, D.b., Naumenko, V., Yates, J. T., Jr., Liu, J., Smalley, R.E. "Enhancement of adsorption inside of single-walled nanotubes: opening the entry ports," *Chem. Phys. Lett.*, Vol.321, pp.292-296, 2000.

[21] E.T. Mickelson, I.W. Chiang, J. L. Zimmerman, P.J. Boul, J. Lozano, J. Liu, R.E. Smalley, R.H. Hauge, J.L. Margrave, "Solvation of fluorinated single wall carbon nanotubes in alcohol solvents," *J. Phys. Chem. B*, Vol.103, pp.4318-4322, 1999.

[22] Star, A., Stoddart, J.F.,Steuerman, D., Diehl, M., BoukaiA., wong, E.W., Yang, X. Chung, S. W. Choi, H. Heath, J.R.," Preparation and properties of polymer-wrapped single-walled carbon nanotubes," *Angew. Chem. Int. Ed*, Vol.40, pp 1721-1725, 2001.

[23] Uwe H. F. Bunz, "Poly(aryleneethynylene)s: syntheses, properties, structures, and applications," *Chem. Rev.,* Vol.100, pp.1605-1644, 2000.

[24] Ago, H., Petritsch, K.,Shaffer, M.S. P., Windle, A.H., Friend, R. H., "Composites of carbon nanotubes and conjugated polymers for photovoltaic devices," *Adv. Mater.* Vol.11, pp.1281-1285, 1999.

[25] Ago, H., Shaffer, M. S. P., Ginger, D.S., Windle, A.H., Friend, R. H., "Electronic interaction between photoexcited poly(p-phenylene vinylene) and carbon nanotubes," *Phys. Rev. B*, Vol.61, pp.2286-2290 , 2000.

[26] David W. Steuerman, Alexander Star, Riccardo Narizzano, Hyeon Choi, Ryan S. Ries, Claudio Nicolini, J. Fraser Stoddart and James R. Heath, "Interactions between conjugated polymers and single-walled carbon nanotubes," *J. Phys. Chem. B*, Vol.106, pp.3124-3130, 2002.

[27] MJ O'Connell, P. Boul, LM Ericson, C. Huffman, YH Wang, E. Haroz, C. Kuper, J. Tour, KD Ausman and RE Smalley, "Reversible water-solubilization of single-walled carbon nanotubes by polymer wrapping," *Chem. Phys. Lett.*, Vol. 342, pp.265-271, 2001.

[28] Rajdip bandyopadhyaya, Einat Nativ-Roth, Oren Regev, Rachel Yerushamlmi-Rozen, Nano Lett., "Stabilization of individual carbon nanotubes in aqueous solutions," Vol. 2, pp.25, 2002.

[29] Robert J. Chen, Yuegang Zhang, Dunwei Wang, and Hongjie Dai, "Noncovalent sidewall functionalization of single-walled carbon nanotubes for protein immobilization," *J. Am. Chem. Soc.*, Vol.123, pp.3838, 2001.

8. Prototype of Manufacturing Process for Buckypaper/Foam Wing Structure

For this project, a subscale prototype LOCAAS extensional wing structure using the developed SWNT buckypaper-reinforced nanocomposite technology was fabricated to demonstrate the feasibility of manufacturing composite structures using the developed technique.

8.1. Structure Design

The concept of LOCAAS extensional wing structure is shown in Figure 8.1. LOCAAS will provide an extra-long patrol time of the missile to acquire and strike high value targets. Figure 8.2 shows the structural design and material selection for manufacturing the subscale wing structure. In the design, the unidirectional (UD) carbon fiber frame and structural foam core provide stiffness for the structure. The thin skin of two-layer buckypaper/epoxy composites on the wing surface provides lightweight, additional strength for the structure.

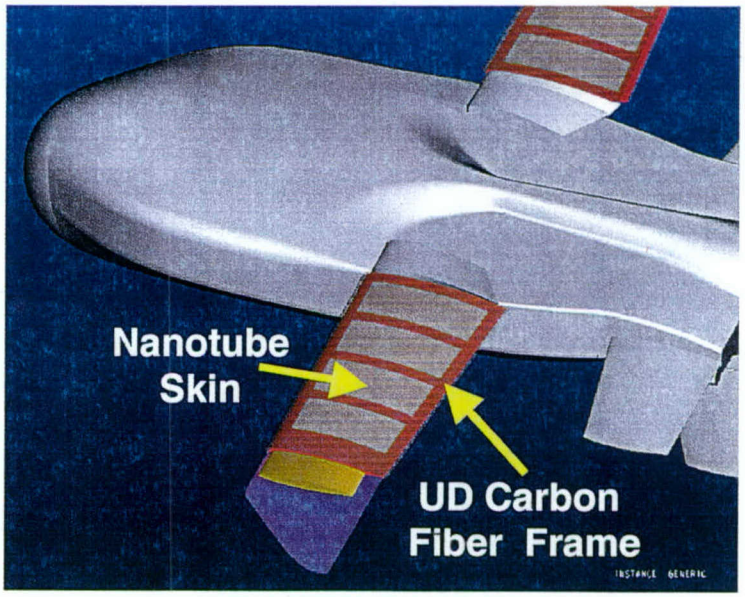

Figure 8.1 Concept of the extensional wing design

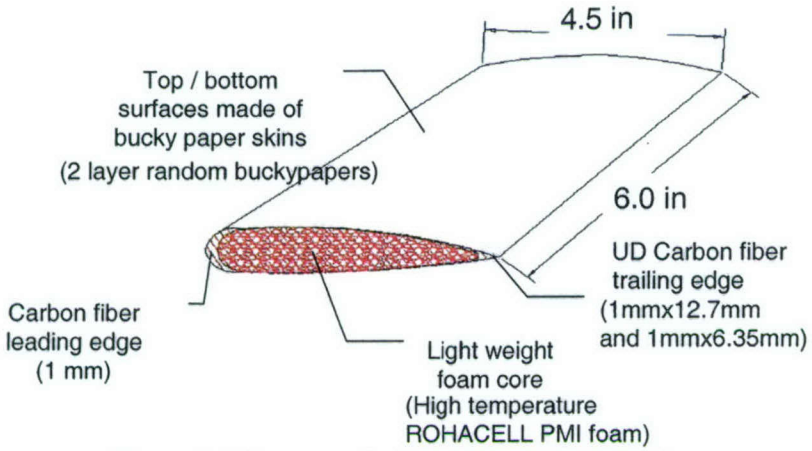

Figure 8.2 Structure design and material selection

8.2. Development of the Manufacturing Process

Using room temperature curing epoxy resin (Western 105), the wing structure was manufactured with a vacuum bagging/co-curing method. Since the wing structure has a symmetric geometry, to simplify the manufacturing process, the wing was fabricated in two halves separately along its symmetric plane, and then the halves were bonded together to form the wing structure. The geometry of the wing structure was designed and provided by Lockheed Martin Missiles and Fire Control – Orlando. A steel mold was designed and manufactured using a CNC machine, as shown in Figure 8.3. The three-piece mold design allows for demolding easily, since the buckypaper/epoxy skin is very thin.

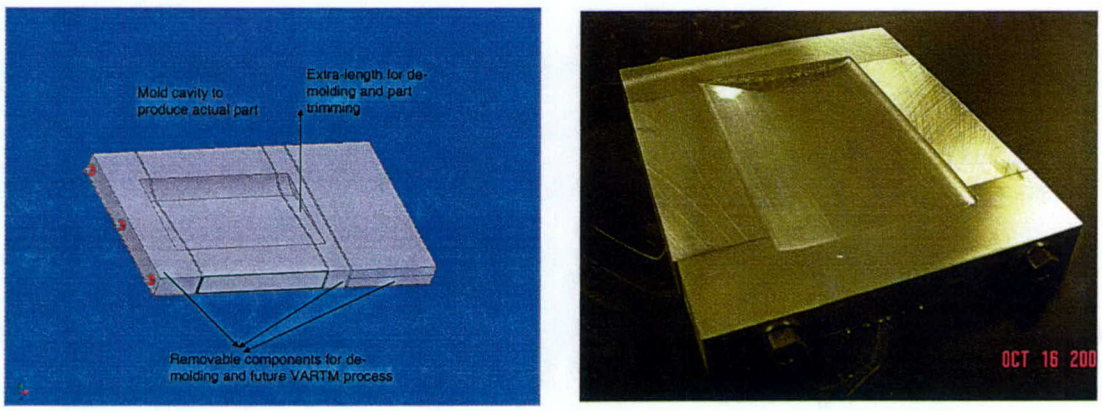

Figure 8.3 Design and the manufactured steel mold

The ROHACELL PMI structure foam (2.0 lbs./cu. Ft) was selected to manufacture the core for the fabrication of the wing. The foam was machined to the desired geometry with

a CNC machine. The conduits for positioning unidirectional carbon fiber frames were also machined out on the foam core structures.

The procedure of the wing manufacture involved several steps. The resin-impregnated carbon fiber tows were laid into the conduits on the foam core structure according to the design requirement, as shown in Figure 8.4. Then, the epoxy resin wet the produced randomly oriented buckypapers (Chapters 2 and 3) and placed on the surface of the foam core with UD carbon fiber frames. Finally, a vacuum bag was used for co-curing the UD carbon fiber frame and resin-impregnated buckypaper on the foam core to make the final integrated sandwich structure, as shown in Figure 8.5. The wing structure was cured overnight at room temperature.

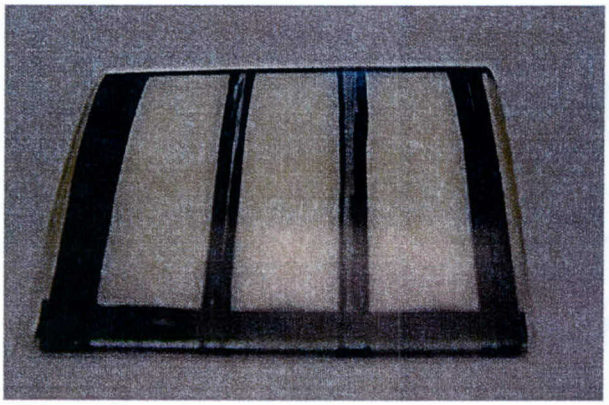

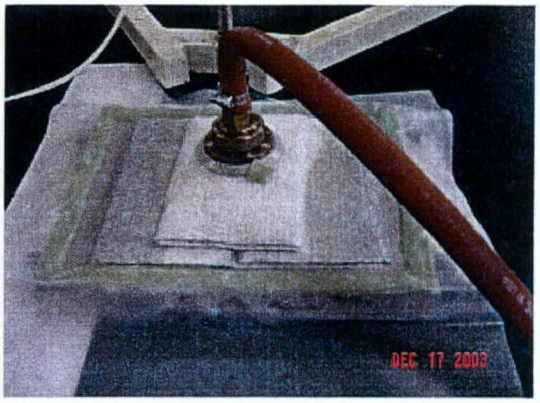

Figure 8.4 Foam core with UN carbon fiber frames Figure 8.5 Vacuum bag processing

8.3. Final Wing Structures

Figure 8.6 shows the final wing structure fabricated in the project. The finished wing structure has a very good surface quality and the thin (~ 120 microns) buckypaper/epoxy skin completely cover the foam core surface and form the lightweight sandwich structure.

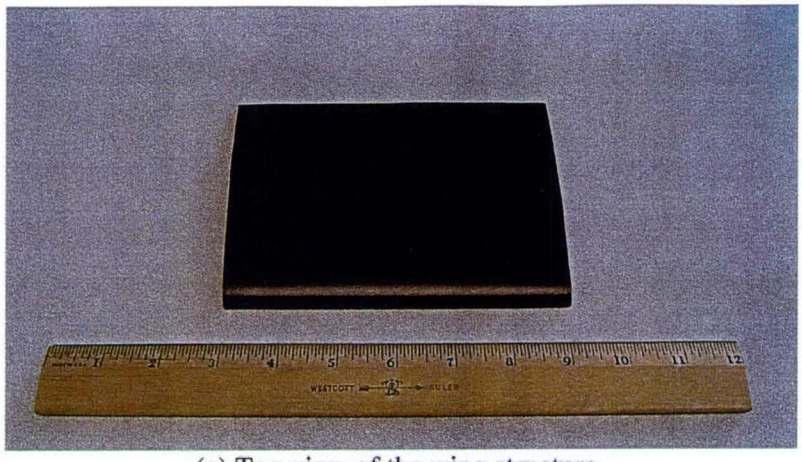

(a) Top view of the wing structure

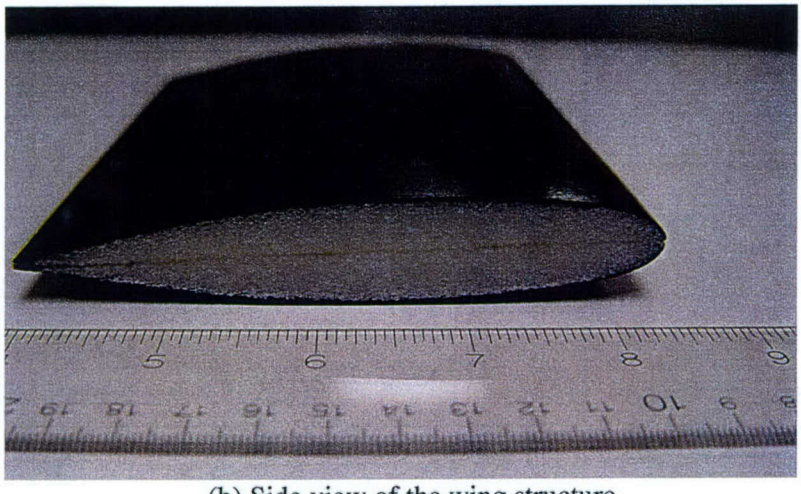

(b) Side view of the wing structure

Figure 8.5 Finished wing structure

8.4. Conclusions

The subscale extensional sandwich structure demonstrating the feasibility of using buckypaper/epoxy resin nanocomposites was successfully fabricated. The produced buckypapers have a very good processibility and can be handled as surface veil materials in the manufacture process. A wide range of applications of the lightweight, high electrical and thermal conductivities of the buckypaper/epoxy resin composite structures can be expected.

9. Conclusions

SWNTs possess remarkable mechanical, electrical and thermal properties, which exceed those of any existing composite reinforcement materials, such as IM7 carbon fibers. However, using nanotubes as reinforcements to produce quality composites is still a very challenging issue due to their nanoscale dimension, unique chemical characteristics and intensive molecular interactions of the nanotubes and resin molecules during composite processing.

In this research, a novel technical approach of buckypaper/resin infiltration was developed to fabricate bulk polymeric nanocomposites with controlled nanostructures, desired alignment and high tube loading. The influences of suspension concentration, type of surfactant, strength of magnetic field, as well as sonication and filtration parameters on the quality and tube alignment of buckypaper materials were investigated. Good tube dispersion and uniform pore structure of the produced buckypaper was demonstrated. Significant tube alignment in the magnetically aligned buckypapers was observed. A systematical characterization and model of the nanostructure and quality of the produced buckypapers was conducted. The results can be used for further prediction and optimization of buckypaper processing. The results also show that the developed new processing approach can effectively fabricate nanotube composites with controlled nanotube network structures. The storage modulus of the magnetically aligned nanocomposites was as high as 45 GPa. The produced nanocomposites can have nanotube loading from 20w/w% to 60w/w%. Both good dispersed tube networks and good tube alignment have been observed in the resultant random and aligned nanocomposites. During the research, the world's largest magnetically aligned buckypaper with a working area of 60 in^2 was successfully manufactured, which provides the possibility for making bulk nanocomposites or devices with desired tube orientation.

The influences of the formation of tube ropes in SWNT-reinforced nanocomposites were revealed by using composite models of short fibers and observed nanostructures of the produced buckypaper and nanocomposites. The effects of the molecular interactions

between SWNTs and the resin matrix molecules on processing and interface of the composites were also explored using molecular dynamic simulation, which revealed that both EPON 862 and DETDA curing agent molecules tried to wrap on the surface of the SWNT due to van der Waals force, indicating attractive interactions. The result of SWNT pullout simulation based on molecular models of SWNT/EPON 862 resin matrix indicated that the interfacial shear stress was about 75 MPa, which is higher than that of fiber reinforced composites but still is not as high as expected for SWNT composites. This research project also shows that molecular wrapping of SWNTs is an effective method to enhance the interface in the nanocomposites.

The electrical and thermal conductivities of the produced buckypapers and nanocomposites were also measured. The aligned buckypaper can achieve 9.46 anisotropy ratio of electrical resistivity and 42 W/m/K thermal conductivity along tube alignment direction. Finally, a subscale sandwich wing structure using buckypaper-reinforced composites was successfully constructed to demonstrate the feasibility for structural applications.

This project demonstrated the feasibility of using buckypaper/resin filtration process to make nanocomposites with controlled nanostructure and high tube loading, which is critical for developing high performance composite materials. The amount of nanostructure and property data provided from this research will enhance our understanding of nanocomposite processing and properties.

10. Acknowledgements

This work is supported by MN and ML Directorates of the Air Force Research Laboratory (Grant #: F08630-01-1-0010). The authors would like to thank the project managers, Mr. Charles Cottrell, Mr. John Busbee, Mr. Chuck Wagner and Dr. Steve LeClair, for supporting this research effort. The authors would also like to thank the support of the National High Magnetic Field Laboratory (NHMFL).

We also would like to acknowledge the other contributors for this research at the FAMU-FSU College of Engineering and NHMFL:

Dr. James Simpson

Dr. James Brooks

Dr. Eun Sang Choi

Dr. Jihua (Jan) Gou

Mr. Zhi (Michael) Wang

Mr. Gonnet Philippe

Mr. Ravi Shankar

Mr. Olivier Marietta-Tondin

Ms. Liao (Ashley) Yu-Hsuan

Ms. Yeh (Irene) Chreng-Shii

Ms. Oni Sadiki

Mr. Clinton Baker

Mr. Kevin Barefield

Mr. Blake Cullum

DISTRIBUTION LIST
AFRL-MN-EG-TR-2004-7112

Defense Technical Information Center Attn: Acquisition (OCA) 8725 John J. Kingman Road, Ste 0944 Ft Belvoir, VA 22060-6218	1

EGLIN AFB OFFICES:

AFRL/MN CA-N	1
AFRL/MNOC (STINFO Office)	1
AFRL/MNA	1
AFRL/MNG	1
AFRL/MNM	1
AFRL/MNAV	3
AFRL/ML CA-N	1